TENSION STIFFENING AND CRACK WIDTHS IN REINFORCED CONCRETE BEAM AND SLAB ELEMENTS

Dissertation submitted to the University of Cambridge for the degree of Doctor of Philosophy

by

Marwan Alfred KISHEK

Selwyn College

December 1983

PREFACE

The research described in this dissertation was carried out in the Engineering Laboratories of the University of Cambridge between October 1979 and December 1983.

I wish to record here the fact that the most important of the findings I came across during my research period in Cambridge is not discussed in this dissertation. I have come to discover the reality and truth of God's unfailing love to me as I encountered the person of the risen Lord Jesus Christ through the power of the Holy Spirit. As a result of receiving the Lord into my Life, I was granted, along with other gifts, a qualification that is far more significant than the one to which I am a candidate: I was made a child of the living God in fulfilment to the promise ...

> "Yet to all who received him (the Lord Jesus), to those who believed in his name, he gave the right to become children of God." [1]

I would like to express my gratitude to my parents for bringing me up, among other things, on the love of knowledge and education. In particular, I note with thankfulness the efforts they provided which led to my coming up to Cambridge and their generous-unlimited moral and financial support since.

I am very grateful to my supervisor, Dr. C.T. Morley, who first introduced me to the research topic, for his invaluable advice and wise guidance as well as his very helpful co-operation throughout the period of my research.

I would also like to extend my gratitude to all who assisted me in various ways in carrying out the work described in this dissertation. In particular, my thanks are due to:

Dr. L.A. Clark, Lecturer at Birmingham University, for prompt co-operation in sending his experimental test results from tests on beams and slabs [51],[57] used in Chapter 3;

Mr. C.J. Mason of the Concrete Laboratory for help beyond measure,

Mr. R. Buck of the Concrete Laboratory;

Mr. E. Silk and his staff, Miss. J. Barlow, Mr. B.Symes and Mr. P. Radford, of the Structures Research Laboratory;

Mr. A. Timbs and the staff of the Design Office,

Mr. R. Julian and the staff of the Instrument Workshop,

Mr. W. Gillman and the staff of the Machine Workshop;

Mr. J. Flaxman of the Carpentery Workshop,

Mr. B. Butler of the Materials Laboratory,

Mr. R. Denston of the Stress Laboratory;

Mr. D. Travis for his efficiency and patience in typing the text,

Miss. D. Gray and the staff of the printing service of the C.U.P.

This Dissertation is the result of my own work, unless otherwise stated in the text, and includes nothing which is the outcome of work done in collaboration. I further state that no part of this dissertation has already been or is being concurrently submitted for any degree, diploma or other qualification at any other university.

M.A. KISHEK

SUMMARY

A new method is developed of representing the tension stiffening of cracked tensile concrete in r. c. beams and slabs, by modifying the properties of the main reinforcing steel. This new method was derived from experimental data from specimens with only longitudinal steel bars and extended to cover specimens with steel bars running at an angle to the principal stresses' direction.

Experiments on slabs with skew reinforcement tested in uniaxial bending are described. They provide direct information on the effect of the angle between the direction of reinforcing bars and the principal bending direction on crack widths and the tension stiffening effect of concrete between major cracks.

The analysis of more than 4200 crack width measurements has led to a new hypothesis for cracking over reinforcing bars which cross the cracks at an angle. A new formula for predicting crack widths in such situations was derived. A procedure is given for calculating the crack width at any point on the surface of an r. c. member taking into account the interaction between two intersecting sets of steel reinforcement.

The work on tension stiffening has led to formulae for calculating 'enhanced stress' - strain curves for the tension steel. These curves have been successfully used to model the tension stiffening of concrete in a nonlinear structural analysis of flexural r. c. members by computer.

TABLE OF CONTENTS

NOTATION

The following is a list of the main symbols used in the dissertation; it does not include symbols that are used locally. The symbols are also defined in the text as they occur.

A is the area of concrete symmetric with reinforcing steel divided by number of bars

a_{cr} is the distance from point of measurement of crack to surface of nearest reinforcing bar

α is a factor giving the average concrete tensile stress as a proportion of the average tensile stress in concrete at $F_t = F_{tp}$

A_s is the cross-sectional area of the tension steel

A_{tm} is the average area of concrete below the neutral axis

a_{x1}, a_{x2} are the space distances from grid lines type B1 and B2 to nearest bar in directions 1 and 2 respectively, both measured in the direction of cracks

b is the breadth of the cross-section of an r. c. member

β is a factor defining the effective area of concrete contributing to the tension stiffening

c is the minimum cover

$C1$, $C2$ are respectively the larger and smaller average covers in the rectangle of concrete surrounding a particular bar as defined in Figure 2.2-6

D is the diameter of the reinforcing bar

d_c is the depth of the average compressive force below comp. face

δ is the angle between the reinforcement direction and that of the principal stresses

d_s is the depth of main tension steel measured from the compression face

d_t is the depth of the total tensile force measured from the compression face

d_{ts} is the depth of the line of action of the tension stiffening force F_t measured from the compression face

d_{s1}, d_{s2} are the effective depths of reinforcement in directions 1 and 2

E_c is the initial tangent modulus of elasticity for concrete

ε is the average surface strain at the level where the crack width is sought

ε_s is the steel strain

ε_{sm} is the average steel strain

ε_{sp} is the average strain at steel level when tension stiffening is maximum

F_t is the tension stiffening force

f_t is the concrete tensile strength

F_{tp} is the peak value of F_t

h is the overall depth of the member

h_o is the initial crack height

h_{tm} is the average height of the tension zone

K_1, K_2, and K_3 are constants which are chosen so that the calculated crack width has some specified chance of being exceeded; values are given in Tables 2.2-1 and 2.2-2

k_1, k_2, and k_3 are coefficients that determine the manner of decay of tension stiffening and are given by Equations 3.4-30 and 3.4-31

l_i is the length of the part of the grid line, running in the direction of bars of set i, within one region

l_{oi} is the length projected from l_i on to the principal bending direction

n_r is the number of regions of the type under consideration

n_{cr} is the number of cracks measured in a certain region at a given load stage

M_a is the applied bending moment

ρ_e is the effective steel percentage (i.e. the steel area as a ratio of the concrete area below the neutral axis)

s_{cr} is the average crack spacing

σ_{cu} is the cube strength of concrete in compression

σ_s is the steel stress

σ_{se} is the enhanced stress in the tension steel corresponding to an average strain ε_{sm}

σ_{sm} is the average tensile stress in the tension steel found from the uniaxial stress-strain curve for the bare steel bar

σ_{scr} is the stress in the steel just after cracking and neglecting concrete in tension

σ_{sy} is the steel characteristic strength

s_1 and s_2 are the spacings of the steel bars in directions '1' and '2'

t is the distance from the point considered to the center of the nearest bar

t_c is the thickness of cover from tension face to center of nearest bar

W is the crack width at the point considered

W_o is the crack width directly over a bar where $a_{cr}=c$

W_{lim} is the crack width which is approached as $a_{cr} \rightarrow \infty$

$W_{n\%}$ is the crack width with n% chance of being exeeded

x is the neutral axis depth found by the modular ratio method neglecting concrete tension

x_m is the average neutral axis depth

x_p is the average n.a. depth for $F_t = F_{tp}$

y is the distance, measured from the netural axis, of the point at which thw crack width is sought

Ψ is the angle between the reinforcement direction and that of cracks

Subscripts

av	average	n	normal (perpendicular)
c	concrete, compressive	o	naught, initial
cr	cracking, critical	p	peak
e	enhanced, effective	r	ratio
i	initial, a direction	s	steel
j	a second direction	t	tension, tensile
lim	limiting	u	ultimate
m	mean, average	un	uncracked
max	maximum	y	yield

1. INTRODUCTION

The main subject of the dissertation is prediction of crack widths and post-cracking stiffness of reinforced concrete members in bending. In order to set the work described in the dissertation in context, brief descriptions are first given (Sections 1.1 to 1.5) of concrete, reinforced concrete and methods of design for reinforced concrete structures. Outlines of the scope of the dissertation and the order of presentation of the material are then given in Sections 1.6 and 1.7.

1.1 Structural Concrete

Concrete is an artificial stone-like material that consists of a carefully proportioned mixture of inert materials called aggregates (sand, gravel, crushed stone, etc.) with cement and water. The cement and water interact chemically to bind the aggregate particles into a solid mass that has the shape of the formwork into which the concrete is cast. The resulting hardened concrete possess a high compressive strength but a low tensile strength. This makes concrete unsatisfactory for use in members subject to axial tension, such as tie rods, or in members subject to bending, such as beams and slabs.

However, it has been found possible to use steel bars to reinforce concrete, mainly in the tension zones where the small tensile strength of the concrete would limit the carrying capacity of the member. The reinforcing steel bars (with their high tensile strength) are placed in the forms before casting the concrete mix. When completely surrounded by hardened concrete, the bars form an integral part of the member and the two materials act together as one mass through bond at the concrete-steel interface. The resulting concrete element reinforced by steel is called reinforced concrete (r.c.).

As a building material, reinforced concrete combines many of the following advantages of its constituent materials:

(1) Relatively low cost.

(2) Good weather and fire resistance.

(3) High strength and toughness due to the high compressive strength of the concrete and the high tensile strength, ductility and toughness of the steel.

(4) Good protection for the steel from corrosion, by the surrounding concrete.

One of the main factors which make reinforced concrete a universal building material is the facility with which it can be formed to almost any practical required shape.

1.2 Limit State Design

The object of design is the achievement of acceptably low probabilities that the structure being designed will become unfit for the use for which it is required, during some specified design life. A structure, or a part of a structure, is considered unfit for use when it has passed through a particular state, called a limit state, beyond which it infringes one of the criteria governing its performance or use.

The limit states can be placed in two categories:

(a) the ultimate limit states, which are those corresponding to the maximum load-carrying capacity; and

(b) the serviceability limit states, which are related to the criteria governing normal use and durability.

The ultimate limit state provides adequate safety against failure (including overturning, buckling, etc.) due to elastic, plastic or dynamic instability. Meanwhile, the serviceability limit states ensure that the

deflection of a structure, or any part of a structure, will not adversely affect the appearance and efficiency of the structure; and that any cracking of the concrete will not adversely affect its appearance or durability.

Of the serviceability limit states, those of excessive flexural deflection and of excessive flexural cracking are currently the two that should normally be considered in design. However, other limit states might be considered in design for unusual or special functions.

The usual approach will be to design on the basis of the most critical limit state and then to check that the remaining relevant limit states will not be reached.

1.3 Governing Design Criterion

Traditionally, the only design criterion for reinforced concrete structures was that of safety against outright failure. However, in recent years, many situations are met in which crack control and/or deflection control are the governing design criterion. Such situations arise as a result of some or all of the following factors:

(1) The widely-spread use of ultimate strength methods of design for r.c. structures and the resulting reduced depths of beam and slab sections as compared with those calculated using the traditional elastic theory.

(2) The use of high strength materials and the associated high strains in the steel.

(3) Increasing permissible steel stresses over the years.

(4) The choice of long spans of minimum depth for economical and architectural reasons.

In design, to limit crack widths in a reinforced concrete structure, suitable formulae are needed for predicting the crack widths anywhere on a r.c. member. Likewise, to limit deflections to the specified allowable

values, a suitable method for calculating the actual stiffness of any given r.c. member should be available. In both cases, calculations should yield reasonably accurate values or else the limiting criteria will be rendered meaningless.

1.4 Design for Serviceability Limit State

Research on cracking and on stiffness of r.c. members has occupied the attention of many investigators and workers in the concrete field. Experimental and theoretical work has been carried out in different places as reviewed in Chapter 2. However, the subject is not fully investigated and there are areas where further research is needed as for example situations in which the cracks form at an angle ψ to the main reinforcing direction in slab and plate elements.

1.4.1 Effect of bar direction

The directions of steel bars in reinforced concrete members are usually fixed by practical and constructional requirements. Thus in many cases (e.g. deep beams, web of T-beams, etc.), cracks do not form perpendicular to the reinforcing steel, since the direction of reinforcement in those cases is not the same as that of the principal stresses. In such cases, wider cracks and less stiffness, compared with the case where the direction of the main reinforcement coincides with that of the principal stresses, will be obtained. This was indicated by experiments carried out by J. Peter [11] and others [32],[34],[35]. However, the number and conclusions of such experiments are limited and indecisive and more experiments are needed in which the effect of the angle ψ on cracking and stiffness is isolated and studied.

1.4.2 Interaction between cracking and stiffness

The stiffness of reinforced concrete members is greatly affected by the cracking phenomenon. The presence of cracks subjects the concrete medium to discontinuities so that the behaviour of the r.c. elements cannot be considered by a simple extension of elastic theory from elementary

strength of materials. It is therefore of great importance to investigate the way in which cracking does affect the stiffness of r.c. members and how to incorporate the factors governing cracking into formulae for calculating the actual stiffness. It is also necessary for predicting crack widths to be able to calculate the actual deformations of the r.c. element, since the calculated width of a crack will depend on the actual strain at the place where the crack width is sought. Thus, in stiffness calculations, the contribution to stiffness made by the concrete between the cracks in the tension zone should be taken into account. This contribution is quite significant at service loads and can greatly affect the calculated values of stiffness and crack widths especially in members with small amount of reinforcement.

Research on crack widths and on stiffness of r.c. members has usually been carried out separately and in most cases by different investigators. Thus, many present formulae for calculating the stiffening effect of tensile concrete do not incorporate parameters related to crack width. Meanwhile, procedures for calculating crack width, a direct function of the average surface strain at the place where the crack width is sought, use semi-empirical equations to find this average strain.

1.4.3 Nonlinear solutions for r.c. elements

Reinforced concrete is a material that exhibits a nonlinear behaviour due to cracking of concrete, yielding of steel, nonlinearity of concrete in compression, creep, shrinkage, etc. The most significant of these nonlinearities under service loads is cracking of concrete in tension. In the recent past, nonlinear numerical procedures had been developed to analyse r.c. structures by computers. Of these procedures the finite element method is most popular. However, a major difficulty with such methods is modelling the concrete material after cracking in tension. The present methods for calculating the stiffening effect of the tensile concrete for beam design are not readily used in modelling this tension stiffening in a finite element programme. Tension stiffening models currently used in nonlinear finite element analysis, though often successful, are unreliable and can cause serious problems of numerical convergence and local instability [73].

1. Crack Width Limits: Are They Necessary?

As mentioned above, the brittle behaviour of concrete in tension causes many well-designed reinforced concrete members subject to bending or tension to crack under their design service load. As far as safety is concerned, these resulting cracks are not serious but for the sake of appearance and durability, i.e. reduction in the risk of steel corrosion, it is often thought necessary to limit crack widths.

1.1 Crack widths and corrosion of steel

Most codes of practice impose a limit on crack widths nearest to the reinforcement as a provision to protect the steel from corrosion. For example, CP110 [37] states that the surface widths of cracks at points nearest the main reinforcement should not, in general, exceed 0.004 times the nominal cover of the reinforcement where members are exposed to particularly aggressive environments. The issue however is controversial.

Some recent investigations [52],[58],[75] indicate that too much attention has been paid to crack widths at the surface and too little to factors like crack shape and permeability of concrete. However, more recent exposure tests on concrete for offshore structures [77] showed that early corrosion of the reinforcement is associated with cracks in the concrete and is initiated by depassivation by chlorides which rapidly penetrate down the cracks. It was also reported that as a result, cover thickness and grade of concrete do not directly control the incidence of corrosion.

More results are expected from long term exposure tests [77] and until then the correct answer to whether crack width has a direct influence on steel corrosion in the long term is not yet known. However, there is little disagreement about the fact that narrower cracks slow down the processes which lead to corrosion and thus delay the onset of corrosion till later life [58],[76].

1.5.2 Appearance

Cracks impair the appearance of the structure and can cause dissatisfaction among its occupants as shown by research on the human response to cracking in slabs [30]. Excessive cracking can lead to serious complaints from the tenants who might eventually quit the building if nothing is done about it. I myself have a single wide crack running across the ceiling in my office and passing right over my head; though an engineer, I still feel uneasy about it.

According to reference [30], appearance is impaired when crack widths exceed 0.25 mm. This value is close to that given by CP110 [37] which specifies a maximum crack width of 0.3 mm.

The effect of cracks on the appearance of buildings is not confined to problems of visibility of the crack itself. Cracks can be stained as a result of rust being mixed up with rain water on external surfaces. Wide internal cracks can work as a hiding place for home insects where they can find the right environment to multiply. This might be more of a problem in hot countries. However, the relationship between crack width and any of these factors is not yet known.

1.5.3 Water- or air-tightness

The new BS5337 [48] allows an alternative design of water retaining structure to that traditionally practiced in which limiting crack widths are satisfied, whereas traditionally cracking is avoided by designing to very low levels of stress. The code specifies crack width limits even for cases of pure tension where the crack penetrates right through the member. Experience with water retaining structures showed that cracks tend to seal themselves and thus stop leakage.

Air-leakage problems can be met in structures such as nuclear reactors. Such structures are usually designed so that there is always a permanent compression zone in the designed sections thus making sure that cracks do not penetrate through the members. Whether significant air-leakage can be prevented by limiting crack widths in members where cracks penetrate through the section is yet to be established.

1.5.4 Crack width limits: Summary

Crack width limits are necessary and useful in many ways. They slow down the process that leads to corrosion of steel reinforcement till later life. They can prevent unsightly cracks from ruining the appearance of the structure and from causing dissatisfaction among its occupants. Finally, they can ensure liquid- or air-tightness in certain structures.

1.6 Scope of Work

This dissertation is concerned with the behaviour of reinforced concrete beams and slabs in the service range. Special attention is paid to the effect of the angle between the direction of main reinforcement and that of the principal stresses. Calculating the actual flexural stiffness after cracking and predicting the widths and spacing of flexural cracks are of major interest. The work is limited to the study of short term behaviour so that the effects of shrinkage and creep are not included.

The dissertation seeks to provide a new method for calculating the flexural stiffness of r.c. members taking into account the stiffening effect of tensile concrete between major cracks. The factors governing the cracking phenomenon were taken into consideration when evaluating the tension stiffening of concrete. The aim of this work is to find a reliable model that can embody the actual behaviour of r.c. beam and slab elements for use in nonlinear procedures, such as a finite element programme, for the analysis of complete cracked structures.

1.7 Outline of Dissertation

In Chapter 2, previous work on cracking in r.c. members and ways of predicting crack widths and spacing are reviewed. A survey is presented of literature on tension stiffening by concrete between major cracks and ways of modelling it for use in nonlinear finite element methods.

A method of representing the tension stiffening of cracked tensile concrete, by modifying the tension-steel properties, is developed in

Chapter 3. The experimental results on reinforced concrete beams and slabs in uniaxial bending tested by Clark et al [51],[57] are used to determine the modified properties of the tension steel.

Chapter 4 describes experiments carried out on 8 concrete slabs reinforced with skew reinforcement and tested in uniaxial bending. The experimental work was designed to investigate the effect of the angle δ, between the direction of the steel reinforcement and that of the principal bending, on tension stiffening and crack properties.

The results of the experiments of Chapter 4 that have relevance to the tension stiffening phenomenon are presented and discussed in Chapter 5. The new approach developed in Chapter 3 for calculating the tension stiffening and the modified steel properties is applied to the results from the slab tests. The effect of the angle δ is allowed for and the results of the analysis are discussed.

In Chapter 6, the results from the slab tests of Chapter 4 that have connection with crack width analysis are presented and discussed. A new hypothesis is given, describing cracking over a reinforcing bar that crosses cracks at an angle. Formulae based on Beeby's approach [54] are proposed for calculating crack widths in such situations both over and midway between bars.

Finally, conclusions drawn in different places in this dissertation are summarised and collated in Chapter 7 where suggestions for further research are also made.

2. REVIEW OF LITERATURE

2.1 Introduction

The purpose of this chapter is to describe the current state of knowledge of, and to provide the background to, problems related to the behaviour of reinforced concrete members in the post-cracking stage, such as crack control and the stiffening effect of concrete in tension between major cracks. It should be emphasised here that crack widths and tension stiffening are inter-related: formulae for predicting crack widths depend on the actual average surface strain and not the strain calculated ignoring concrete tension. Interaction between concrete and reinforcement affects crack spacing, crack widths, and tension stiffening simultaneously.

Also in this chapter a survey is presented of literature on modelling the stiffening effect of cracked tensile concrete for use in a nonlinear numerical procedure such as a finite element programme which considers the overall behaviour of r.c. members. This chapter is therefore organised into three sections describing previous work on crack widths, tension stiffening, and finite elements respectively.

2.2 Crack Widths and Spacing in R.C. Beams and Slabs

2.2.1 Beams

It had traditionally been accepted that the width and spacing of cracks were mainly controlled by bond failure at the points where the reinforcement passed across cracks. This meant that crack widths were related to slip of the concrete relative to the reinforcement, governed by the force that can be transmitted from the steel to the concrete and, thus,

by the bond characteristics of the steel. In the simplest form this led to the following relationship:

$$\frac{W}{D} = B\left(\frac{\varepsilon_s}{p_e}\right) \quad \ldots \qquad \ldots (2.2\text{-}1)$$

where

W is the crack width (assumed to be uniform between the steel and side of the beam);

D is the bar diameter;

p_e is the effective reinforcement ratio;

ε_s is the steel strain; and

B is a constant which depends on the type of bar used.

This basic approach may be called the bond-slip hypothesis and many variants of Equation 2.2-1 have been proposed.

In experiments, Broms [5],[6] found little influence of any of the variables in the classical formulae (such as Equation 2.2-1) and proposed the proximity of the bar as the only significant variable; thus,

$$W_{max} = K\ t\ \sigma_s \quad \ldots \qquad \ldots (2.2\text{-}2)$$

where

K is a constant;

t is the distance from the point considered to the center of the nearest bar; and

σ_s is the steel stress.

The unexpected findings of Broms were supported in a comprehensive series of tests carried out by Base and his colleagues [7],[9],[10] in which a number of variables were investigated in a programme involving the testing of 133 r.c. beams in pure bending. Little difference was found between the cracking in beams reinforced with deformed bars and plain bars and neither the number of bars nor the proportion of steel was found to be of major influence. As for the concrete properties, there was no evidence that the concrete strength or the condition of curing had a significant effect on cracking. The two important variables were found to be the proximity of steel reinforcement and the surface strain. Crack width and crack spacing were both found to be linearly related to the distance a_{cr} from the point where the crack was measured to the surface of the nearest longitudinal reinforcing bar. Meanwhile, crack width was found to be proportional to the measured surface strain ε (less than that calculated ignoring the tensile strength of concrete) at the level where the cracks were measured. This led to the following equation for the prediction of crack widths.

$$W = K' a_{cr} \varepsilon \quad \ldots \qquad \ldots (2.2\text{-}3)$$

where K' is a constant chosen to give a crack width with some specified probability of being exceeded. For deformed bars, the values of K' required to give the average and the maximum (1% probability of being exceeded) crack widths are 1.67 and 3.3 resectively.

Base et al [9],[10] proposed the 'no-slip' hypothesis that cracks taper from a certain width on the surface of the beam to approximately zero width at the steel-concrete interface. This implies that the crack width is basically a function of the elastic recovery of the concrete between major cracks and of the restraining effect of the nearby reinforcement.

The no-slip theory requires the condition that significant bond failure or slip does not occur at a crack until after the adjacent cracks have formed. Once the basic crack pattern is established, bond failure becomes irrelevant to the W-ε relation.

Although the no-slip hypothesis was found to be in much better agreement with the test results than the bond-slip hypothesis, it is still not the ideal. Experimental research on the nature of cracking (as described below) showed that although significant slip did not occur when deformed bars were used, internal failure in the form of internal cracking did occur. Thus, a better theory would be one which takes into account the 'no-slip' theory plus the effect of internal failure and/or slip.

Several attempts were made to assess how the width of cracks varied internally. Some of these attempts [58], which go as far back as 1930, used the technique of measuring the deformations of a concrete surface with a bar embedded in it. A typical result of such tests is shown in Figure 2.2-1; the concrete deformations very close to the bar could not be defined by measurement and hence no direct measurement of slip could be made.

Attempts have also been made to define the shape of cracks by filling them with resin while loaded, the load being held till the resin has set and then the specimen sawn open. This has been done by Broms [2], Atlas et al [4], Husain and Ferguson [16], and Illston and Stevens [36], all of whom found much smaller crack widths near the bar than at the concrete surface. Figure 2.2-2 gives results for the widths of cracks measured on beams with various covers but at the same steel stress: it can be seen that, though the surface crack width increases with increasing cover, the widths at the bar remain roughly constant for a given steel stress. Illston and Stevens' tests confirm the picture provided by Husain and Ferguson but add the important information that the resin was found to penetrate along the surface of the bar for a considerable distance on either side of the crack into which the resin was inserted, which indicates a degree of separation between concrete and steel in this region.

It may thus be concluded, from the experimental evidence provided so far, that cracks are not parallel-sided, as assumed in some theories, but are tapered, being smaller at the bar than at the surface. It remains necessary though to define the mechanism by which strains in the concrete close to the bar surface (when they exceed the tensile capacity) are accomodated as discussed below.

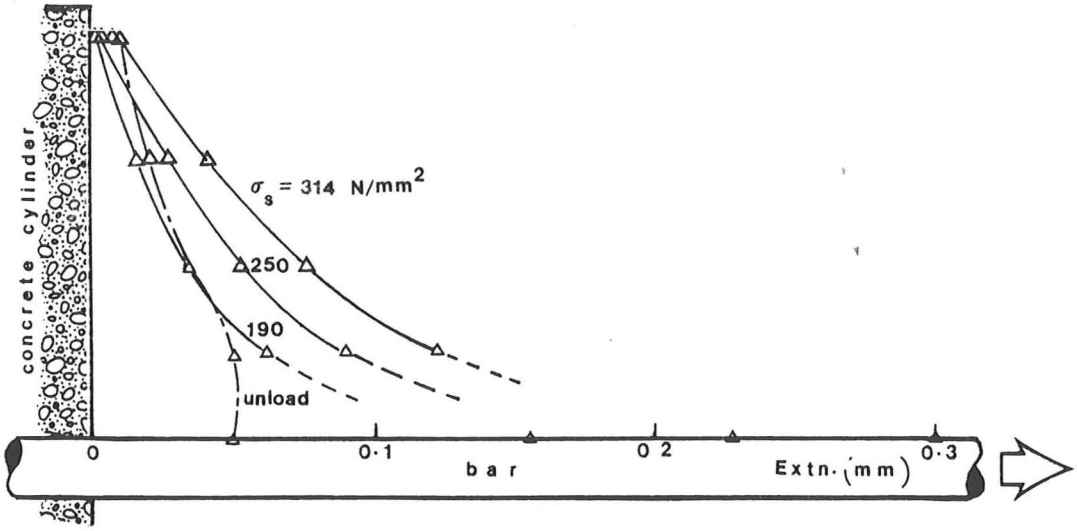

Figure 2.2-1 A typical result from tests by Beeby and Taylor (reproduced from reference [58]).

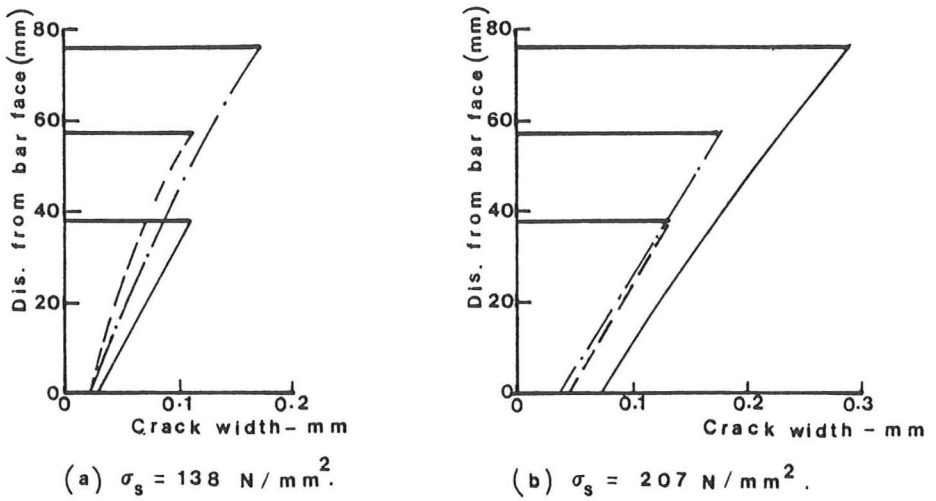

Figure 2.2-2 Internal crack widths measured by Husain and Ferguson (redrawn from reference [16]).

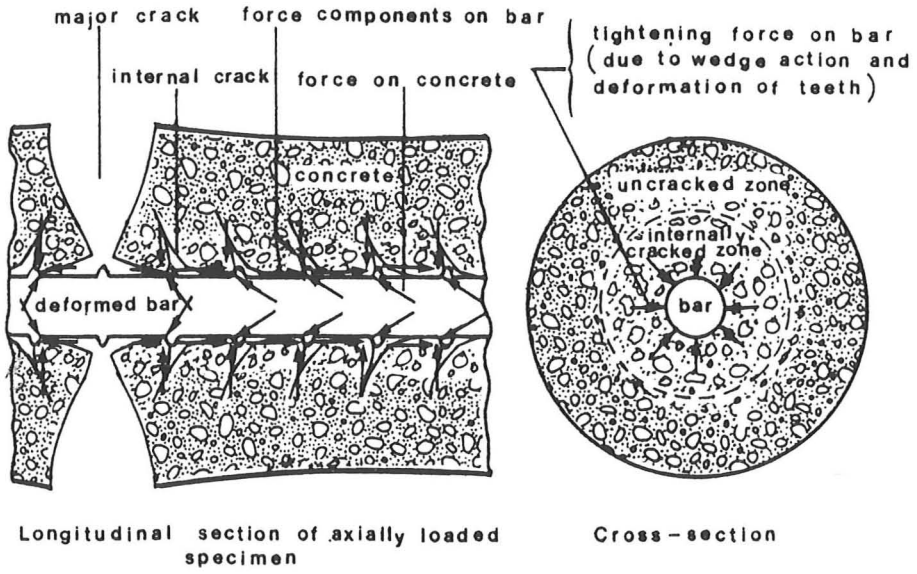

Figure 2.2-3 Schematic diagram of conditions close to a deformed reinforcing bar (redrawn from reference [24]).

Goto [24] tested long, axially reinforced tension specimens with narrow ducts formed parallel to the reinforcing bar. Ink run into these ducts during loading, penetrated all the cracks formed under load so that they could then be located after the test by sectioning the specimen. The external cracks were sealed so that the ink did not escape down them. Photographs of the specimens after test showed that internal cracks, generally related to the ribs on the bar, formed between the major cracks. Goto states that these cracks form cones with their apexes near the ribs and their bases generally directed towards the nearest major crack. These internal cracks generally form an angle with the bar of 45 - 80°, commonly about 60°. A loss of adhesion bond was indicated by penetration of the ink along the bar-concrete interface as found by Illston and Stevens [36].

From his tests, Goto proposed an idealised picture (see Figure 2.2-3) of the deformations around a bar. Internal cracks usually start shortly after major cracks are formed. The formation of the internal cracks is considerably influenced by the surface deformation of the reinforcing bars: they first develop around ribs near the major cracks, then with increase in steel stress or with repetition of load, at ribs progressively farther from the major cracks. These internal cracks have a great influence on the bond mechanism between deformed steel and concrete. The deformation of the concrete teeth formed by internal cracking serves to tighten the concrete around the reinforcing bar and thus increases the frictional resistance between concrete and steel. The reaction of this tightening force also produces ring tension in the concrete around the bar, which can be the principal cause of the splitting mode of bond failure usually associated with deformed bars.

However, fewer internal cracks were found in earlier tests by Broms [2] and Broms and Lutz [6] in which resin was injected into loaded tensile concrete members, centrally reinforced with deformed bars. The sum of the widths of all cracks along the reinforcement was less than the total measured elongation of the reinforcement. This indicates the presence of additional minute cracks close to the reinforcement the widths of which are so small that resin could not penetrate into them.

Broms found that cracks which were confined to the reinforcement (and did not penetrate to the surface) reach their maximum widths at or near the steel bar. Whereas, for major cracks, the crack width at the surface of the member were three to five times the width close to the reinforcement.

Thus, internal cracking seems to give a reasonable explanation as to how the strain in concrete (nearly the same as the steel's) is accomodated. Bond failure or slip would account for the difference in strain between concrete and steel, especially when plain bars are used.

The extensive research on flexural cracks, by Base et al [9],[10], formed the basis of the following crack width formula in CP110 [37]:

$$\text{design surface crack width} = \frac{3\, a_{cr}\, \varepsilon}{1 + 2\left(\dfrac{a_{cr} - c}{h - x}\right)} \quad \ldots\ \ldots\ (2.2\text{-}4)$$

where

a_{cr} is the distance from point of measurement of crack to surface of nearest reinforcing bar;

c is the minimum cover;

h is the overall depth of the member;

x is the neutral axis depth found by the modular ratio method neglecting concrete tension; and

ε is the actual average strain at the level considered, given by:

$$\varepsilon = \varepsilon_o - \frac{1.2\, b\, h\, y\, 10^{-3}}{A_s\,(h - x)\,\sigma_{sy}} \quad \ldots \qquad \ldots \quad (2.2\text{-}5)$$

The second term on the right of Equation 2.2-5 allows empirically for the stiffening effect of concrete in tensile zone between cracks, where

ε_o is the strain at the level considered calculated ignoring the stiffening effect of the tensioned concrete; in calculating ε_o, the concrete modulus E_c should be taken half the value given for short term loading.

y is the distance, measured from the neutral axis, of the point at which ε_o is sought;

A_s is the cross-sectional area of the tension reinforcement; and

σ_{sy} is the steel characteristic strength.

The CEB :1970 Recommendations [20] gives the following formula for the prediction of the maximum crack width in reinforced concrete members subject to non-repetitive loads:

$$W_{max} = (1.5\, c + 16\, D/p_f)(\sigma_s - 300/p_f)\, 10^{-5} \quad \ldots \qquad \ldots \quad (2.2\text{-}6a)$$

For members subject to loads repeated more than 100 times at their maximum value, Equation 2.2-6a becomes

$$W_{max} = (1.5\, c + 16\, D/p_f)(\sigma_s\, 10^{-5}) \quad \ldots \qquad \ldots \quad (2.2\text{-}6b)$$

where

p_f is the percentage of reinforcement in the cross-section of concrete affected by cracking. For rectangular sections this

area can be taken as 1/4 of the total area.

In the CEB/FIP Model Code [47], the following equation is given for calculating the design crack width:

$$\text{Design crack width} = (2\,c + k\,D/p)\,\varepsilon_m \quad \ldots \qquad \ldots (2.2\text{-}7)$$

where

p is the reinforcement percentage related to the area of concrete surrounding the bars and having the same centroid;

k is a coefficient depending upon the ratio of the depth of the tension zone to the cover. Values are:

c/(h-x)	0.0	0.05	0.1	0.15	0.2	0.3	0.4	0.5
k	20.0	15.0	9.0	5.0	3.0	1.6	0.9	0.6

ε_m is the average strain which, for frequent loadings, may be taken as equal to that calculated neglecting tension stiffening. In other cases, it is proposed that the strain may be reduced according to the relationship:

$$\varepsilon_m = \frac{\sigma_s}{E_s}\left(1 - 0.7\,\frac{\sigma_{scr}}{\sigma_s}\right)^2 \quad \ldots \qquad \ldots (2.2\text{-}8)$$

where σ_{scr} is the steel stress at a cracked section just after cracking .

The ACI Committee 224 report [64] gives the following simplified equation for the prediction of the most probable maximum crack width.

$$W_{max} = 11\,\lambda\,\sigma_s\,\sqrt[3]{t_c\,A}\,(10^{-6}) \quad \ldots \qquad \ldots (2.2\text{-}9)$$

where

A is the area of concrete symmetric with reinforcing steel divided by number of bars;

t_c is the thickness of cover from tension face to center of nearest bar; and

λ is the ratio of the tension zone height (h-x) to the depth (d_s-x) below the neutral axis of the tension steel.

Regan and Yu [42] derived a semi-theoretical equation for predicting crack widths which is similar to that given in CP110. Their explanation of the development of the crack pattern (as explained by Broms [5]) can be outlined as follows.

Owing to the curvature of the compressive zone, the tensile zone adjacent to the very first crack is strained by stresses from the compressive zone. These stresses produce direct longitudinal tension in the tensile zone at some distance from the original crack. This action causes additional cracks to form, until the effect of the vertical stresses is insufficient to produce further cracking. The average spacing of these primary cracks is about 1.67(h-x).

Secondary cracks are then formed due to bond failure; these are situated about midway between the earlier ones. This process continues as the region of concrete affected by the bond forces extends across the whole tensile zone; but at some stage the spread of the tensile stresses, which is limited to an approximately spherical region around each bar, is insufficient to cover the whole zone (see Figure 2.2-4).

The tensile stresses then exist only near the bars. New cracks are still formed, but their extent is limited to the spherical regions stressed by individual bars. This process continues until the bond is inadequate to produce any further cracks.

According to this explanation of cracking process, the resulting crack spacing on any line at a distance t from the center of the nearest

reinforcing bar should lie between a maximum equal to the diameter of a stress-sphere drawn between the bar and the line and a minimum equal to half that value. The average crack spacing should therefore be expected to be of the order of 1.5t. But according to experimental work [9],[10], average spacing is in fact slightly greater than this and can well be taken as 1.67t when normal deformed bars are used and 2.0t for plain round bars.

Ignoring the tensile deformation of the concrete between cracks, the following formula, given by Regan and Yu [42], can be written:

$$W_{av} = \varepsilon_o \{1.67\ t \leq 1.67\ (h - x)\} \quad \ldots \qquad \ldots (2.2\text{-}10a)$$

when deformed bars are used.

By taking the maximum width to be twice the average, as recommended by Base et al [9],[10], they obtained a crack width with a chance of about one in a hundred of being exceeded. And so, for deformed bars and allowing for the tension stiffening effect on strains using Equation 2.2-5,

$$W_{max} = \left\{\frac{y\ \bar{\sigma}_s}{E_s\ (d - x)}\right\} - \left\{\frac{0.7\ b\ h\ y\ 10^{-3}}{A_s\ (h - x)\ \bar{\sigma}_s}\right\} \{3.33\ t \leq 3.33\ (h - x)\} \quad \ldots$$

$$\ldots (2.2\text{-}10b)$$

It can thus be seen that the formulae given by CP110, Regan and Yu, and the ACI are all variants of the basic Broms/Base approach, with crack width depending on steel strain and distance from the nearest reinforcing bar. Numerical factors of course differ, but predictions are broadly similar. The CEB adds the influence of bond failure to its equation, a function of the ratio of the bar diameter to the effective steel percentage. Note that when calculating the steel strain for use in one of the crack width formulae, some allowance is made for tension stiffening.

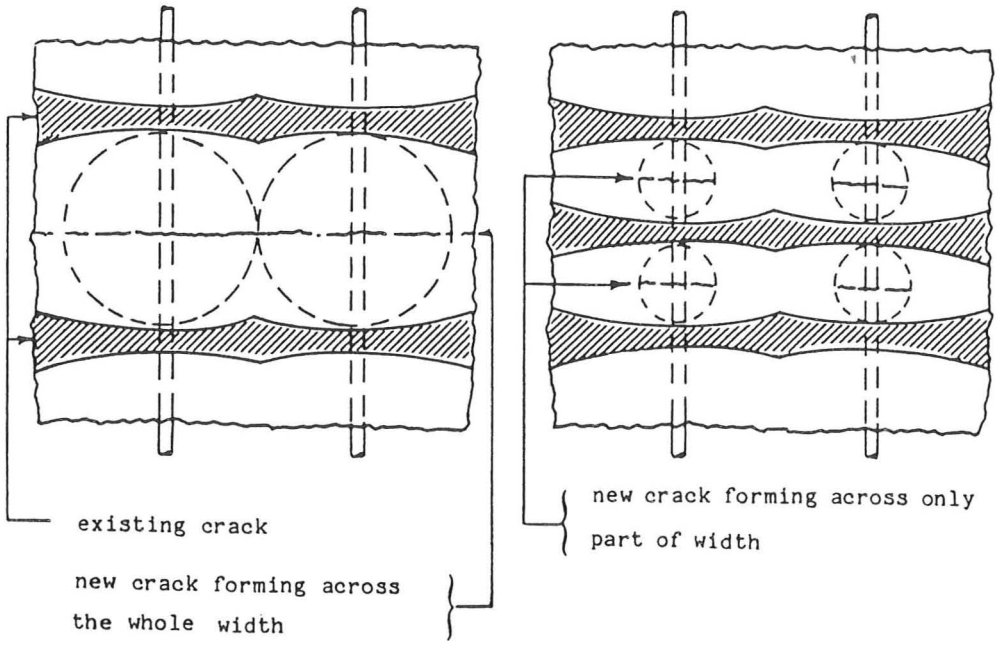

Figure 2.2-4 Development of crack pattern (after Broms [5]).

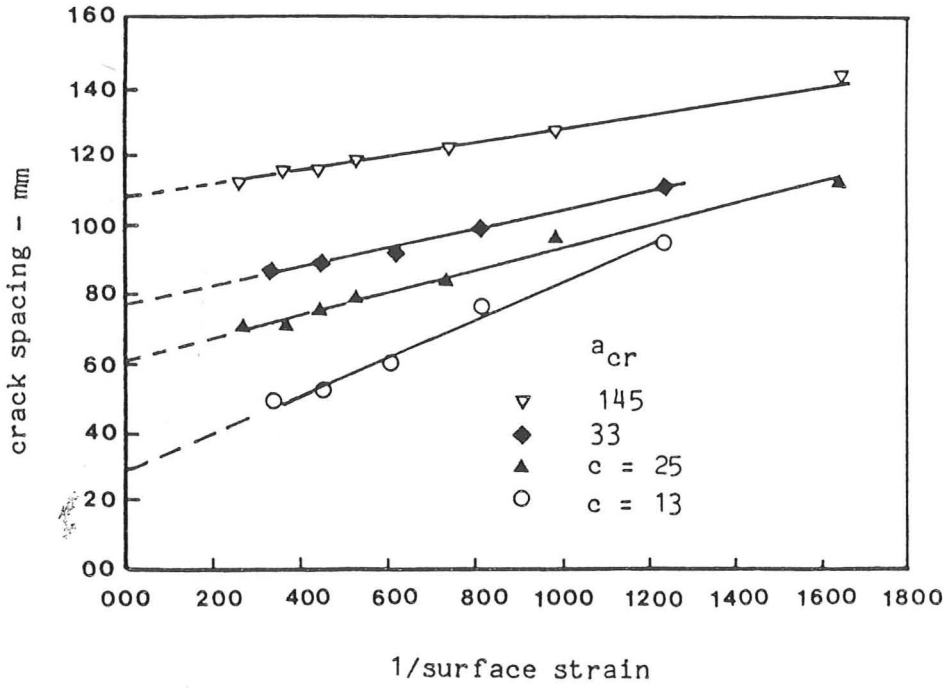

Figure 2.2-5 Typical plots of crack spacing against the inverse of the surface strain (redrawn from reference [19]).

2.2.2 Slabs spanning one way

The formulae derived from the results of Base et al's beam tests [9],[10] worked well for beams where the steel was fairly closely spaced. However, bar spacing in slabs and hence the distance a_{cr} can be much larger than in beams which would imply very large crack widths if Equation 2.2-3 was still applicable.

Beeby [19] decided to study cracking in slabs and carried out a series of tests on one-way spanning slabs reinforced with deformed bars. It was observed that:

(a) The average crack spacing along any line parallel to the reinforcement decreases towards a minimum with increase in strain.

(b) This minimum spacing is approached more rapidily by the cracks between bars than by those over bars.

(c) More cracks develop over the bars than develop between the bars.

By plotting test results on any line parallel to the reinforcement, Beeby [19] showed that there is a fairly linear relationship between crack spacing and the inverse of the strain $1/\varepsilon$ (see Figure 2.2-5). The following description was proposed for the cracking process in reinforced concrete members.

The actual crack pattern occurring at any point on a member is the result of an interaction between two basic crack patterns:

(1) A crack pattern controlled by the deformation imposed on the section or, more specifically, by the initial crack height. The only influence that the reinforcement has on this pattern is to control the crack height. The crack width and crack spacing in this pattern are directly proportional to the initial crack height $h_o(=h-x)$.

(2) A crack pattern controlled by the proximity of the reinforcement. A predominantly linear relationship is predicted between crack width and distance from the points where the cracks are measured to the surface of the nearest reinforcing bar. Slip or internal cracking occuring before the crack pattern has fully developed modify this linear relationship by causing the distribution of crack widths to be skewed towards the larger values. The magnitude of this skew depends on the amount of premature internal failure that occurs (a function of A/D, where A is the area of concrete surrounding a bar; D is the bar diameter), and the ratio of the cover to the initial crack height c/h_o.

Directly over the reinforcement, pattern 2 dominates but, with increasing distance from the bars, the crack pattern approaches 1 asymptotically. The following formulae were derived:

$$W = \frac{a_{cr}\, W_{lim}\, W_o}{c\, W_{lim} + (a_{cr} - c)\, W_o} \quad \ldots \quad \ldots (2.2\text{-}11)$$

$$\frac{W_{lim}}{\varepsilon} = K_1\, h_o \quad \ldots \quad \ldots (2.2\text{-}12)$$

$$\frac{W_o}{\varepsilon} = K_1\, c + K_2 \left(\frac{A}{D}\right) \exp(-K_3\, c/h_o) \quad \ldots \quad \ldots (2.2\text{-}13)$$

$$s_{cr} = \frac{W_{av}}{\varepsilon} + \left(\frac{0.05}{\varepsilon}\right) \exp(-0.0135\, a_{cr}) \quad \ldots \quad \ldots (2.2\text{-}14)$$

where

W is the crack width at the point considered;

W_o is the crack width directly over a bar where $a_{cr}=c$;

W_{lim} is the crack width which is approached as $a_{cr} \rightarrow \infty$;

ε is the average surface strain at level where crack is measured;

s_{cr} is the average crack spacing;

A is the area of concrete surounding a bar as defined in Figure 2.2-6b; and

K_1, K_2, and K_3 are constants which are chosen so that the calculated crack width has some specified chance of being exceeded. Values are given in Table 2.2-1.

Table 2.2-1 Coefficients for Equations 2.2-12 and 2.2-13 [19].

Probability of width being exceeded	2%	5%	20%	mean
K_1	2.27	2.15	1.75	1.33
K_2	0.27	0.22	0.12	0.075
K_3	5.0	4.2	3.2	3.5

In order to check the validity of the proposed theory of flexural cracking described above, Beeby [33] carried out further tests on axially reinforced concrete prisms subject to pure tension. Such members form a limiting case in the application of the theory and are also suited to investigation of the effects of certain parameters in the formulae derived (Equations 2.2-11 to 2.2-14). The results of the tests confirmed the predictions of the theory and also led to some minor modifications of the formulae for predicting crack widths as follows:

In Equation 2.2-13, the variable A/D, taken from the classical bond-slip theory of cracking, was used to define the probability of internal failure occuring prior to the complete formation of the basic crack pattern. Results from the tension tests showed that a better variable was $\sqrt{C1/c}\,(c^2/D)$ where C1 and c are the larger and smaller covers respectively in a rectangular cross-section.

This improved variable has been used to modify Equation 2.2-13 for the general case of flexural members. The modified form of this equation is:

$$\frac{W_o}{\varepsilon} = K_1 c + K_2 \sqrt{\frac{C1}{C2}} \left(\frac{c\ C2}{2\ D}\right) \exp(-4\ c/h_o) \quad \ldots\ldots (2.2\text{-}15)$$

where

K_1, K_2 are coefficients which depend on the required probability of the calculated width being exceeded. Values are given in Table 2.2-2.

C1, C2 are respectively the larger and smaller average covers in the rectangle of concrete surrounding a particular bar as defined in Figure 2.2-6.

Table 2.2-2 New coefficients for Equations 2.2-12 and 2.2-15 [33].

Probability of width being exceeded	2%	5%	20%	mean
K_1	1.94	1.86	1.59	1.33
K_2	3.0	2.6	1.4	0.8

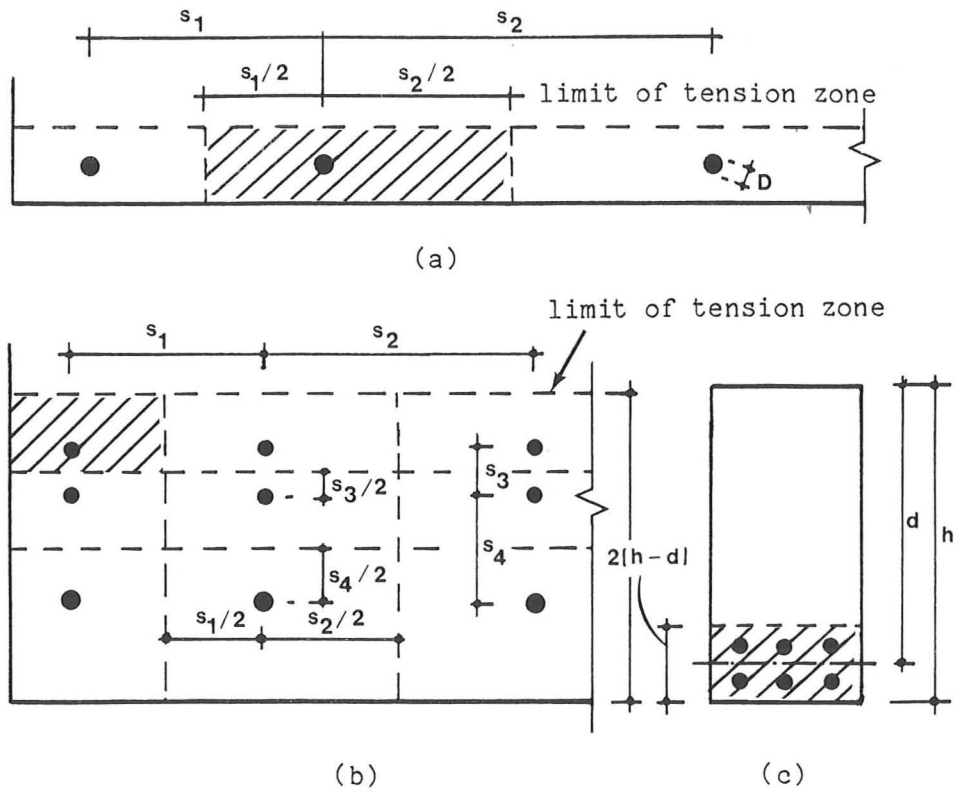

Figure 2.2-6 Definition of prism of concrete surrounding a bar. (a) Slab. (b) Beam. (c) Definition of tension zone. (Redrawn from reference [33]).

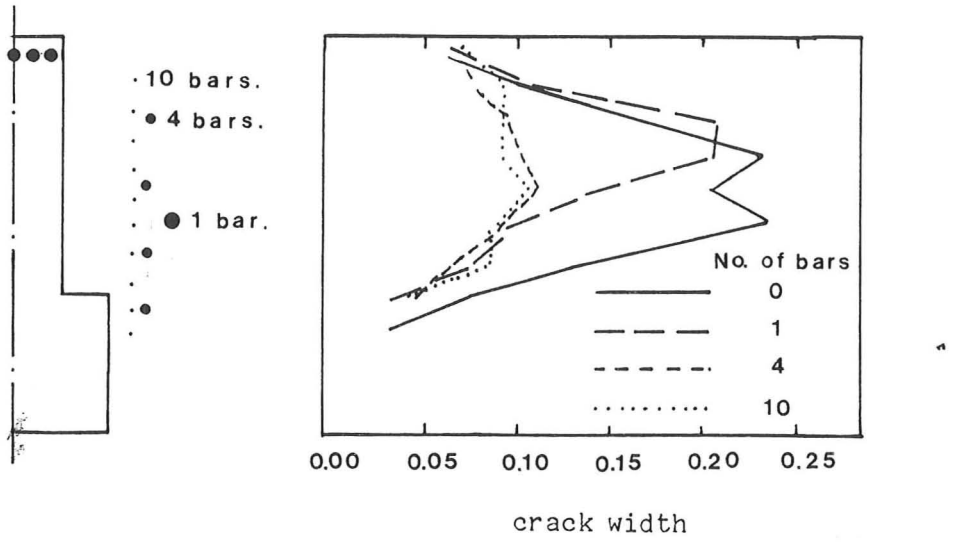

Figure 2.2-7 Effect of skin reinforcement on crack widths on the side faces of beams (redrawn from reference [63]).

Beeby [27] carried out tests on five 750 mm deep T-beams primarily to check the validity of the theory and the formulae derived from the slab tests [19] when applied to cracking on the side of beams at points well away from the tension steel. Also studied was the influence of stirrups and longitudinal anti-crack bars in controlling cracking on the side faces of beams. The results indicated that the theory and formulae do work adequately in these cicumstances and that, over the range of bar sizes used in these tests, stirrups and skin reinforcement had little significant influence on cracking. It was absolutely clear from the test evidence that cracks down the sides of beams are not wedge shaped, that is, widest at the tension face and tapering uniformly to zero at the neutral axis. In the beams reported by Beeby [27], the maximum widths were always at about mid-height.

Frantz and Breen [63] carried out tests on forty-four large reinforced concrete beams to study the effect of skin reinforcement on side face cracking. Variables included amount, location, distribution, cover, and type of skin reinforcement, web width, and the beam depth. Test results showed that skin reinforcement affects only a narrow strip of concrete along each side face of the web independent of the web width. Thus, the effectiveness of skin reinforcement in controlling cracking can be related to a simple skin reinforcement ratio. As the beam depth increases, the skin reinforcement ratio required to provide the same degree of crack control also increases. It was found to be most effective to distribute the skin reinforcement as many small bars rather than as few large bars (See Figure 2.2-7).

2.2.3 Slabs: the general case

The formulae derived by Beeby for the prediction of crack widths in flexural members are only directly applicable in cases where cracks are perpendicular to the steel reinforcement. But in many cases the cracks form at an angle to the directions of the slab reinforcement. In these cases, problems of interpreting the formulae (Equations 2.2-11 to 2.2-15) are introduced.

The major problems are:

(1) The calculation of the initial crack height h_o. It is not clear what steel area should be used in calculating the neutral axis depth, and hence h_o, using the modular ratio theory.

(2) The evaluation of the area of concrete surrounding a bar in Equation 2.2-13. The definition given by Beeby [19],[33] (Figure 2.2-13) is purely empirical.

(3) The direction in which the distance a_{cr} should be measured - either along the crack or at right angles to the bar.

A method, based on Beeby's approach [19], for calculating crack widths when the cracks do not form perpendicular to the reinforcing bars was proposed, and checked against experimental data, by Clark [38]. The above three problems were considered and the following solutions were given.

(1) The steel area used in calculating the neutral axis depth, and hence h_o, should be equal to that obtained from resolving all the reinforcement into the direction normal to the crack. This is done by multiplying the individual steel areas per unit length by the fourth power of the cosine of their respective orientations to the normal.

(2) The definition given by Beeby, defining the area of concrete surrounding a bar, was retained for each set of bars, and the crack width was calculated over each set of bars using Equation 2.2-13.

(3) The distance a_{cr} was measured at right angles to the bar.

Calculations of crack widths using the procedure proposed by Clark [38] were compared with experimental data from tests by Clark [32],[34],[38] and found to be in acceptable agreement. However, the conclusions drawn by Clark concerning cracking in slabs with skew reinforcement are still uncertain since the data available are few. Only five slab models [34],[38], with skew reinforcement, were tested under

The major problems are:

(1) The calculation of the initial crack height h_o. It is not clear what steel area should be used in calculating the neutral axis depth, and hence h_o, using the modular ratio theory.

(2) The evaluation of the area of concrete surrounding a bar in Equation 2.2-13. The definition given by Beeby [19],[33] (Figure 2.2-13) is purely empirical.

(3) The direction in which the distance a_{cr} should be measured - either along the crack or at right angles to the bar.

A method, based on Beeby's approach [19], for calculating crack widths when the cracks do not form perpendicular to the reinforcing bars was proposed, and checked against experimental data, by Clark [38]. The above three problems were considered and the following solutions were given.

(1) The steel area used in calculating the neutral axis depth, and hence h_o, should be equal to that obtained from resolving all the reinforcement into the direction normal to the crack. This is done by multiplying the individual steel areas per unit length by the fourth power of the cosine of their respective orientations to the normal.

(2) The definition given by Beeby, defining the area of concrete surrounding a bar, was retained for each set of bars, and the crack width was calculated over each set of bars using Equation 2.2-13.

(3) The distance a_{cr} was measured at right angles to the bar.

Calculations of crack widths using the procedure proposed by Clark [38] were compared with experimental data from tests by Clark [32],[34],[38] and found to be in acceptable agreement. However, the conclusions drawn by Clark concerning cracking in slabs with skew reinforcement are still uncertain since the data available are few. Only five slab models [34],[38], with skew reinforcement, were tested under

uniform uniaxial bending, and although provision was made to allow for modelling effects, scaling errors might have been introduced.

According to Clark [38], the interaction between the bars need only be considered when calculating strains, neutral axis depth and h_o; each set of bars has little effect on the crack control properties of the other set. This conclusion was founded on the agreement of results from tests on members reinforced only in the principal loading direction with results from tests on identical members but with the addition of transverse steel bars [25]. More information is needed to clear up this point, since the effect of transverse bars on the crack control properties of longitudinal bars is not quite the same as one would expect if the 'transverse' bars ran across cracks rather than parallel to them.

Nawy et al [17],[18],[29] proposed a fracture hypothesis based on stress concentration at the points of intersection of ordinary reinforcing bars and at the welded joints of wire mesh. Thus, for control of cracking in two-way action floors, the major parameter to be considered is the spacing of the reinforcement in the two orthogonal directions. Concrete cover has only minor effect in such slabs, since it is usually of a constant small value of about 20mm, whereas it is a major variable in the crack control equations for beams.

As a result of the proposed fracture hypothesis, and on the basis of statistical analysis of the test data of 90 slabs tested to failure, a basic cracking equation was proposed as follows:

$$w_{max} = K' \lambda \sigma_s \sqrt{G_I} \quad \ldots \qquad \ldots (2.2\text{-}16)$$

where

K' is a fracture coefficient dependent on loading and boundary conditions; and

G_I is termed the grid index = $D_1 s_2 / p_1$, and can be transformed into

$$G_I = \frac{s_1 \, s_2 \, (h - d_{s1})}{D_1 \, \pi/8} \quad \ldots \quad \ldots (2.2\text{-}17)$$

where

p_1 is the active steel percentage in direction '1';

s_1 and s_2 are the spacings of the steel bars in directions '1' and '2';

d_{s1} is the effective depth of reinforcement in direction '1';

D_1 is the bar diameter in direction '1'; and

'1' is the direction of reinforcement closest to the concrete tension face; this is the direction for which crack control check is to be made.

Nawy et al [29] concluded that crack control is best accomplished through development of numerous narrow orthogonal cracking grids reflecting the reinforcement grids, rather than through a few wide diagonal yield-line cracks. This might well be the result of a crack-inducing action by the welded joints of the wire-mesh reinforcement that was used in their experiments. Thus, Equation 2.2-16 is not directly applicable to the general situation more likely to be encountered when ordinary reinforcing steel is used. In such situations, parallel cracks form, almost normal to the principal stress direction, at an angle to the steel bars [11],[21] and thus wider cracks are to be expected.

Desayi et al [56] presented a method for the determination of crack spacing and maximum crack width for rectangular and skew two-way action slabs reinforced with welded wire fabric. Cracks were assumed to form in two directions parallel to the reinforcement; thus, the maximum crack

width in any of the two directions, of a crack running in the other direction, is given by:

$$W_{max} = \lambda \varepsilon_s s_{cri} \quad \ldots \qquad \ldots (2.2\text{-}18)$$

where s_{cri} is the initial crack spacing in the direction considered that provides a balance between, on one hand, the tensile force in the concrete surrounding bars crossing the crack and, on the other hand, the sum of the bond forces caused by these bars and the bearing forces from bars parallel to the crack and falls within s_{cri}.

It can thus be seen that Equation 2.2-18 is basically the same as the bond-slip approach. Furthermore, the crack spacing s_{cri} used in this equation is that obtained immediately after cracking and not the theoretical crack spacing obtained at large strain. The use of an intermediate crack spacing (such as s_{cri}) as a measure of the ratio W/ε is incorrect since a crack would affect concrete-stress only over a relatively short distance on either side of the crack. The stress conditions in all other parts of the member are independent of the crack. Thus, the ratio W/ε is a direct function of the distance affected by the crack and hence of the final crack pattern (at $\varepsilon \rightarrow \infty$) which is directly related to their distance(see Figure 2.2-5).

Experiments on two tension series of r.c. slab elements, reinforced with two orthogonal sets of bars with direction-difference δ (angle between the main-steel direction and that normal to the cracks') and tested under uniaxial stretching, were carried out by J.Peter [11]. In the first series, steel area and spacing in x and y directions were kept constant while the direction-difference δ was varied from 0^o to 40^o in steps of about 10^o. In the second series, different strength reinforcement in x and y directions were provided, and the direction-difference δ was 20^o or 30^o. Both series had elements with aspect dimensions of 1600 mm x 1600 mm and a thickness of 80mm.

Results were as follows:

(1) The cracks ran, independently of the reinforcement direction, almost at right angles to the principal stress trajectory especially for the isotropically reinforced specimens.

(2) The number of cracks and there-with the crack density increases only insignificantly with the angle δ.

(3) The crack widths increase markedly with direction-difference, in the same ratio as the total extension of the element.

The experiments of J. Peter [11] preceded those of Beeby [19]; however, it was thought that crack spacing and widths are predominantly influenced by the steel percentage, bar diameter, and bond properties.

Tests on composite girders with concrete flanges in uniaxial and biaxial tension were carried out by Johnson and Arnaouti [50]. Cruciform specimens of half full size were used; at this scale it was not practicable to test regions of uniform biaxial tension.

Different methods of analysing test data and predicting crack widths were compared graphically with the experiments. These graphs showed a big scatter of test results. This is mainly due to the uncontrolled parameters which affect cracking: the test specimens were subjected to stresses which varied from one section to another.

The main conclusion from the biaxial tests, where cracks ran at 45° to the steel direction, is that the narrower cracks are in general wider (often over twice as wide) than would be predicted by existing methods for regions of (uniaxial) tension in concrete beams. However, the error is less for the wider cracks, and is <u>not</u> significant at mean widths exceeding about 0.25mm.

2.2.4 Concluding Remarks

In conclusion, the above review of work on cracking in r.c. members showed that there is a need for further research on the effect of the angle between the general crack direction (normal to the principal stresses') and that of the reinforcing bars.

In part of the work of Clark [32],[34] and that of Johnson and Arnaouti [50], the stress field was either complex or variable and no areas of uniform strains were tested.

In experiments by Nawy et al [29] and Desayi et al [56] on two-way action slabs, welded wire fabric was used in place of ordinary reinforcing steel. This meant that a different cracking mechanism was obtained with crack forming in a grid reflecting that of the welded wire mesh.

In Peter's tension tests [11], orthogonal reinforcement was used with cracks crossing each set of bars at a different angle. This introduced shear stresses and displacements along the cracks adding to the parameters involved in the analysis of test results.

Clark [34],[38] tested few slab models with skew reinforcement and subject to uniform bending moment. However, scale effects were involved in the analysis which made the interpretation of test results an indirect one, since cracks do not scale [22],[43].

Thus, required is an experimental programme that will isolate and study the effect of the angle between the directions of cracks and steel bars. Such an experimental programme is described in Chapter 4. The results obtained from this experiment are analysed and discussed in Chapter 6. The procedure given by Clark [38] for estimating crack widths and spacing in slabs with skew reinforcement (which is based on Beeby's formulae [19]) is discussed in the light of these experimental results. A new hypothesis is given describing cracking over a reinforcing bar that crosses cracks at an angle. Formulae are proposed for calculating crack widths in such situations both over and midway between bars. These formulae are closely based on those derived by Beeby [54].

2.3 Tension Stiffening in R.C. Beams and Slabs

Early theoretical studies of deflection used the classical elastic equations to calculate curvature under load. These equations ignored the contribution to stiffness made by the cracked tensile concrete following a traditional concentration on strength rather than stiffness. However, experimental evidence shows that substantial areas of significant tensile stress exist in the concrete between major cracks at advanced strains as described in detail in the previous section in work on the nature of cracks. The problem therefore deserves some detailed consideration.

2.3.1 Members subject to pure tension

Experiments on axially reinforced concrete prisms tested in pure tension [33] showed that, even at advanced load stages, the load carried by the member is higher than the force which can be carried by the steel alone at the same average strain. Thus, the remaining part of the load must be carried by the concrete even when the load exceeds the cracking load as shown in Figure 2.3-1. This conclusion is supported by results from experiments by Evans and Marathe [14] who were able to obtain the complete stress-strain curves for plain concrete in direct tension by using a modified testing machine. Large strains (several times that of cracking) were observed at some percentage of maximum stress, primarily due to initiation of a microcrack within the gauge length. This 'falling branch' might be explained by the pulling-out of interlocking aggregate particles. In reinforced concrete members, however, where cracks of substantial widths can be present (major cracks), it is reasonable to assume that tensile stresses carried by the concrete across cracks are negligible.

Thus, in our example of Figure 2.3-1, it seems obvious that, at a major crack the total load must be carried by the steel but between cracks a substantial proportion of the force will have been transferred to the concrete. The force in the steel, therefore, varies from one section to another along the member and hence the average strain ε_m in the steel is less than the strain ε_1 at a cracked section. The difference between the strain in the steel at a major crack and the average strain $(\varepsilon_1 - \varepsilon_m)$ may be referred to as the reduction in strain due to tension stiffening.

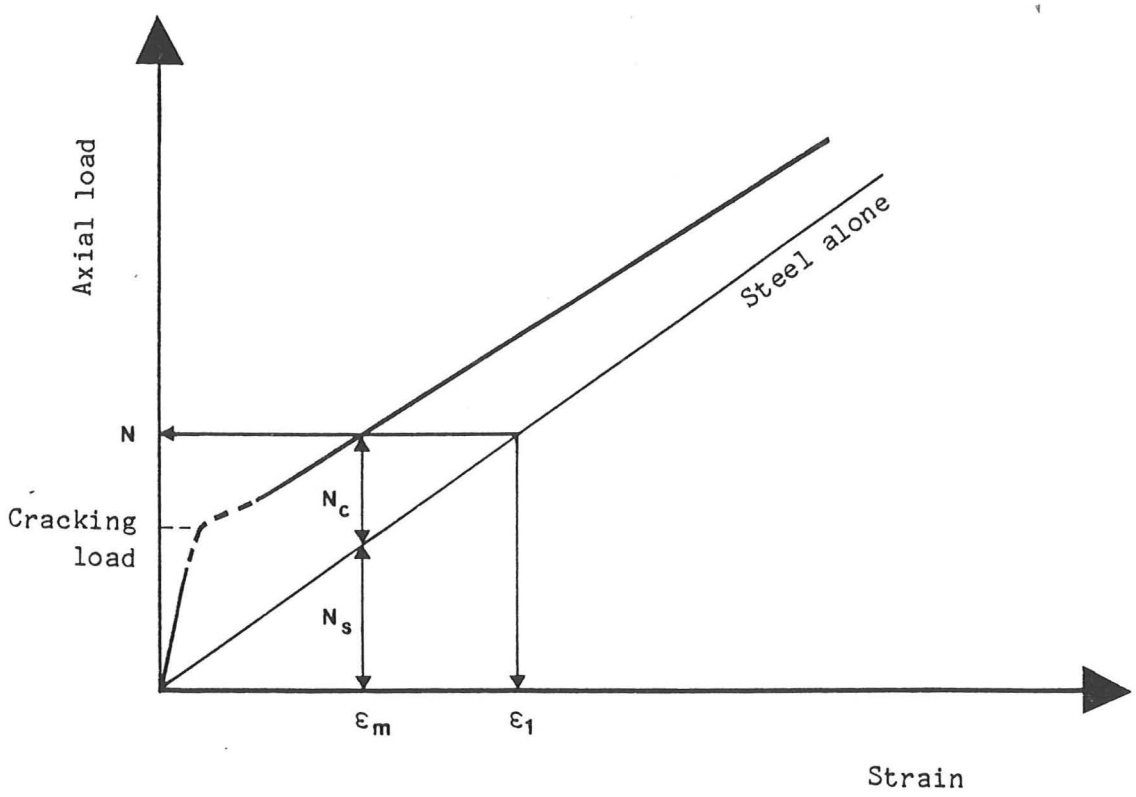

Figure 2.3-1 Idealised load-strain relation for a reinforced concrete member subject to pure tension.

If a particular total load N is considered, corresponding to an average strain of ε_m, it can be seen from Figure 2.3-1 that N may be regarded as

$$N = N_s + N_c \quad \ldots \qquad \ldots (2.3\text{-}1)$$

where

N_s is the force in bare steel with strain ε_m and is given by $N_s = \varepsilon_m A_s E_s$;

N_c is the force carried by the concrete and can be expressed in terms of an equivalent average tensile stress in the concrete f_{tm}; thus, $N_c = A_c f_{tm}$.

The total force N can be expressed in terms of the steel strain ε_1 at a major crack:

$$N = E_s \varepsilon_1 A_s \quad \ldots \qquad \ldots (2.3\text{-}2)$$

Hence:

$$E_s \varepsilon_1 A_s = \varepsilon_m E_s A_s + A_c f_{tm}$$

On rearranging, this gives

$$\varepsilon_m = \varepsilon_1 - \frac{A_c f_{tm}}{A_s E_s}$$

Thus, the tension stiffening effect is given by:

$$\varepsilon_1 - \varepsilon_m = \frac{f_{tm}}{E_s p} \quad \ldots \qquad \ldots (2.3\text{-}3)$$

where p is the proportion of steel (A_s/A_c).

2.3.2 Flexural members: beams

While the discussion in the previous section has been based on members subject to pure tension, the same interaction between steel and concrete obviously occurs in flexural members as well. However, a difficulty of applying Equation 2.3-3 to flexural situations is that it has to be decided what area of concrete in the tension zone corresponds to the area of the equivalent tension member since this is required for the calculation of p. The various formulae developed for predicting tension stiffening actually differ only in the means adopted for defining p and f_{tm}. The CEB 1970 recommendations assume a constant value for f_{tm} and adopt

a value for p equal to p_f as defined for use in the crack formula. As this definition varies according to the type of member considered, this results in the relationship:

$$\Delta \varepsilon_s = 0.0015/p_f \quad \ldots \qquad \ldots (2.3\text{-}4)$$

In fact, f_{tm} is not constant but reduces with increasing strain due to the propagation of external and internal cracks. Thus, a better formula would be one which gave a value of f_t (the tensile strength of concrete) for f_{tm} at the cracking load and then caused this to reduce towards zero with increasing load. A number of formulae of this type have been developed; for example, Rao and Subrahmanyan [39] developed the formula given below for beams:

$$\varepsilon_{s1} - \varepsilon_{sm} = 0.18 \left(\frac{\sigma_{scr}}{\sigma_s}\right)\left(\frac{f_t}{p\ E_s}\right) \quad \ldots \qquad \ldots (2.3\text{-}5)$$

where

ε_{s1} is the strain in steel at a major crack;

ε_{sm} is the average steel strain;

f_t is the tensile strength of concrete;

σ_{scr} is the stress in the steel just after cracking and neglecting concrete in tension; and

p is the reinforcement ratio and is equal to A_s/bd_s, where b is the breadth of the concrete section and d_s is the effective depth of steel reinforcement.

The coefficient 0.18 is an empirical factor determined using 'existing' test results from 35 beams reinforced with round smooth bars and

15 beams reinforced with deformed bars. The range of variables covered reinforcement percentages p from 0.3 to 1.66 %, concrete cube strength from 16 to 26 N/mm^2, bar diameters from 6 to 32 mm, and beam depths from 200 to 625 mm. Interestingly, no significant difference was observed between round smooth bars and deformed bars at any load stage in spite of the basically different behaviour of the two types of steel.

The approach developed by Clark and Spiers [51] for evaluating tension stiffening was based closely on suggestions made by Rao and Subrahmanyan. They gave the following formula for beams:

$$\varepsilon_s - \varepsilon_{sm} = 0.3 \left(\frac{f_t}{p_e E_s}\right)\left(\frac{\varepsilon_{sp}}{\varepsilon_{s1}}\right) \quad \ldots \qquad \ldots (2.3\text{-}6)$$

where

p_e is the effective steel percentage taken as a ratio of the area of concrete below the neutral axis, i.e. $b(h-x)$;

ε_{sp} is the steel strain at a major crack when tension stiffening is maximum and is given by:

$$\varepsilon_{sp} = 200\left(\frac{I_{un}}{I_{cr}}\right) 10^{-6} \quad \ldots \qquad \ldots (2.3\text{-}7)$$

where I_{un} and I_{cr} are the 'uncracked' and 'cracked transformed' moments of inertia.

ε_{s1} is the steel strain at the stage considered; where $\varepsilon_{s1} > \varepsilon_{sp}$.

The coefficient 0.3 is an empirical factor defining the average tensile stress over the effective area.

The formula given in the CP110 [37] (see Equation 2.2-5) is based on the same general principle with the simplifying omission of the term ε_{sp}.

In addition, f_t was assumed to be constant and thus the reduction in steel strain due to tension stiffening is given by:

$$\Delta \varepsilon_s = \frac{0.7\ 10^{-3}}{\rho\ \sigma_s} \quad \ldots \qquad \ldots (2.3\text{-}8)$$

where the steel percentage ρ is equal to A_s/bh.

The CEB/FIP Model Code [47] recommends that tension stiffening should be estimated from the relation (see Equation 2.2-8):

$$\Delta \varepsilon_s = K'' \varepsilon_s \left(\frac{\sigma_{scr}}{\sigma_s} \right)^2 \ldots \qquad \ldots (2.3\text{-}9)$$

This equation might seem to be very different from the formula given above while in fact it is not. If we consider the pure tension case, it can be seen that the cracking load is given approximately by $f_t A_c$ (ignoring the effect of steel). But by definition, the cracking load is also equal to $A_s \sigma_{scr}$, and so

$$A_s\ \sigma_{scr} = A_c\ f_t$$

hence

$$\sigma_{scr} = f_t/\rho$$

Thus, Equation 2.3-9b can be rewritten as

$$\Delta \varepsilon_s = K'' \left(\frac{\sigma_{scr}}{\sigma_s} \right) \left(\frac{f_t}{\rho\ E_s} \right) \quad \ldots \qquad \ldots (2.3\text{-}10)$$

which is very similar to Equation 2.3-5.

Moosecker and Grasser [70] carried out a comparative study on some of the above plus other methods for evaluating tension stiffening.They concluded that the influence of concrete tension at first loading on mean steel stresses, moment-curvature relations, and deformations can be well aproximated by most methods.

It can be seen from this review of the various formulae that there is no disagreement in principle about tension stiffening. Equation 2.3-10 serves as a general expression of the tension stiffening; however, there are some disadvantages, practically speaking, in using such equations, as follows.

(1) In calculating strains and stresses, one has to resort to the traditional no-tension approach.

(2) The formulae presented above cannot be directly used in modelling the tension stiffening effect of concrete for use in a non-linear structural analysis as discussed in Section 2.4.

(3) Formulae such as Equation 2.3-10 do not allow for the effect of some of the parameters connected with the steel arrangement and only incorporate the average effect of these parameters into the empirical coefficient.

(4) Equation 2.3-10 does not take into consideration situations in which the principal stresses' direction do not coincide with those of the steel.

Thus, an alternative method for calculating tension stiffening is needed. It should, however, be based so far as possible on experimental results with a minimum of intervening theory. Such a method is developed as described in Chapters 3 and 5.

2.3.3 Slabs: Effect of bar spacing

Experimental results from tests by Clark and Speirs [51] on 9 r.c. slabs showed that there is a tendency for tension stiffening and for the calculated ε_{sp} value to decrease with an increase in bar spacing. The rate of decay of tension stiffening was found to increase as the bar spacing increases. However, in view of the large scatter of the slab data, Clark and Cranston [57] decided to test further 8 slabs. The experimental results from the 16 slabs were analysed; the following are among the conclusions drawn:

(1) Maximum tension stiffening can be considered independent of bar spacing for design purposes.

(2) The value of ε_{sp} is independent of bar spacing.

(3) Tension stiffening decays with strain at a rate which increases with bar spacing when the latter exceed about 1.5 times the slab depth.

2.3.4 The general case

An analytical and experimental study of the in-plane and flexural stiffnesses of reinforced concrete plates and slabs was carried out by Gardenas et al [15],[35]. Forty-one isotropically and nonisotropically reinforced plate elements were tested under different combinations of flexural and torsional moments to check the theory.

Results showed that the stiffness of plates depends on the relative orientation of the reinforcement with respect to the applied forces, the combinations of the applied forces and the amounts of reinforcement in the two orthogonal directions. For isotropically reinforced plate elements, the in-plane and flexural stiffnesses may decrease to one-half or less by rotating the reinforcement from 0° to 45° with respect to the direction of the applied bending moments. This phenomenon is even more pronounced in the case of nonisotropically reinforced elements.

2.4.1 Introduction

The development of numerical procedures for the post-cracking analysis of reinforced concrete members is a research area of continued interest. Different methods of solution have been used, of which the finite element method appears to be the most versatile and powerful one. The accuracy of nonlinear finite element programmes depends greatly on the reliability of the description of the material behaviour.

Under service loads, the most significant contribution to the nonlinear behaviour of reinforced concrete structures is the concrete cracking under tensile stresses. This led some investigators [40],[41],[44] to neglect the stiffening effect of concrete between the cracks in the tension zone. By neglecting tensile strength entirely, one can produce a linear easy-to-compute theory (the 'cracked-elastic' theory) in which no iteration is needed until the steel yields or the concrete becomes non-linear in compression. This gives a lower bound on the load for a given deflection. Unfortunately, such a theory does not model the sudden change of stiffness at cracking, and can seriously overestimate deflection and crack widths at a given load. Thus, most finite element idealizations [26],[45],[49],[53],[59],[60], [61],[62] adopt some concept of tension stiffening. This is often done by assuming a falling branch for the concrete stress-strain relationship in tension. Such a strain softening technique can lead to localized instabilities and non-unique solutions [73] and to difficulties in achieving numerical convergence [60],[61],[62]. Furthermore, the simple addition of a strain-softening branch to the tensile properties of concrete does not ensure satisfactory results since the amount of tension stiffening depends not only on the concrete properties but also on the degree of interaction between the steel bars and the surrounding concrete.

In what follows, a review is presented of the relevant literature on modelling tension stiffening of cracked tensile concrete for use in nonlinear finite element analysis. An alternative method of representing

tension stiffening is considered; it consists of modifying the stress-strain diagram for the tension steel.

2.4.2 Methods of analysis

Two basically different approaches have been used to obtain idealized constitutive relations for use in finite element programmes.

In the first approach (e.g. [26],[45],[49]), each finite element is divided into layers parallel to the plane of the member, and each layer may have different properties. This approach is based on idealized stress-strain relationships for concrete and steel, together with some assumptions regarding compatibility of deformation between the two constituent materials. The element stiffness matrix can be obtained from summation involving the constitutive relations for the individual layers.

Material nonlinearity due to tensile cracking of concrete is included in the analysis. The cracks are assumed to form perpendicular to the major principal stress direction when this stress reaches a specified limiting value; this crack direction is then fixed for all subsequent loadings. An unloading curve is assumed to account for tension stiffening in cracked concrete. The stress level is interpolated using the tension stiffening curve depending on the degree of straining in the concrete. Concrete cracked in one direction is assumed to have uniaxial properties in that direction only. However, additional cracks are permitted to form perpendicular to the original crack direction if the minor principal stress reaches the specified limiting value.

The assumed stress-strain relationships for concrete with a crack oriented at an angle θ counterclockwise with respect to the x-axis are:

$$\begin{bmatrix} \sigma_x \\ \sigma_y \\ \tau_{xy} \end{bmatrix} = [T] \begin{bmatrix} E & 0 & 0 \\ 0 & 0 & 0 \\ 0 & 0 & \eta G \end{bmatrix} [T]^t \begin{bmatrix} \varepsilon_x \\ \varepsilon_y \\ \gamma_{xy} \end{bmatrix} \quad \ldots \qquad \ldots \text{(2.4-1a)}$$

or

$$\{\sigma'\} = [T]\,[D_L]\,[T]^t\,\{\varepsilon'\} \quad \ldots \qquad \ldots\ (2.4\text{-}1b)$$

where

$\sigma_x, \sigma_y, \tau_{xy}$ are the incremental direct and shear stresses;

$\varepsilon_x, \varepsilon_y, \gamma_{xy}$ are the incremental direct and shear strains;

E is the tangent modulus of elasticity of concrete;

G is the shear modulus of uncracked concrete;

η is a coefficient ($0 < \eta < 1$) which allows for the shear stress transmitted across the cracks by means of aggregate interlock and dowel action of reinforcement [72];

$\{\sigma'\}$ is the incremental stress vector;

$\{\varepsilon'\}$ is the incremental strain vector;

$[D_L]$ is the tangential elasticity matrix (material properties matrix) for the layer; and

$[T]$ is the transformation matrix from the θ direction coordinate system to the x,y coordinate system.

Some investigators [41],[44] assumed that no shear stress is transmitted across the crack once it has formed and thus they took η=0. However, other values of η had been adopted, e.g. η=0.4 which was adopted by Hand et al [40].

In the second approach, exemplified by the work of Jofriet and McNeice [23] and Bell and Elms [31], a semi-empirical overall moment-curvature relation is employed which attempts to take into consideration the various stages of material behaviour. For a cracked concrete element, Jofriet and McNeice adopt the following moment curvature relations using classical theory (Timoshenko).

$$\begin{bmatrix} m_n \\ m_t \\ m_{nt} \end{bmatrix} = \begin{bmatrix} D_n & D_1 & 0 \\ D_1 & D_t & 0 \\ 0 & 0 & D_{nt} \end{bmatrix} \begin{bmatrix} K_n \\ K_t \\ 2K_{nt} \end{bmatrix} \quad \ldots \qquad \ldots \text{ (2.4-2a)}$$

or

$$\{m\} = [D_E]\ \{K\} \quad \ldots \qquad \ldots \text{ (2.4-2b)}$$

where

m_n, m_t, m_{nt} are the incremental moments per unit length in the n and t directions, normal and parallel to the crack direction;

K_n, K_t, K_{nt} are the incremental curvatures in the n and t directions;

D_n is the flexural sitffness normal to the crack;

D_t is the flexural stiffness parallel to the crack;

D_1 is the cross-flexural stiffness;

D_{nt} is the torsional stiffness;

$\{m\}$ is the incremental moment vector in the n and t coordinate system;

$\{K\}$ is the incremental curvature vector in the n and t coordinate system; and

$[D_e]$ is the plate tangential stiffness matrix in the n and t coordinate system.

The $[D_E']$ matrix with respect to the x,y coordinate system is given by:

$$[D_E'] = [T]\ [D_E]\ [T]^t$$

The terms in the $[D_E]$ matrix are calculated using Huber suggested relations. These are as follows:

$$
\left.
\begin{aligned}
D_{11} = D_n &= \frac{E_c \left(I_{cr}\right)_n}{1 - \nu_c^2} \\
D_{22} = D_t &= \frac{E_c \left(I_{cr}\right)_t}{1 - \nu_c^2} \\
D_{12} = D_{21} = D_1 &= \nu_c \sqrt{D_{11}\, D_{22}} \\
D_{33} = D_{nt} &= \frac{1 - \nu_c}{2} \sqrt{D_{11}\, D_{22}} \\
D_{13} = D_{23} = D_{32} &= D_{31} = 0
\end{aligned}
\right\} \quad \ldots (2.4\text{-}3)
$$

where ν_c is poisson's ratio for concrete and I_{cr} is the moment of inertia for cracked transformed cross-section.

In calculating I_{cr}, an effective steel area in a direction normal to the cracks is used. Jofriet and McNeice [23] used the formula given by Lenschow and Sozen [13] for calculating this effective area, a function of $\cos^4\theta$. The assumptions for the orientation of cracks are the same as those given in the layered approach.

The main disadvantage of the second approach is that it is only applicable to bending elements and membrane stresses are assumed to be negligible. Also, the moment-curvature relation used in the analysis is a semi-empirical bi-linear one and a more reliable relation is required in this case.

2.4.3 Modelling of tension stiffening

Various models have been proposed for modelling the stress-strain response of concrete in tension. Scanlon [26] considered average tensile stress over a relatively long gauge length to be related to the corresponding average strain by means of an unloading relation for cracked tensile concrete. A stepped piecewise linear unloading relation was used. A similar approach was used by Lin and Scordelis [45] and Abdel Rahman et al [62] who used a smooth curve instead of a straight line for the falling branch. A linear unloading model with a discontinuity at the initial cracking stress was used by Cope et al [60],[61].

Gilbert and Warner [53] carried out a comparative finite element analysis using the above three types of tension concrete stress-strain diagram. They considered the proximity of the steel to be of major importance in assessing tension stiffening. Thus, in their layered finite element, they used reduced tensile stress values for concrete layers once and twice away from the steel. However, Gilbert and Warner gave no recommendation as to choice of the number of layers in the element. Both the stepped and discontinuous stress-strain diagrams produced numerical load-deflection curves in close agreement with test results.

One structural problem which arises from using a stress-strain model for concrete in tension is that it does not account for the fact that, at a major crack, the concrete tensile stresses fall to negligible values and thus all tension must be carried by the steel bars crossing this crack. Changing the relative orientation of the cracks with respect to the steeldirection would also affect the degree of tension stiffening. In addition, some practical problems arise when the tensile-concrete model is used in a finite element procedure as pointed out by Crisfield [73] and others, e.g. Cope et al[60],[61] and Abdel Rahman et al [62], who reported great difficulties in achieving numerical convergence.

Gilbert and Warner [53] also proposed an alternative method for modelling the tension stiffening effect in which the concrete is assumed to carry no stress normal to a crack but an additional stress will be carried at the steel level. This additional stress represents the total internal tensile force in fact carried by the concrete between the cracks, conveniently added up at the level of tension reinforcement and oriented in the directions of the bars. It was reported that the results obtained using this method were at least as good as those obtained using stress-strain diagrams for concrete in tension, but with significantly less computing time.

The shape of the 'saw-teeth' stress-strain curve used by Gilbert and Warner was kept unchanged for situations where steel passed across cracks at an angle, whereas, one expects that the angle between steel and cracks would have some influence on the shape of this curve.

Mang and Floegl [69],[74] considered a tension stiffening concept based on 'tension stiffening factors' that depend on bond-slip between the steel and the surrounding concrete.They assumed that these factors are directly proportional to the average bond stress between the adjacent cracks, the crack spacing, the cosine of the angle enclosed by the normal to the crack and the reinforcement, and inversely proportional to the average steel stress and the bar diameter.

An experimental derivation of a general modified stress-strain curve for the tension steel is presented in Chapters 3 and 5. It takes into account the effect on tension stiffening of parameters such as the cross-sectional area of concrete in tension, steel percentage, bar spacing, and the angle enclosed by the normal to the cracks and the reinforcement direction.

3. TENSION STIFFENING: A NEW APPROACH

3.1 Introduction

The tensile strength of concrete is of the order of 1/10th of its compressive strength and most reinforced concrete members subjected to tension or bending are expected to crack under their working loads. This in the past led to ignoring the tensile strength of concrete in the tension zone and for many years, the no-tension theory was used in concrete design. However, the advent of ultimate strength methods of design for reinforced concrete structures together with the use of high-strength steel has led to a reduction in depths of designed members (as compared with those designed using conventional methods). As a result, the idea of taking into account the contribution to stiffness made by the tensile concrete between cracks has since occupied the attention of many researchers and workers in the concrete field. This is because excessive flexural deflections and excessive flexural cracking are likely to occur in the case of smaller sections and thus deflection control and/or crack control can be the governing design criterion.

In analysing a reinforced concrete member using a nonlinear numerical procedure such as a finite element program, a way of modelling the stiffening effect of cracked tensile concrete, the so-called tension stiffening effect, is needed. Although several methods for calculating the amount of tension stiffening are available, most of these methods use an unloading stress-strain relationship for concrete in tension after cracking; such methods can lead to problems of numerical convergence in a nonlinear analysis. Also they conflict with the obvious fact that, at a major crack, all the tension must be carried by reinforcement since the concrete itself cannot carry tension across the crack. Thus, a new method of representing the tension stiffening of cracked tensile concrete, by modifying the tension steel properties, will be developed in the following

sections of this chapter.

Several formulae to evaluate the tension stiffening effect of concrete between major cracks have been introduced. Most of these formulae give the reduced average strain at steel level as a function of the steel strain calculated using the classical no-tension theory. This requires the assumption that the tension stiffening force acts at the same level as the tension steel. This is not necessarily the case at early load stages; nonetheless, the total tensile force line of action tends towards the steel level as the strain in this steel increases. This assumption will usually be adopted in the following new approach since our interest lies in evaluating the stiffening effect of tension concrete at service load stages.

As a result of the additional stiffness contributed by the tension concrete, the mean strain at steel level (measured on a gauge length crossing several cracks) is less than the steel strain at a crack. If we assume that the stress in the tension steel at a crack is likely to approximate that given by the classical no-tension theory, then we are led to introduce the concept of an 'effective stress'-strain relationship for the tension steel, stiffer than the behaviour of a bare steel bar. The behaviour of reinforced concrete members could then be predicted using no-tension theory but with an 'enhanced stress'-strain curve for the tension steel. The enhanced properties of reinforcing steel will depend on the various parameters that affect the tension stiffening. The experimental results on reinforced concrete beams and slabs in uniaxial bending tested by Clark et al [51],[57] will be used to determine such relations.

The concept of an adjusted stress-strain curve for the tension steel after the surrounding concrete has cracked has already been used by Gilbert and Warner [53] as reviewed in Chapter 2. However, this method has not been taken any further nor has it been extensively compared with experimental results, especially those from tests on beams.

3.2.1 Theoretical background

Consider the reinforced concrete beam with bending cracks in Figure 3.2-1. At a cross-section in the region of constant bending moment containing a major crack, the tensile strength of concrete is completely destroyed and the tensile force is resisted solely by the steel reinforcement. Meanwhile, at a section midway between two major cracks the uncracked concrete in the tensile zone may carry tensile stress (up to its tensile strength) dependent on the strain level in the steel -- and thus is capable of carrying part of the tensile force. Tensile force is transferred to this concrete from two sources: firstly, from its being strained by stresses from the compression zone owing to the curvature of the beam; secondly, from the reinforcing steel through bond. Thus at such a section between major cracks the steel carries a reduced tensile force. The tension in the tensile zone produced by stresses from the compression zone and bond causes more major cracks to form until the effect of these stresses is insufficient to produce further major cracking. From this stage onwards the continuing formation of minor and internal cracks is dependent on the detailing of reinforcement.

Figure 3.2-2 shows a part of the beam containing two major cracks. At a section containing a major crack, section I, the neutral axis depth is less than that at a section midway between two major cracks, section II. This means that at section I the lever arm is greater, while the flexural rigidity is less than at section II. It follows that at section I the total tensile force is less, while the strain at steel level is greater than at section II for a given applied bending moment (of course, the same at every cross-section).

In the remainder of this chapter, the strains mentioned are, unless otherwise stated, 'average' strains measured over long gauge lengths crossing several major cracks in the region of constant bending moment. These are the strains which would be calculated by a structural analysis,

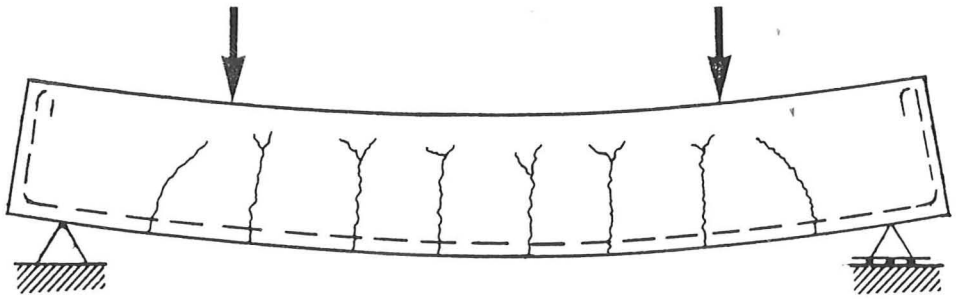

Figure 3.2-1 A reinforced concrete beam with bending cracks.

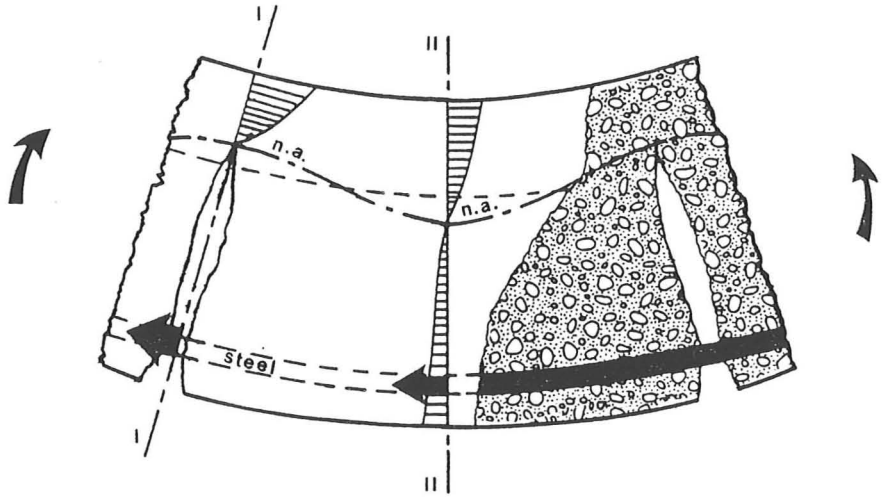

Figure 3.2-2 A reinforced concrete beam element in pure bending.

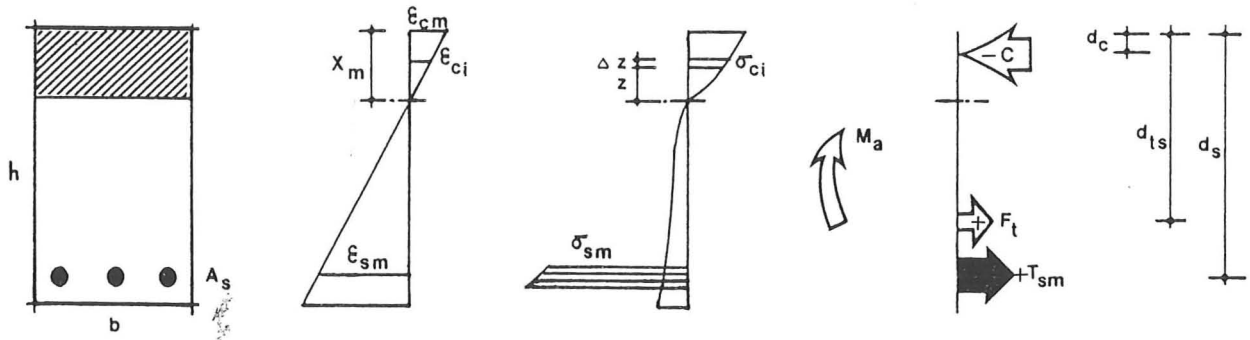

Figure 3.2-3 Average behaviour of a reinforced concrete beam element in pure bending.

e.g. a finite element program with elements of length several times their depth, which considered overall behaviour of the beam without investigating the formation of individual cracks.

The 'average' strains, assumed to vary linearly across the beam depth, may be converted into 'stress' using the stress-strain properties of separate control specimens. However, the status of these computed stresses is unclear; it is not known where they occur, if at all, because of the change of the stress profile between cracked and uncracked cross-sections as described above. What is needed is a method of deriving the applied moment as a function of the 'average' strains, incorporating tension stiffening and based so far as possible on experimental results with a minimum of intervening theory.

In deriving the applied moment, the concept of a 'tension stiffening force' is used. This is the apparent extra force in the tension zone in the experiments, above the force calculated from the average strains in the steel bars and the stress-strain characteristics of bare reinforcement. Also of interest is the level in the beam at which this tension stiffening force acts. Before cracking, this level will presumably be at the centroid of a triangular distribution of tensile stress in the concrete. After cracks are well established the tension stiffening force will tend to act at the steel level -- since the only way in which extra force can be transmitted across major cracks is by increased stress (above the value for the 'average' strain) in the steel bars crossing the cracks.

Two different approaches based on the above discussion can be used to evaluate the tension stiffening force and the 'enhanced stress'-strain curve for steel from experimental results. These are presented in the following subsections.

3.2.2 First approach

In this approach, knowledge of the exact properties of materials, and in particular those of concrete in uniaxial compression, is assumed. From the measured distribution of average strains (on long gauge lengths) across the depth of the beam (see Figure 3.2-3), both the 'average' compressive force and the 'average' force in the bare tension steel can be

found from the material properties. Assuming that these 'average' forces and the tension stiffening force F_t must satisfy equilibrium, F_t will be equal to the average compressive force C_m minus the average tensile force T_{sm} in the bare tension steel as shown in Figure 3.2-3. Thus, if compression is negative and tension is positive,

$$F_t = -C_m - T_{sm} \quad \ldots \qquad \ldots (3.2\text{-}1)$$

$$F_t = b \int_{\varepsilon_{ci} = 0}^{\varepsilon_{ci} = \varepsilon_{cm}} (-\sigma_{ci})\, dz - \sigma_{sm} A_s \quad \ldots \qquad \ldots (3.2\text{-}2)$$

where

b is the breadth of the beam;

ε_{ci} is the average compressive strain in concrete at a distance of z_i above the neutral axis;

σ_{ci} is the corresponding average compressive stress;

σ_{sm} is the average tensile stress in the tension steel found from the uniaxial stress-strain curve for the bare steel bar; and

A_s is the cross-sectional area of the tension steel.

The line of action of the tension stiffening force F_t is found from satisfying the condition that the applied bending moment is equal to the resisting moment. If d_{ts} is the depth, below the compression face, at which F_t acts, then

$$d_{ts} = \frac{M_a - T_{sm}\, d_s - C_m\, d_c}{F_t} \quad \ldots \qquad \ldots (3.2\text{-}3)$$

where

d_{ts} is the depth of the line of action of the tension stiffening force F_t measured from the compression face;

d_c is the same, for the average compressive force C_m;

d_s is the same, for the average tensile force T_{sm} in the bare tension steel and is equal to the depth of this steel; and

M_a is the applied bending moment.

The force F_t calculated using this approach was found to be sensitive to small errors in measuring the neutral axis depth; also detailed knowledge of the behaviour of concrete in the compression zone is required.

3.2.3 Second approach

In this approach, the magnitude of the total tensile force T_t was found by dividing the applied bending moment M_a by the lever arm. This can be written as

$$T_t = \frac{M_a}{(d_t - d_c)} \quad \ldots \qquad \ldots (3.2\text{-}4)$$

where d_t is the depth of the total tensile force measured from the compression face.

The tension stiffening force is equal to the total tensile force minus the average tensile force in steel i.e.

$$F_t = T_t - \sigma_{sm} A_s \quad \ldots \qquad \ldots (3.2\text{-}5)$$

In Equation 3.2-4, the depth d_t is unknown and was therefore calculated using an iterative procedure in which the depth d_{ts} below the

compressive face, as well as the magnitude of the tension stiffening force, were obtained. This iterative procedure used Equations 3.2-4 and 3.2-5 plus the following equation (obtained by taking moments about the compression face level):

$$d_t = \frac{F_t\, d_{ts} + \sigma_{sm}\, A_s\, d_s}{T_t} \quad \ldots \quad \ldots (3.2\text{-}6)$$

The initial value of d_t in Equation 3.2-4, used in the first step of the first load-stage calculation, was taken to be equal to the steel depth d_s. At each successive step in the iterative procedure, the initial value of d_t was taken as the value of d_t from the previous step. For load stages before cracking (i.e. with $M_a < M_{cr}$), iteration was carried out until the values of the depth (of the total tensile force below the n.a.) from two successive steps fell within ± 5 % of each other. The value of d_{ts} in Equation 3.2-6 was taken to be equal to 2/3 of the tension zone height plus the 'uncracked' neutral axis depth. However, for load stages beyond cracking, the depth d_{ts} of the tension stiffening force is an unknown value; thus the number of iterations was limited to one so that the value of d_{ts} can be calculated using Equation 3.2-6. A check was carried out, at each load stage, on the difference between the depths of the total tensile force and the force in the bare steel. The load stage at which this difference ($= d_t - d_s$) fell within ± 5 % of the depth of the steel below the neutral axis, was termed the limiting stage. At and beyond this limiting stage (the stage at which primary cracks have ceased to form), the depth d_t was assumed to be equal to the steel depth d_s, since the only way in which the tensile stresses can be transmitted across major cracks beyond this stage is through the steel reinforcement.

The great merit of this second approach is that knowledge of the concrete properties is not required, except for the purpose of finding the depth d_c of the compressive force -- the magnitude of the compressive force does not enter into equations for the tension stiffening force. This means that possible differences between narrow beams and wide slabs in 'compression zone' properties are not of great importance. Conversely,

however, the axial force equation (Equation 3.2-1) may not be satisfied although one can use this equation to calculate C_m from known F_t and T_{sm} (thus giving the effective compression properties of the concrete in the beam).

3.2.4 Modified steel properties

Once the tension stiffening force is obtained using one of the above two approaches, the enhanced stress of the tension steel at a given load stage can be obtained from the following equation:

$$\sigma_{se} = F_t/A_s + \sigma_{sm} \quad \ldots \qquad \ldots (3.2\text{-}7)$$

where

σ_{se} is the enhanced stress in the tension steel corresponding to an average strain ε_{sm}; and

F_t is the tension stiffening force as calculated using one of the two approaches described above;

If the enhanced stress σ_{se} is plotted against the average steel strain, a modified stress-strain curve such as that shown in Figure 3.2-4 will be obtained.

3.3 Application to Test Results

The above two approaches were applied to the results of experiments on 14 r.c. beams and 9 r.c. slabs tested in uniaxial bending by Clark and Speirs [51], and to the experimental results from tests on further 8 slabs by Clark and Cranston [57]. Copies of the two experimental results were sent to us by Dr. Clark (private communication). The measured dimensions and details of each of the beams and slabs and the results for concrete control specimens are given in Table 3.3-1 -- the letter 'R' after a specimen number indicates that a second nominally identical specimen was tested. The stress-strain curve for concrete in compression was assumed to be parabolic with a peak stress σ_{cc} and a corresponding strain ε_{cc}, the

values of which were taken as follows:

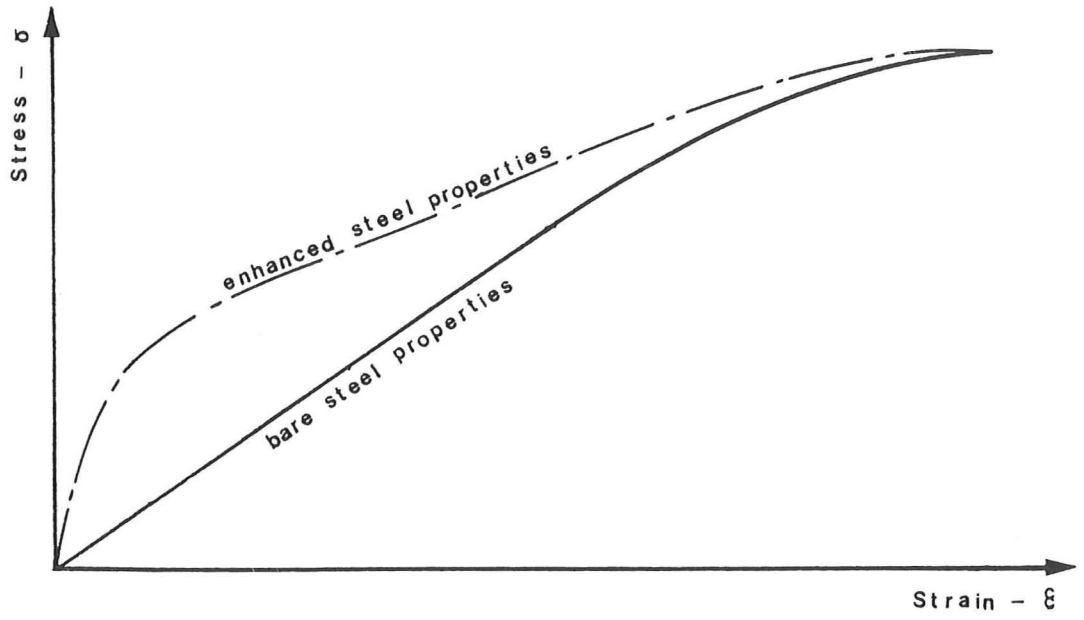

Figure 3.2-4 A typical 'enhanced stress' - strain relationship for the tension steel in relation to the bare steel bar properties.

$$\sigma_{cc} = k' \; k'' \; \sigma_{cu} \quad \ldots \qquad \ldots (3.2\text{-}8)$$

$$\varepsilon_{cc} = 2 \; (\sigma_{cc}/E_c) \quad \ldots \qquad \ldots (3.2\text{-}9)$$

where

σ_{cu} is the cube strength of concrete in compression;

Table 3.3-1 Measured dimensions and concrete properties of specimens tested by Clark et al [51],[57].

Specimen Type	No.	Width mm	Depth mm	Bottom steel No. bars*	Diam. mm	Depth mm	Top steel Area mm^2	Depth mm	Concrete prop. Cu. st. N/mm^2	Ten. st. N/mm^2	E_{ci} KN/mm
Beam	1	203	410	3	25	380	402	37	33.8	2.08	26.5
	1R	202	412	"	25	368	402	35	34.7	2.78	29.9
	2	203	408	"	20	363	101	20	33.3	2.12	28.0
	2R	204	408	"	20	367	101	24	39.6	2.74	30.5
	3	204	407	"	16	373	101	33	38.1	3.05	30.3
	3R	204	409	"	16	376	101	34	36.5	2.51	35.1
	4	204	409	"	12	379	101	35	28.9	2.17	25.0
	4R	204	406	"	12	370	101	38	31.1	2.31	28.9
	5	203	204	"	16	167	226	26	29.3	2.18	21.0
	5R	202	202	"	16	169	226	28	35.3	3.19	26.6
	6	203	306	"	16	268	101	30	26.3	2.64	25.2
	6R	203	308	"	16	273	101	30	34.1	2.88	28.0
	7	203	513	"	16	480	101	37	23.0	2.05	25.0
	7R	204	511	"	16	473	101	32	29.3	2.18	27.5
Slab	1	902	204	6x1	20	169	201	35	35.4	2.65	27.8
	1R	902	203	6x1	20	169	"	"	-	1.96	
	2	904	204	3x2	20	168	"	"	35.9	2.74	27.1
	2R	901	203	3x2	20	168	"	"	-	2.06	-
	3	902	205	2x3	20	169	"	"	33.9	2.92	26.1
	3R	902	204	2x3	20	166	"	"	-	1.88	-
	4	901	204	6x1	16	169	201	35	33.0	3.26	28.9
	4R	902	204	6x1	16	169	"	"	-	2.04	-
	5	901	203	3x2	16	169	"	"	26.8	2.26	27.1
	5R	903	202	3x2	16	168	"	"	-	2.50	-
	6	903	203	2x3	16	171	"	"	27.0	2.22	22.8
	6R	901	205	2x3	16	"	"	"	-	2.24	-
	7	900	201	6x1	12	170	"	"	28.1	2.04	25.9
	8	901	203	3x2	12	168	"	"	33.6	2.65	22.7
	9	901	204	2x3	12	172	"	"	33.7	2.72	26.3
	9R	904	204	2x3	12	165	"	"	-	3.01	-

* For slabs this is given as the no. of groups x the no. of bars per group.

k' is a coefficient equal to the cylinder compressive strength divided by the cube strength and is taken as 0.85;

k'' is a coefficient giving the long term response and is chosen so that the (concrete) stress-strain curve for Beam B2 matches that in Figure 9 of reference [51] -- it took a value of 0.9; and

E_c is Young's modulus for concrete.

For the 8 slabs tested by Clark and Cranston [57], the values of $\bar{\sigma}_{cu}$ and E_c were not provided so the average values from the other nine slabs were used instead.

Application to the author's test results from experiments on eight concrete slabs reinforced with skew steel mesh and tested in uniaxial bending will be presented in Chapter 5.

3.3.1 Computer programs

Two computer programs were written for the University Computer IBM 370, the first of which carried out the analysis mentioned above. The second computer program had the task of plotting the results of this analysis, as presented in Figures 3.3-1 to 3.3-34.

3.3.2 Comparison between first and second approaches

Figures 3.3-1a and 3.3-2a show two examples of typical experimental relationships between $\bar{\sigma}_{se}/\bar{\sigma}_{sy}$ (where $\bar{\sigma}_{sy}$ is yield stress of steel) and $\varepsilon_{sm}/\varepsilon_{syi}$ (= $\bar{\sigma}_{sy}/E_s$, where E_s is Young's modulus for steel) calculated using the above two approaches and compared with the bare steel bar curve. Figures 3.3-1b and 3.3-2b show the variation with the ratio $\varepsilon_{sm}/\varepsilon_{syi}$ of the positions of the total tensile force, the total compressive force, and of the neutral axis. It can be seen from Figure 3.3-1 that the irregularities in the 'enhanced stress'-strain (experimental) relationship obtained using the first approach (Subsections 3.2.1 and 3.2.3) reflects markedly the irregularities in the 'neutral axis depth'-strain curve.

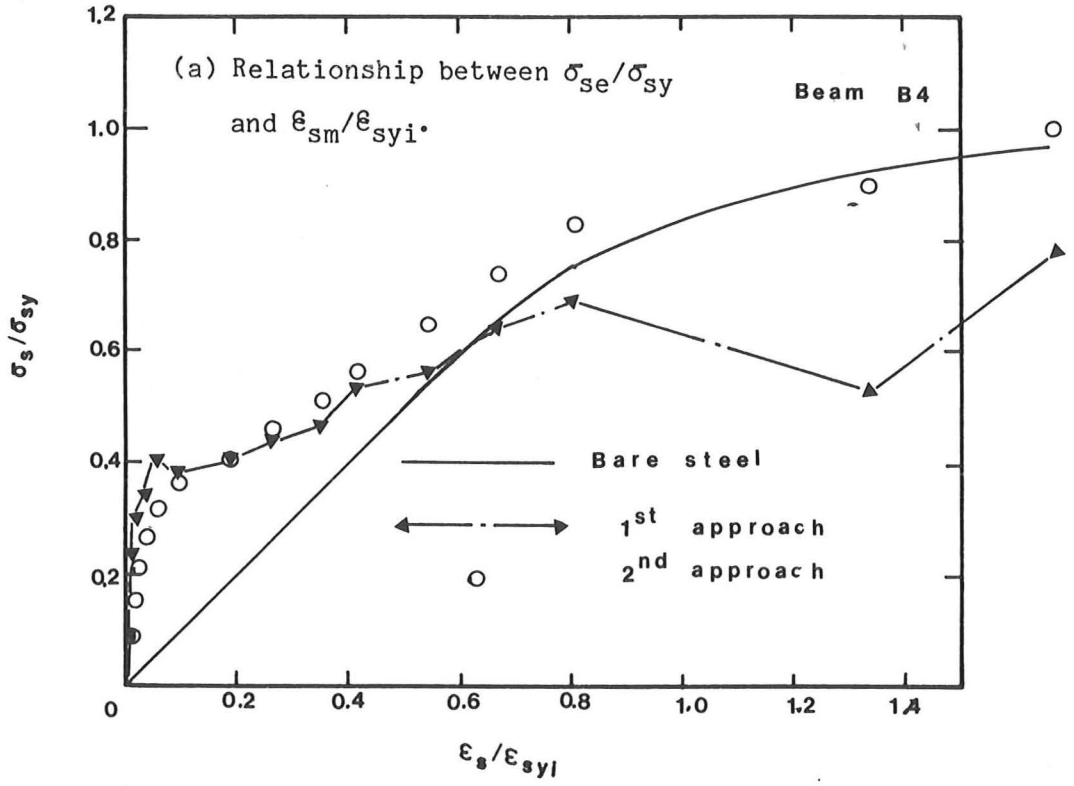

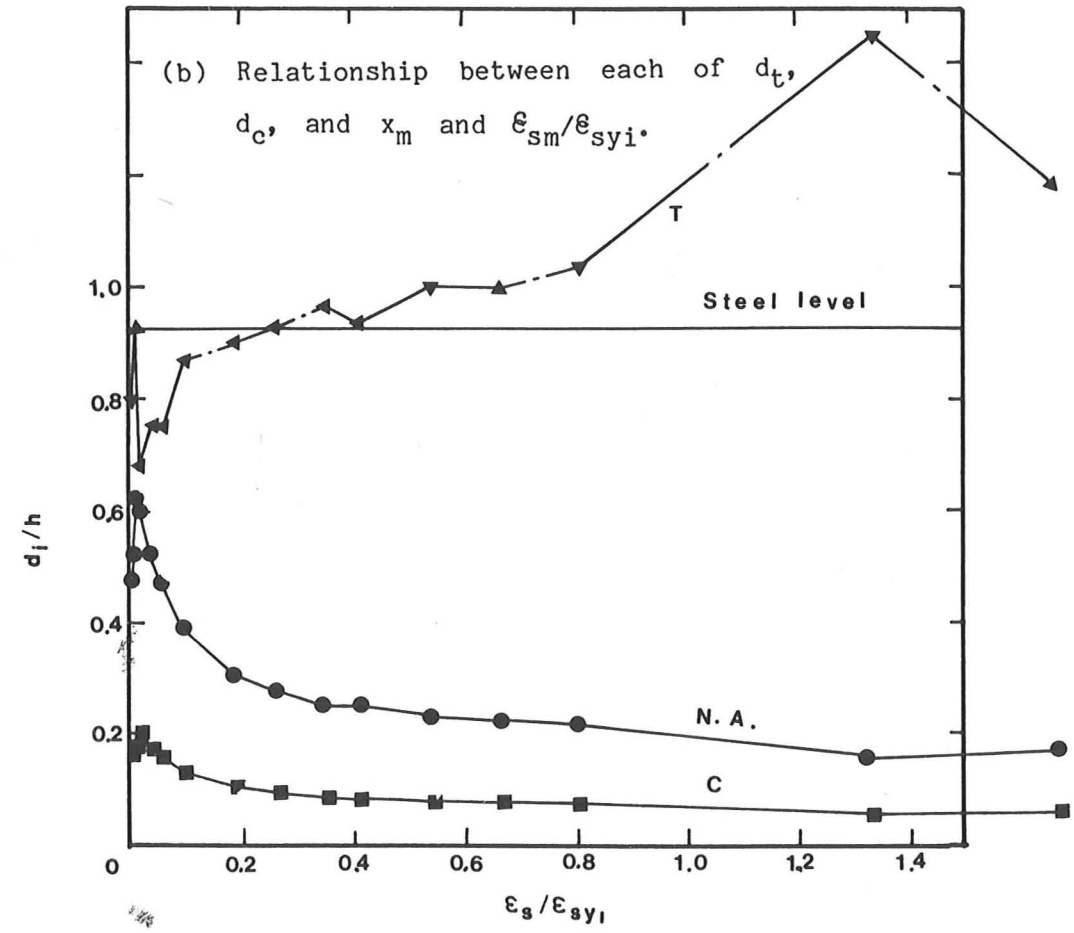

Figure 3.3-1 Analysis of the experimental results of beam B4 according to the first and second approaches.

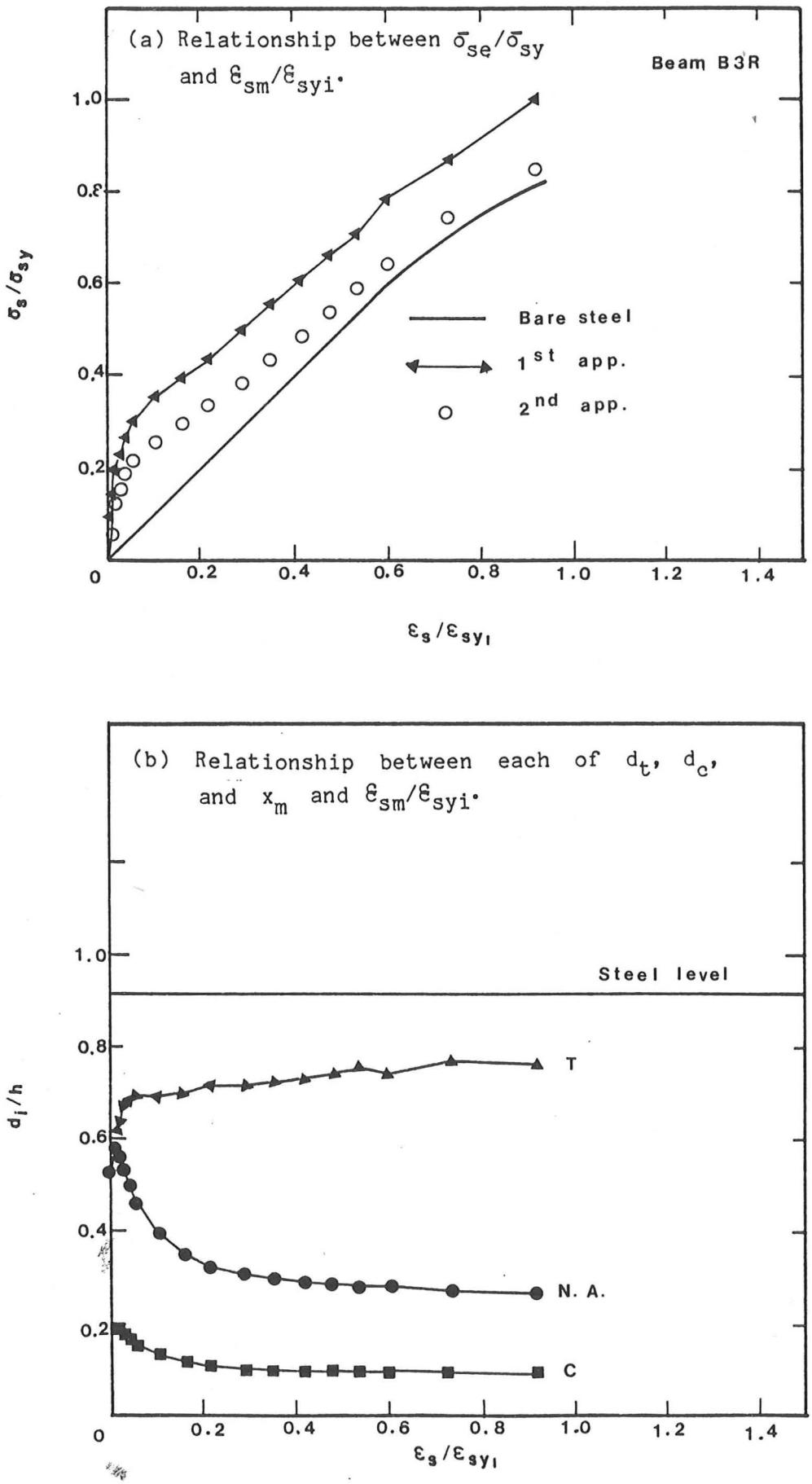

Figure 3.3-2 Analysis of the experimental results of beam B3R according to the first and second approaches.

It can also be seen from Figure 3.3-2a that the 'enhanced stress' calculated using the first approach is overestimated due to an overestimate in the uniaxial compressive strength of concrete. On the other hand, the 'enhanced stress'-strain (experimental) relationships obtained using the second approach (Subsections 3.2.2 and 3.2.3) are less sensitive to any possible error in measuring the neutral axis depth and are almost independent of the concrete compressive properties. For the above two reasons, it was decided to use the second approach of Subsection 3.2.2 in analysing the experimental data mentioned above. The results of this analysis will be used in the next section in deriving formulae for estimating the tension stiffening force and the enhanced steel stress at any strain level for a given r.c. beam or slab.

3.3.3 Application of second approach to the experimental results

The experimental data from two series of tests on beams and slabs by Clark and Speirs [51] and Clark and Cranston [57] were analysed using the second approach (Subsection 3.2.2 above). In Figures 3.3-3 to 3.3-18, the tension stiffening force F_t as a ratio of the theoretical tensile force F_{tcr} in concrete at cracking (= $f_t bh/4$, where f_t is the tensile strength of concrete) is plotted against the average steel strain ε_{sm} as a ratio of ε_{syi}. In Figures 3.3-19 to 3.3-34, the 'enhanced stress' σ_{se} as a ratio of σ_{sy} is plotted against the average strain ε_{sm} as a ratio of ε_{syi}.

Figures 3.3-3 to 3.3-6 show the effect of steel percentage (taken as a ratio of the area of the tension zone) on the maximum tension stiffening.

The higher the steel percentage, the smaller the tension stiffening effect. The influence of the cover ratio (i.e. the ratio of the cover to the reinforcement to the height of the tension zone) can be seen from Figures 3.3-7 to 3.3-10. The greater the cover ratio, the smaller the stiffening effect. This behaviour was expected since a greater cover ratio would result in smaller crack spacing according to Equations 2.2-7 and 2.2-14, and hence gives less tension stiffening.

In Figures 3.3-11 to 3.3-18, the effect of bar spacing on tension stiffening can be seen. There is little influence on the maximum tension stiffening force while the influence on the decay of the tension

stiffening force is clear from the graphs. The tension stiffening decays more quickly in slabs with greater bar spacing. The effect of bar spacing on tension stiffening is the subject of the paper by Clark and Granston [57] refered to earlier and is discussed in Chapter 2.

In practice however one would like to be able to predict the tension stiffening force at any given average steel strain, or to determine the enhanced properties for the tension steel. Thus, formulae for estimating the tension stiffening force and the ' enhanced stress'-strain curve for the tension steel will be derived in the next section. The theoretical curves determined using these formulae are plotted in Figures 3.3-3 to 3.3-34 and will be discussed later in Section 3.4. In Section 3.5, these theoretical curves, together with the approach used in deriving the theory presented here, will be compared with, and discussed in relation to the theory obtained by Clark et al [51],[57], and to the approach which they had adopted to derive this theory.

3.4 Tension Stiffening: Formulae Derivation

3.4.1 Computer programs

A computer program was written for the University Computer to carry out the analysis described in Subsections 3.4.4 and 3.4.5 and to plot the results of this analysis. The programs mentioned in Subsection 3.3.1 were extended to cover the theoretical analysis derived in this chapter and summed up in Subsections 3.4.6 to 3.4.8.

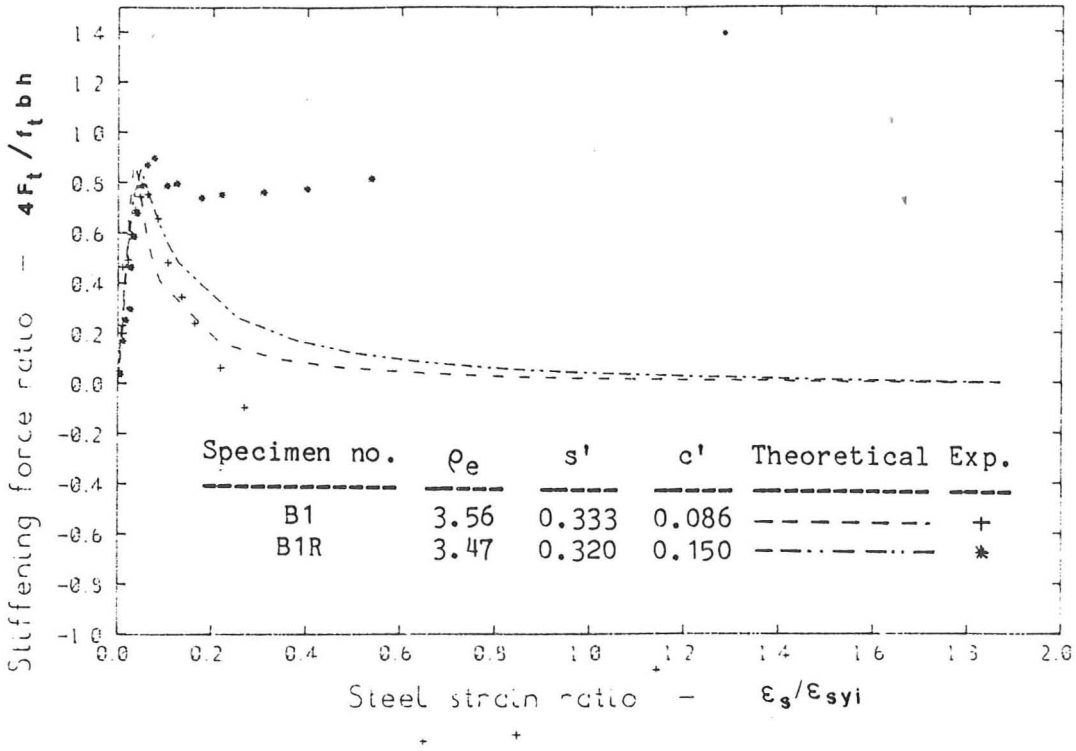

Figure 3.3-3 Tension stiffening force - steel strain relations for beams B1 and B1R.

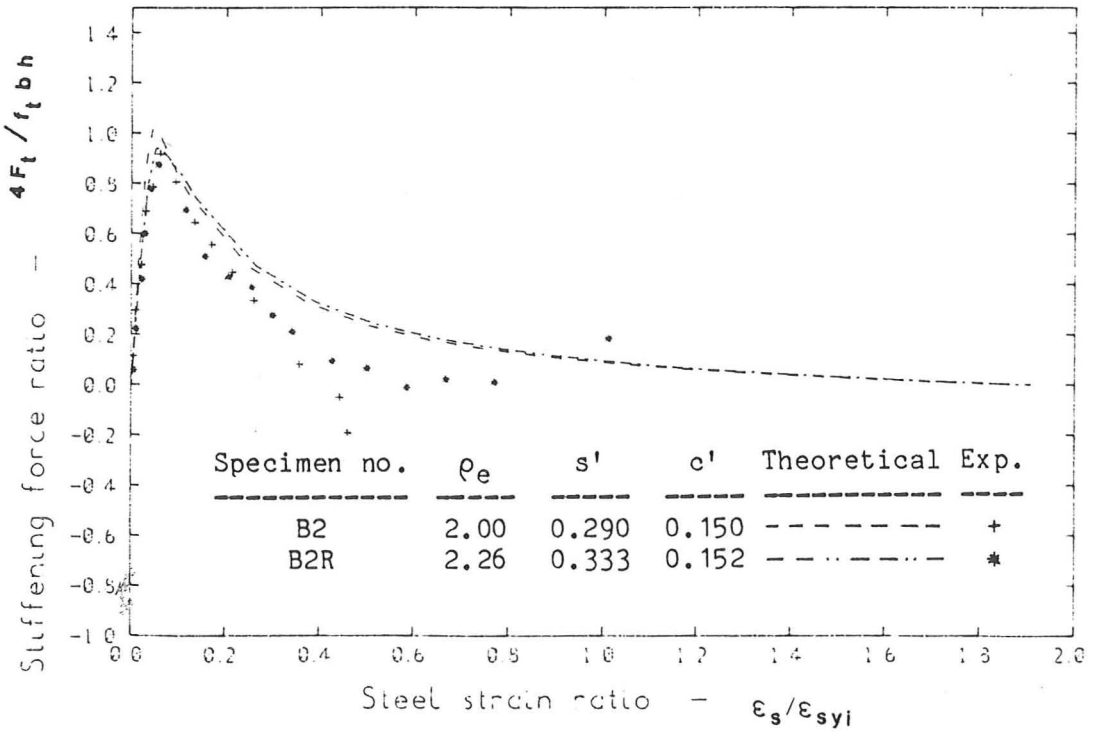

Figure 3.3-4 Tension stiffening force - steel strain relations for beams B2 and B2R.

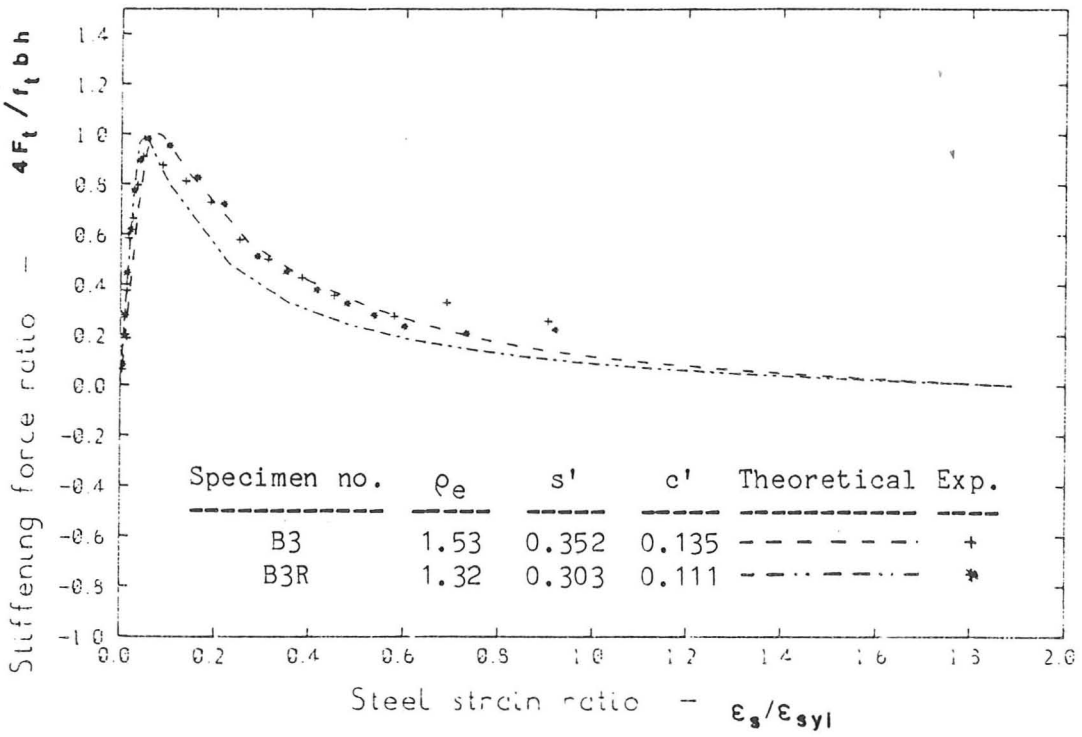

Figure 3.3-5 Tension stiffening force - steel strain relations for beams B3 and B3R.

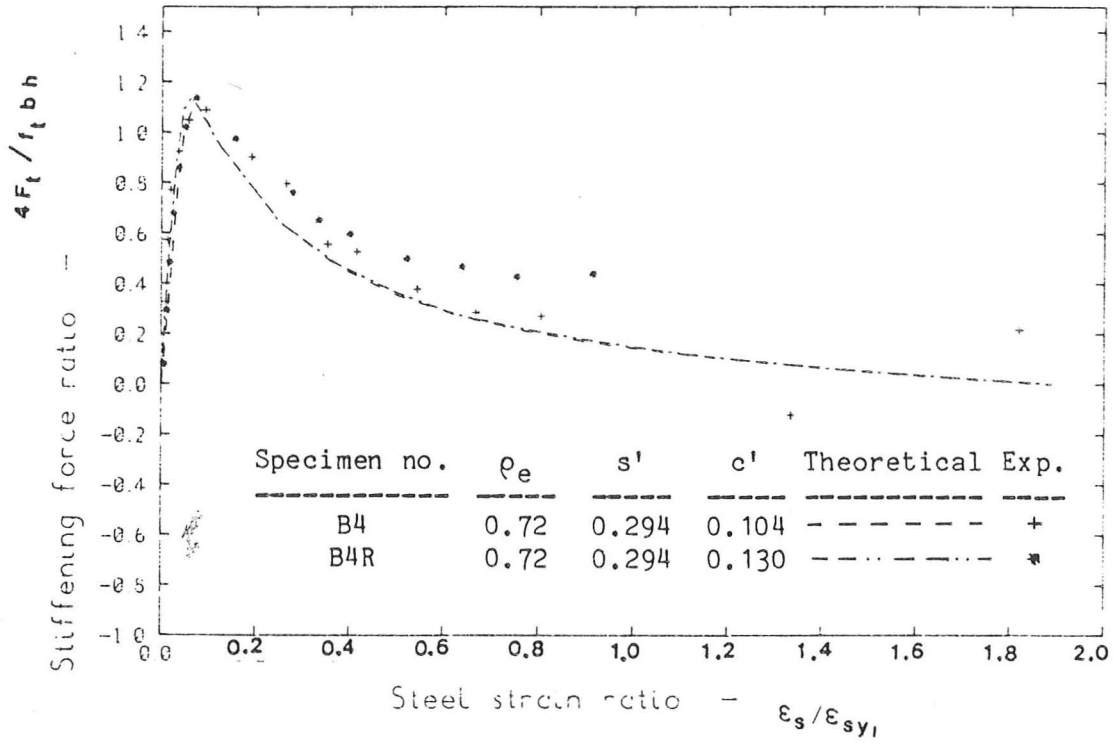

Figure 3.3-6 Tension stiffening force - steel strain relations for beams B4 and B4R.

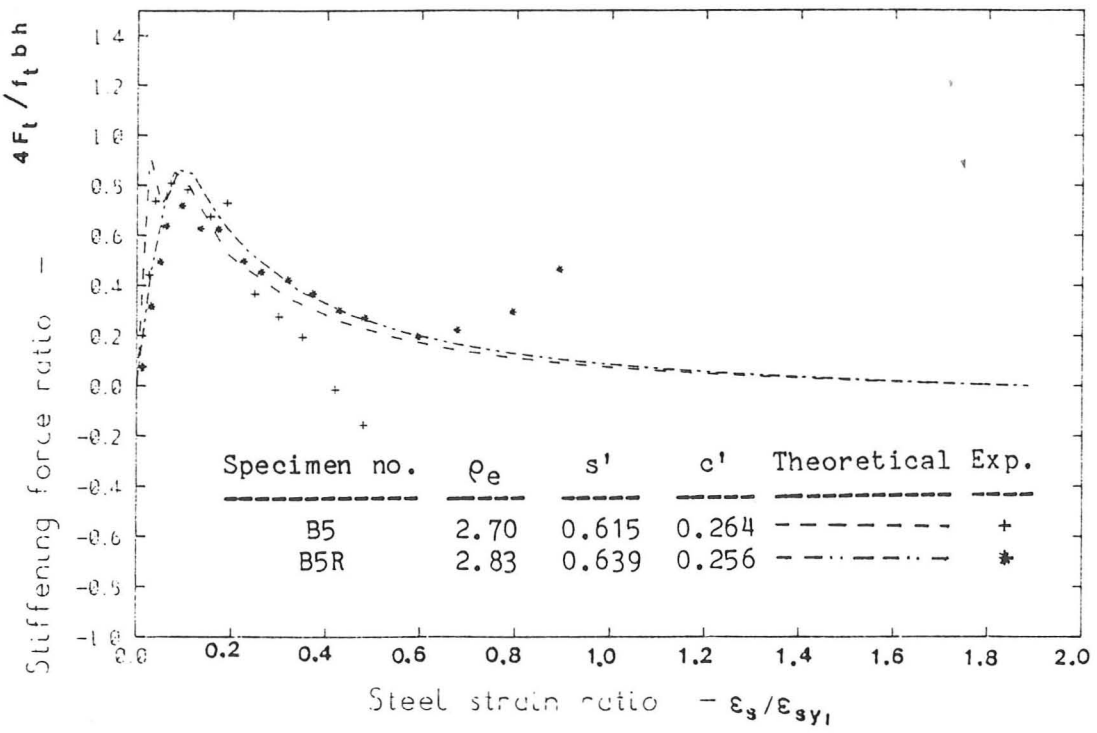

Figure 3.3-7 Tension stiffening force - steel strain relations for beams B5 and B5R.

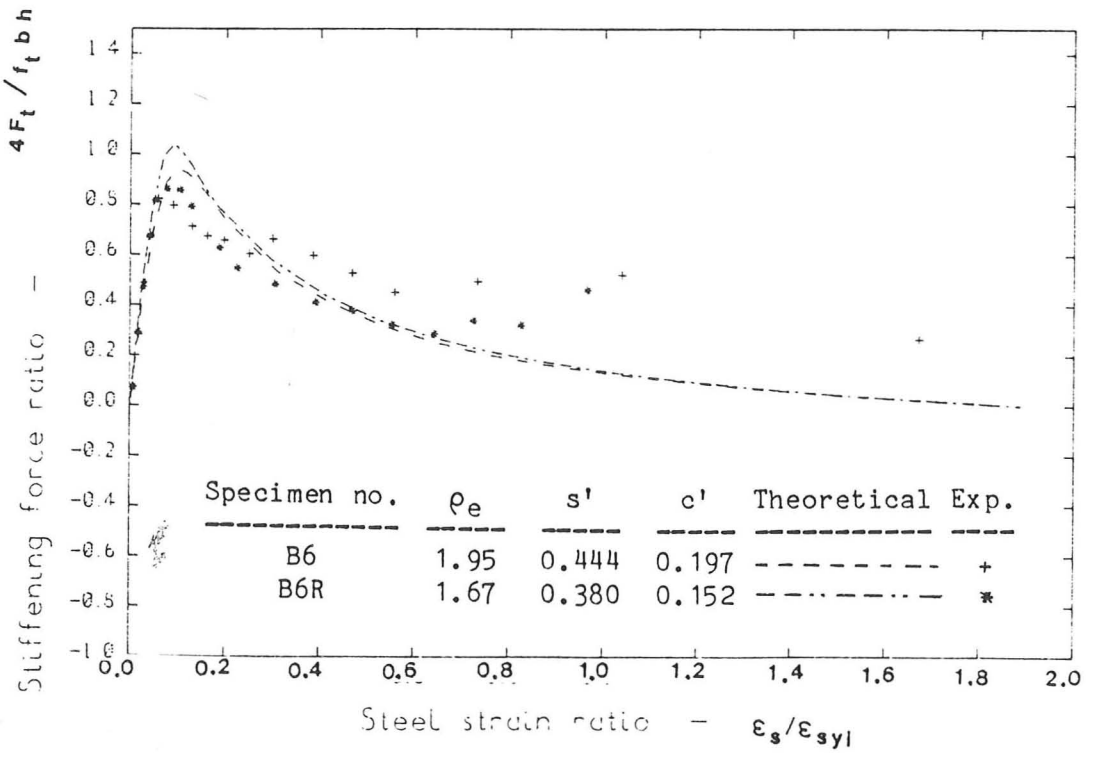

Figure 3.3-8 Tension stiffening force - steel strain relations for beams B6 and B6R.

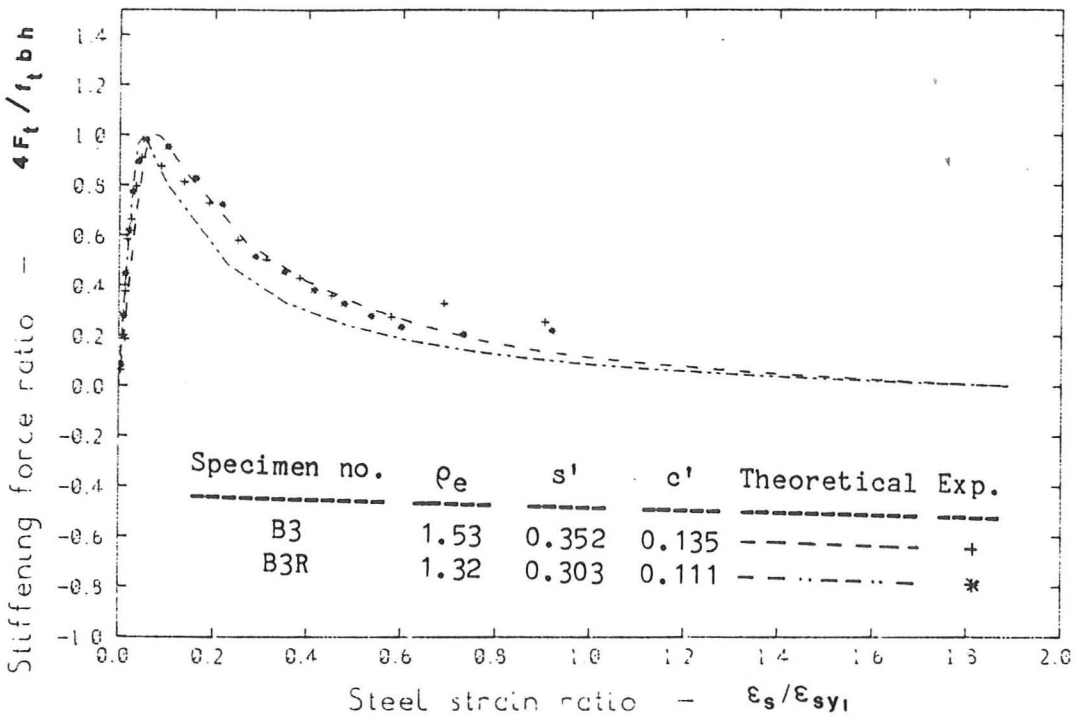

Figure 3.3-9 Tension stiffening force - steel strain relations for beams B3 and B3R.

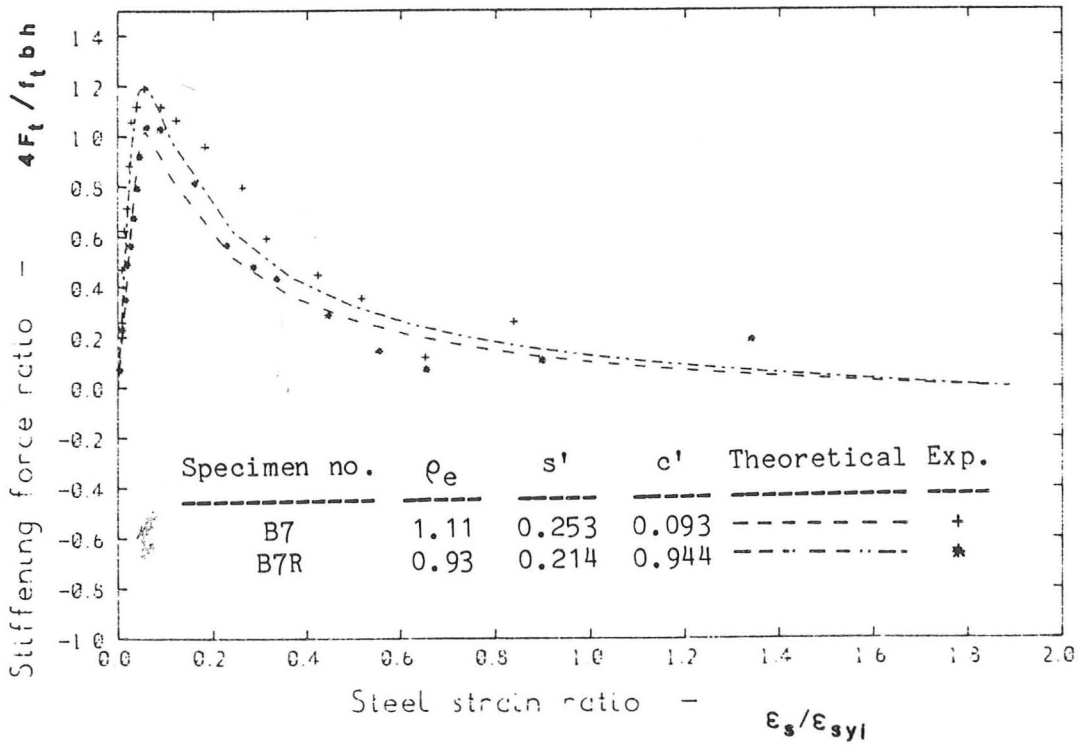

Figure 3.3-10 Tension stiffening force - steel strain relations for beams B7 and B7R.

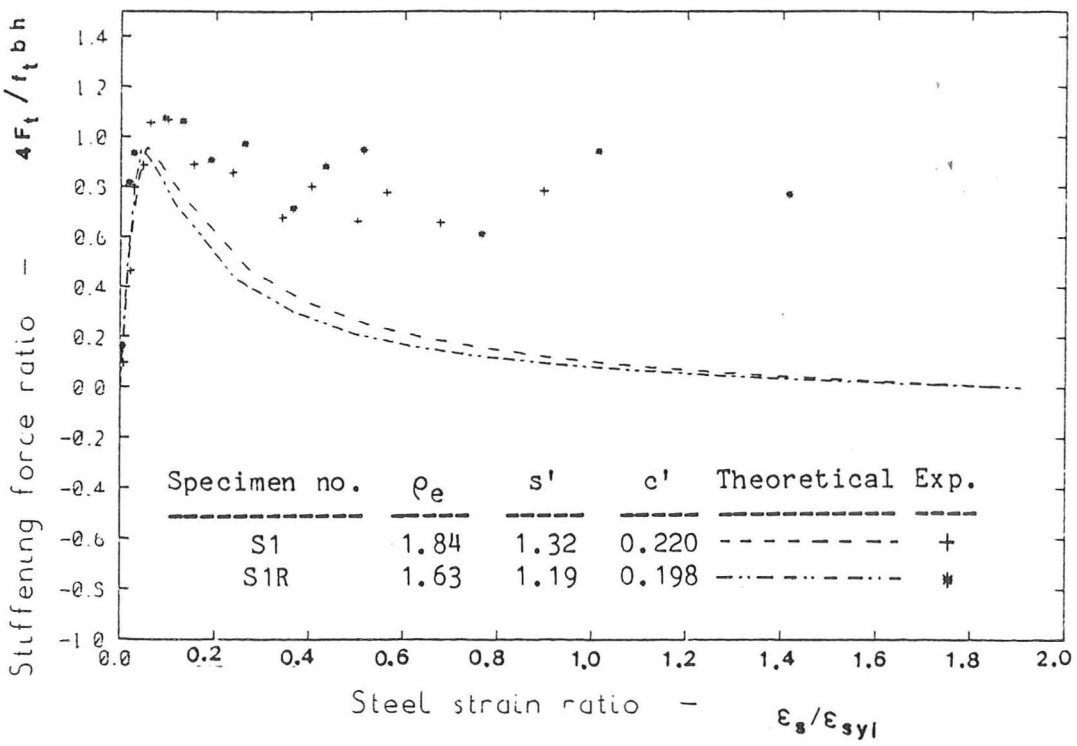

Figure 3.3-11 Tension stiffening force - steel strain relations for slabs S1 and S1R.

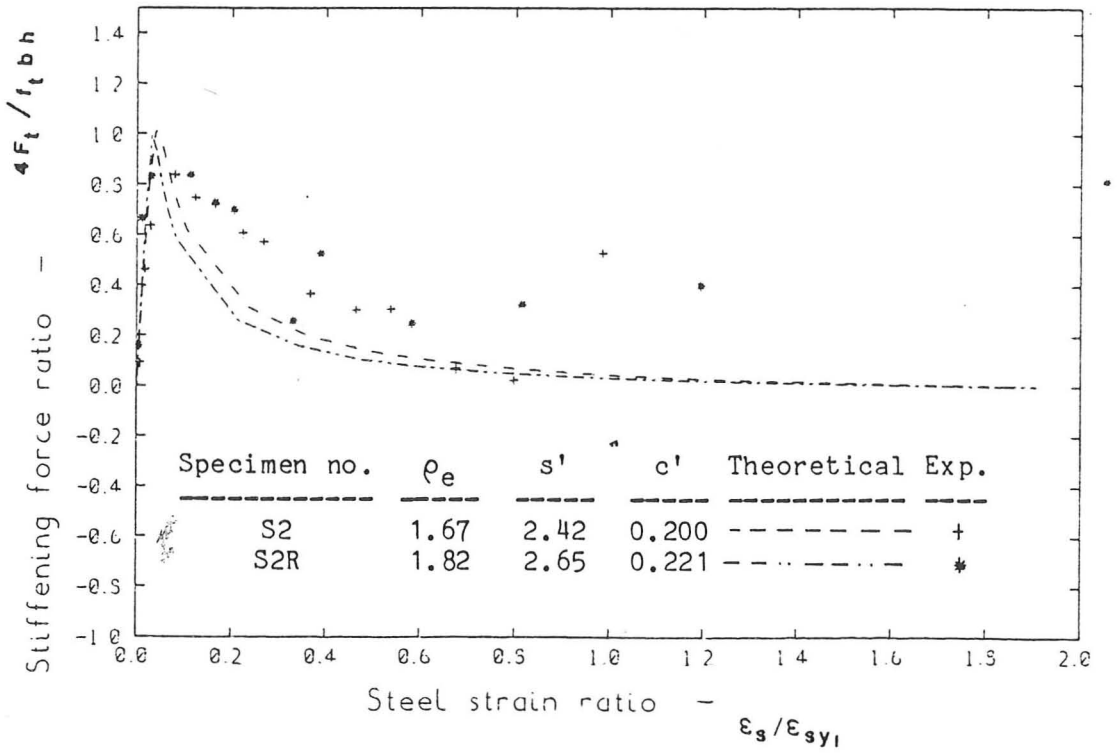

Figure 3.3-12 Tension stiffening force - steel strain relations for slabs S2 and S2R.

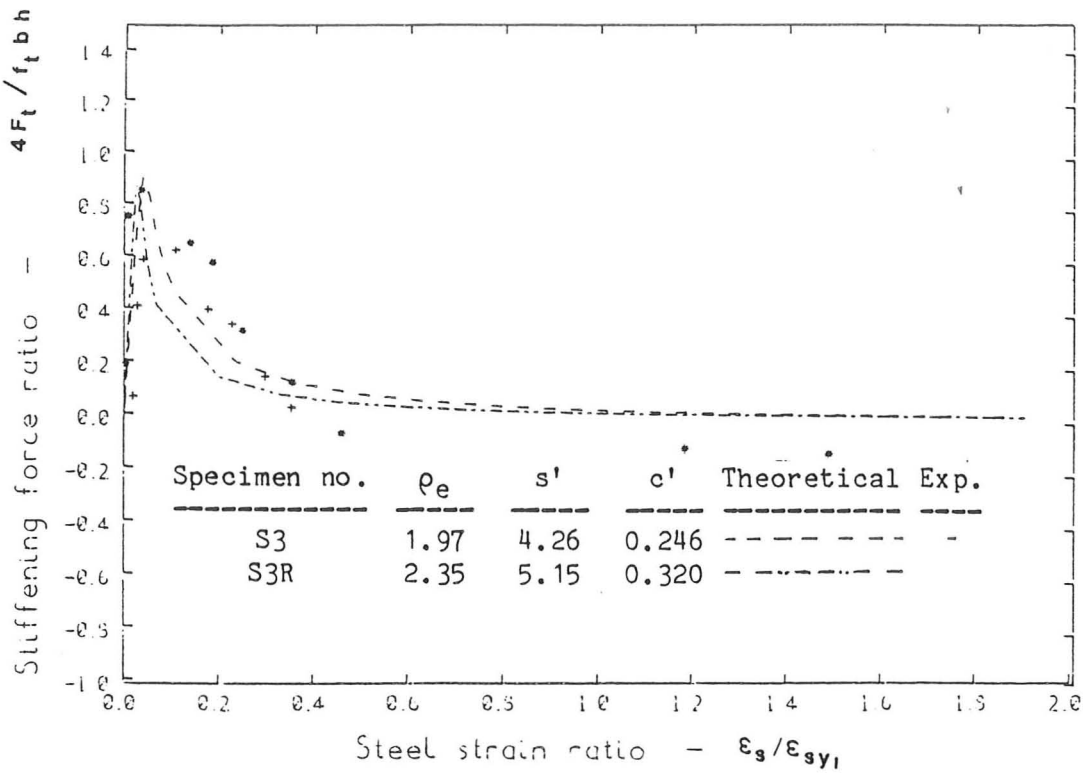

Figure 3.3-13 Tension stiffening force - steel strain relations for slabs S3 and S3R.

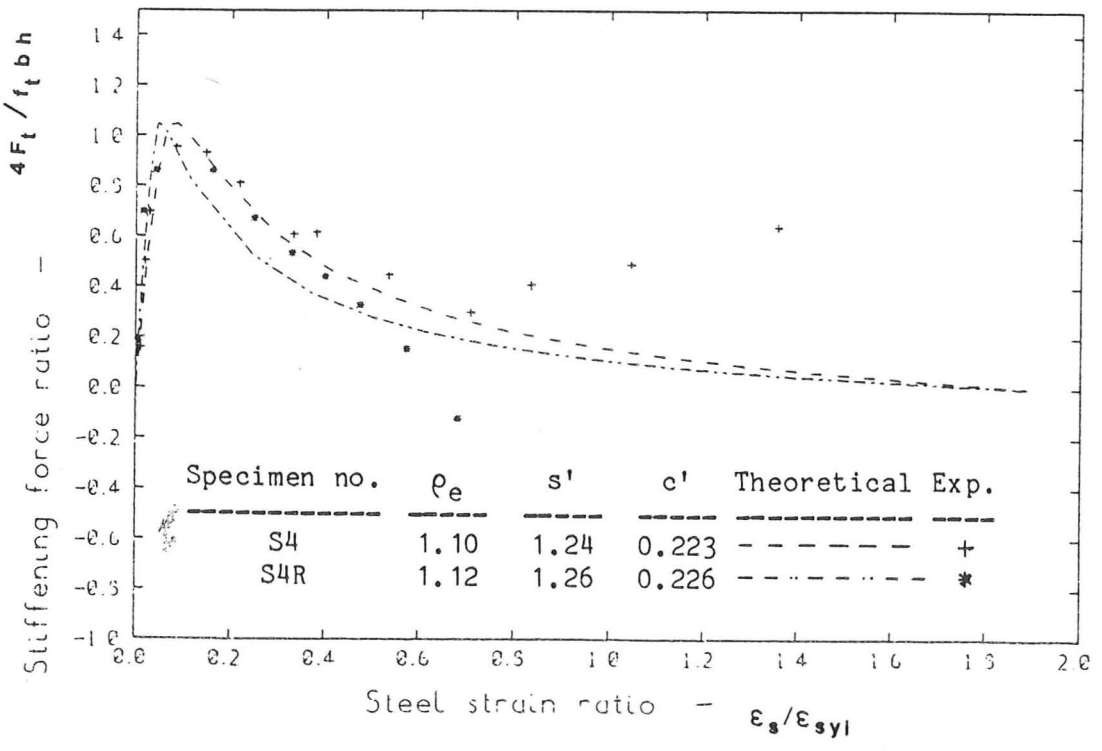

Figure 3.3-14 Tension stiffening force - steel strain relations for slabs S4 and S4R.

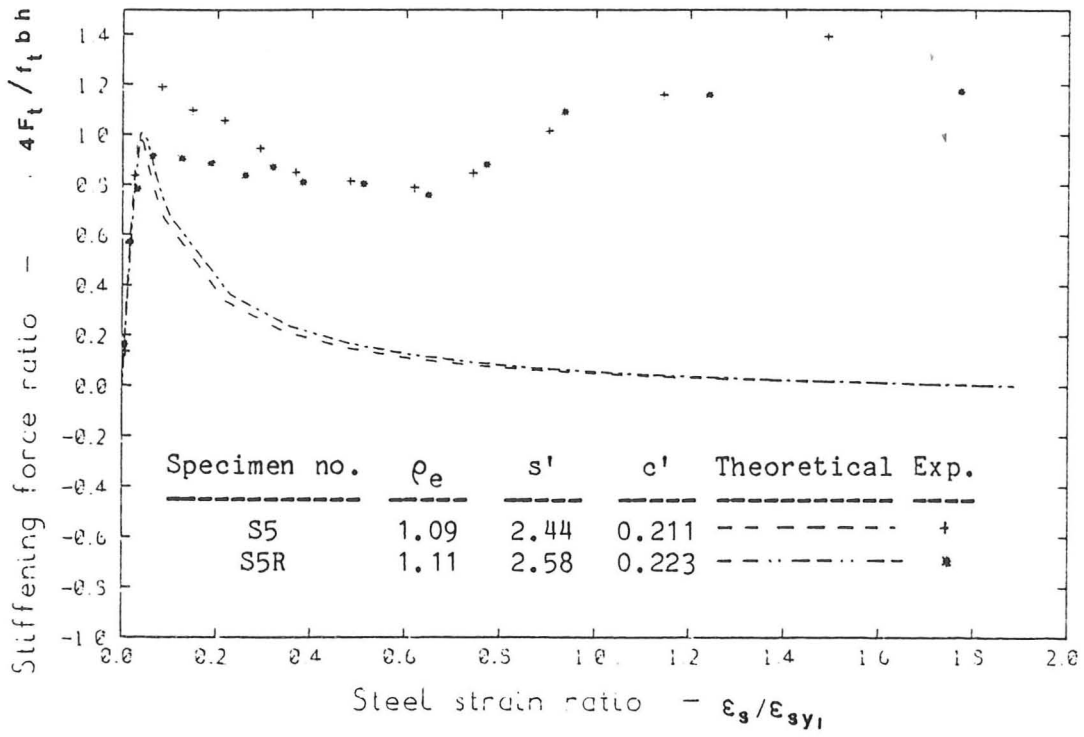

Figure 3.3-15 Tension stiffening force - steel strain relations for slabs S5 and S5R.

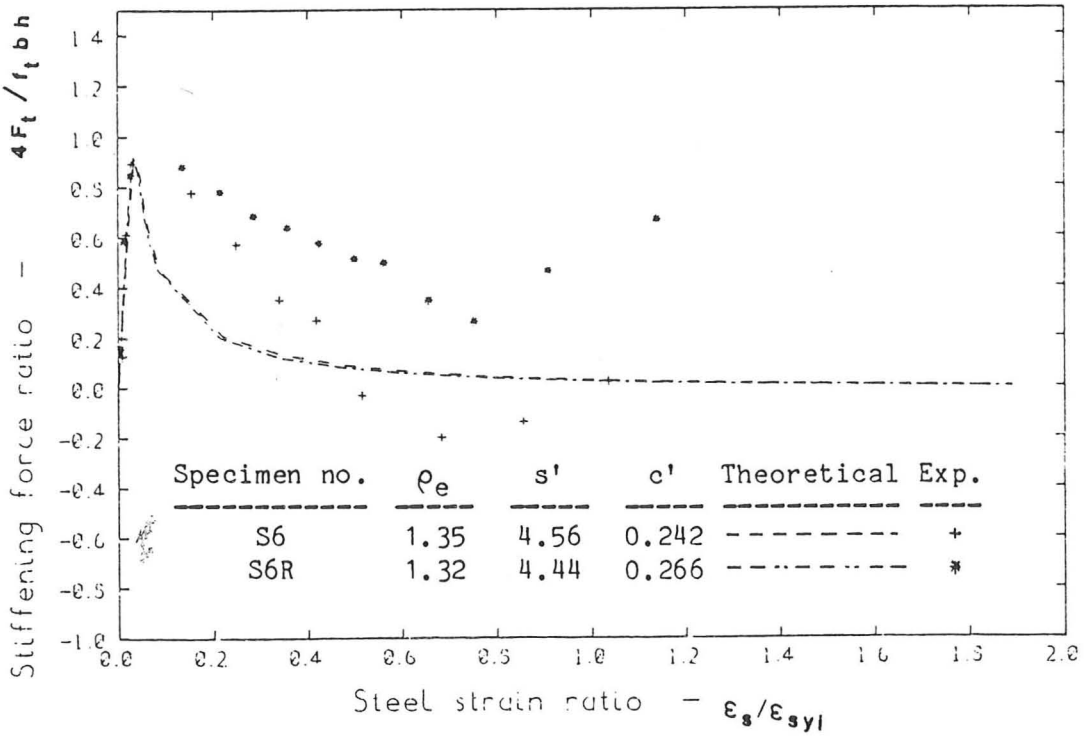

Figure 3.3-16 Tension stiffening force - steel strain relations for slabs S6 and S6R.

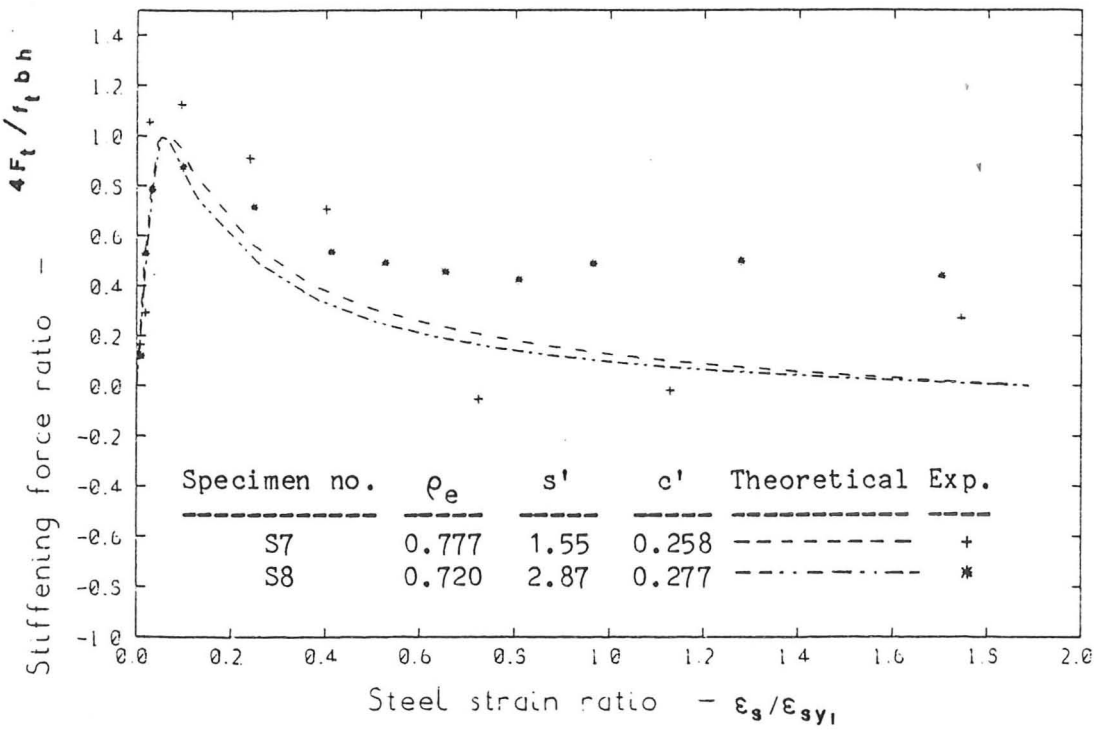

Figure 3.3-17 Tension stiffening force - steel strain relations for slabs S7 and S8.

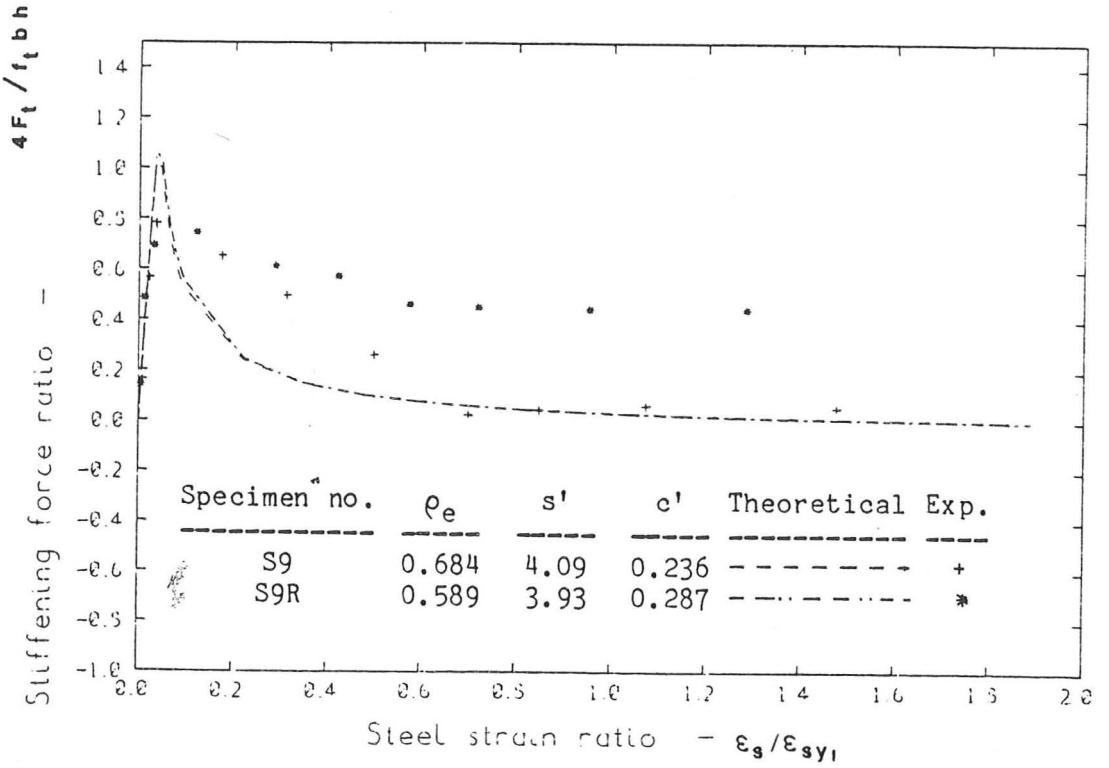

Figure 3.3-18 Tension stiffening force - steel strain relations for slabs S9 and S9R.

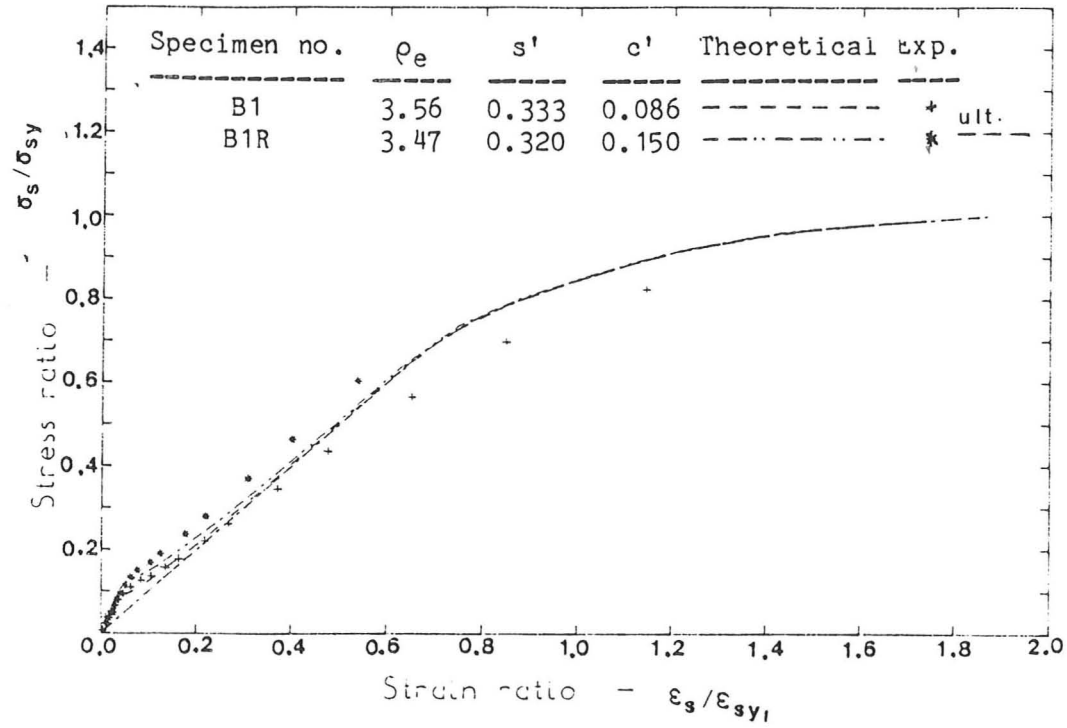

Figure 3.3-19 Enhanced steel properties for beams B1 and B1R.

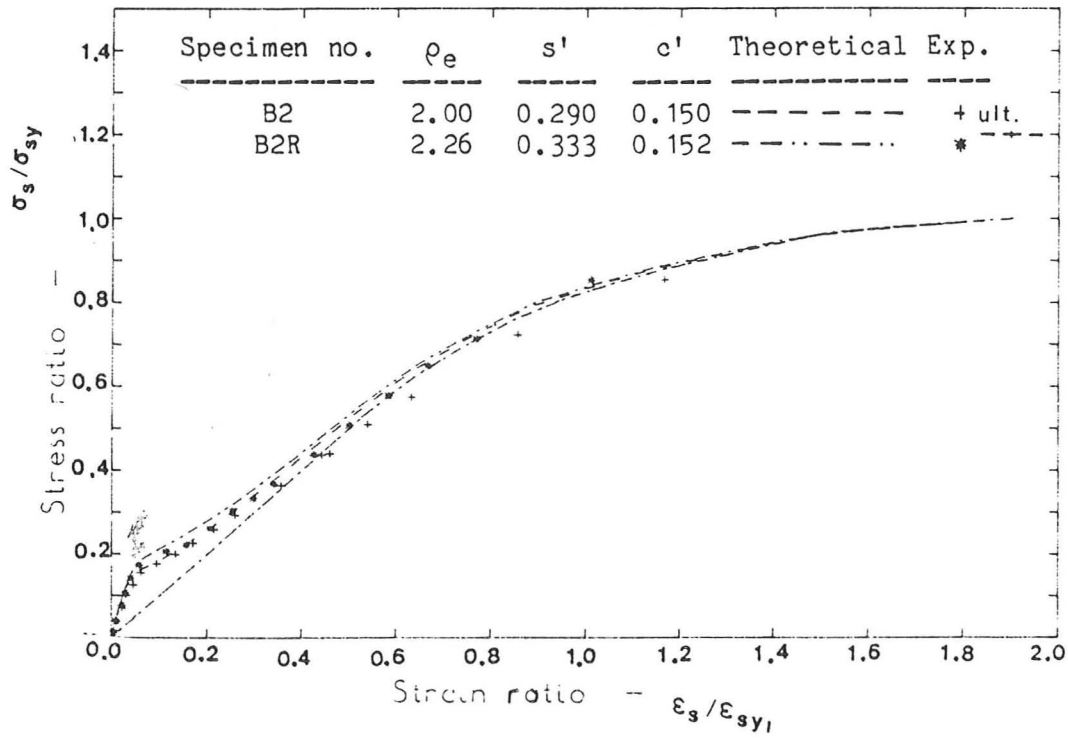

Figure 3.3-20 Enhanced steel properties for beams B2 and B2R.

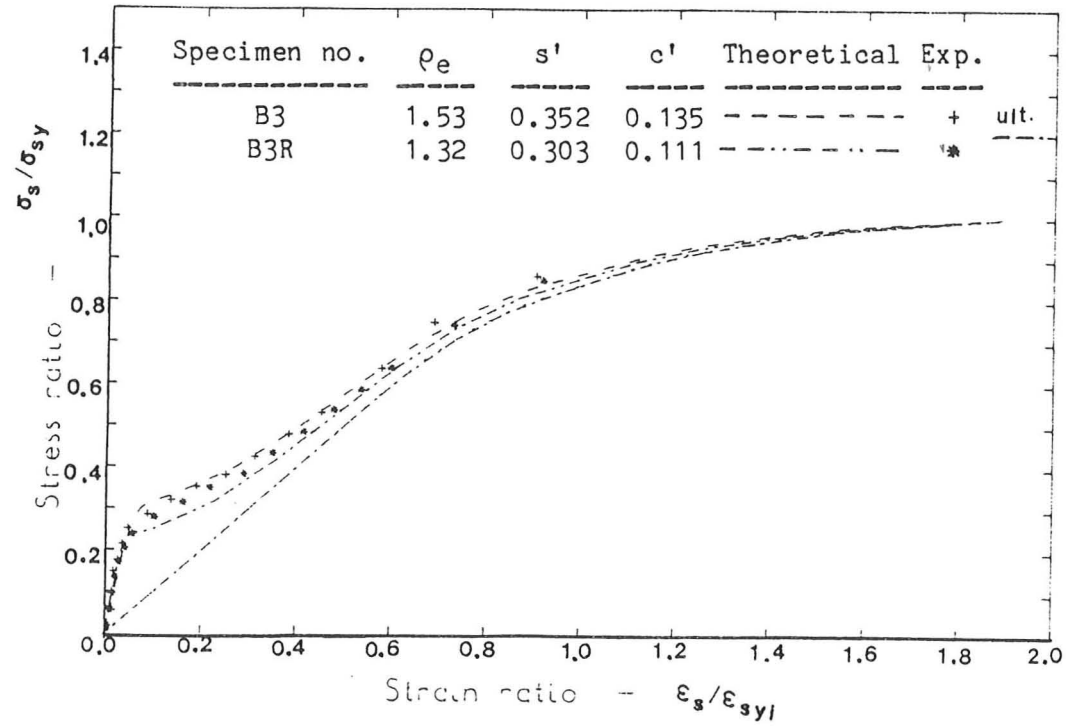

Figure 3.3-21 Enhanced steel properties for beams B3 and B3R.

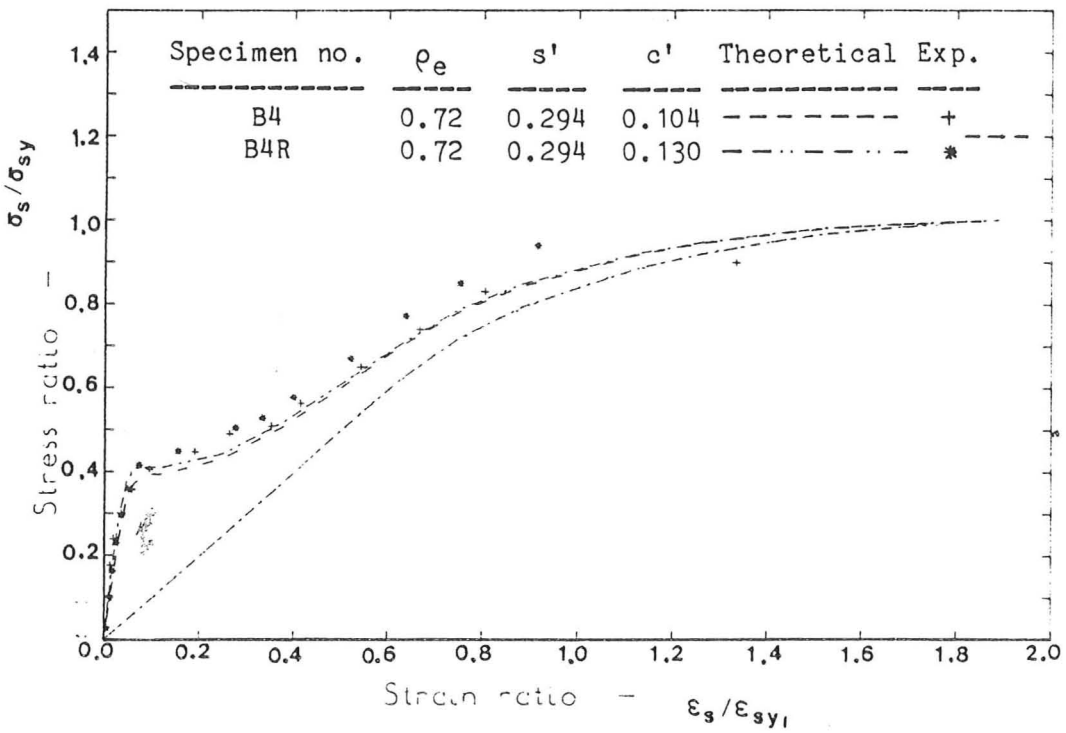

Figure 3.3-22 Enhanced steel properties for beams B4 and B4R.

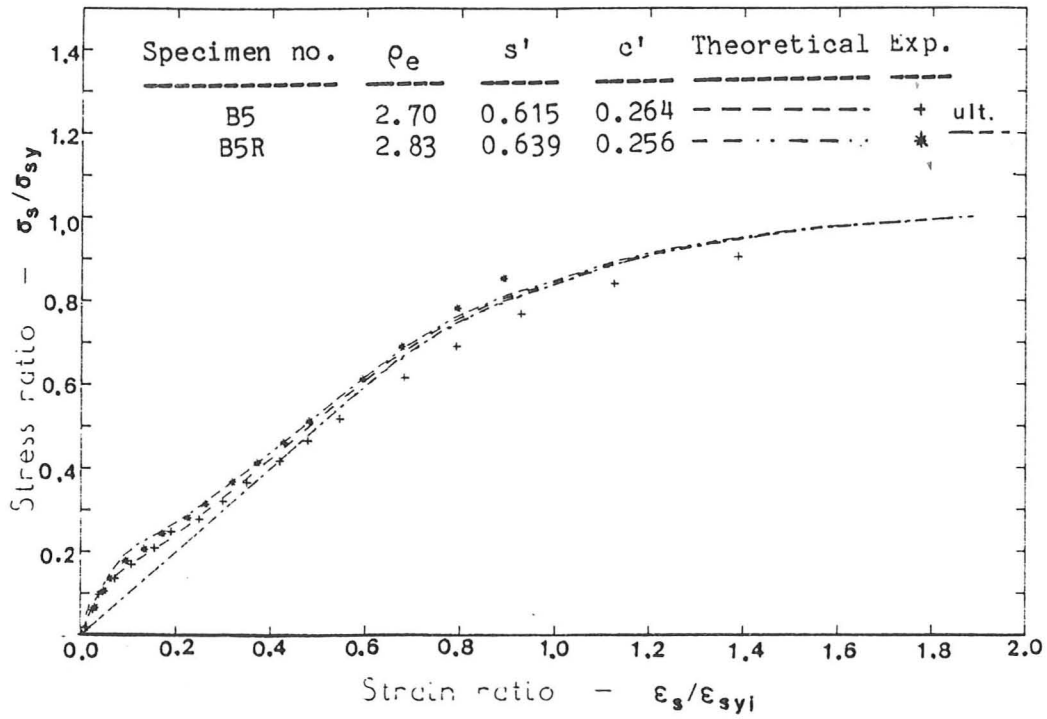

Figure 3.3-23 Enhanced steel properites for beams B5 and B5R.

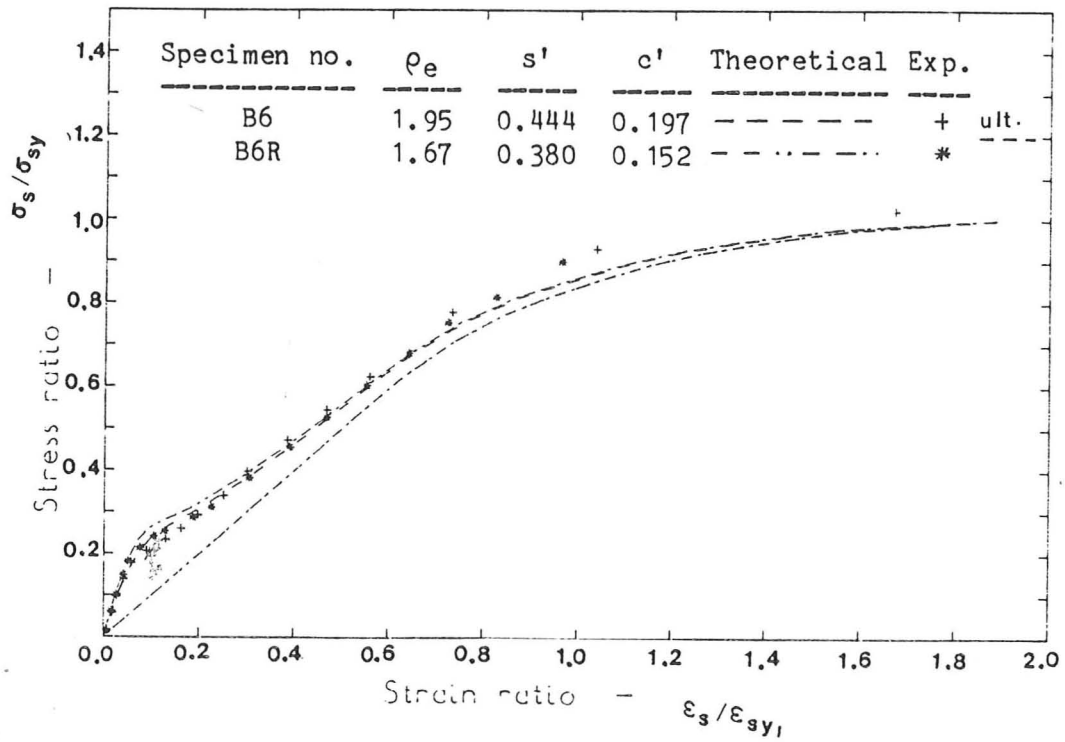

Figure 3.3-24 Enhanced steel properties for beams B6 and B6R.

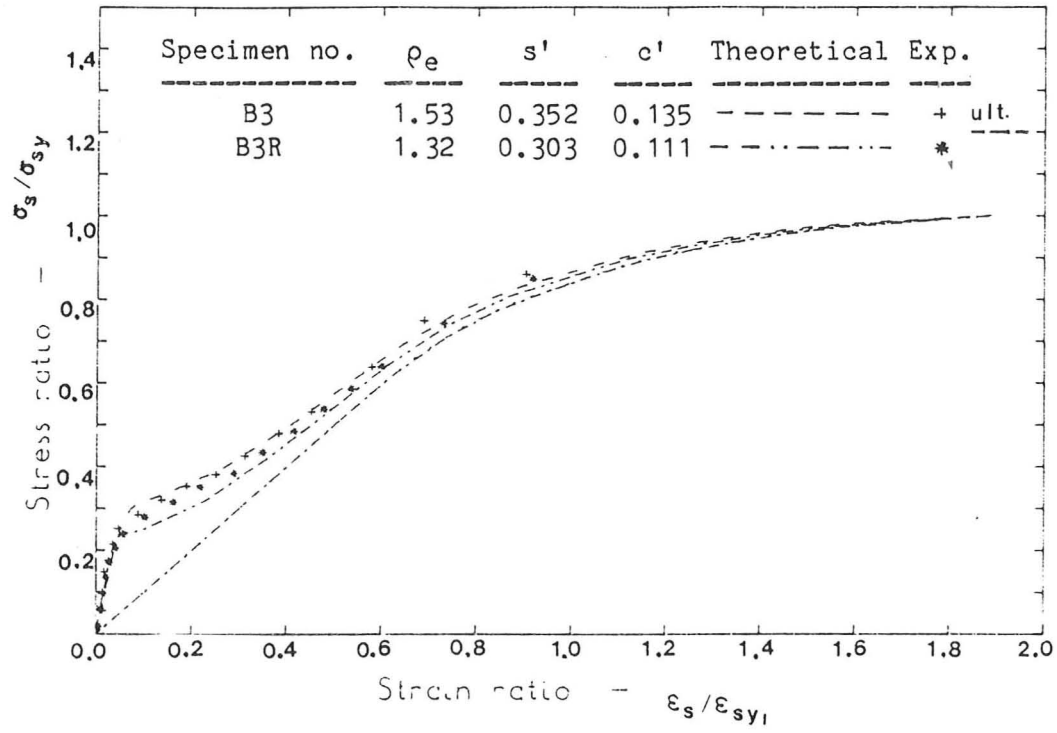

Figure 3.3-25 Enhanced steel properties for beams B3 and B3R.

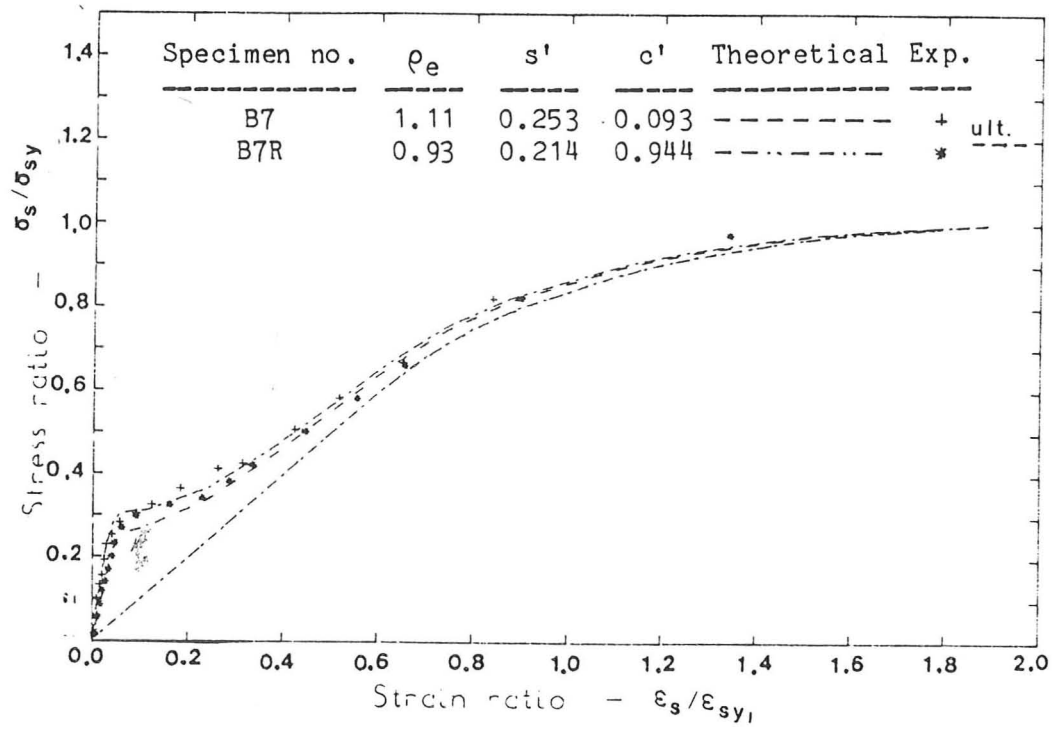

Figure 3.3-26 Enhanced steel properties for beams B7 and B7R.

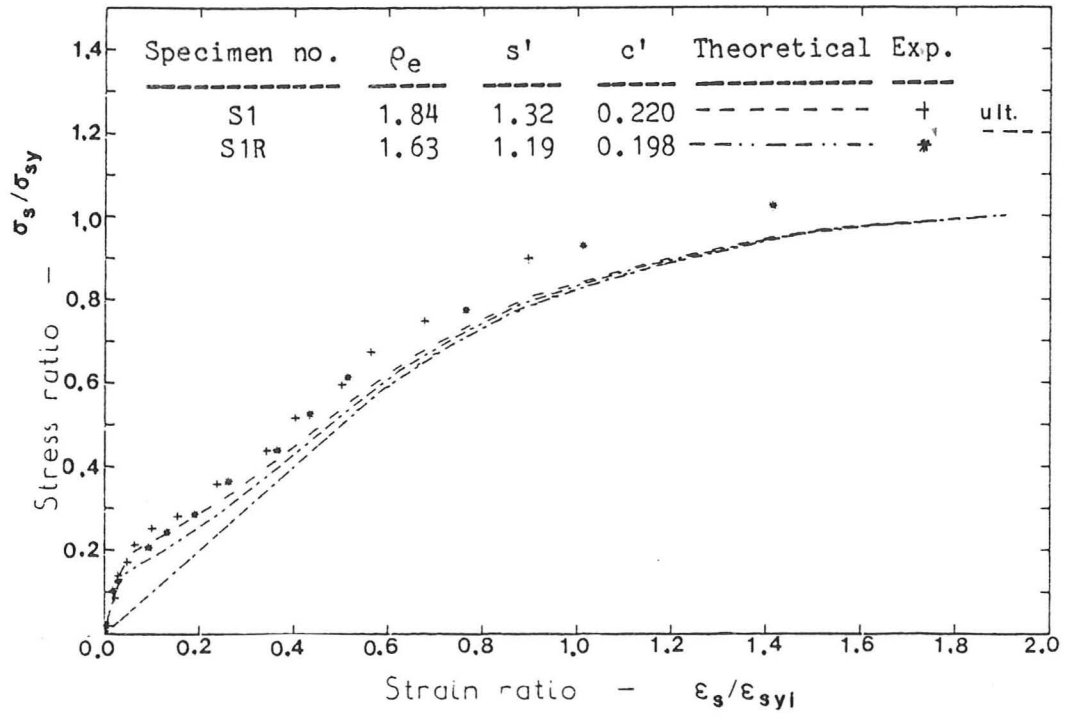

Figure 3.3-27 Enhanced steel properties for slabs S1 and S1R.

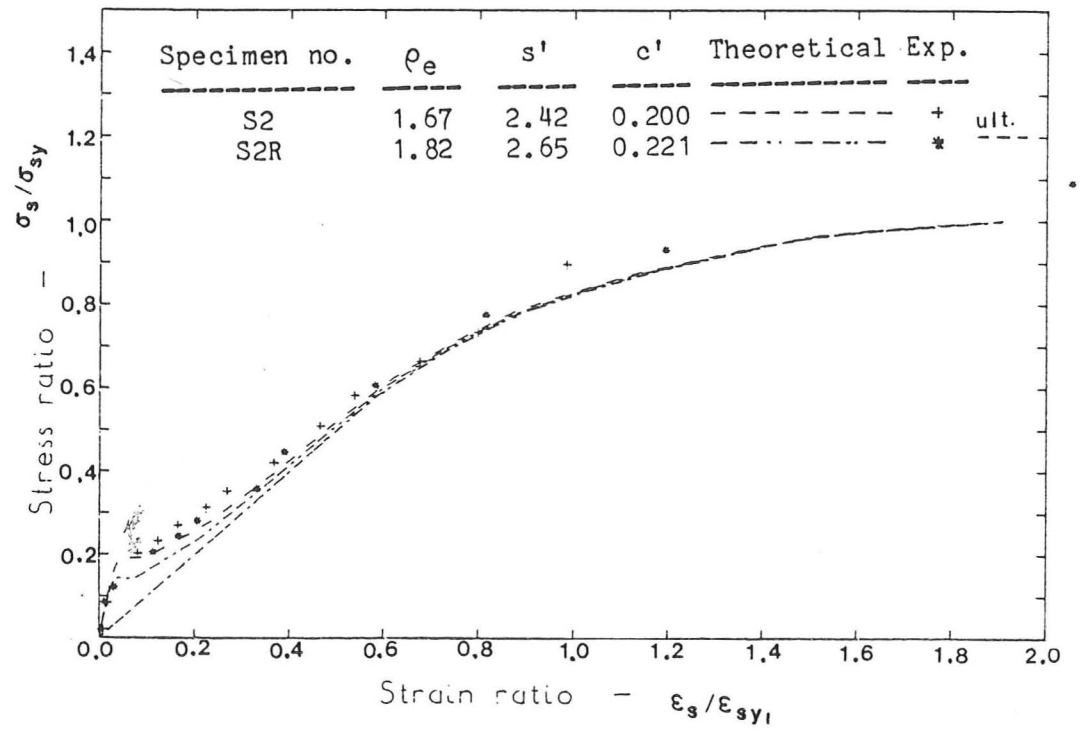

Figure 3.3-28 Enhanced steel properties for slabs S2 and S2R.

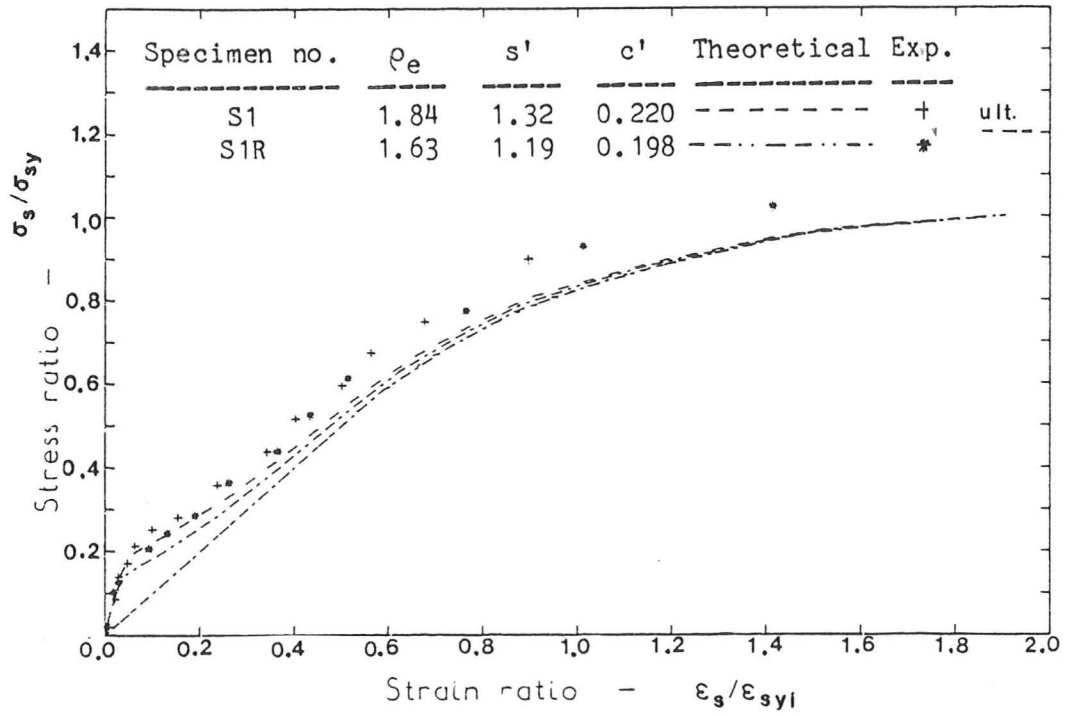

Figure 3.3-27 Enhanced steel properties for slabs S1 and S1R.

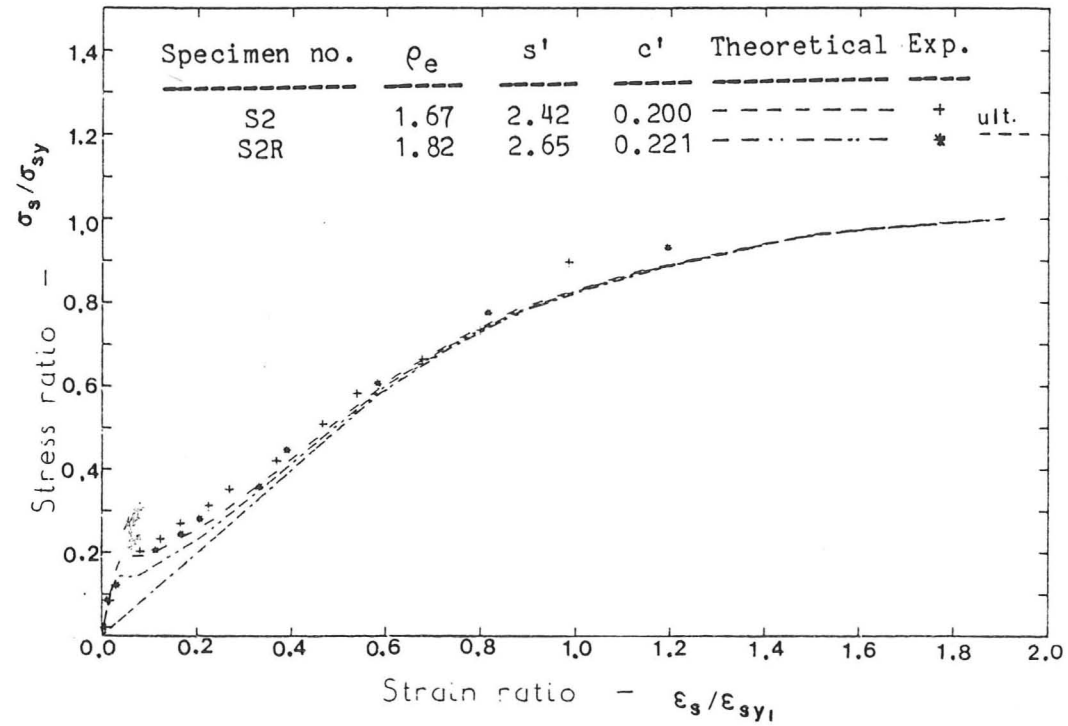

Figure 3.3-28 Enhanced steel properties for slabs S2 and S2R.

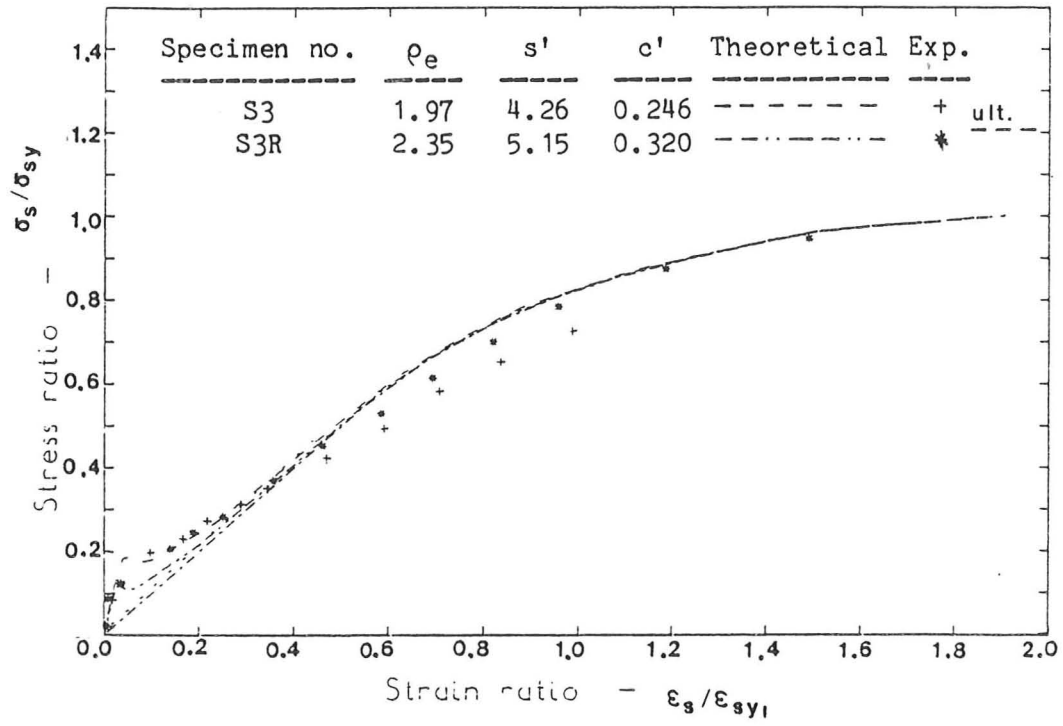

Figure 3.3-29 Enhanced steel properties for slabs S3 and S3R.

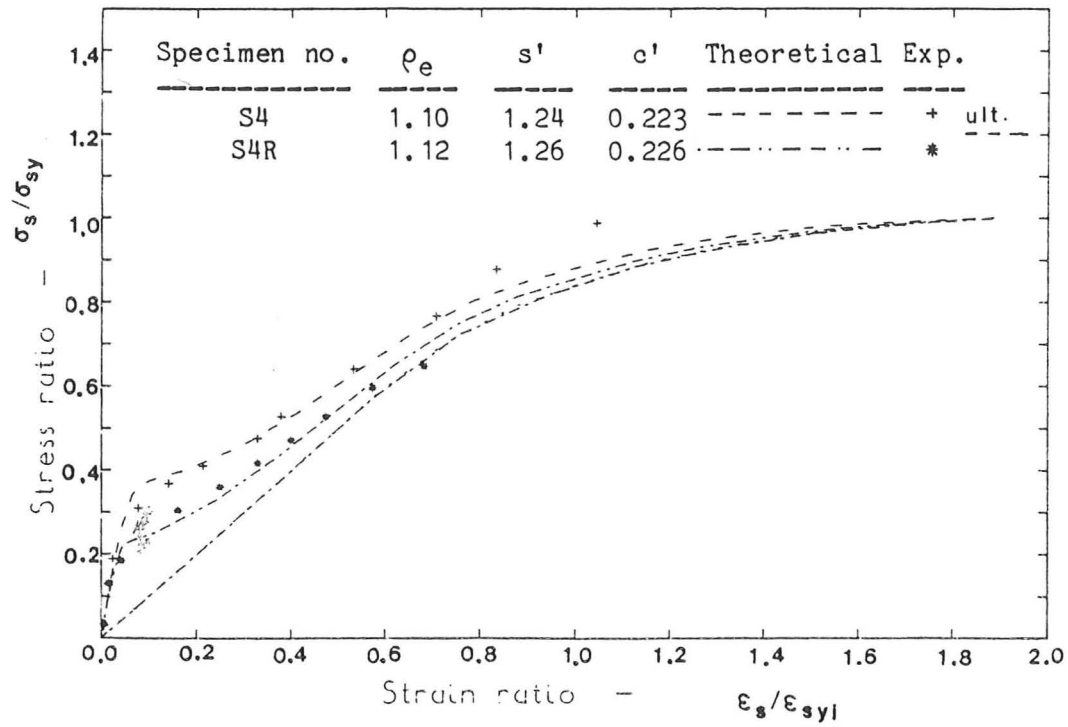

Figure 3.3-30 Enhanced steel properties for slabs S4 and S4R.

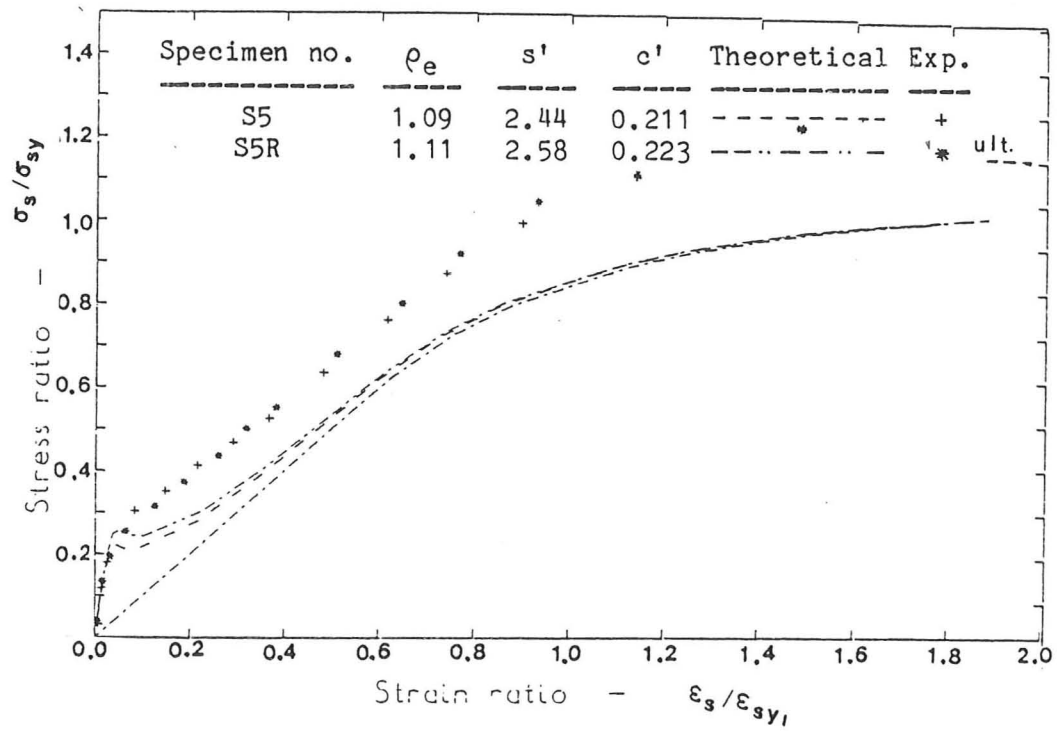

Figure 3.3-31 Enhanced steel properties for slabs S5 and S5R.

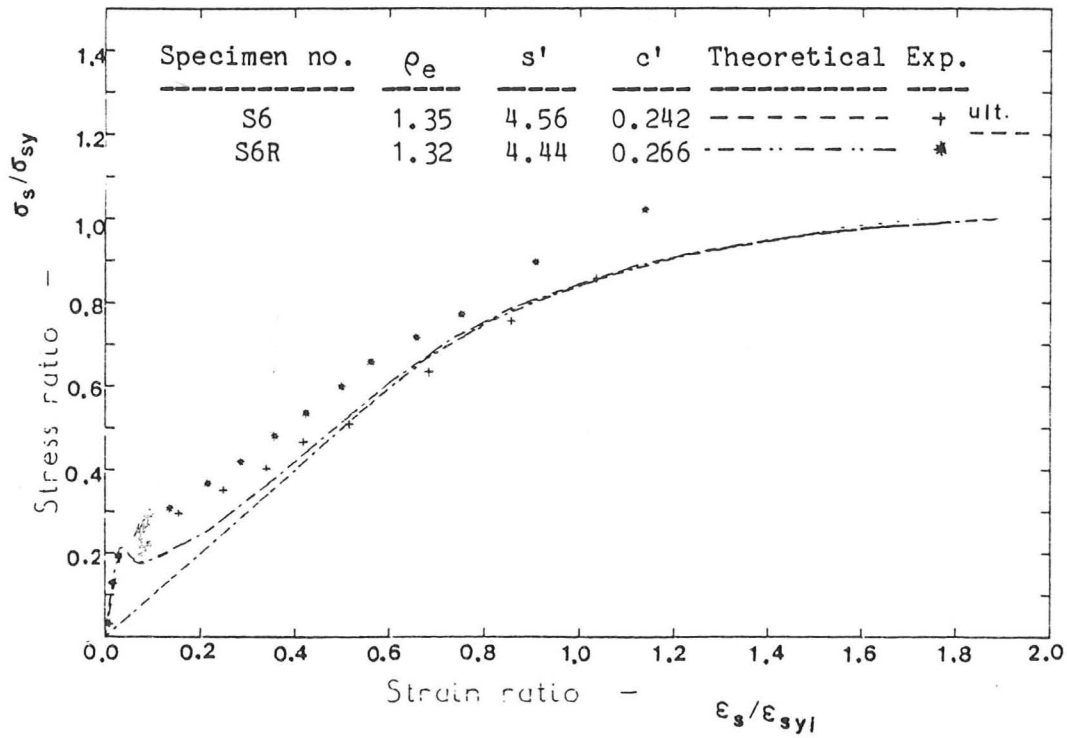

Figure 3.3-32 Enhanced steel properties for slabs S6 and S6R.

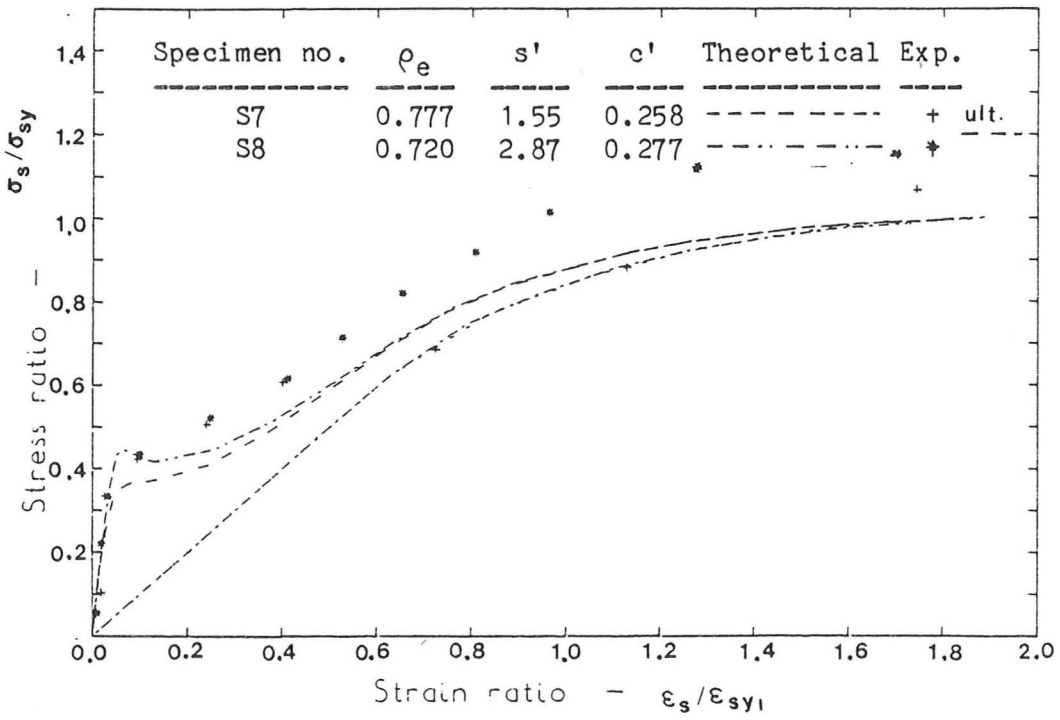

Figure 3.3-33 Enhanced steel properties for slabs S7 and S8.

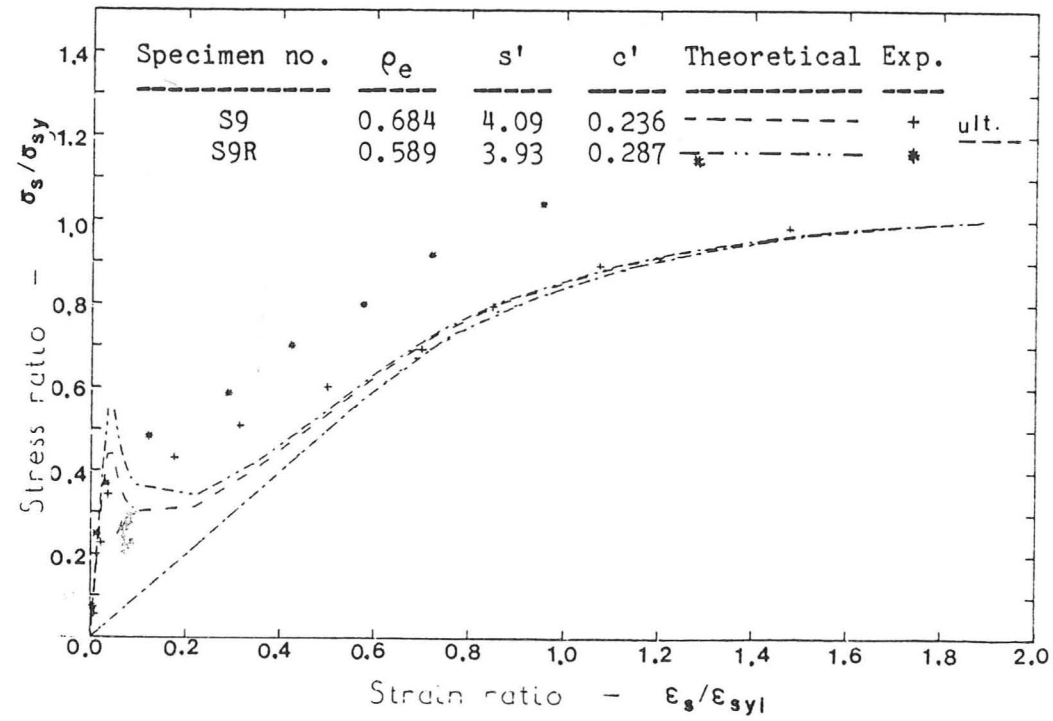

Figure 3.3-34 Enhanced steel properties for slabs S9 and S9R.

3.4.2 Tension stiffening force - average steel strain relations

Figure 3.4-1 shows a typical F_t-ε_{sm} curve where ε_{sm} is the experimental average strain at steel level and F_t is calculated by the second approach. This curve has the following main characteristics:

(1) A linear part up to point 1 where cracking first begins;

(2) as the strain increases, F_t increases but at a gradually decreasing rate until it reaches a maximum value.

(3) After reaching its peak value, the tension stiffening force falls down in two stages. The first is a stage of rapid breakdown of tension stiffening; point 2 on the curve marks the end of this stage -- it is also the point at which major cracks stop forming. The reduction in tension stiffening beyond this stage as strains increase is a gradual one.

The experimental analysis described in Section 3.3 above showed that the peak value of F_t occur before all major cracks have formed, rather than, as Clark and Speirs [51] assumed, at the stage when major cracks stop forming. Note that Clark and Speirs used a semi-empirical approach to calculate the tension stiffening force: the formula included two theoretical terms, namely the strain at steel level ε_s and the neutral axis depth x, which were found using the classical no-tension theory.

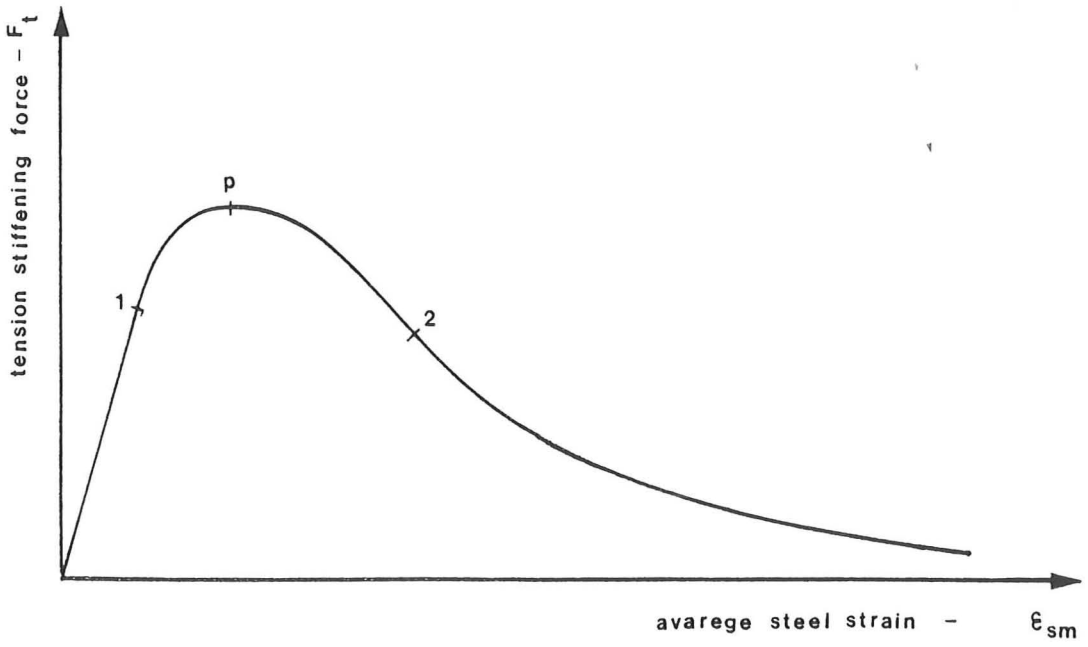

Figure 3.4-1 A typical experimental relationship between the tension stiffening force F_t and the average strain at steel level ε_{sm}.

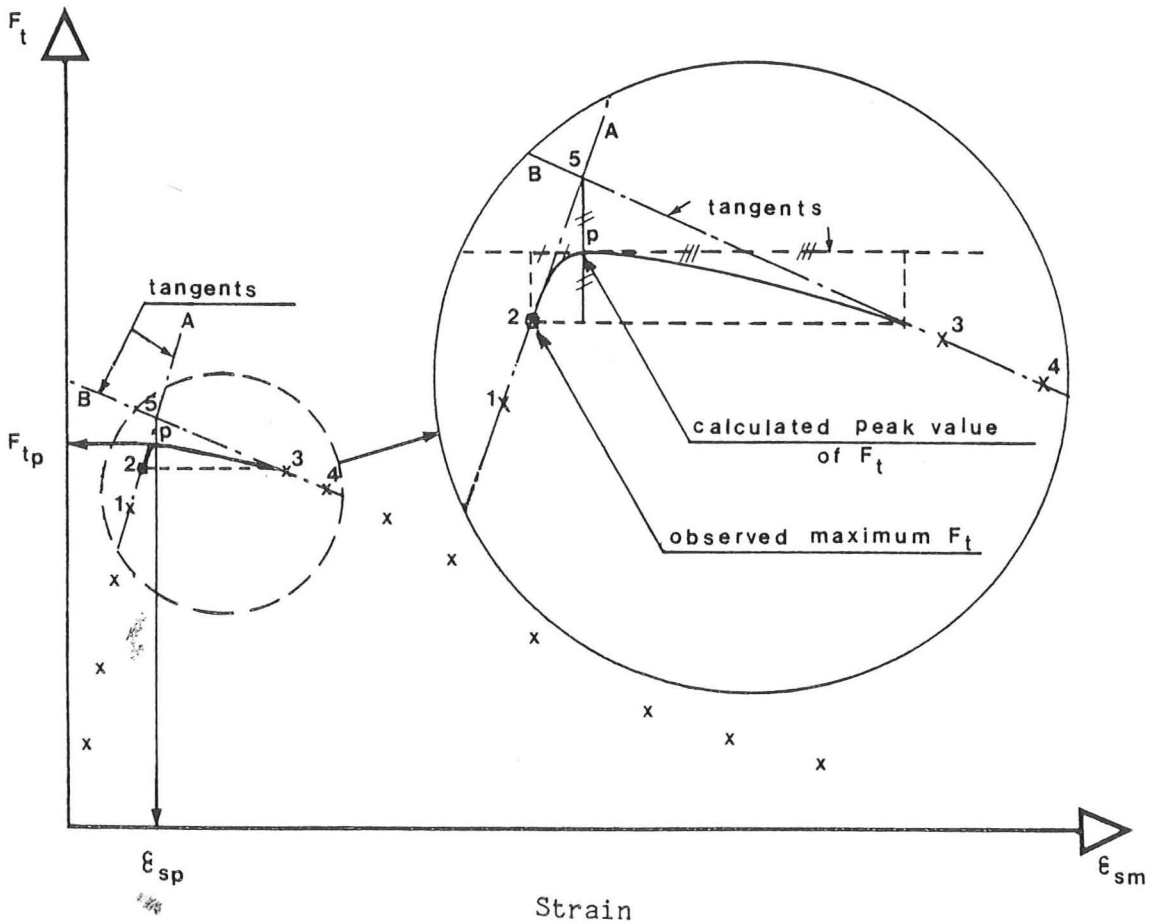

Figure 3.4-2 Interpolation of the peak value of F_t and the value of ε_{sp} from the experimental F_t - ε_{sm} relationship obtained by the second approach.

3.4.3 Tension stiffening force: general

The tension stiffening force is a direct function of the tensile strength of concrete and the average area of concrete in the tension zone. This can be expressed as:

$$F_t = \alpha \alpha_o f_t \beta A_{tm} \quad \ldots \quad \ldots (3.4\text{-}1)$$

where

α is a factor giving the average concrete tensile stress as a proportion of the average tensile stress in concrete at $F_t = F_{tp}$;

α_o is a constant;

f_t is the concrete tensile strength;

β is a factor defining the effective area of concrete contributing to the tension stiffening; and

A_{tm} is the average area of concrete below the neutral axis.

The factor α is equal to the ratio F_t/F_{tp} multiplied by the ratio h_{tp}/h_{tm} where F_{tp} is the maximum (peak) tension stiffening force and h_{tp} and h_{tm} are the mean height of the tension zone at F_{tp} and F_t respectively. The vaue of α depends mainly on the mean strain at steel level ε_{sm}, taking a value of 1.0 at a steel-level strain of ε_{sp} (i.e. when $F_t = F_{tp}$) and decreases from 1.0 to 0.0 as ε_{sm} increases from ε_{sp} to ε_{sy} (the yield strain for steel).

The constant α_o depends mainly on the average profile of the tensile stress, across the height of the tension zone, at the peak value of F_t and on the ratio between the effective tensile strength of concrete in the beam or slab and the measured f_t. In the tests under consideration, f_t was measured from the indirect tension test.

3.4.4 Maximum tension stiffening

When tension stiffening is maximum, Equation 3.3-1 reduces to:

$$F_{tp} = \alpha_o \, f_t \, \beta \, b \, (h - x_p) \quad \ldots \quad \ldots (3.4\text{-}2)$$

where

F_{tp} is the peak value of F_t;

b is the breadth of the cross-section;

h is the total height of the section; and

x_p is the average neutral axis depth when $F_t = F_{tp}$.

Thus,

$$\alpha_o \, \beta = \frac{F_{tp}}{f_t \, b \, (h - x_p)} \quad \ldots \quad \ldots (3.4\text{-}3)$$

The value of $\alpha_o\beta$ was evaluated from Clark et al [51],[57] experimental data for each beam and slab using the peak values of F_t and the corresponding neutral axis depth values x_p. The values of F_{tp} and ε_{sp} were interpolated from the F_t-ε_{sm} graph (obtained by the second approach) as explained below.

The experimental point with maximum F_t, and hence the four successive points (points 1 to 4 in Figure 3.4-2) with this point of maximum F_t as point 2, was first determined. The point of intersection (point 5) between line A (which passes through points 1 and 2) and line B (which passes through points 3 and 4) was found. The ε_{sp} value was taken as the ε_{sm} value for point 5 while the peak value of F_t was taken as the average of maximum F_t and the F_t value for point 5. This peak point can be connected with point 2 (the point of maximum F_t) by means of a parabolic

curve which has a horizontal tangent at the peak point while the tangent at point 2 will be line A as it is clear from the geometry of the figure; line B is the tangent for another parabolic curve that has a horizontal tangent at the peak point. This procedure was repeated with the point of maximum F_t as point 3. Of the two, the peak point with the higher F_{tp} was chosen. This method of interpolation gave better results than those obtained using three other solutions, the first of which was to find the peak of the parabolic curve passing through points 1,2, and 3. In the other two solutions, the peak of the F_t-ε_{sm} curve was taken to be the peak of the cubic curve passing through points 2,3, and 4 with line A as a tangent at point 2, and the peak of the cubic curve which passes through points 1,2,3, and 4. For each of the four solutions, a subroutine was written for the University Computer and a Computer printout of the results was obtained. It was decided to adopt the values of F_{tp} and ε_{sp} found using the first of these four solutions since it gave the better results and needed less computational efforts and checks.

The value of α_o in Equation 3.4-3 depends mainly on the degree of confidence in estimating the actual tensile strength of concrete though there may also be some systematic difference between tensile behaviour in beam and in split cylinder. Thus α_o will be assumed to have the same value for each of the beams and slabs on the grounds that each of the test specimens had the same number of indirect tensile tests to determine f_t. However, it should be noted that the ratio of the volume of the control specimens to the overall volume of the test specimens is greater in beams than it is in slabs giving more credibility to the value of f_t for beams than for slabs. Having fixed the value of α_o for all the test specimens, the values of $\alpha_o\beta$ become a direct measure of β which is the ratio between the effective area of concrete contributing to tension stiffening and the average area of concrete in the tension zone.

The main variables likely to affect the value of β are the effective steel percentage ρ_e in the tension zone, bar spacing s, and cover to the main reinforcement c. Table 3.4-1 gives the values of $\alpha_o\beta$, ρ_e, bar spacing ratio s', and cover ratio c' for each of the beams and slabs, where

$$\rho_e = \frac{A_s}{b\,(h - x_p)} \quad \ldots \qquad \ldots (3.4\text{-}4)$$

$$s' = s/(h - x_p) \quad \ldots \qquad \ldots (3.4\text{-}5)$$

$$c' = c/(h - x_p) \quad \ldots \qquad \ldots (3.4\text{-}6)$$

The test specimens can be grouped into 3 groups: for each, one or more of the above main parameters is variable while the rest (if anything) remain more or less constant. The first group consists of the first 8 beams B1 to B4R. The main variable in this group is ρ_e. Beams B5 and B5R together with the slabs form the second group which has two main variables namely s' and ρ_e. Beams B3 and B3R in addition to the last 6 beams B5 to B7R form the last group in which the 3 parameters are variable.

A study of Table 3.4-1 shows that $\alpha_o\beta$ decreases with an increase of ρ_e, s', or c'. A linear relation between $\alpha_o\beta$ and each of the three parameters is suggested. A variety of other possible non-linear relations have been investigated and were ruled out, since the straight line relation was found to be in better agreement with the results. If the effect of the three parameters is added together, the following linear expression can be written:

$$\alpha_o \beta = \alpha_o \{ \beta_o - B_1 \rho_e - B_2 s' - B_3 c' \} \quad \ldots \qquad \ldots (3.4\text{-}7)$$

where

β_o is the value of β when the effect of reinforcement is zero (e.g. in an unreinforced or an uncracked situation) and is thus equal to unity.

B_1, B_2, B_3 are constants which will be determined empirically.

Table 3.4-1 Values of $\alpha_o \beta$, ρ_e, s', and c' as defined by Equations 3.4-3 to 3.4-6.

Specimen No.	Steel percentage ρ_e	Spacing ratio s'	Cover ratio c'	Value of $\alpha_o \beta$
B1	3.56	0.333	0.086	0.381
B1R	3.47	0.320	0.150	0.410
B2	2.00	0.290	0.150	0.416
B2R	2.26	0.333	0.152	0.443
B3	1.53	0.352	0.135	0.480
B3R	1.32	0.303	0.111	0.466
B4	0.72	0.294	0.104	0.508
B4R	0.72	0.294	0.130	0.521
B5	2.70	0.615	0.264	0.381
B5R	2.83	0.639	0.256	0.356
B6	1.95	0.444	0.197	0.421
B6R	1.67	0.380	0.152	0.379
B7	1.11	0.253	0.093	0.574
B7R	0.93	0.214	0.944	0.452
S1	1.84	1.32	0.220	0.498
S1R	1.63	1.19	0.198	0.438
S2	1.67	2.42	0.200	0.389
S2R	1.82	2.65	0.221	0.411
S3	1.97	4.26	0.246	0.352
S3R	2.35	5.15	0.320	0.546
S4	1.10	1.24	0.223	0.378
S4R	1.12	1.26	0.226	0.413
S5	1.09	2.44	0.211	0.554
S5R	1.11	2.58	0.223	0.397
S6	1.35	4.56	0.242	0.494
S6R	1.32	4.44	0.266	0.473
S7	0.777	1.55	0.258	0.606
S8	0.720	2.87	0.277	0.441
S9	0.684	4.09	0.236	0.364
S9R	0.589	3.93	0.287	0.345

To determine the values of the constants B_1, B_2, and B_3 in Equation 3.4-7, we consider the beams B1 to B4R in which ρ_e is the only variable. In this case Equation 3.4-7 can be rewritten as:

$$\alpha_o \beta = \alpha_o \{(\beta_o - B_2 s' - B_3 c') - B_1 \rho_e\}$$

or,

$$\alpha_o \beta = \alpha_o B_4 - \alpha_o B_1 \rho_e$$

$$\beta' = B_4' - B_1' \rho_e \quad \ldots \qquad \ldots (3.4\text{-}8)$$

A linear regression on the 9 data points gives:

$$B_4' = 0.534, \text{ and } B_1' = 4.14$$

Thus,

$$\beta' = 0.534 - 4.14 \rho_e$$

This gives a good fit to the data points as shown in Figure 3.4-3.

Similarly, to find B_2 from the second group of test specimens (Beams B5 and B5R plus 16 slabs), Equation 3.4-7 is rewritten as follows:

$$\beta + B_1 \rho_e = (\beta_o - B_3 c') - B_2 s'$$

or

$$\beta' + 4.14 \rho_e = B_5' - B_2 s' \quad \ldots \qquad \ldots (3.4\text{-}9)$$

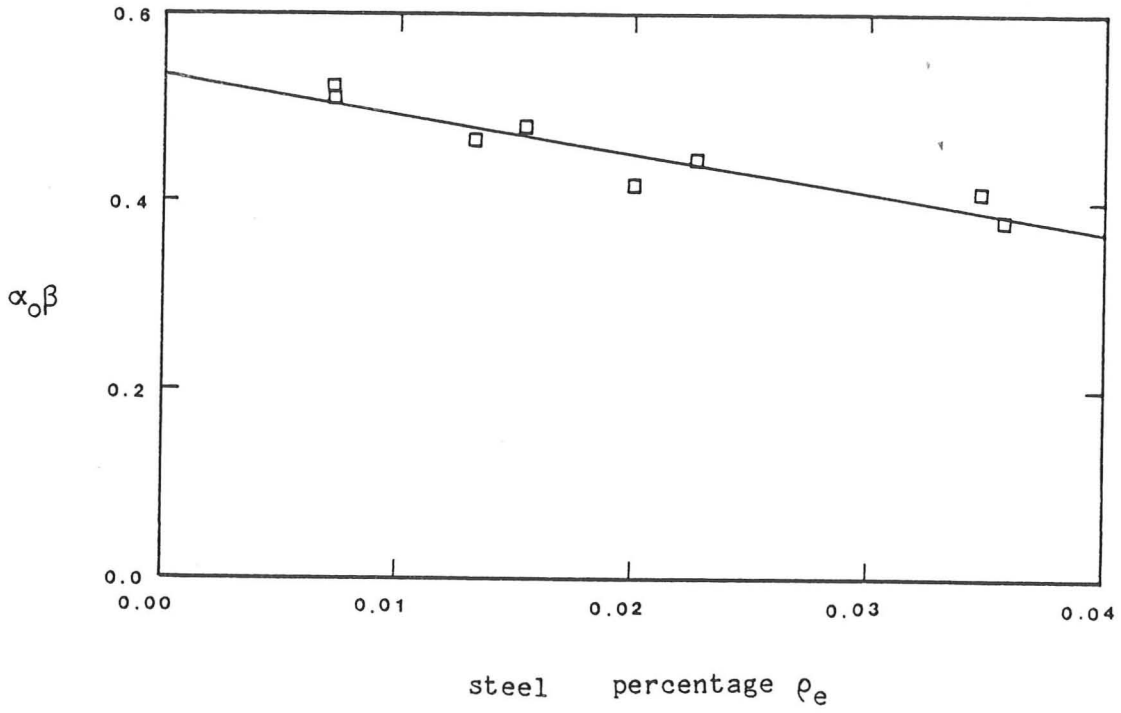

Figure 3.4-3 A graph of $\alpha_o\beta$ (Equation 3.4-3) against the effective steel percentage ρ_e (Equation 3.4-4) for data from beams B1 → B4R.

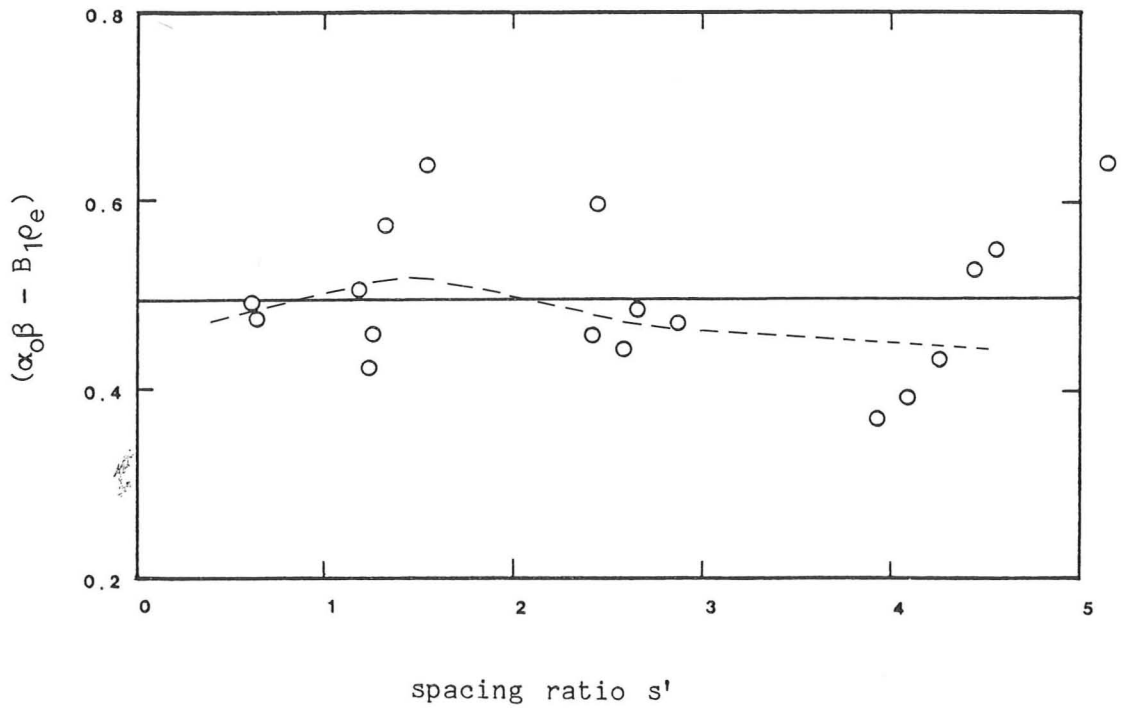

Figure 3.4-4 A graph of $(\alpha_o\beta - B_1\rho_e)$ against the bar spacing ratio s' (Equation 3.4-5) for data from beams B5 and B5R plus the sixteen slabs.

In Figure 3.4-4, $\{\beta' + 4.14\ \rho_e\}$ is plotted against s' and a straight line is fitted to the data. This gives a zero value for B_2' and a value of 0.495 for B_5' i.e. there is no influence of bar spacing on the value of β. However, if the average value of $\alpha_o\beta$ at each of the four positions where the spacing is nominally the same is plotted against the average spacing ratio, a curved relation can be obtained with a peak value at a spacing of about 1.5 times the height of the tension zone as shown by the broken line in Figure 3.4-4. A similar relation was indicated by Clark and Cranston [57] who also ignored the effect of bar spacing on β. However, attention must be drawn to the different way in which the values of F_t were calculated in our approach: the analysis was based so far as possible on experimental results with little of intervening theory. The scatter in the slab results could be explained by the small number of data points around the peak of the F_t-ε_{sm} graph.

Using the data from the third group of test results, B_3 can be found in a similar way. Rearranging Equation 3.4-7 gives:

$$\beta' + 4.14\ \rho_e = B_6' - B_3\ c' \quad \ldots \qquad \ldots (3.4\text{-}10)$$

Values of $\{\beta' + 4.14\ \rho_e\}$ are plotted against c' in Figure 3.4-5. It can be seen that the straight line best fit agrees well with the data points. The value of B_3' was found to be equal to 0.378.

Having found the values of B_1' and B_3' it remains necessary to find the value of α_o. From Equation 3.4-7 (with B_2' equal to zero) we can write:

$$\beta' = \alpha_o - A\ (4.14\ \rho_e + 0.378\ c') \quad \ldots \qquad \ldots (3.4\text{-}11)$$

where A is a constant which will equal unity if the values of B_1' and B_3' were found using the same set of test results. But since each of the two constants were found from a different set of results, 'A' would be expected to be different from but close to unity.

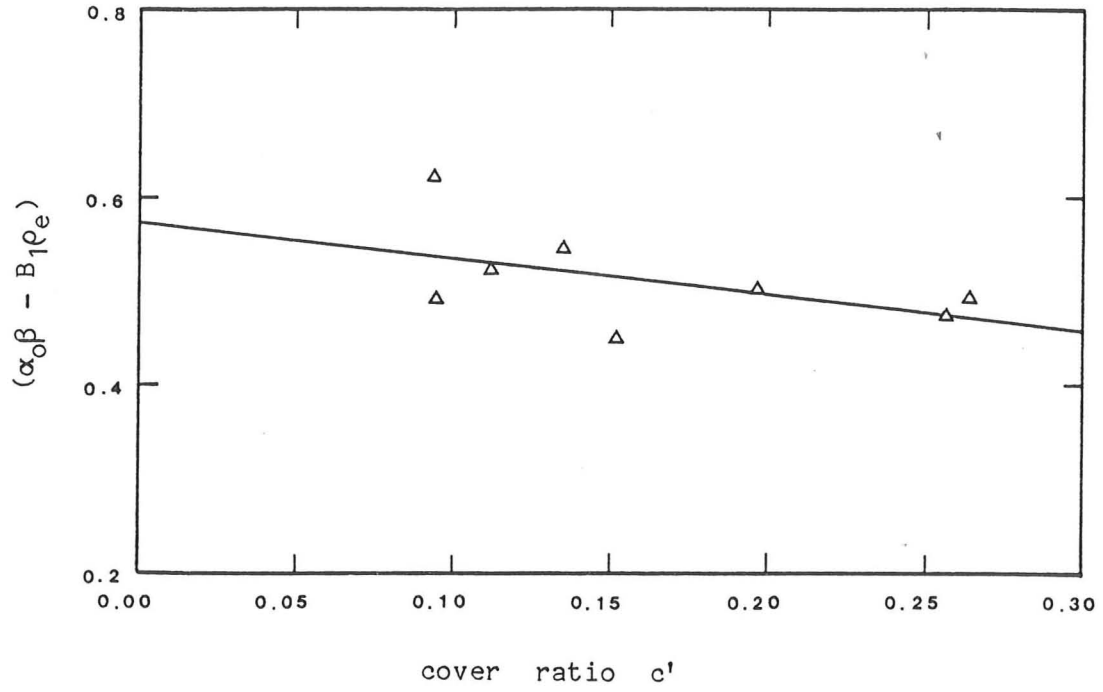

Figure 3.4-5 A graph of $(\alpha_o\beta - B_1\rho_e)$ against the cover ratio c' (Equation 3.4-6) for data from beams B3 and B3R plus beams B5 → B7R.

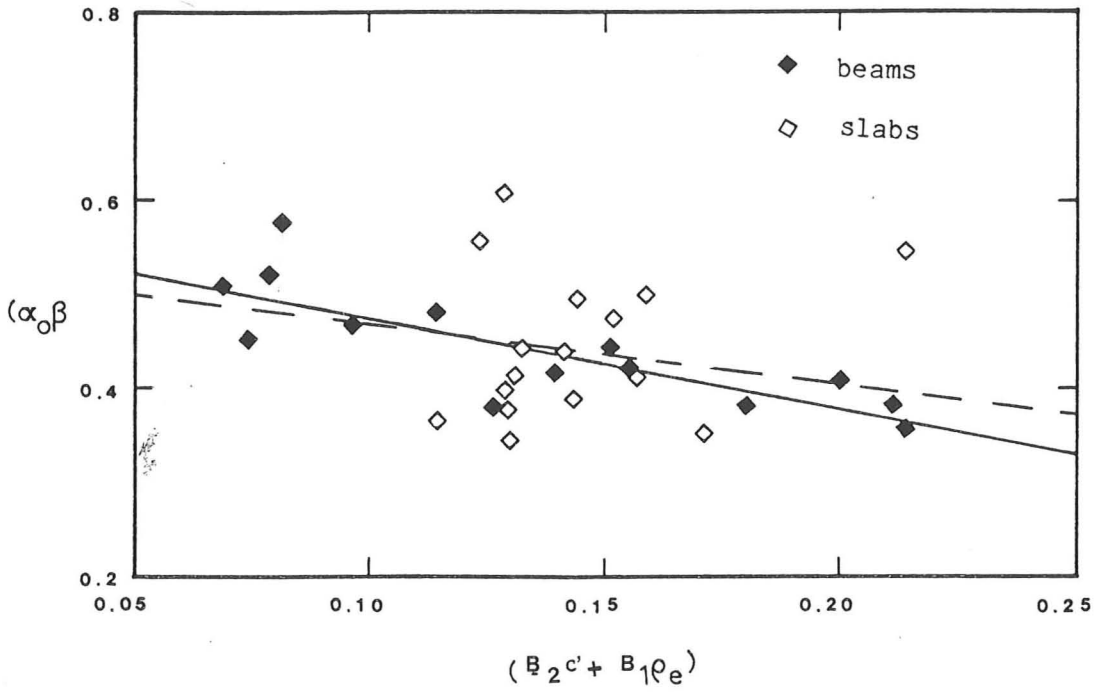

Figure 3.4-6 A graph of $\alpha_o\beta$ (Equation 3.4-3) against $(B_1\rho_e + B_2c')$ for data from beams.

A linear regression to fit best the data points (from the beam results only) of the graph of $\{4.14\ \rho_e + 0.378\ c'\}$ versus β' gives a value of 0.98 for A and a value of 0.575 for α_o -- see Figure 3.4-6. The value of A shows that the evaluation of the constants B_1' and B_3' is very satisfactory. Dividing both sides of Equation 3.4-11 by α_o we obtain the following expression which gives the value of β in terms of ρ_e and c'.

$$\beta = 1.0 - 7.07\ \rho_e - 0.645\ c' \quad \ldots \qquad \ldots (3.4\text{-}12)$$

Multiple regression of $\alpha_o\beta$ on ρ_e and c' was carried out on data from beams only (14 in all). As a result, the following equation was obtained (see Figure 3.4-7):

$$\beta = 1.0 - 6.95\ \rho_e - 0.669\ c' \quad \ldots \qquad \ldots (3.4\text{-}13)$$

and α_o had a value of 0.575. It can be seen that Equations 3.4-12 and 3.4-13 are not much different and although derived from data on beams only, they will be used for both beams and slabs since the influence of bar spacing on the β value is neglected.

Equation 3.4-13 can be rewritten as:

$$\beta\ (h - x_p) = (h - x_p) - \{7\ A_s/b + 2\ c/3\} \quad \ldots \qquad \ldots (3.4\text{-}14)$$

This equation gives the effective height of the concrete tension zone when F_t is maximum. It can be thought of as the actual height of the tension zone minus a height equal to 2/3 of the cover plus 7 times the thickness of a smeared sheet of steel equivalent in area to the main reinforcing steel and having the same breadth as the concrete section.

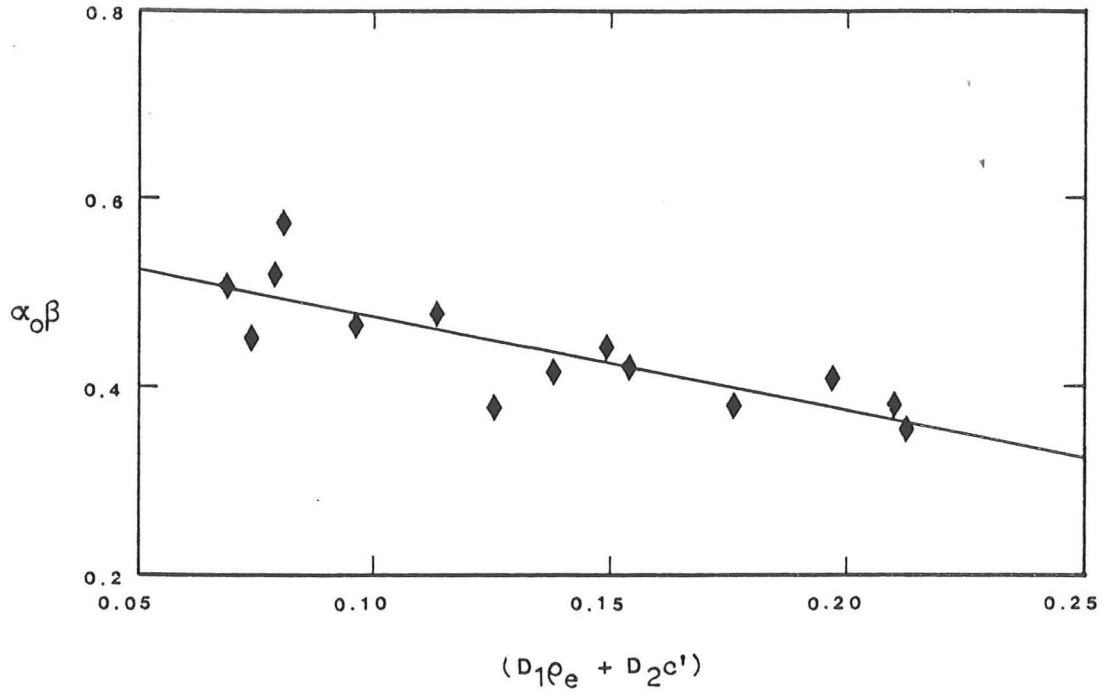

Figure 3.4-7 A graph of $\alpha_o\beta$ (Equation 3.4-3) against $(D_1\rho_e + D_2c')$ for data from beams only.

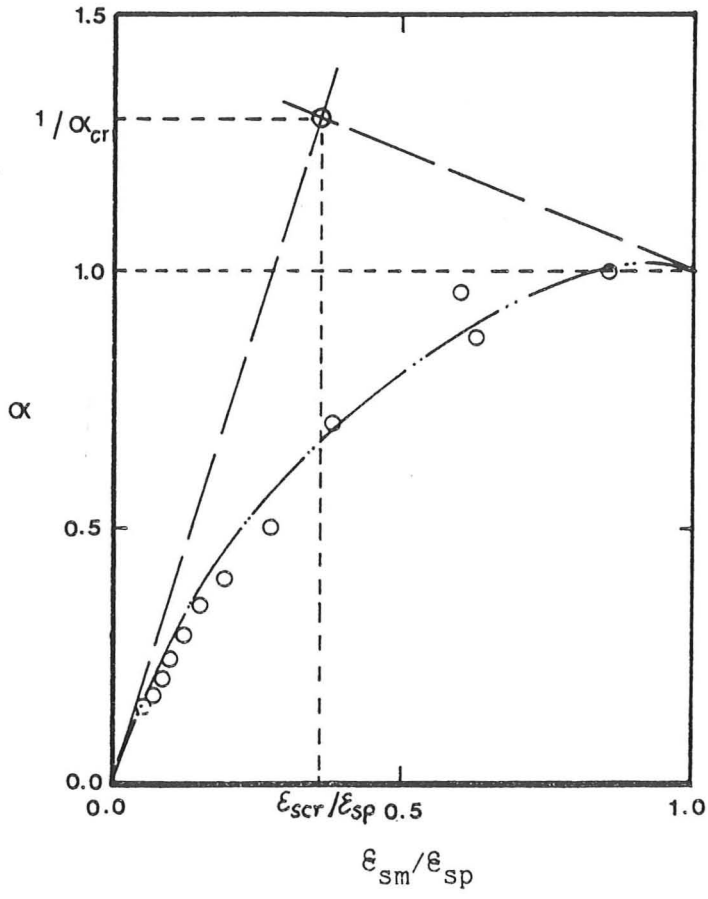

Figure 3.4-8 Typical experimental relationship between α and the ratio $\varepsilon_{sm}/\varepsilon_{sp}$ for values of $\varepsilon_{sm} < \varepsilon_{sp}$.

3.4.5 Variation of the tension stiffening force with strain

The factor α in Equation 3.4-1 describes the manner in which F_t attains its maximum and then falls down to zero as ε_{sm} increases from zero to ε_{sy}. The values of α can be calculated from the F_t values (calculated according to the second approach described in Subsection 3.2.2 above) and the measured mean neutral axis depth x_m for each load stage. The value of β is evaluated for each specimen using Equation 3.4-14. The value of α_o for the present test results (beams only) is 0.575 and should be taken as 0.5 if unknown. Hence,

$$\alpha = \frac{F_t}{\alpha_o f_t \beta b (h - x_m)} \quad \ldots \quad \ldots (3.4\text{-}15)$$

The two parts of the relationship between α and ε_{sm} will be dealt with separately. The first part describes the attainment of maximum tension stiffening force and the second part, the decay of tension stiffening.

-I- Attainment of maximum tension stiffening force:

If α for data points with $\varepsilon_{sm}<\varepsilon_{sp}$ (where ε_{sp} is the interpolated steel-level strain at peak tension stiffening) is plotted against the ratio $\varepsilon_{sm}/\varepsilon_{sp}$, a graph similar to that in Figure 3.4-8 can be obtained. The theoretical cracking point for a beam of linear-elastic material with tensile strength f_t is also shown on the graph, it has an α value of

$$\alpha_{cr} = \frac{F_{tcr}}{\alpha_o f_t \beta b (h - x_{un})} \quad \ldots \quad \ldots (3.4\text{-}16)$$

$\therefore \quad \alpha_{cr} = 1/\beta$

The ε_{sm} value for the cracking point is

$$\varepsilon_{scr} = \left(\frac{2\,\alpha_o\,f_t}{E_c}\right)\left(\frac{d_s - x_{un}}{h - x_{un}}\right) \quad \ldots \qquad \ldots (3.4\text{-}17)$$

where

E_c is the initial tangent modulus of elasticity for concrete;

d_s is the depth of main tension steel measured from the compression face; and

x_{un} is the neutral axis depth for the uncracked section (calculated).

The relationship between α and the average steel strain ratio $\varepsilon_{sm}/\varepsilon_{sp}$ is chosen to be a curve with both its initial and final tangents passing through the theoretical cracking point as illustrated in Figure 3.4-8. The initial tangent slope at the origin is thus equal to $\alpha_{cr}\,\varepsilon_{sp}/\varepsilon_{scr}$ and the final tangent slope at the point where $\varepsilon_{sm}/\varepsilon_{sp} = \alpha = 1$ is equal to $(1-\alpha_{cr})/(1-\varepsilon_{sm}/\varepsilon_{sp})$. This can be expressed as follows:

$$\alpha = K_1\left(\frac{\varepsilon_{sm}}{\varepsilon_{sp}}\right)^{K_2} + K_3\left(\frac{\varepsilon_{sm}}{\varepsilon_{sp}}\right) + K_4 \quad \ldots \qquad \ldots (3.4\text{-}18)$$

where K_1, K_2, K_3, and K_4 are constants that can be determined by solving the four equations that satisfy the boundary conditions namely the two points and the two tangents. The solution of such equations gives the following values for these constants:

$$K_4 = 0$$

$$K_3 = \alpha_{cr}\ \varepsilon_{sp}/\varepsilon_{scr}$$

$$K_1 = 1 - K_3$$

$$K_2 = \frac{1 - K_3}{K_1\ (1 - \varepsilon_{scr}/\varepsilon_{sp})} = \frac{\varepsilon_{sp}}{\varepsilon_{sp} - \varepsilon_{scr}}$$

In order to be able to calculate α in Equation 3.4-18, a way of estimating ε_{sp} should be available since ε_{sp} is an experimental not a calculated quantity. The ratio $\varepsilon_{sp}/\varepsilon_{scr}$ (i.e. the experimental steel-level strain at maximum tension stiffening divided by the estimated steel-level strain at cracking) was tested against several variables or combinations of variables and was found to be dependent on some of them. The ratio $\varepsilon_{sp}/\varepsilon_{scr}$ was found to decrease with an increase in each of the effective steel percentage ρ_e", bar spacing ratio s", and the steel depth ratio y_s" within the tension zone, where

$$\rho_e" = \frac{A_s}{b\ (h - x_{un})} \quad \ldots \qquad \ldots\ (3.4\text{-}19)$$

$$s" = \frac{s}{(h - x_{un})} \quad \ldots \qquad \ldots\ (3.4\text{-}20)$$

$$y_s" = \frac{(d_s - x_{un})}{(h - x_{un})} \quad \ldots \qquad \ldots\ (3.4\text{-}21)$$

Notice that here we are using x_{un} (the neutral axis depth for uncracked behaviour) in defining ρ_e", s", and y_s", whereas earlier we used x_p -- the neutral axis depth at peak tension stiffening -- in defining ρ_e, s', and c'.

Table 3.4-2 Values of the ratio $\varepsilon_{sp}/\varepsilon_{scr}$, ρ_e", s", and y_s" as defined by Equations 3.4-19 to 3.4-21.

Specimen No.	Steel percentage ρ_e"	Spacing ratio s"	Cover ratio y_s"	Value of $\varepsilon_{sp}/\varepsilon_{scr}$
B1	3.82	0.356	0.842	1.26
B1R	3.76	0.347	0.773	1.86
B2	2.40	0.350	0.767	2.03
B2R	2.39	0.351	0.789	1.29
B3	1.50	0.345	0.827	1.14
B3R	1.49	0.342	0.834	2.11
B4	0.829	0.339	0.851	1.95
B4R	0.83	0.341	0.820	1.80
B5	3.04	0.693	0.621	2.49
B5R	3.07	0.693	0.643	1.84
B6	2.03	0.463	0.740	1.54
B6R	2.01	0.458	0.763	2.33
B7	1.20	0.273	0.867	1.55
B7R	1.19	0.274	0.847	2.00
S1	2.14	1.54	0.642	2.26
S1R	2.12	1.55	0.640	4.48
S2	2.13	3.08	0.642	2.37
S2R	2.12	3.09	0.640	1.64
S3	2.13	4.60	0.633	1 17
S3R	2.10	4.61	0.612	0.49
S4	1.35	1.51	0.648	2.44
S4R	1.35	1.51	0.647	2.63
S5	1.35	3.04	0.656	2.98
S5R	1.32	3.06	0.654	2.03
S6	1.36	4.60	0.674	0.98
S6R	1.36	4.56	0.646	1.05
S7	0.762	1.51	0.691	1.01
S8	0.754	3.00	0.650	0.99
S9	0.75	4.48	0.682	1.04
S9R	0.67	4.48	0.614	1.05

The values of the ratio $\varepsilon_{sp}/\varepsilon_{scr}$, ρ_e", s", and d_s" for each of the beams and slabs are given in Table 3.4-2. Linear regression similar to that used in Subsection 3.4.3 above was carried out on this data, and once again the specimens were grouped into three groups according to the main variables. The following best fit linear relations were obtained:

(1) For Group 1 (beams B1 to B4R) with one main variable -- ρ_e".

$$\frac{\varepsilon_{sp}}{\varepsilon_{scr}} = 1.87 - 8.87\ \rho_e" \quad \ldots \qquad \ldots (3.4\text{-}22)$$

(2) For Group 2 (beams B5 and B5R plus the 16 slabs) which has two main variables, ρ_e" and s".

$$\frac{\varepsilon_{sp}}{\varepsilon_{scr}} = 3.23 - 8.87\ \rho_e" - 0.45\ s" \quad \ldots \qquad \ldots (3.4\text{-}23)$$

(3) For Group 3 (beams B3 and B3R plus beams B5 to B7R) which has all three parameters (ρ_e", s", and y_s") as variables.

$$\frac{\varepsilon_{sp}}{\varepsilon_{scr}} = 5.0 - 8.87\ \rho_e" - 0.45\ s" - 3.6\ y_s" \quad \ldots \quad \ldots (3.4\text{-}24)$$

(4) For all the specimens with $\varepsilon_{sp}/\varepsilon_{scr}$ taken as a function of $\{8.8\ \rho_e"+0.45s"+3.6y_s"\}$.

$$\frac{\varepsilon_{sp}}{\varepsilon_{scr}} = 4.61 - 0.81(8.87\ \rho_e'' + 0.45\ s'' + 3.6\ y_s'')$$

$$\frac{\varepsilon_{sp}}{\varepsilon_{scr}} = 4.61 - 7.2\ \rho_e'' - 0.366\ s'' - 2.92\ y_s'' \quad \ldots\ \ldots\ (3.4\text{-}25)$$

The slope of the line in Equation 3.4-25a ought to have been close to unity, but since the constants of the expression in between the brackets were obtained from analysis of three different groups of data, the slope differed from 1.0. Multiple regression was also carried out on data from all the beams and slabs (30 specimens in all); the following equation was obtained:

$$\frac{\varepsilon_{sp}}{\varepsilon_{scr}} = 7.1 - 10.9\ \rho_e'' - 0.44\ s'' - 6.15\ y_s'' \quad \ldots\ \ldots\ (3.4\text{-}26)$$

The best fit lines of Equations 3.4-22 to 3.4-26 together with the experimental data points are drawn in Figures 3.4-9 to 3.4-13. It can be seen that a good correlation was obtained except for the graph of Figure 3.4-10 where the scatter in the slabs' results can be attributed to the small number of data points around the peak of the F_t-ε_{sm} graph -- another cause for this scatter might be the bundling of bars which was done to vary the bar spacing in the slabs. This equation is to be adopted for use in the theory in preference to Equation 3.4-25, since the scatter around the best fit line of Equation 3.4-26 is less than that in the latter case -- compare Figure 3.4-13 with 3.4-12.

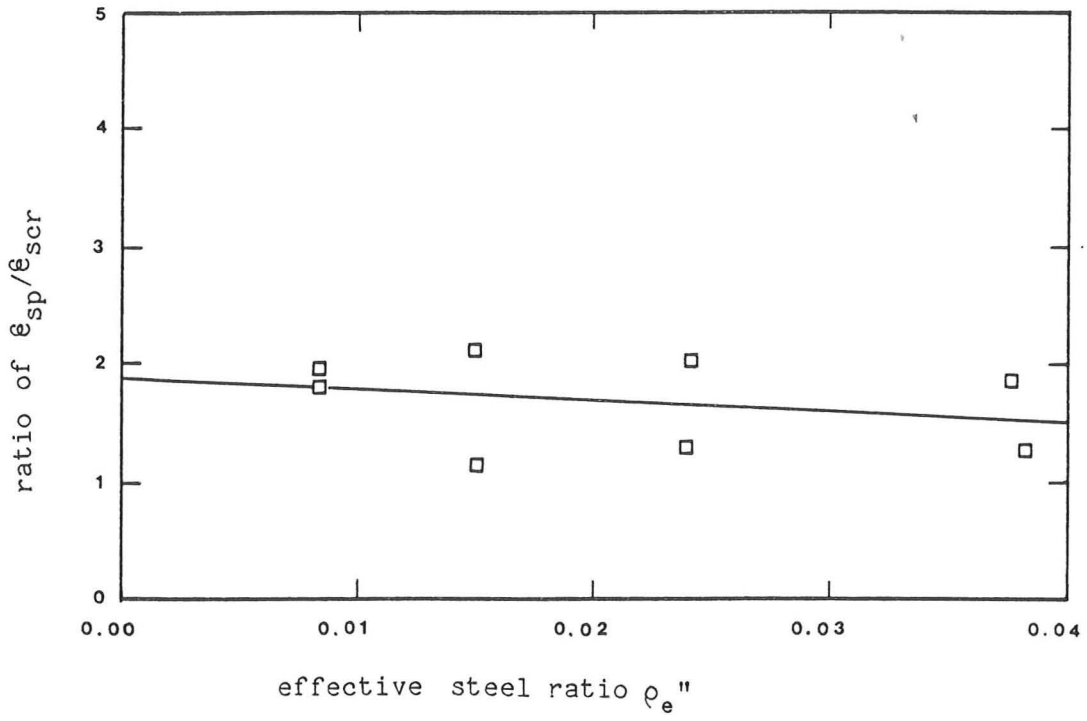

Figure 3.4-9 A graph of the ratio of $\varepsilon_{sp}/\varepsilon_{scr}$ against the effective steel ratio ρ_e" (Equation 3.4-18) for data from beams B1 → B4R.

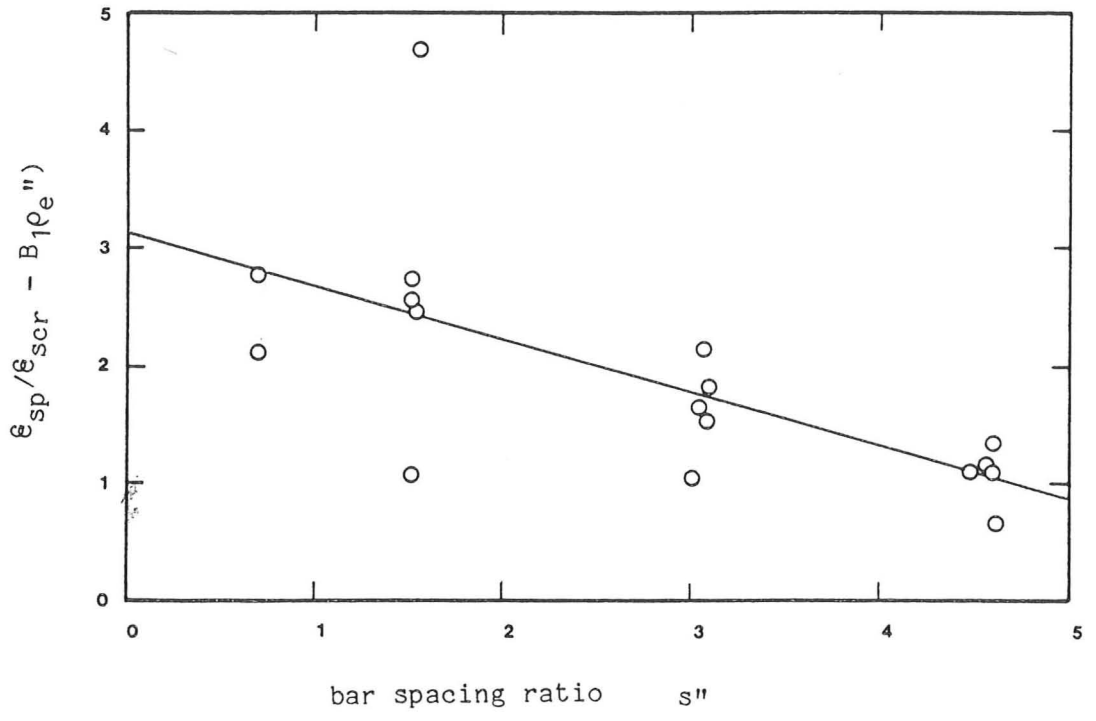

Figure 3.4-10 A graph of $\varepsilon_{sp}/\varepsilon_{scr} - B_1\rho_e$") against the bar spacing ratio s" (Equation 3.4-19) for data from beams B5 and B5R plus the sixteen slabs.

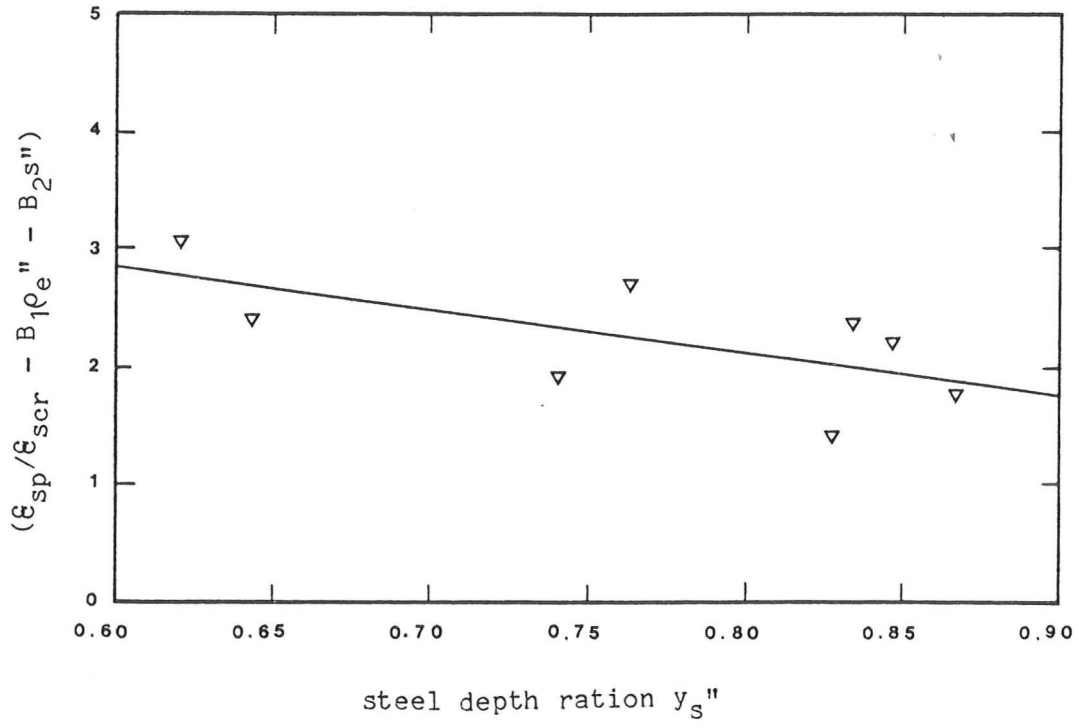

Figure 3.4-11 A graph of $(\varepsilon_{sp}/\varepsilon_{scr} - B_1\rho_e'' - B_2s'')$ against the steel depth ration y_s'' within the tension zone (Equation 3.4-20) for data from beams B3 and B3R plus beams B5 → B7R.

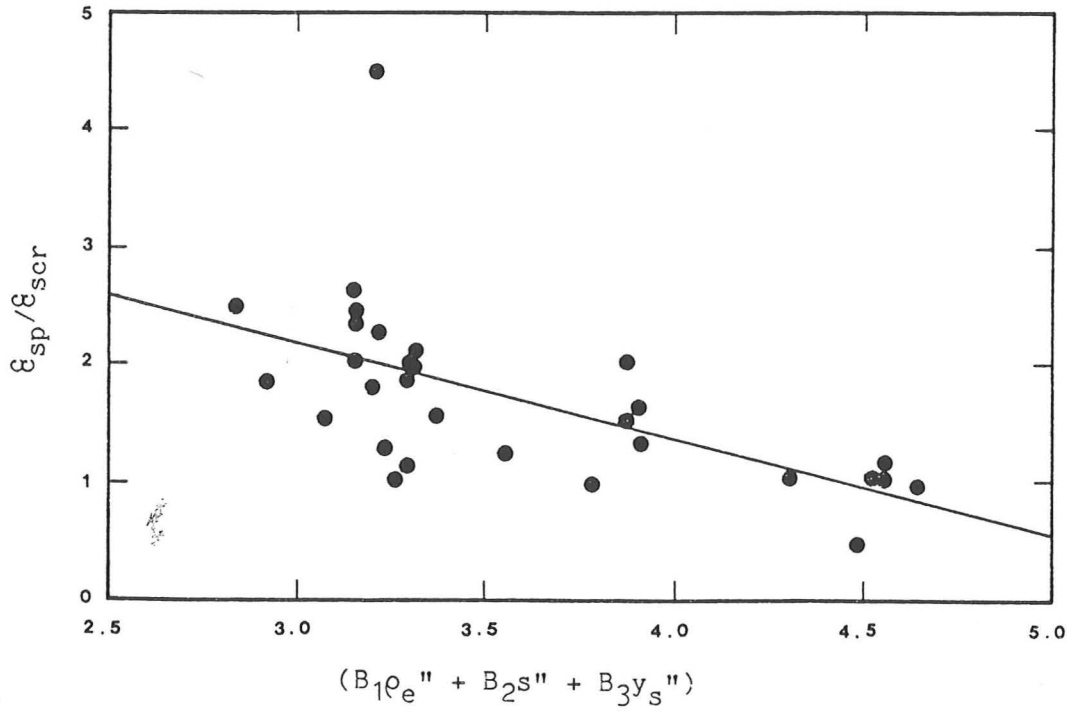

Figure 3.4-12 A graph of $\varepsilon_{sp}/\varepsilon_{scr}$ against $(B_1\rho_e'' + B_2s'' + B_3y_s'')$ for data from all thirty specimens.

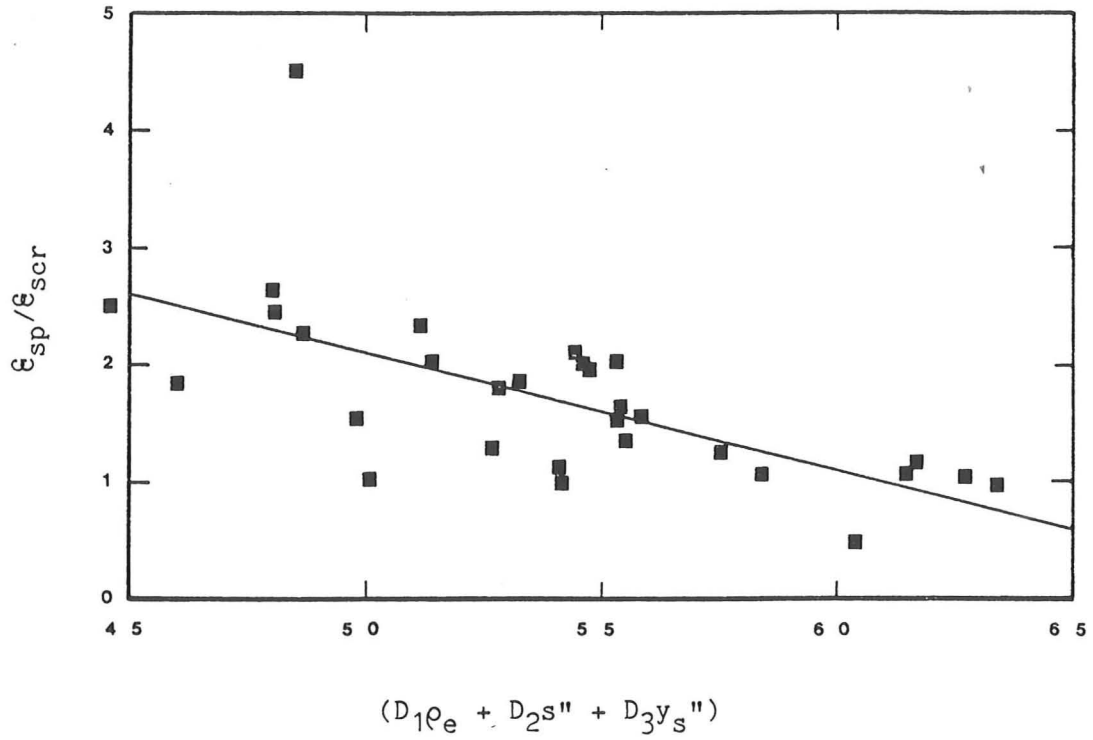

Figure 3.4-13 A graph of $\varepsilon_{sp}/\varepsilon_{scr}$ against $(D_1\rho_e + D_2 s'' + D_3 y_s'')$ for data from all specimens.

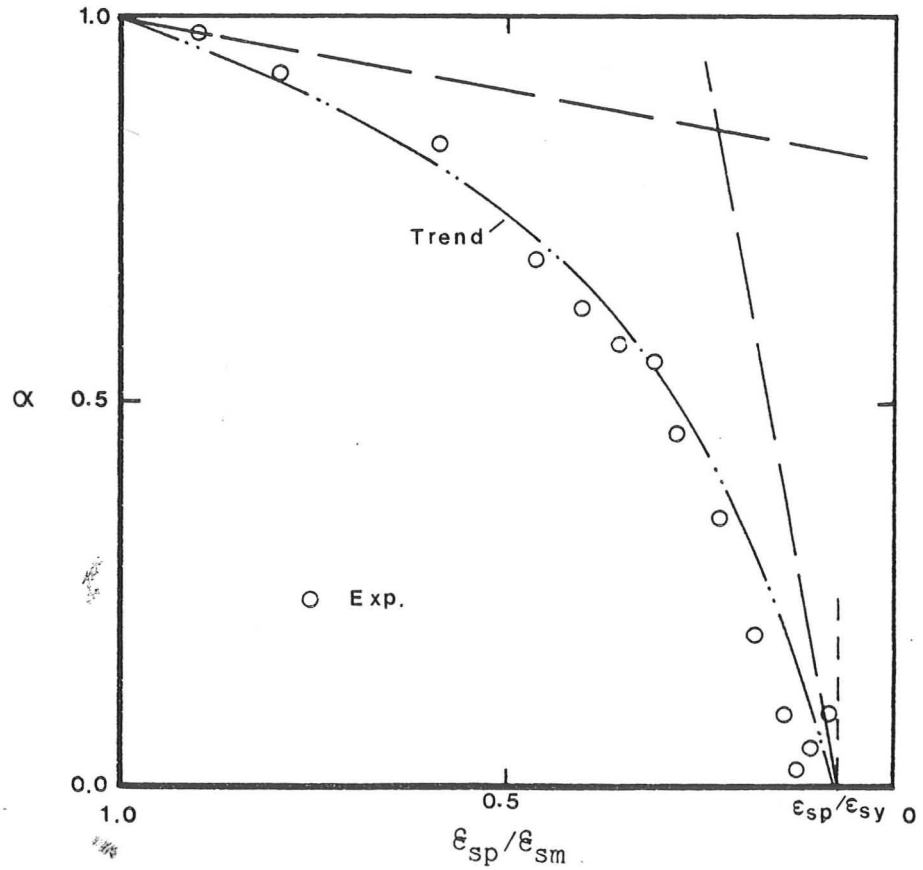

Figure 3.4-14 A typical experimental relationship between α and the ratio $\varepsilon_{sp}/\varepsilon_{sm}$ for values of $\varepsilon_{sm} > \varepsilon_{sp}$.

-II- Decay of tension stiffening force:

The decay of the tension stiffening force as ε_{sm} approaches the yield strain of the tension steel ε_{sy} occurs in two phases. A phase of rapid decline in tension stiffening is followed by another of rather slow breakdown. The factor α in Equation 3.4-15 describes the manner and rate at which F_t decays.

If α for data points with $\varepsilon_{sm}>\varepsilon_{sp}$ is plotted against $(\varepsilon_{sp}/\varepsilon_{sm})$, a graph similar to that of Figure 3.4-14 can be obtained. This suggests a non-linear relation between the two variables with $\alpha = 1$ when $\varepsilon_{sm} = \varepsilon_{sp}$ and $\alpha = 0$ when $\varepsilon_{sm} = \varepsilon_{sy}$. To normalize the results, α is plotted against the ratio $(\varepsilon_{sp}/\varepsilon_{sm})_n$, where

$$\frac{\varepsilon_{sp}}{\varepsilon_{sm\ n}} = \frac{\varepsilon_{sp}\ (\varepsilon_{sy} - \varepsilon_{sm})}{\varepsilon_{sm}\ (\varepsilon_{sy} - \varepsilon_{sp})} \quad \ldots \qquad \ldots\ (3.4\text{-}27)$$

as shown in Figure 3.4-15. The tangent at the point with $\varepsilon_{sm} = \varepsilon_{sp}$ is assumed to pass through the cracking point (i.e. the point with coordinates $(\varepsilon_{sp}/\varepsilon_{scr})_n$ and α_{cr}) and thus the slope of this tangent takes the value of $\{(1-\alpha_{cr})/((\varepsilon_{sp}/\varepsilon_{scr})_n-1)\}$. The tangent slope at $\varepsilon_{sm} = \varepsilon_{sy}$ will be taken as the inverse of the tangent at $\varepsilon_{sm} = \varepsilon_{sp}$ i.e. is equal to $\{((\varepsilon_{sp}/\varepsilon_{scr})_n-1)/(1-\alpha_{cr})\}$. The following equation can now be written for calculating α when $\varepsilon_{sm}>\varepsilon_{sp}$:

$$\alpha = K_5\left(\frac{\varepsilon_{sp}}{\varepsilon_{sm}}\right)_n^{K_6} + K_7\left(\frac{\varepsilon_{sp}}{\varepsilon_{sm}}\right) + K_8 \quad \ldots \qquad \ldots\ (3.4\text{-}28)$$

where K_5, K_6, K_7, and K_8 are constants that are determined by solving the four equations that satisfy the boundary conditions of two points and two tangents. Such analysis gives the following values for these constants:

$$K_8 = 0$$

$$K_7 = \frac{(\varepsilon_{sp}/\varepsilon_{scr})_n - 1}{\alpha_{cr} - 1}$$

$$K_5 = 1 - K_7$$

$$K_6 = \frac{1/K_7 - K_7}{K_5} = \frac{1 + K_7}{K_7}$$

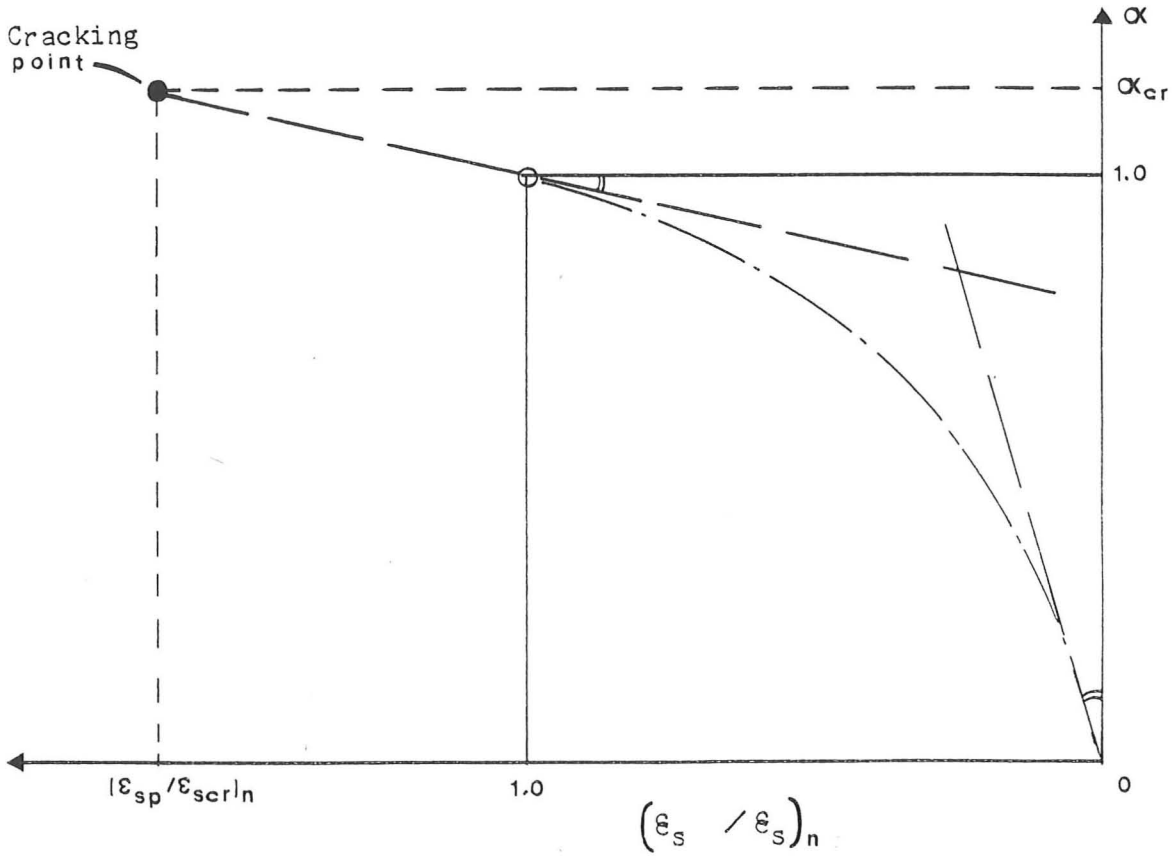

Figure 3.4-15 A typical experimental relationship between α and the normalized ratio $\varepsilon_{sp}/\varepsilon_{sm}$ for values of $\varepsilon_{sm} > \varepsilon_{sp}$.

3.4.6 General formula for tension stiffening

Thus the tension stiffening force at any given average steel-level strain ε_{sm} can be calculated from the following general expression:

$$F_t = \alpha_o f_t \beta b (h - x_m) \{k_1 \varepsilon_{sr}^{k2} + k_3 \varepsilon_{sr}\} \quad \ldots \quad \ldots \quad (3.4\text{-}29)$$

where $\alpha_o = 0.575$

$$\beta = 1.0 - \frac{7 A_s}{b (h - x_p)} - \frac{2/3\ c}{(h - x_p)} \quad \ldots \quad \ldots \quad \text{(Equation 3.4-14)}$$

The values of x_m in Equation 3.4-29, and of x_p in Equation 3.4-29, can be interpolated from the experimental relation between the neutral axis depth and the strain at steel level ε_{sm}, once this strain is known. The steel strain ε_{sp} at peak force when $F_t = F_{tp}$ must first be determined before x_p can be interpolated. If however, the n.a. depth-ε_{sm} relationship is not available, as in a design problem, then the value of x_p has to be estimated and x_m will then be calculated using an iterative procedure; such a technique is used in calculating the moment-curvature relations for beams and slabs as explained in Chapter 5. Finally one must check that the estimated value of x_p was reasonable.

The value of ε_{sp} is calculated using Equation 3.4-26, i.e.

$$\varepsilon_{sp} = \varepsilon_{scr} \left\{ 7.1 - \frac{10.9 A_s}{b (h - x_{un})} - \frac{0.444 s}{(h - x_{un})} - \frac{6.15(d_s - x_{un})}{(h - x_{un})} \right\} \ldots$$

$$\ldots \text{(Equation 3.4-26)}$$

where

$$\varepsilon_{scr} = \left(\frac{2 \alpha_o f_t}{E_c} \right) \left(\frac{d_s - x_{un}}{h - x_{un}} \right) \quad \ldots \quad \ldots \text{(Equation 3.4-17)}$$

In Equation 3.4-29, the value of the strain ratio ε_{sr} and of the coefficients k_1, k_2, and k_3 depend on whether or not the steel-level strain ε_{sm} is greater than ε_{sp}; they take the following values:

(i) $\varepsilon_{sp} \geq \varepsilon_{sm} \geq 0$

$$\varepsilon_{sr} = \frac{\varepsilon_{sm}}{\varepsilon_{sp}}$$

$$\left.\begin{aligned} k_3 &= \frac{\alpha_{cr}\, \varepsilon_{sp}}{\varepsilon_{scr}} \\ k_1 &= 1 - k_3 \\ k_2 &= \frac{1}{1 - \varepsilon_{scr}/\varepsilon_{sp}} \not< 1 \end{aligned}\right\} \quad \ldots (3.4\text{-}30)$$

where

$$\alpha_{cr} = 1/\beta \leq 1$$

(ii) $\varepsilon_{sy} \geq \varepsilon_{sm} \geq \varepsilon_{sp}$

$$(\varepsilon_{sr})_n = \frac{\varepsilon_{sp}\,(\varepsilon_{sy} - \varepsilon_{sm})}{\varepsilon_{sm}\,(\varepsilon_{sy} - \varepsilon_{sp})} \quad \ldots \quad \ldots \text{(Equation 3.4-27)}$$

$$k_3 = \frac{(\varepsilon_{sp}/\varepsilon_{scr})_n - 1}{\alpha_{cr} - 1}$$

$$k_1 = 1 - k_3$$

$$k_2 = \frac{1 + k_3}{k_3} \quad \not< \quad 1$$

... (3.4-31)

The theoretical relationship between the ratio $F_t/(f_t.b.h^2/4)$ and the ratio $\varepsilon_{sm}/\varepsilon_{syi}$ was determined using Equation 3.4-29 for each of Clark's beams and slabs, and is plotted on the experimental graph of that specimen for comparison as shown with the lines in Figures 3.3-3 to 3.3-18 (pages 65 - 72). Good agreement was obtained in the case of the beams (except for B1 and B1R) and at early load stages in slabs S3, S4, S4R, and S7 -- the rest of the slabs had reasonable agreement and showed more tension stiffening than was predicted by the theory.

Note that at high steel strains where the tension stiffening force ought to have diminished, most specimens showed some extra tensile force additional to that in the steel reinforcement (calculated using the uniaxial stress-strain curve for a bare steel bar, and the corresponding measured ε_{sm}). In Figures 3.3-3 to 3.3-18, the tension stiffening force F_t can be seen to fall to a minimum at a steel stress equal to about 70% of the steel yield stress. After this, the value of F_t rises once again, indicating an extra tensile force to that calculated for the steel. This extra force which appears as the stress-strain curve for steel enters its plastic phase (i.e. deviates from the linear), should not be confused with the tension stiffening force that exists at service load stages (i.e. while the steel reinforcement is still in the elastic phase). At service loads, our interest lies in the overall average behaviour of the reinforced concrete member, and thus the tension stiffening force should be accounted for; but as the steel reinforcement approaches its yield stress, the overall average behaviour ceases to represent the critical condition of that member since, at such a high stress, the deformations tend to be concentrated at certain major cracks that are potential yield lines. Thus,

when Equation 3.3-5 is used to obtain F_t at high stress levels (according to the second approach), the average steel stress σ_{sm} (corresponding to the average strain ε_{sm} measured over a great length of the constant moment zone) is less, and hence F_t is greater than at the critical section.

Another reason for this apparent extra tensile force at high steel strains may be a difference in behaviour at such high strain levels between, on one hand, the steel embedded in concrete with only short lengths of the bars exposed at major cracks (where, despite bond slip and internal cracking, deformations tend to be concentrated), and on the other hand, the steel control specimen in the uniaxial tensile test -- where the comparatively long gauge length gives a stress-strain curve which is less stiff at high strain levels than the actual behaviour. This becomes clearer when the tension stiffening force is converted into an extra steel stress, as can be seen from the 'enhanced stress'-strain curves for the steel in Figures 3.3-19 to 3.3-34. For the same stress level, the strain in the bare steel bar is larger than the average experimental one at high stress levels -- though as expected none of the experimental curves exceeded the ultimate steel stress.

The procedure outlined above, Equations 3.4-29 to 3.4-31, can be used directly for calculating the tension stiffening force if desired and does not have to be incorporated in the 'enhanced steel stress' approach. This procedure has been experimentally verified for the following ranges of the effective steel percentage ρ_e", the bar spacing s", the cover ratio c", and the steel depth ratio y_s" within the tension zone.

$$0.67\% \leq \rho_e'' = \frac{A_s}{b\,(h - x_{un})} \leq 3.8\%$$

$$0.27 \leq s'' = \frac{s}{(h - x_{un})} \leq 4.6$$

$$0.09 \leq c'' = \frac{c}{(h - x_{un})} \leq 0.30$$

$$0.62 \leq y_s'' = \frac{(d_s - x_{un})}{(h - x_{un})} \leq 0.84$$

For values of ρ_e'', s", c", and y_s'' outside the above ranges, more experimental results are needed to improve on the values of constants and coefficients in Equations 3.4-29 to 3.4-31. Nevertheless, the variables affected by steel arrangement that are likely to be met in practice (i.e. the commonly used values of ρ_e'', s", c" and y_s'') are more or less covered by the ranges given above. However, the range of y_s'' is practical only when one layer of steel is used, since in this case the steel will be placed as near as possible to the tension face in order to give the largest lever arm. The question about the influence of y_s'' when it takes smaller values, arises when dealing with beams which have a significant amount of skin reinforcement, or when the r.c. member has got two or more layers of tension steel.

3.4.7 Line of action of the total tensile force

The position inside the tension zone at which the tension stiffening force acts, and hence the position of the total tensile force, depends on several factors such as: the overall dimensions of the r.c. member; the position, type, and amount of steel reinforcement; the properties of materials; and on the stage of loading that is to say the strain level. In analysing the beams and slabs (under consideration in this chapter) according to the second approach, an iterative procedure was employed to find out the depth below the neutral axis, as well as the magnitude, of the tension stiffening force. Figures 3.4-16 to 3.4-23 show the relationships of the position of each of the total tensile force, the total compressive force, versus the neutral axis, and the average strain at the steel level. It can be seen from these graphs that the line of action of the total

tensile force starts at a depth d_t below the neutral axis equal to 2/3 of the tension zone height and then, as the strain increases, moves towards the steel level. Once cracks are well established (i.e. after the peak tension stiffening is attained and major cracks have ceased to form), the only way the tensile forces can be transmitted across major cracks is through the tension steel. Hence, beyond some limiting steel-level strain ε_{slim}, the total tensile force will act at the tension steel level.

In order to be able to predict the strain ε_{slim} beyond which d_t is equal to d_s, the ratio $\varepsilon_{slim}/\varepsilon_{scr}$ was tested against the variables ρ_e" and c" where ρ_e" is given by Equation 3.4-19 and the cover ratio c" is given by

$$c'' = \frac{c}{(h - x_{un})} \quad \ldots \qquad \ldots (3.4\text{-}32)$$

The influence of spacing on the ratio $\varepsilon_{slim}/\varepsilon_{scr}$ could not be investigated because in the slabs, as in beams B5 and B5R (see Figure 3.4-20), the thickness of the slab was such that the total tensile force always acted at the steel level.

Linear and multiple regressions, similar to those in Subsection 3.4.5, were carried out on data from the beams only (beams B5 and B5R were excluded); the following results were obtained:

(i) From linear regression on two sets of beams: the first set consisted of beams B1 to B4R (the main variable in this set is ρ_e"); the second set consisted of beams B3, B3R, and beams B6 to B7R (the main variables were ρ_e" and c").

$$\frac{\varepsilon_{slim}}{\varepsilon_{scr}} = 15.54 - 206.0\ \rho_e'' - 40.0\ c'' \quad \ldots \qquad \ldots (3.4\text{-}33)$$

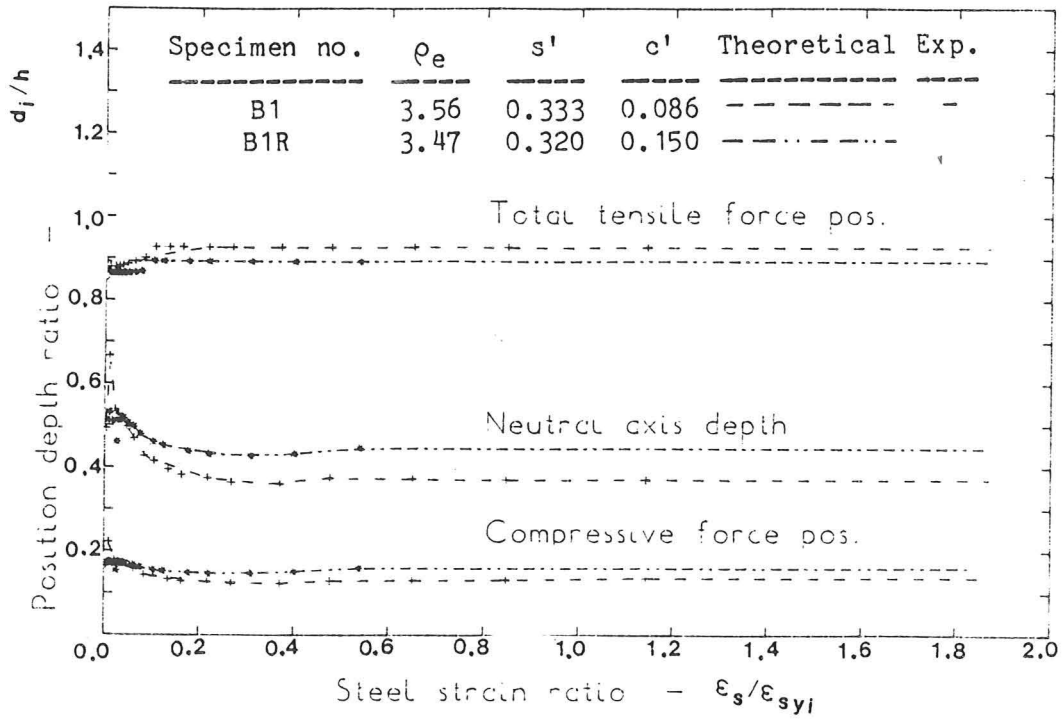

Figure 3.4-16 Force position - steel strain relations for beams B1 and B1R.

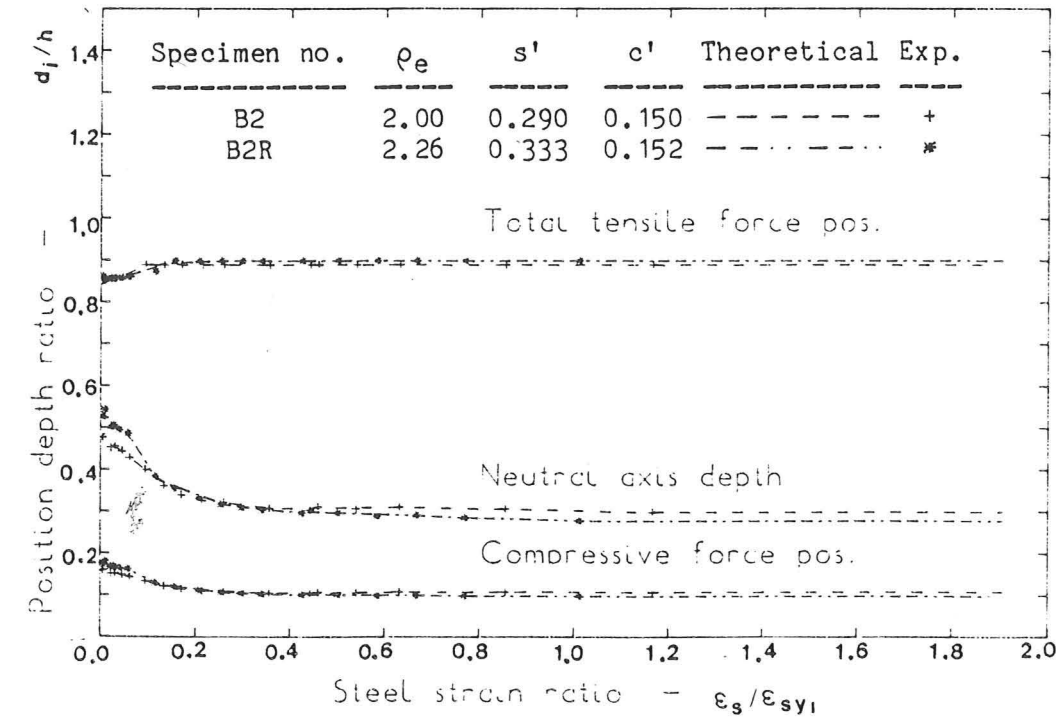

Figure 3.4-17 Force position - steel strain relations for beams B2 and B2R.

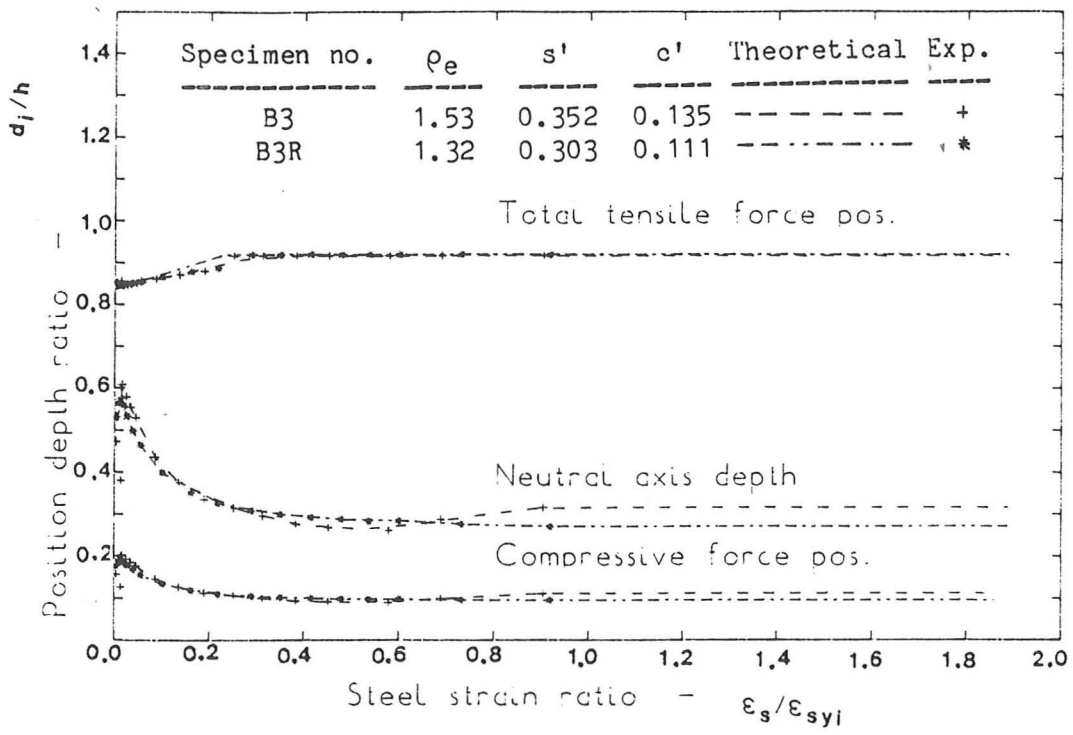

Figure 3.4-18 Force position - steel strain relations for beams B3 and B3R.

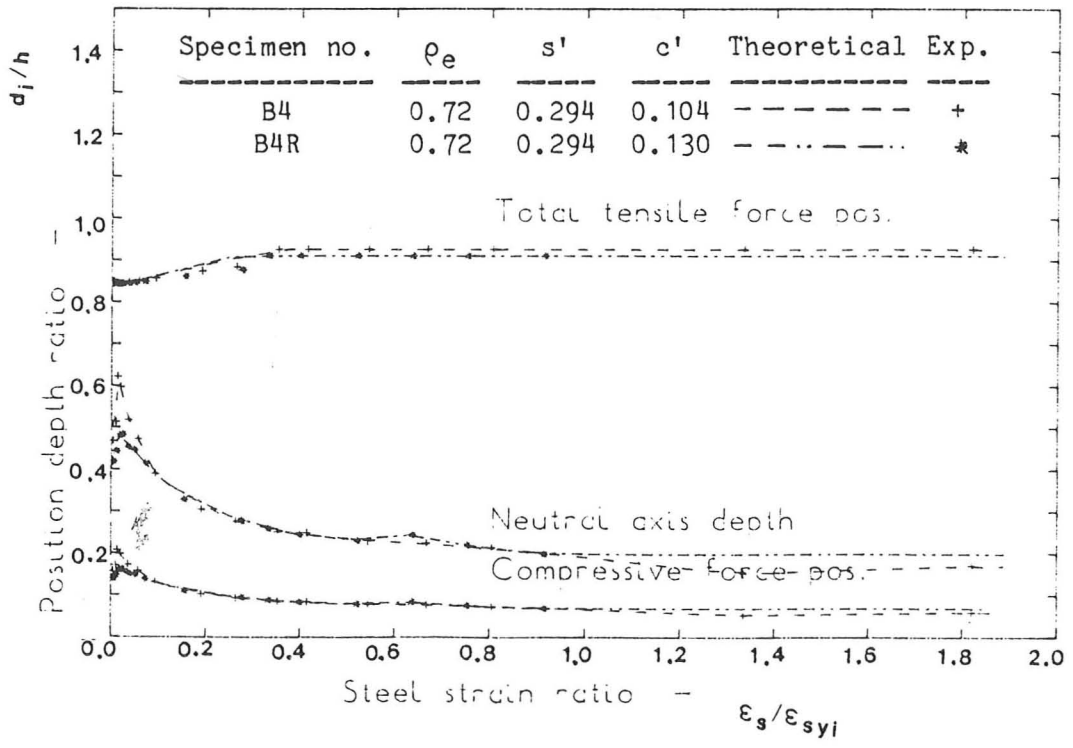

Figure 3.4-19 Force position - steel strain relations for beams B4 and B4R.

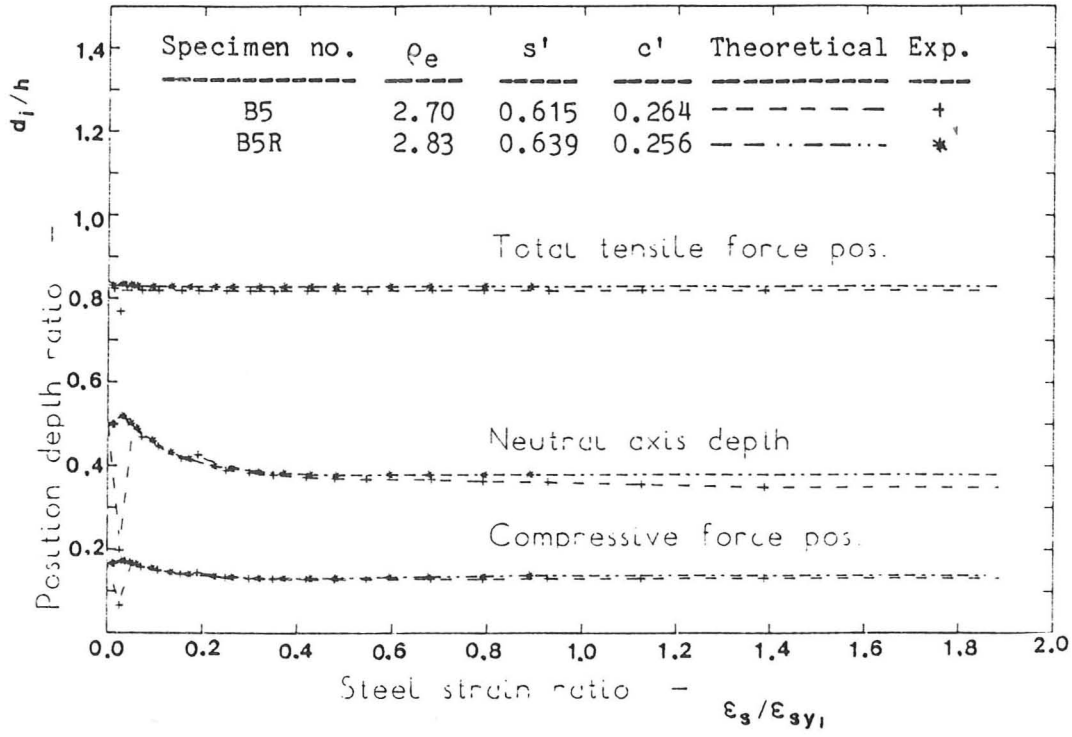

Figure 3.4-20 Force position - steel strain relations for beams B5 and B5R.

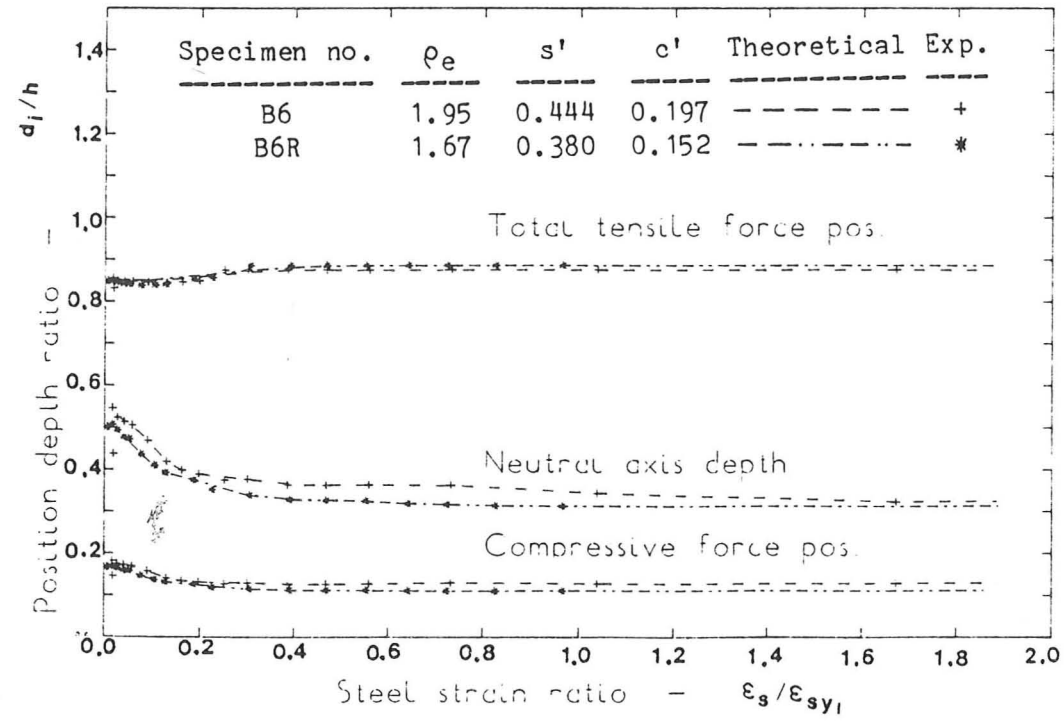

Figure 3.4-21 Force position - steel strain relations for beams B6 and B6R.

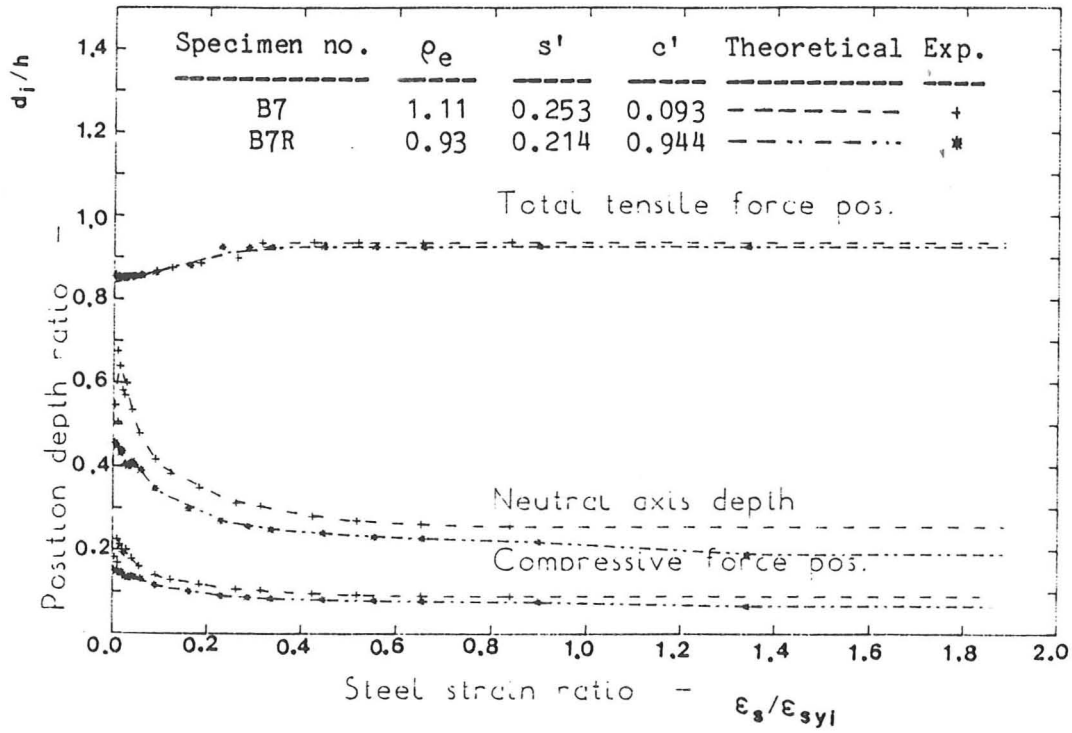

Figure 3.4-22 Force position - steel strain relations for beams B7 and B7R.

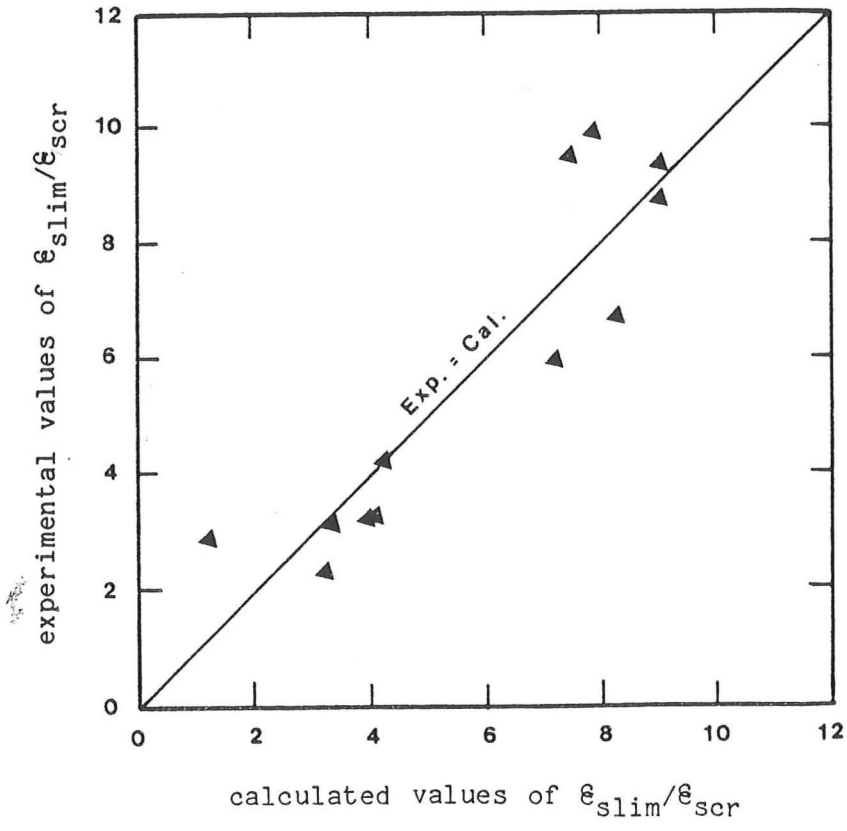

Figure 3.4-23 A graph of the experimental values of $\varepsilon_{slim}/\varepsilon_{scr}$ plotted against the values of $\varepsilon_{slim}/\varepsilon_{scr}$ calculated using Equation 3.4-34 for data from 12 beams only.

(ii) From multiple regression on the twelve beams

$$\frac{\varepsilon_{slim}}{\varepsilon_{scr}} = 15.44 - 209.0\ \rho_e'' - 39.0\ c'' \quad \ldots \quad \ldots (3.4\text{-}34)$$

The agreement between the above two equations is quite good, and the second of them will be adopted. Equation 3.4-34 is plotted on the experimental graph as shown in Figure 3.4-23. It can be seen from this graph that the straight line fit is sufficient for such a small number of data points and range and number of variables.

Having determined the strain at which the line of action of the total tensile force joins that of the tension steel, a transition curve is needed between this point and the cracking point at which the depth of the total tensile force below the neutral axis is equal to 2/3 of the height of the tension zone. It can be seen from Figures 3.4-16 to 3.4-23 that, with very few data points on this transition curve, a straight line connecting the cracking point with the limiting point will achieve the purpose. Thus, the depth of the total tensile force d_t measured from the compressive face can be calculated from the following equations.

(i) for $0 < \varepsilon_{sm} \leq \varepsilon_{scr}$

$$d_t = \frac{F_t\ (d_{ts})_{un} + \sigma_{sm}\ A_s\ d_s}{(F_t + \sigma_{sm}\ A_s)} \quad \ldots \quad \ldots \text{(Equation 3.2-6)}$$

where

$$(d_{ts})_{un} = x_{un} + 2/3\ (h - x_{un}) \quad \ldots \quad \ldots (3.4\text{-}35)$$

(ii) for $\varepsilon_{scr} < \varepsilon_{sm} < \varepsilon_{slim}$

$$d_t = \frac{\varepsilon_{slim} - \varepsilon_{sm}}{\varepsilon_{slim} - \varepsilon_{scr}} (d_s - (d_t)_{un}) \quad \ldots \quad \ldots (3.4\text{-}36)$$

where $(d_t)_{un}$ is the value of d_t when $\varepsilon_{sm} = \varepsilon_{scr}$.

(iii) for $\varepsilon_{slim} < \varepsilon_{sm} < \varepsilon_{sy}$

$$d_t = d_s$$

3.4.8 Enhanced stress - strain relations for tension steel

The enhanced steel stress σ_{se} for a given mean steel strain can be obtained by dividing the total tensile force by the steel area, thus:

$$\sigma_{se} = \frac{F_t + A_s \sigma_{sm}}{A_s} \quad \ldots \quad \ldots \text{(Equation 3.2-7)}$$

Substituting for F_t from Equation 3.4-29, we obtain:

$$\sigma_{se} = \sigma_{sm} + \alpha_o f_t \beta (b/A_s) (h - x_m) \{k_1 \varepsilon_{sr}{}^{k2} + k_3 \varepsilon_{sr}\} \quad \ldots \quad \ldots (3.4\text{-}37)$$

The theoretical relationship between the ratio σ_{se}/σ_{sy} and the ratio $\varepsilon_{sm}/\varepsilon_{syi}$ was determined using Equation 3.4-37 for each of the beams and slabs, and is plotted on the experimental graph of that specimen for comparison as shown in Figures 3.3-19 to 3.3-34 (pages 73 - 80) with the lines. Good agreement between the experimental and theoretical graphs was obtained in the case of beams, except for B1 and B1R (the beams with the highest steel percentage), and at early load stages in slabs S3, S4, B4R and S7. In the rest of the slabs, the agreement was reasonable; however, the experimental steel stress, at early post-cracking load stages, was higher than that predicted by the theory, even in the slabs with greater bar

spacing ratio. This means that the influence of bar spacing on the value of ε_{sp}, and hence on the rate of decay of extra steel stress, was exaggerated; this can be attributed to the small number of data points around the peak of the F_t-ε_{sm} curve, as can be seen from Figures 3.3-11 to 3.3-18, and thus to an inaccuracy in interpolating the ε_{sp} value for the slabs.

It can be seen from Figures 3.3-19 to 3.3-34 that at high load stages, the experimental enhanced steel stress was in most cases higher than that predicted by the theory. This phenomenon of extra steel stresses existing at high load stages was discussed in detail when commenting on the 'theoretical tension stiffening -- steel strain' curves in Subsection 3.4.6 above. However, in some of the test specimens, less stress than that in the bare steel bar was obtained at high load stages; these are the specimens with high steel percentage which are sensitive to experimental inaccuracies in the analysis, based on the second approach, used in obtaining the tension stiffening force.

The 'enhanced stress'-strain relationship for the tension steel gives the stress in the steel at a major crack, in the post-cracking phase, since the total tensile force is carried across the cracks by the steel. Thus, we expect σ_{se} never to exceed the ultimate stress σ_{sy}, of the tension steel; this expectation was fulfilled by the test results -- the ultimate stress is assumed to be equal to 1.2 times the yield stress for this type of steel.

Once the 'enhanced stress'-strain relationship for the tension steel is obtained, it will be ready for use in non-linear structural analysis such as a macroscopic finite element program. It might be necessary, however, in order to be able to obtain the tension stiffening force needed for calculating σ_{se}, to make an assumption concerning the neutral axis depth at $F_t = F_{tp}$. As calculations go on step by step, the neutral axis depth at each stage is determined using an iterative procedure, so that compression equals tension. A check should then be carried out on the value of neutral axis depth at the peak strain ε_{sp} to see if it agrees with the assumed value -- x_p can be assumed equal to a constant times x_{un}. In Chapter 5, this new approach, i.e. the 'enhanced steel properties' approach, will be used in obtaining the moment-curvature relations for concrete

slabs with skew reinforcement tested by the author.

3.5 General Discussion in Relation to Clark et al's Approach

The analysis of the experimental data from tests by Clark et al as described in this chapter, differed substantially from the analysis carried out by Clark et al (on the same data of course). These differences can be summarized as follows:

(1) In deriving the experimental values of F_t using the second approach presented here, only one assumption, about the centroid of the compression block, was used in addition to the experimental results. In fitting curves through the experimental F_t-ε_{sm} relations obtained by this analysis, we used the neutral axis depth x_{un}, and the steel strain ε_{scr} for the uncracked behaviour. Clark et al, on the other hand, used classical no-tension theory to calculate the neutral axis depth x and then the steel strain ε_s, and both values were used at the two stages. First, ε_s was used with given experimental ε_{sm} and steel properties to calculate F_t; then, both ε_s and x were used to predict F_t from given steel and concrete properties. It should be pointed out though, that the classical no-tension theory will be a long way from the truth when tension stiffening is largest, both on x_m and ε_{sm}.

(2) The value of β (Equation 3.4-14), giving the effective area of tension concrete, was found to be a function of the effective steel percentage ρ_e, the cover ratio c', and to some extent the bar spacing ratio s', however, the bar spacing effect was neglected. In the case of Clark et al's analysis, β was taken as a constant value for beams while the effect of bar spacing was neglected for slabs.

(3) The constant α_o, giving the average tensile stress in concrete at $F_t = F_{tp}$ as a ratio of the measured tensile strength of concrete, was introduced here but not used by Clark et al

(4) The average experimental strain ε_{sp} at $F_t = F_{tp}$ was found, in our case, to be a function of the average strain at cracking ε_{scr}, the effective steel ratio ρ_e", bar spacing ratio s", and the depth ratio y_s" of the steel below the neutral axis depth. Clark et al used 'ε_{sp}', the theoretical strain at peak tension stiffening force obtained using the classical no-tension theory, instead of the average experimental strain as in our case. They gave 'ε_{sp}' as a function of I_{cr}/I_{un} -- the ratio between the theoretical second moment of area of the cracked section and that of the uncracked behaviour.

(5) The experimental neutral axis depth x_p at $F_t = F_{tp}$, was used in defining the ratios ρ_e, s', and c' mentioned in (2) above, and the calculated neutral axis depth x_{un} for the uncracked section was used in defining the ratios ρ_e", s", and y_s" mentioned in (4) above. Clark et al used the theoretical neutral axis depth x for the cracked section in defining the bar spacing ratio.

(6) The factor α, giving the average concrete tensile stress in the tension zone as a proportion of the average tensile stress in concrete at $F_t = F_{tp}$, was found to be a function of, mainly, the strain ratio ε_{sr}, and of β and the ratio $\varepsilon_{sp}/\varepsilon_{scr}$. In the case of Clark et al, it was taken as a direct function of $\varepsilon_{sm}/'\varepsilon_{sp}'$, and of the bar spacing when it exceeds 1.5 times the slab depth.

(7) The degree of agreement between the experimental and the theoretical curves was almost the same in our case as in Clark et al's. However, the theory obtained by Clark et al covers only the post-cracking phase, and also it predicts some tension stiffening after the steel yields whereas a prudent approach to design at ultimate limit state suggests that this late tension-stiffening ought to be rejected.

The approach adopted in this chapter, for predicting the tension stiffening force in a reinforced concrete member in uniaxial bending at a given load stage, might be preferable to Clark et al's approach for the

following reasons:

(a) Derivation of formulae was based on purely experimental results with only one assumption made -- concerning the line of action of the compression force.

(b) In predicting the 'tension stiffening force -- steel level strain' (F_t-ε_{sm}) curve, there is no need at all to resort to the classical no-tension theory. Analysis of the uncracked section only, together with the section and materials properties, is needed.

(c) The values of the steel strains given by the F_t - ε_{sm} curve are the average strains such as those calculated by a macroscopic finite element programme. This means that our approach can readily be used in such programmes after incorporating the tension stiffening force into the 'enhanced steel stress' approach.

(d) The average strains obtained by this approach are those which directly enter into formulae for predicting crack widths.

(e) There is no discontinuity in the approach given here: the predicted F_t-ε_{sm} relation covers the whole range of loading from zero up to the ultimate load, with the tension stiffening force reducing to zero as the steel strain reaches its yield value.

(f) Steel arrangement (or the ratios ρ_e", s", c", and y_s") has more influence, according to this approach, on the values of β, ε_{sp}, and α as supported by the experimental results.

4.1 Introduction

While many tests have been carried out on reinforced concrete slabs by other researchers to provide information on tension stiffening and crack widths, few tests were performed in situations where bending cracks form at an angle to the direction of main bending reinforcement. Such situations are very often encountered in the case of slabs and thin walled structures, where the direction of main bending reinforcement does not necessarily coincide with that of the principal stresses as in beams.

The experimental work described in this chapter was designed to investigate the effect of the angle δ, between the direction of the steel reinforcement and the principal bending direction, on tension stiffening and crack widths. The tests were carried out on reinforced concrete slabs in uniaxial bending. The main parameter which was varied between specimens was the angle δ.

Since experimental studies of cracking at small scales can be unreliable [24],[44], it was decided to perform the tests on slabs of a size approaching practical dimensions. Eight slabs were tested under uniaxial bending with a constant moment over a region of more than one meter square. All but one of these slabs were reinforced with two sets of bars arranged symmetrically with respect to the principal bending

direction (see Figure 4.1-1). The angle δ between each set of bars and that direction varied from 10^{o} to 60^{o} in steps of 10^{o}. The other slab had only one set of longitudinal bars. The slabs were designated Sn, where S stands

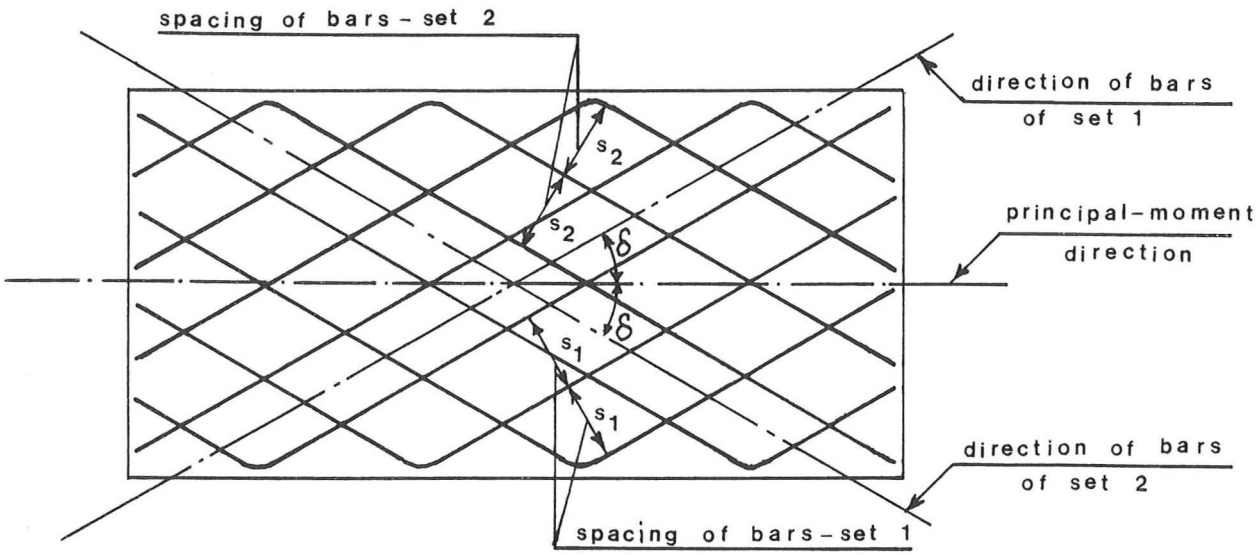

Figure 4.1-1 Steel arrangement for the slab tests.

for 'Skew' and n is the angle δ in degrees divided by 10. A repeat of the slab with $\delta=30^{o}$ was designated S3N (New) while the "old" slab S3 became S30. In slabs S1 to S6, the bar spacing in the set which had the smaller effective depth was reduced to give the same moment of area about the neutral axis (in the elastic range) as that of the other set of bars. The symmetrical arrangement of reinforcing bars with respect to the

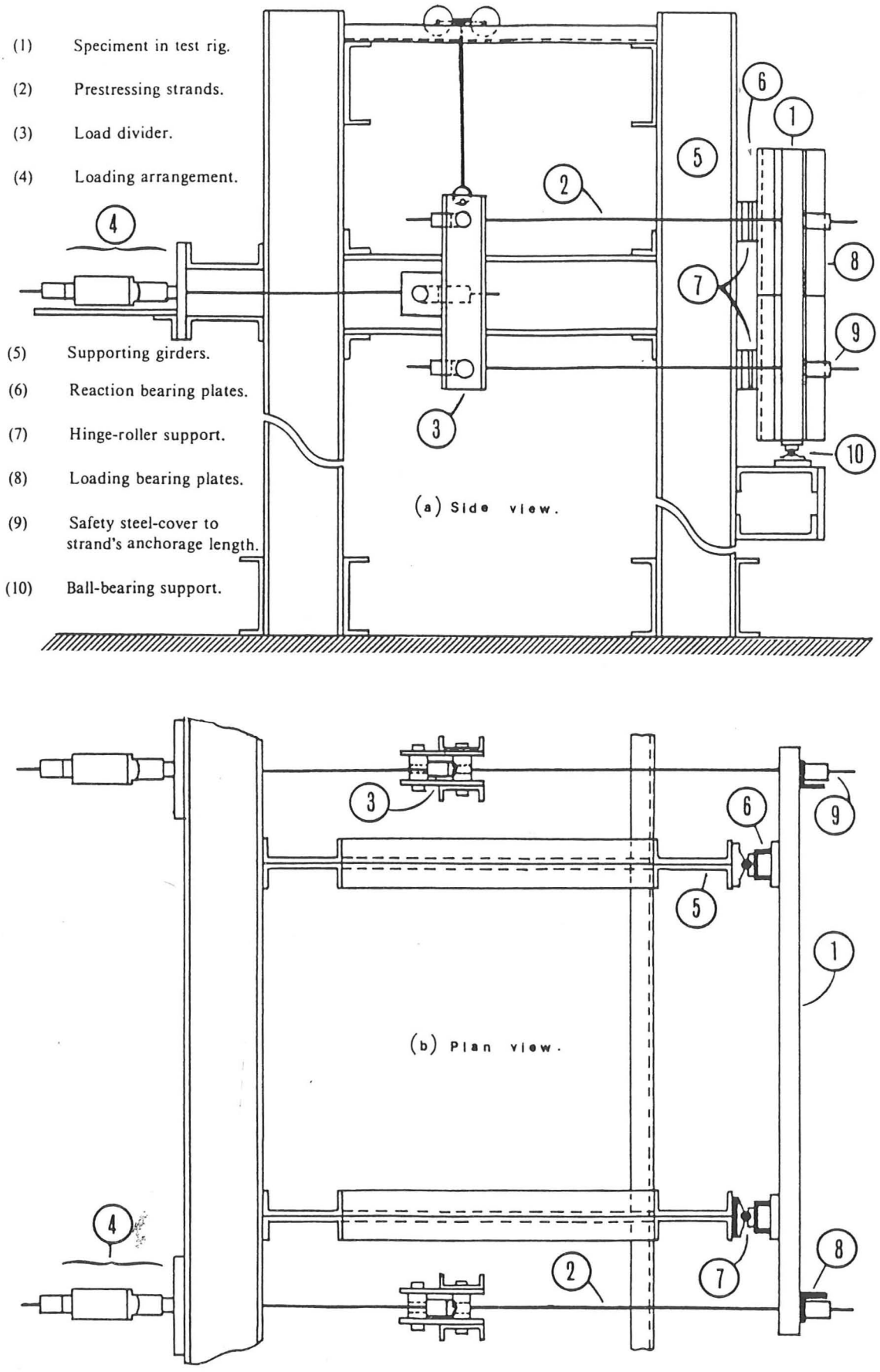

Figure 4.2-1 Schematic illustration of test rig. (a) Side view. (b) Plan view.

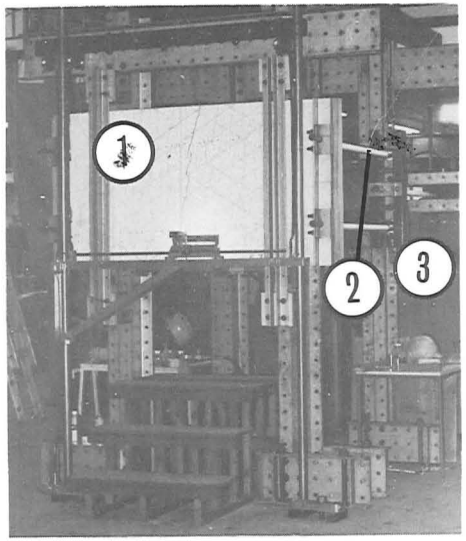

(a)

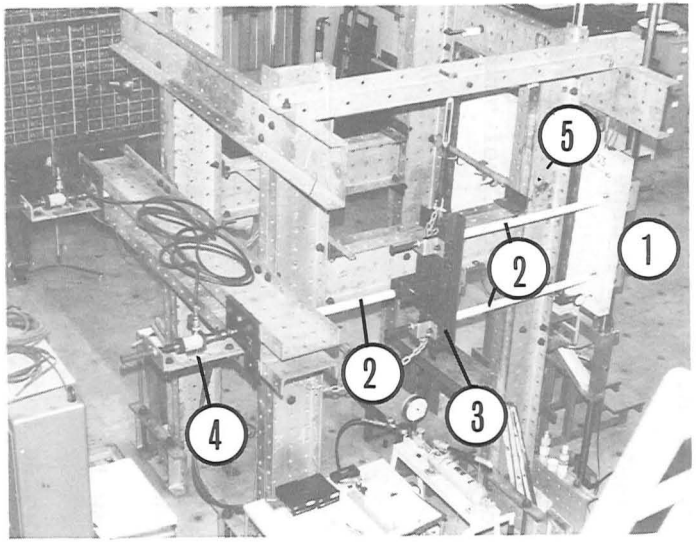

(b)

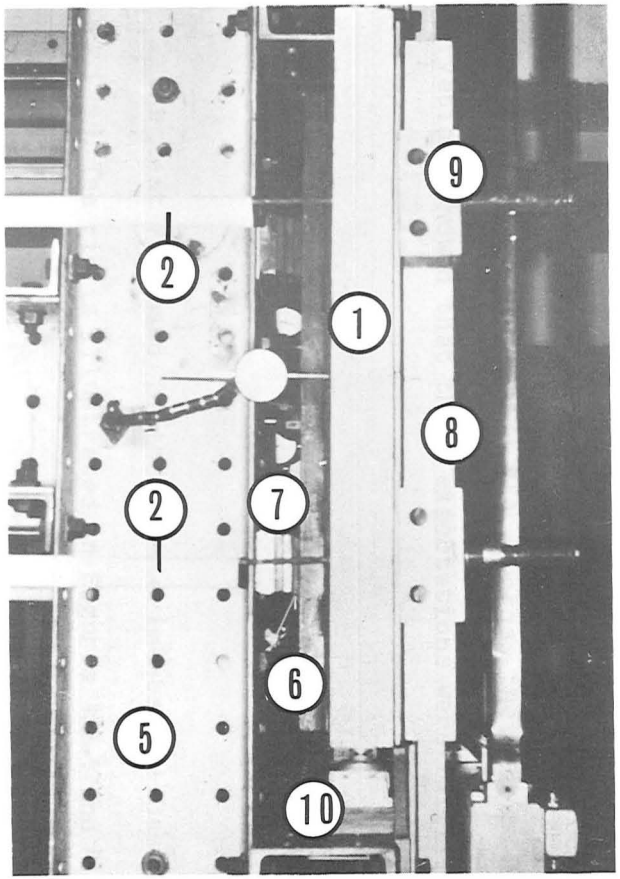

(c)

(1) Specimen in test rig.

(2) Prestressing strands (covered with safety plastic tubes).

(3) Load divider.

(4) Loading arrangement.

(5) Supporting girders.

(6) Reaction bearing plates.

(7) Hinge-roller support.

(8) Loading bearing plates.

(9) Safety steel-cover to strand's anchorage length.

(10) Ball-bearing support.

Figure 4.2-2 Photographs of the test rig. (a) Front view. (b) Side view. (c) Details of supporting system.

principal loading direction was chosen to ensure that cracks formed approximately perpendicular to this direction and thus no significant shear displacement would take place across the cracks. In the actual tests observations showed that these expectations were fulfilled.

4.2 Test Rig

The test rig used in these experiments was based on that used by Clark [38]. The rig is illustrated in Figures 4.2-1 and 4.2-2.

The structural system representing the tested specimen is the simply supported beam with two overhanging ends. Loads applied to the overhanging ends produce uniform bending moment in the central region between the supports. The specimen is positioned in a vertical plane with its lower long side standing on two ball bearings, one of them fixed to the rig and the other free to move on rollers in any direction. The principal bending direction is parallel to the longer side of the specimen with tension face outwards. The supports were chosen to be two vertical girders each composed of two steel channels (No. 8"x3.5") back-to-back. Two hollow-ram jacks were used to apply the load through two prestressing strands. The load in each strand was divided into two equal loads by means of the load divider described below. The load from each of the strands was then spread over half the width of the specimen by means of a length of an angle section with a strip of hardboard between it and the specimen as shown in Figure 4.2-2c.

The Load Dividers

Each of the two load dividers consisted of two steel channels (back-to-back). Welded to the back of each channel is a rectangular steel plate which sticks out of the middle section of the channel forming a "T" shape. Passing through the attached plates is a steel roller to carry the applied load. Two more steel rollers pass through the top and bottom edges of the channels (to carry half the load). Each one of these rollers was drilled across its mid diameter so that the prestressing strands could pass through these holes (see Figure 4.2-2b).

4.3 Materials

4.3.1 Reinforcement

Cold worked ribbed reinforcing bars (Tor Bar to B.S. 4461:1969) were used in all the specimens. For slab S0, the bars were 12 mm in diameter (0.2% proof strength of 481 N/mm^2), while 8 mm bars were used in the rest of the slabs (0.2% proof strength of 495 N/mm^2).

4.3.2 Concrete

A trial mix designed according to the DoE mix design method [46] showed that the practical cube strength at a certain age was much greater than expected. Three more trial mixes were needed to arrive at a suitable mix for the slabs, to give a measured strength of about 30 N/mm^2 at 28 days. (It was desireable to have the weakest concrete mix possible so as to arrive at the cracking stage earlier and thus have a larger post-cracking stage; at the same time our concern was to keep the water/cement ratio

reasonable enough to get a medium workability mix).

The mix was of medium workability and had cement, sand and gravel in the proportion 1: 2.64: 3.1 by weight, with 10 mm maximum size of gravel aggregate. Ordinary Portland Cement and a water-cement ratio of 0.6 were used.

4.3.3 Control Specimens

The stress-strain curve for steel in tension was obtained from load-control tests on uniaxially loaded steel bars. Figure 4.3-1 shows the average steel properties from 36 tests on 8 mm diameter bars.

Four 100 mm cubes and four 200x100 mm diameter cylinders were cast with each batch of concrete (i.e. eight cubes and eight cylinders for each slab -- see Subsection 4.4-3). The cubes of the first batch were tested in compression on the first day of the slab test, and those of the second batch on the last day of the test. The cylinders of the first batch were tested in indirect tension on the first day of the slab test, while the other four were tested in compression (to obtain the stress-strain curve) on one of the last two days of the slab test.

The results from the control specimens' tests are summarised in Table 4.3-1.

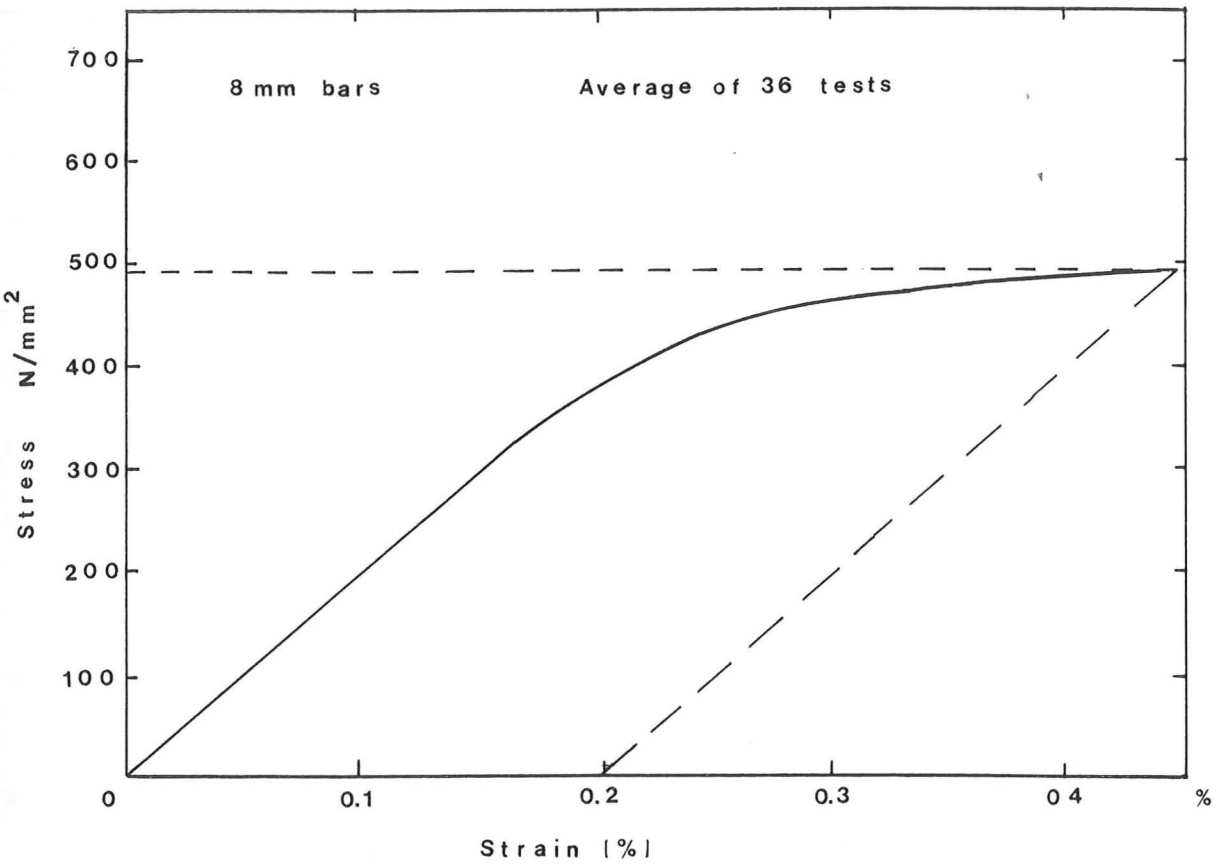

Figure 4.3-1 Stress-strain curve for 8mm reinforcing bars (average of 36 tests).

Table 4.3-1 Results from tests on concrete control specimens.

Slab No.	Cube strength at test N/mm^2	Compressive strength from cylinders N/mm^2	Indirect tensile strength N/mm^2	Age of specimen at test days (months)
S0	50.80	--	3.32	5 months
S1	43.0	35.08	3.17	28 - 35
S2	35.2	29.92	2.84	21 - 29
S30	42.1	--	3.30	5 months
S3N	30.1	28.55	2.5	34 - 42
S4	40.0	30.64	2.80	28 - 36
S5	30.55	19.43	2.81	10 - 12
S6	43.27	34.80	3.32	36 - 37

4.4.1 Dimensions

The test specimens were 2000 mm long by 1000 mm wide and 80 mm deep. Conical shaped holes of 30 mm average diameter were left through the slab near the ends in order to accommodate the stressing strands which were used in loading the specimens (see Figure 4.4-1).

The measured dimensions of the test specimens and the steel arrangment are given in Table 4.4-1.

4.4.2 Reinforcement layout

The specimens were cast horizontally with tension face downwards. A 10 mm (nominal) cover, all over the slab, was achieved by using hard plaster spacers and by suspending the bars at mid-span using thin wires. The plaster spacers, together with clips connecting the two sets of bars, were confined to both ends of the specimen (350mm wide) while the suspending wires were removed half an hour after casting: this left a wide central area completely free of spacers and tying clips (which might have induced cracks at particular positions).

In order to have better anchorage for the reinforcing bars, the bars from the first set were bent where they reached the long edge of the slab to form the second set of bars. The bars were also bent out of plane to allow for the difference in cover between the two sets of bars.

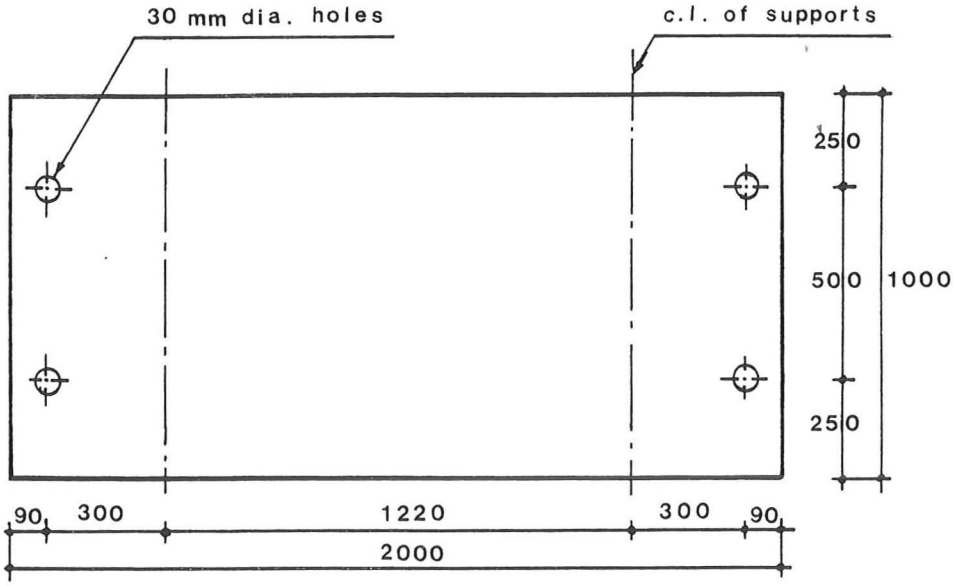

Figure 4.4-1 Dimensions of test specimen.

Table 4.4-1 Measured dimensions of test specimens and of steel arrangement.

Slab No.	Angle of skewness δ^o	Thickness of slab mm	Effective depth of steel - mm		Cover to steel bars		Spacing of steel bars	
			set 1 d_{s1}	set 2 d_{s2}	set 1 c_1	set 2 c_2	set 1 s_1	set 2 s_2
S0	0	81.3	61.5	--	13.8	--	125.0	--
S1	10	81.6	66.5	58.5	11.1	19.1	125.0	100.0
S2	20	80.7	65.4	56.3	11.3	20.4	125.0	100.0
S30	30	80.9	66.3	57.5	10.6	19.4	125.0	105.0
S3N	30	81.4	66.0	57.3	11.4	20.2	125.0	105.0
S4	40	81.3	64.3	55.5	13.0	21.8	125.0	105.0
S5	50	81.4	66.5	58.0	10.9	19.4	125.0	105.0
S6	60	82.0	67.8	59.8	10.3	18.3	125.0	110.0

* bar diameter is 8 mm for all slabs except slab S0 with 12 mm bars.

Because of the slight difference in spacing in the two directions, two small wedges at the top-right and the bottom-left corners were free from reinforcing bars as shown in Figure 4.4-2. An additional length of steel bar was placed near the edge to make up for the absence of reinforcement in these wedges. However, it was impractical to use the "bending of bars" technique for slabs S5 and S6 (because some of the bars had to be bent in more than one place); instead, the ends of both sets of bars were welded together.

4.4.3 Casting

Two batches of concrete were needed to fill up the formwork and so each specimen was cast in two layers. Full compaction was achieved using two vibrators one attached to each end of the formwork as illustrated in Figure 4.4-3.

The formwork base consisted of a resin coated plywood panel (18 mm thick) attached to a rigid framework; this resulted in a flat and smooth tension face.

4.4.4 Preparation

After each specimen was cast, its top (compression) surface was leveled and given a steel float finish, then the specimen was covered with polythene sheeting at the end of the day (casting took place in the mornings). The following morning the slab was covered with damp hessian and polythene sheeting, while the concrete control specimens were demoulded and cured in the same way as the slab. Three or four days later, the formwork was lifted up into a vertical position and then the slab was

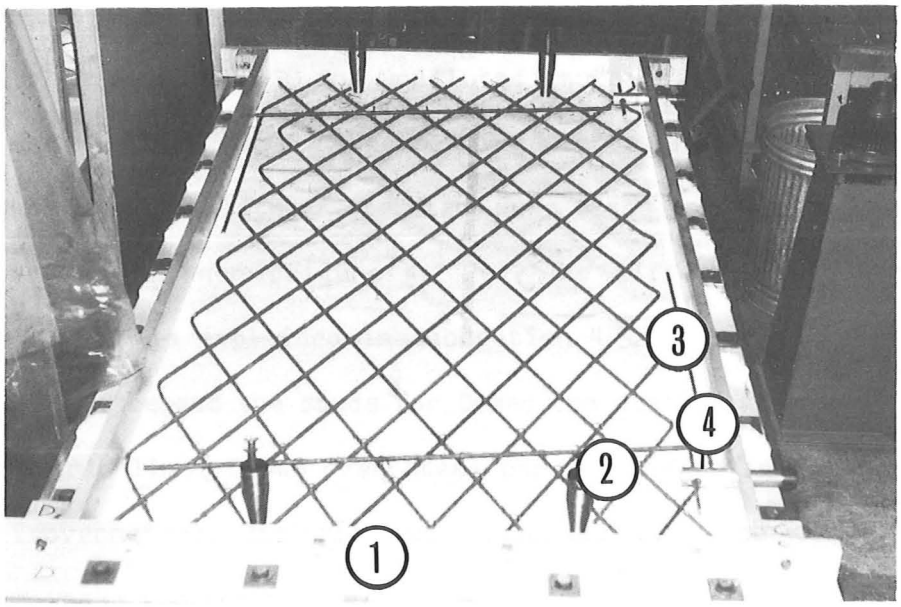

(1) Formwork.

(2) Conical shaped steel hole-former.

(3) Additional steel bar.

(4) Built-in socket for lifting-loop.

Figure 4.4-2 Reinforcement layout for Slab S30. (Photograph taken in long-side direction).

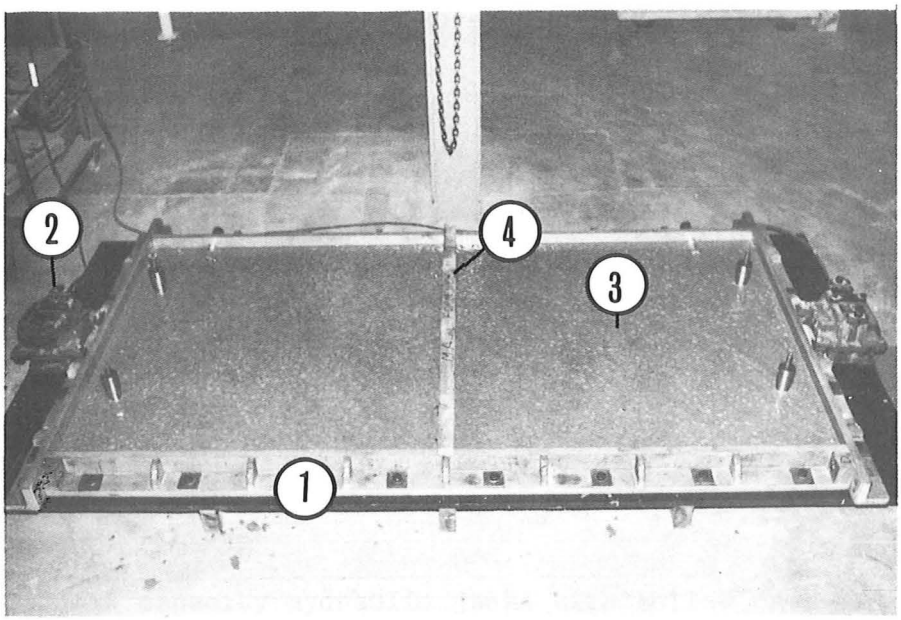

(1) Formwork.

(2) Vibrators.

(3) First batch of concrete mix.

(4) A timber plank on which the steel mesh hangs temporarily.

Figure 4.4-3 Photograph of concrete mix being vibrated after casting.

demoulded and left for about three weeks to dry. Two coats of diluted emulsion paint (white) were applied to both faces of the slab (white-wash was used in slabs S0 and S30 and undiluted emulsion, in slab S2) to enable cracks to be seen more easily. The bearing plates, used to spread the load and reaction over the width of the slab, were fixed to the slab with strips of hardboard in between (Figure 4.2-2c). The different grid lines (the function of which is explained in Subsection 4.5.3 below) were then drawn on the tension face and the studs for Demec and dial gauges were fixed. The position of grid lines drawn over steel bars was determined using a steel detector (covermeter). The slab was inserted into the test rig after nearly four weeks (on the average) from the day of casting.

4.4.5 Core samples

At the end of the test program, three cores were taken by diamond-edged drill out of the middle zone of each slab in places where the steel bars crossed. The average depth of the slab and the average position of the steel bars were measured directly from the core samples. A check was made on the position of the grid lines and gave a positive result.

4.5 Instrumentation

4.5.1 Loading

Two 100 kN capacity hydraulic jacks with hollow rams were used in loading the specimens. A separate pump was used with each jack to give good control over loading.

The loads were measured by means of two 160 kN capacity load cells. Each load cell consisted of a thin walled cylinder (3.5 mm thick) made of Direct Hardening Alloy steel EN16 T (665 N/mm^2 yield strength). The deformation was measured using electric resistance strain gauges arranged in half a bridge and connected to an electronic 'Bridge' that gives a digital reading of the strain. Load cells were calibrated using the compression machine that was used in testing the concrete control specimens. The calibration load - 'strain reading' curves for both cells are shown in Figure 4.5-1: the best fit lines forced through the origin agrees well with the data. Note that since the e.r.s. gauges are arranged in half a bridge, the calibration curve for the load cell will give smaller strain readings if the load is eccentric towards the place where there is no vertical strain gauge. For this reason, care was taken to make sure that in the actual test the applied load was central, by taking some precautionary measures as explained below.

The details of the loading arrangement at each of the two loading positions are shown in Figure 4.5-2. It consists of the following:

(1) A reaction beam made out of two channels connected to the back columns of the test rig.

(2) A bearing plate 25 mm thick bolted to the reaction beam; a 25 mm hole was drilled through the plate to accommodate the stressing strand.

(3) The load cell.

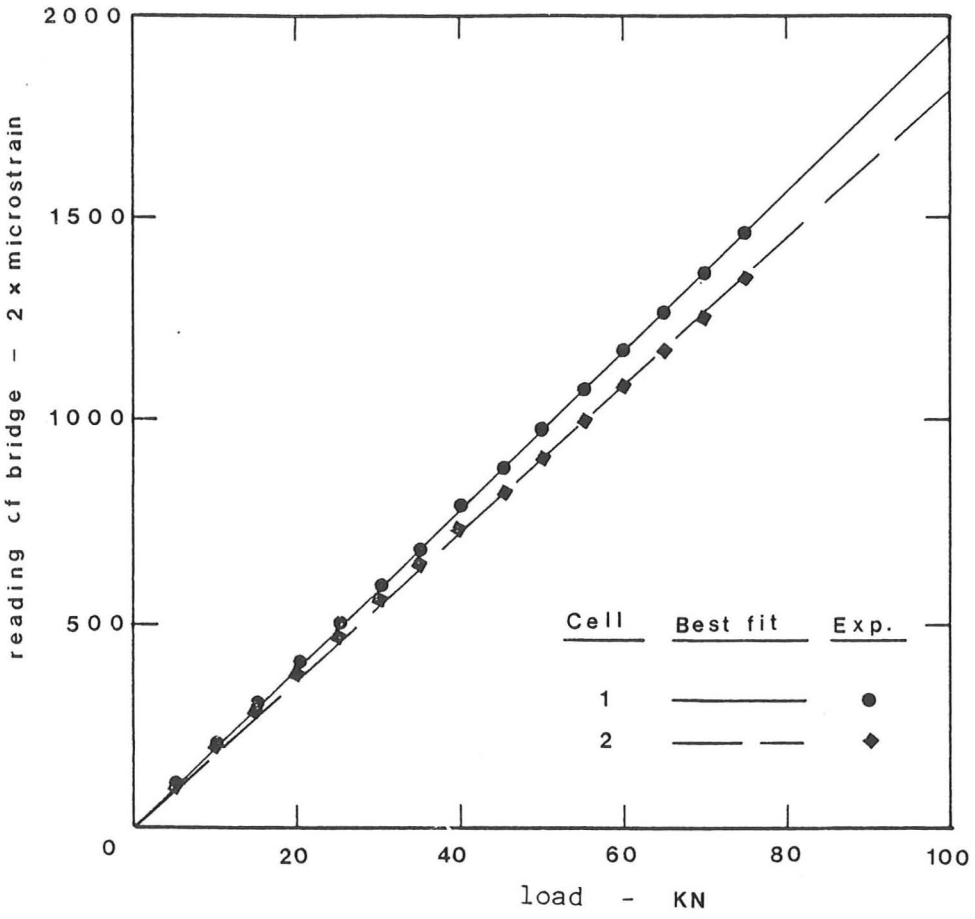

Figure 4.5-1 Calibration curves of load cells.

(4) A wedging device, used to clamp on the stressing strand when the hydraulic jack is not in use, e.g. at night or when the ram runs out of travel and a new travel is needed. It consisted of a wedging barrel and a hollow steel cylinder with openings in its wall to allow access to the wedges so that they can be pushed in or pulled out as necessary.

(5) The hydraulic jack described above.

(6) Another wedging barrel to clamp on the stressing strand when the hydraulic jack is in use.

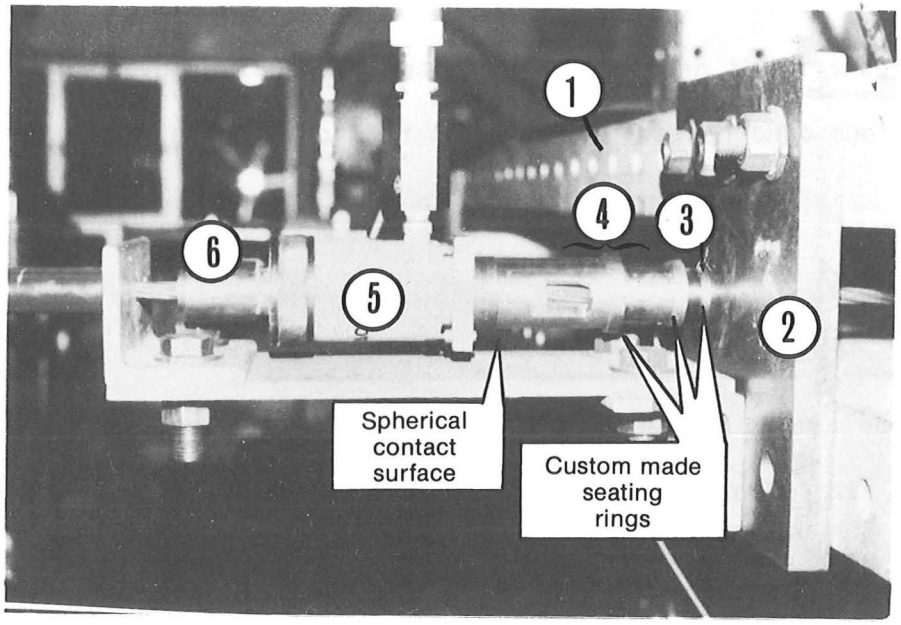

(1) Reaction beam.
(2) Bearing plate.
(3) Load cell.
(4) Wedging device.
(5) Hollow-ram hydraulic jack.
(6) Wedging barrel.

Figure 4.5-2 Details of Loading arrangement.

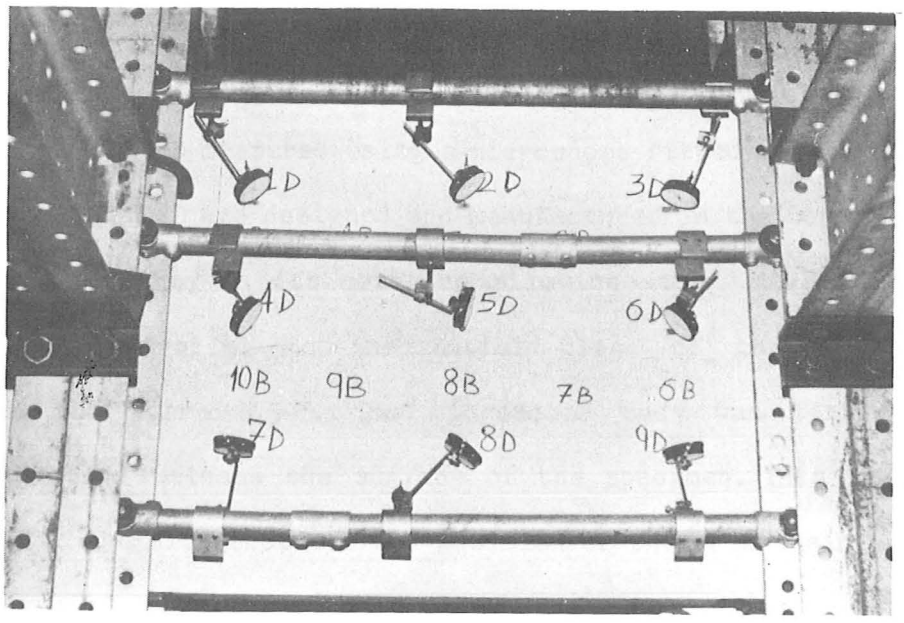

Figure 4.5-3 Deflection rig and dial gauge arrangement for slabs S1, S3N, S5, and S6.

In the absence of an applied load, the above loading elements were held together by custom made seating rings as shown in Figure 4.5-2. These seating rings together with spherical contact between the hydraulic jack and the wedging cylinder (described in 4 above) ensured that the load was as central as possible.

4.5.2 Deflections

Deflections were measured at mid-span and at two points each 400mm distant from either side of midspan (except in slab S2 where this distance was 300mm) by means of 0.01 mm mechanical dial gauges. These were fixed to steel scaffolding tubes which were bolted to the front columns of the test rig (the columns on which the slab is supported) as illustrated in Figure 4.5-3. For slabs S30, S0, S2, and S4 the dial gauges were positioned at mid-breadth and at 100 mm from the lower edge of the compression face of the specimen as illustrated in Figure 4.5-4. For slabs S1, S3N, S5, and S6 they were positioned at mid-breadth and at 250 mm from both the top and lower edge i.e. quarter-breadth (Figure 4.5-3).

4.5.3 Cracks

The cracks were measured using a microscope fitted with a Micrometer Eyepiece. A special frame designed and manufactured in the Department held the microscope firmly in its position allowing it to move freely in a vertical plane parallel to the intial plane of the specimens as illustrated in Figure 4.5-5. The microscope body was fitted with a strip-light to illuminate the surface of the specimen. This light could thus move with the microscope to the position of the crack being measured.

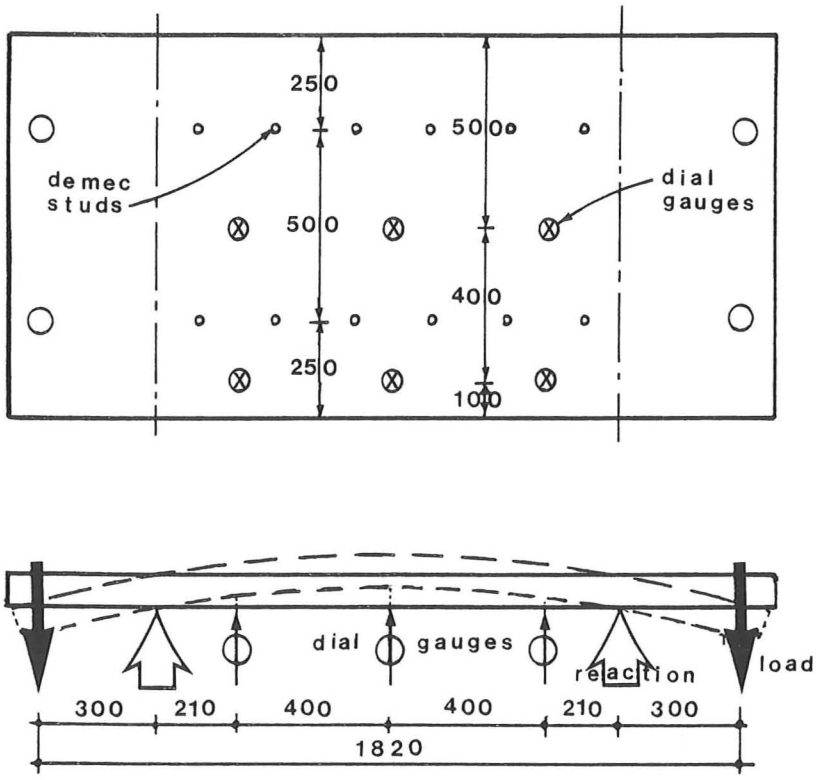

Figure 4.5-4 Dial gauge arrangement for slabs S0, S2, S30, and S4.

The microscope had a 13X magnification when the cracks in slab S0 were measured but the magnification was increased to 36.5X for slabs S1, S2, S3N, S4, and S5 by changing the objective lens. No cracks were measured in slab S6 in which cracks formed outside the test region (the middle 50x50 mm square).

The rotation of the Eyepiece's micrometer results in the movement of one of two parallel hairs fitted to the eye-piece, relative to the other (fixed) hair. Thus, the width of a particular crack could be measured by measuring the distance between the two parallel hairs after positioning each one of them to coincide with one side of the crack as shown in

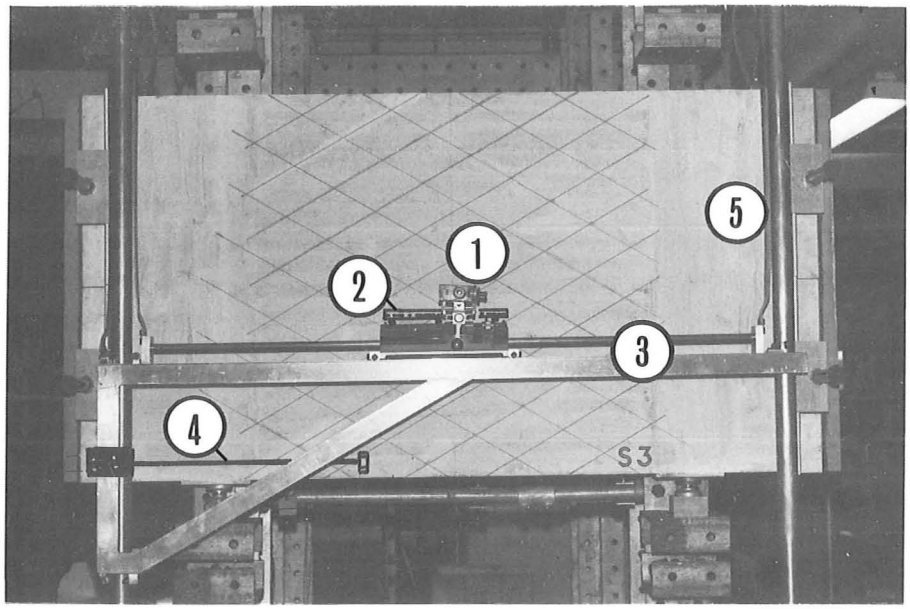

(a)

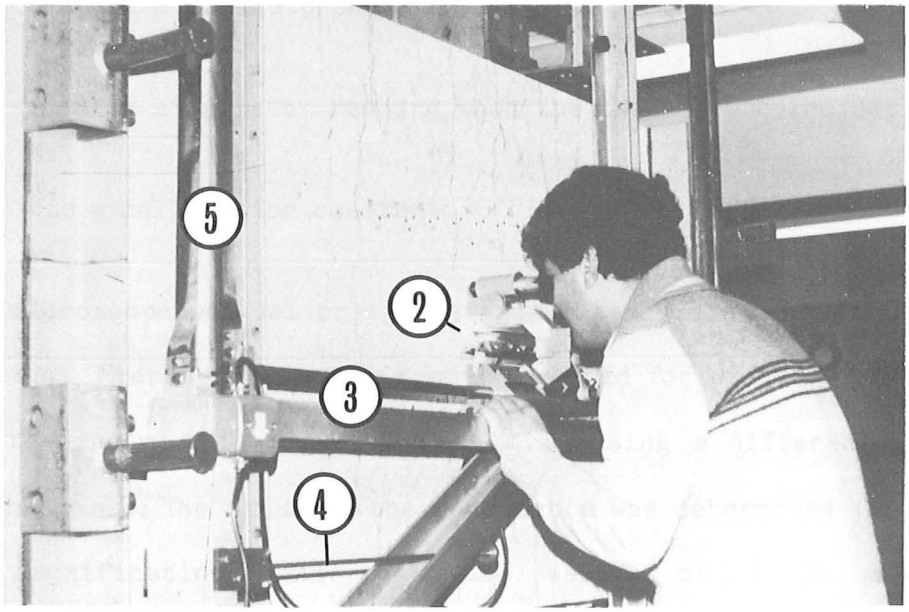

(b)

(1) Micrometer eyepiece.

(2) Strip-light Illumination.

(3) Microscope track.

(4) Brake lever (vertical movement).

(5) Independent microscope frame.

Figure 4.5-5 Microscope and microscope frame.

Figure 4.5-6. This was done by lining up the fixed hair with one side of the crack using the microscope fine movement and then, using the micrometer, moving the other hair to the other side of the crack. The micrometer reading could then be converted into a crack width using a calibration linear equation of the type

$$\left.\begin{aligned} W &= m(R - R_o) \\ \text{or} \qquad W &= m \times \Delta R \end{aligned}\right\} \qquad \ldots (4.5\text{-}1)$$

where

W is the crack width;

R is the micrometer reading;

R_o is the micrometer reading when the two hairs coincide; and

m is a calibration constant.

The microscope was calibrated using a glass scale marked in 1/10 of a mm divisions. Micrometer readings were recorded for widths of 0.1, 0.2, ... 0.8mms on the scale; this was repeated twice using a different starting point on the scale. The value of the constant m was determined for each of the two magnifications and took the values of 1/130 and 1/365 respectively. The micrometer readings were estimated to half a division i.e. 0.005 mm, this corresponds to a width of about 0.0014 mm for the 36.5X magnification.

Crack width at any point on the tension face of an r.c. element is affected by the proximity of the reinforcing bars. If now we consider the slab element with skew widely-spaced reinforcement shown in Figure 4.5-7,

a strip controlled by a minimum cover c will exist over each bar. The width of this strip was taken to be half the spacing of the bars. The two sets of strips (influenced by the two sets of bars) will intersect forming the four regions illustrated in the figure. The regions were designated jk where j and k are labels describing the positions of the two sets of grid lines running in the direction of steel sets 1 and 2 respectively. The labels j and k can either be the letter 'A' for a grid line above a steel bar or the letter 'B' for a grid line midway between bars. Thus, a region of type AB is a region above a steel bar of set 1 and midway between bars of set 2 and so forth as illustrated in the figure.

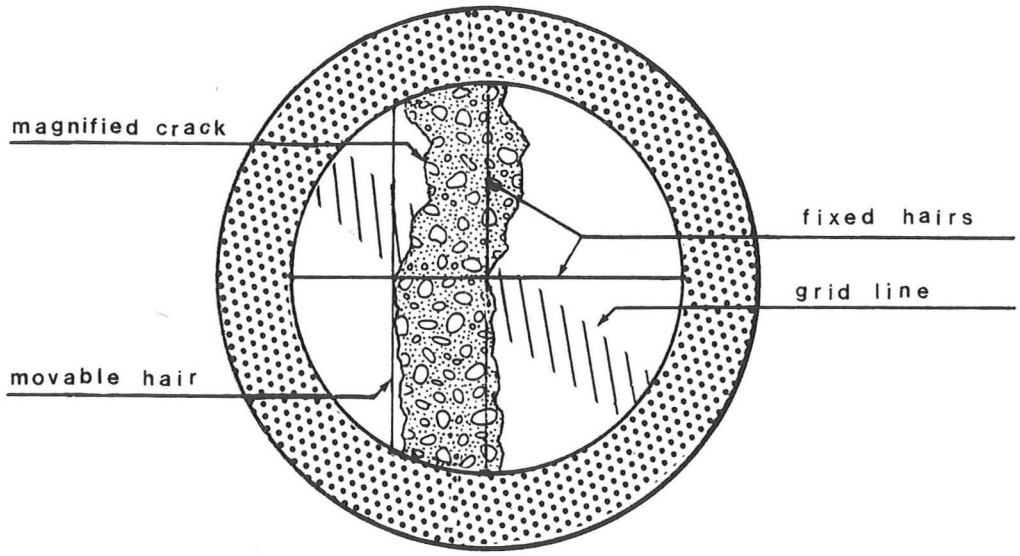

Figure 4.5-6 A typical crack profile as seen under microscope.

Cracking in regions of type AB and BA is affected by the proximity of bars of sets 1 and 2 respectively. In a region of type AA, cracking is

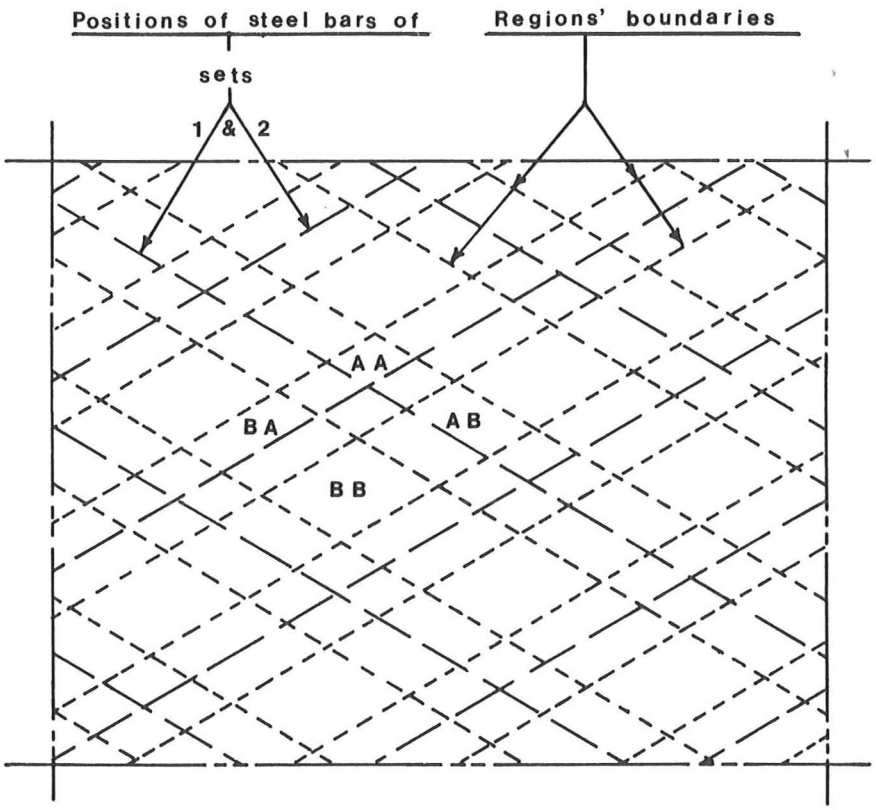

Figure 4.5-7 A slab element with skew widely-spaced reinforcement.

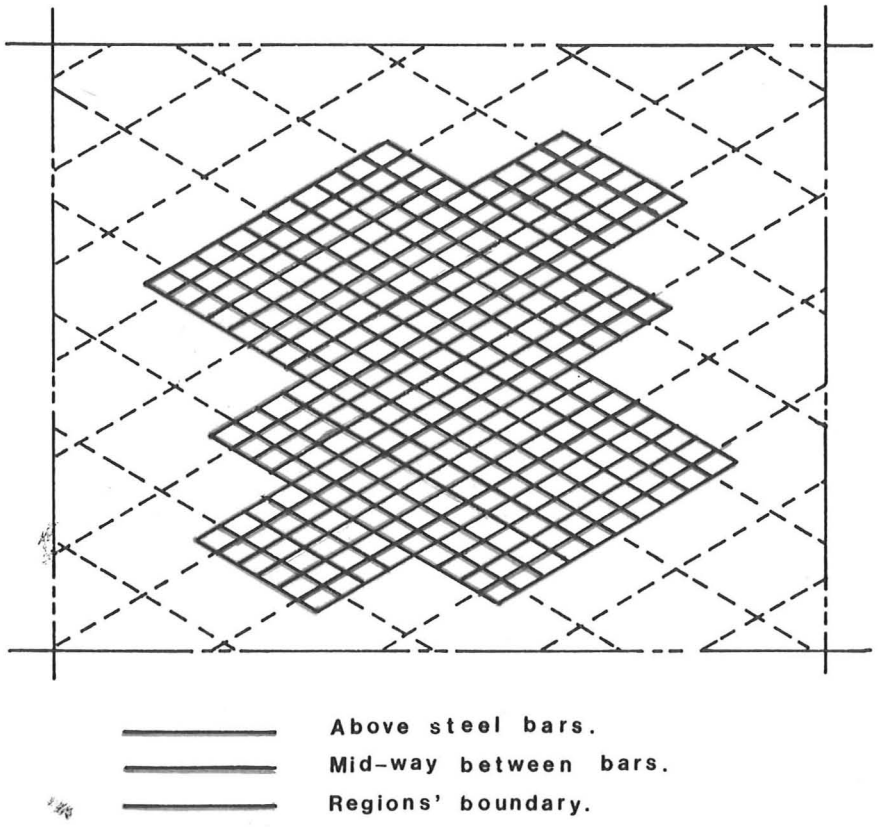

Figure 4.5-8 Grid lines marked on the tension face.

influenced by both sets of bars while a region of type BB is far from the influence of either set of bars. In the actual tests, wider cracks were found in regions of type BB and narrower ones in regions of type AA as was expected.

One of the objectives of the experimental work was the study of cracking in each of these regions. Blue lines defining the boundaries of these regions were marked on the tension face of the specimen. Grid lines were marked along the line of each reinforcing bar (the red lines) and midway between the bars (the green lines), for each steel direction as shown in Figure 4.5-8. At each load stage, the width of each crack, in a direction perpendicular to the general crack direction, was measured where it crossed each of these grid lines (the red and the green lines) inside the test region.

The cracks were not straight-edged, they had a rather rough (zig-zag) profile with the general direction being perpendicular to the principal bending direction. In most cases, the crack edges took a shape similar to that shown in Figure 4.5-6. Having cracks with rough edges was of an advantage as far as lining up the hairs to the edges was concerned: with the two edges having identical and parallel profiles, it was easy to line up the hairs with the crack edges, accurately and in the right position, as it can be seen from Figure 4.5-6. Nevertheless, in few cases, we were met by other types of crack profile, examples of these profiles are shown in Figure 4.5-9. Cracks with the first of these profiles (i.e. perpendicular to the grid line -- Figure 4.5-9a) accounted for 10.5% of the total number of crack measurements in Slab S5. Cracks running for a short distance along the grid line (Figure 4.5-9b) accounted for 7.9% of the total number of crack measurements at the same stage in slab S5; however, a

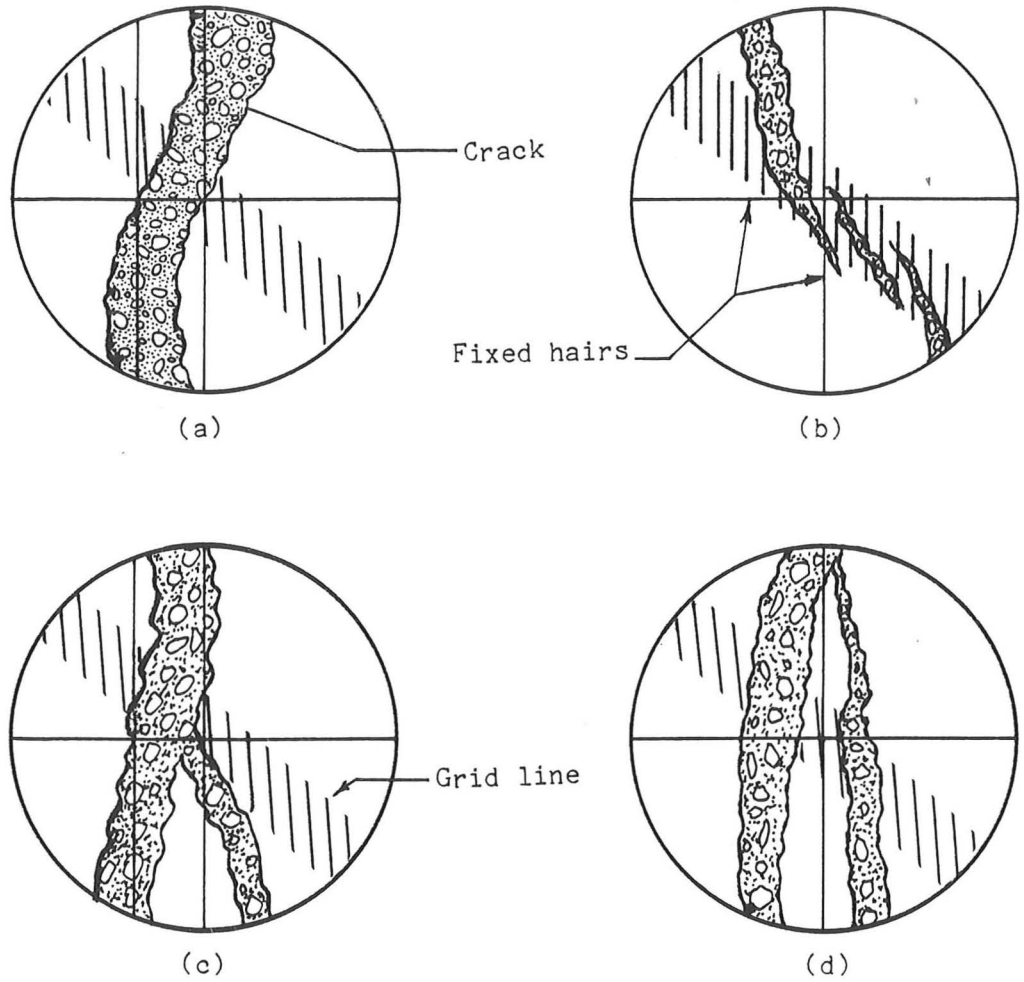

Figure 4.5-9 Examples of less commonly encountered crack profiles.

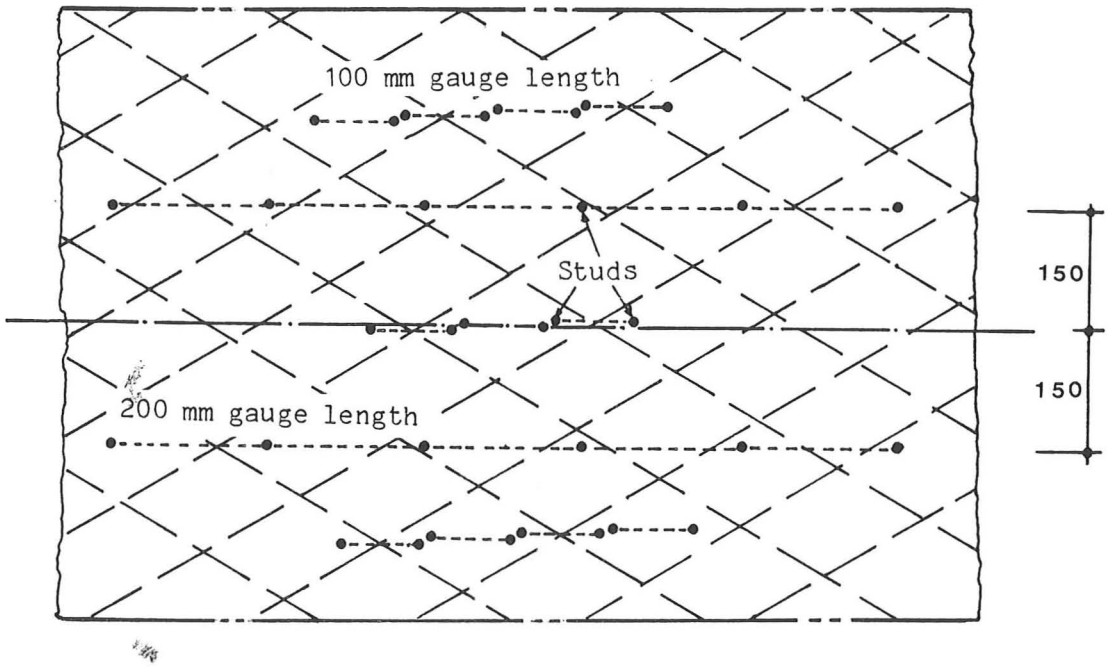

Figure 4.5-10 Strain gauge arrangement on the tension face.

lower percentage (2.7%) for this type of profile was found in the case of slab S3 — the total number of cracks at this stage in Slab S3 was twice as that at a similar stage in slab S5. It is interesting to know that this second profile of Figure 4.5-9b was found to be running always along a grid line which was over a steel bar, whereas in the case of cracks with the first profile, it did not matter which grid line it was formed at.

In some cases where a crack was branched just over the grid line (over steel bars), the width of this crack was measured at a position where the crack is not branched (position 1 in Figure 5.4-9c). If a crack was branched at a point away from the grid line, then it is treated as two cracks as shown in Figure 4.5-9d. Very few cracks were obscured by excessive damage being done to the concrete, in such cases, if any, the crack width was measured at the nearest clear portion of the crack within a distance of $\pm$ 5 mm from the grid line.

In general, the crack width was always measured horizontally i.e. in the principal bending direction. Great consideration was taken in choosing the position at which a crack was to be measured, and so far as possible, this crack was measured at the same position at successive load stages. This was made possible by the rough profile of the cracks since in most cases the profile was memorable.

4.5.4 Strains

The compressive strains were measured along two lines, perpendicular to the general crack direction, by means of a Demec gauge on 200mm gauge lengths as shown in Figure 4.5-4. The surface tensile strains were measured in two different ways. The first way which is the same as the above one was used in slab S0. The second consisted of using two Demec gauges on two

independent gauge lengths that were located alternately in the middle of the regions of types AA and BB that lie along two lines perpendicular to the general crack direction (see Figure 4.5-10). The gauge lengths varied from one slab to the other depending on the region size (200 mm in slab S1, 100 mm in S2 and S3N, and 50 mm in S4, S5, and S6). The second way was used in slabs S2, S3O, and S4 while both ways were used in slabs S1, S3N, S5, and S6.

The measured strains gave information which allowed calculation of the average surface strains, the neutral axis depth and the average curvature for each load stage.

4.6 Test Procedure

A set of zero readings was first taken on the strain and dial gauges and on the load cells. A load was then applied to give a bending moment of about a quarter of the calculated cracking moment. After each increment of load, the readings of the load cells and of the dial and the Demec gauges were recorded. This procedure was continued until the slab had cracked. After cracking, the load was increased in a number of stages, which depended on the progress of cracking, to just below the calculated failure load. The slabs were not tested to failure since the resulting very deformed slabs would have been difficult to handle and since the actual failure was of no particular interest to this investigation.

It is important to have a curvature which is invariant with time during each crack width measuring process, so that the measured crack widths will correspond to the same average tensile strain. In these experiments, the deflection gauge readings were kept more or less constant

at each load stage. To do this, the load should be decreased slowly with time to allow for the creep effect. This was achieved automatically as a natural result of the way in which the rig functions. Under the effect of creep the slab curvature increases i.e. the deflections at the four loading points increase resulting in a decrease in strain in each of the stressing strands and hence a decrease in the applied load. Deflection and strain readings taken at the end of the crack width measuring process showed a very slight difference from those taken at the start.

After each increment of load in the post-cracking stage, the initial readings of the load cells, the deflection and strain gauge readings and the intermediate readings of the load cells were successively recorded. All the cracks visible on the surface were then marked in by painting alongside the cracks with a coloured pen while taking care not to obscure any crack. At each subsequent load stage, the cracks that appeared were marked with a different colour, so that the development of the crack pattern could easily be studied from the coloured photograph that would be taken of the slab after the test (in slab S30 cracks were traced before taking any deflection or strain measurements). The crack widths were measured at three or four of the load stages. A crack width measuring process at a typical load stage took about 3 hours (not including time needed for the eye to rest). Another set of readings of dial and strain gauges and of load cells followed each set of crack width measurements. Finally the crack pattern was photographed for record purposes.

Each test was completed in about seven working days except slabs S5 and S6 which took 3 and 2 days respectively.

4.7.1 Computer programs

Two computer programs were written for the University Computer IBM 370 to carry out the analysis of the experimental data as described below and to plot the results as presented in Chapter 5. The first of these programs dealt with loads, deflections, and strains, while the other dealt with crack width data.

4.7.2 Loads

The initial and intermediate load cell readings (taken before and after recording the deflection and strain gauge readings) were slightly different and well within $\pm$ 5% of each other in the post-cracking stage. Thus, the average load was used to obtain the applied bending moment by multiplying this average load by the lever arm (300.0mm).

During the process of crack width measurements, the load was allowed to gradually drop down, as explained in Section 4.6 above, in order to maintain constant curvature. The final load cell readings that were taken at the end of each crack-measurement process, were always within 10% of the initial load. However, the applied load continued to fall after this until the next load increment was applied i.e. overnight. The loads recorded before a new load increment is applied, were within 25% of the initial load of the previous increment.

With this relaxation of load due to creep in concrete, it was felt necessary that the stress-strain relation for concrete in compression has

to be modified when used in theoretical calculations, so that it gives the long term response.

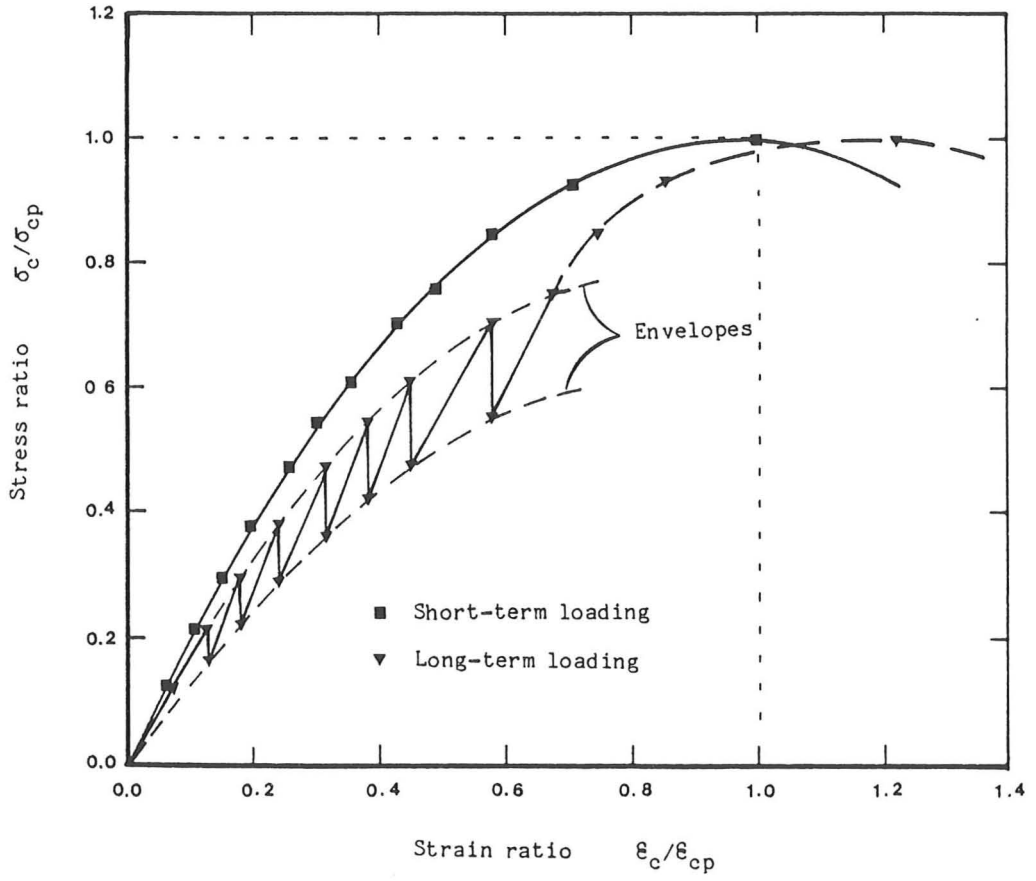

Figure 4.7-1 Long- and short-term stress-strain relations for concrete in compression (average of 3 tests).

In order to find out more about the properties of concrete in compression under long term loading, compression tests were carried out on six 200x100 mm diameter cylinders made out of the same concrete mix as the slabs. Three of these cylinders were tested in a manner similar to that in which the slabs were tested i.e. the load was applied in increments at periods of time similar in length to those in the slab tests during which the strain was held constant and thus due to creep the load fell down. This meant that the stress-strain relation had both an upper and a lower envelope as in the experimental moment-curvature relation of which the

upper envelope is the one presented in Chapter 5. Therefore, the upper envelope of the long term stress-strain relation for concrete in compression (Figure 4.7-1) was used in calculating the theoretical curves described in Chapter 5 (Subsection 5.3.2). Each of the other three concrete cylinders were tested in the usual manner (i.e. under short term loading) immediately prior to one of the long term tests and using the same machine.

The ratio of the long term stress to the short term stress for a given strain level was found to be equal to 0.84 (an average of three tests). Hence, the long term response for the concrete of any of the slabs was obtained from the short term properties for that slab by multiplying the stress by 0.84.

4.7.3 Deflections

The readings of the deflection gauges at either side of mid-span were averaged and then subtracted from the deflection gauge reading at mid-span in order to obtain the relative mid-span deflection. This was done at two positions, at mid-breadth and near the edge of the slab, in the case of slabs S0, S2, S30, and S4. The relative mid-span deflections at each of these two positions fell within $\pm$ 6% of the average relative mid-span deflection (see Figure 4.5-4). In slabs S1, S3N, S5, and S6, the relative mid-span deflection at each of the three positions, at mid-breadth and at quarter-breadths, fell within $\pm$ 12% of the average value.

The curved slab in the constant moment zone was considered to have a cylindrical surface the radius of which, and thus the average curvature, was found from the measured relative mid-span deflection by applying simple geometry rules.

4.7.4 Strains

The strain readings were averaged along each gauge line. These average strains were used to calculate the average curvature, over the constant moment zone, using the measured thickness of the slab and allowing for the thickness of the Demec disc. The average strains were also used to calculate the neutral axis depth over the constant moment zone (for slabs S0, S1, S3N, S5, and S6).

The above values were also calculated for each type of the two types of region AA and BB (over and midway between the steel bars) for all the slabs except S0. Comparing the average curvatures for regions of type 3 and 4 showed little difference in most of the slabs. The number of regions over which strains were measured was small (less than 10 regions for each type) and the gauge length was shorter than that on the compression face and differed from one slab to another. It was therefore decided that the average curvature over the constant moment zone should be used for slabs S2, S4, and S30.

The variation between strains measured at any load stage in the post-cracking phase was reasonable for strains measured over a long gauge length (200mm). On the compression face, the maximum and minimum strains fell within $\pm$ 10% for slabs S0, S2, and S30; within $\pm$ 15% for slabs S1 and S3N; within $\pm$ 20% for S4; and within $\pm$ 45% for slab S5. In slab S5, cracks first appeared on the right side of the tension face and progressed towards the left side.

It was decided that the average values of the neutral axis depth and the surface tensile strain should be calculated, for all the slabs, using the average compressive strain and the curvature derived from the

4.7.4 Strains

The strain readings were averaged along each gauge line. These average strains were used to calculate the average curvature, over the constant moment zone, using the measured thickness of the slab and allowing for the thickness of the Demec disc. The average strains were also used to calculate the neutral axis depth over the constant moment zone (for slabs S0, S1, S3N, S5, and S6).

The above values were also calculated for each type of the two types of region AA and BB (over and midway between the steel bars) for all the slabs except S0. Comparing the average curvatures for regions of type 3 and 4 showed little difference in most of the slabs. The number of regions over which strains were measured was small (less than 10 regions for each type) and the gauge length was shorter than that on the compression face and differed from one slab to another. It was therefore decided that the average curvature over the constant moment zone should be used for slabs S2, S4, and S30.

The variation between strains measured at any load stage in the post-cracking phase was reasonable for strains measured over a long gauge length (200mm). On the compression face, the maximum and minimum strains fell within $\pm$ 10% for slabs S0, S2, and S30; within $\pm$ 15% for slabs S1 and S3N; within $\pm$ 20% for S4; and within $\pm$ 45% for slab S5. In slab S5, cracks first appeared on the right side of the tension face and progressed towards the left side.

It was decided that the average values of the neutral axis depth and the surface tensile strain should be calculated, for all the slabs, using the average compressive strain and the curvature derived from the

deflection readings.

The curvature calculated using the averaged strain measurements was used as a check only: the agreement was quite good and difference percentage ranged from 0% to 10%.

Detailed results on strain analysis and tension stiffening will be presented in Chapter 5.

4.7.5 Crack Data

The total number of crack width measurements in this experiment (slabs S0, S1, S2, S3N, S4, and S5) was over four thousand two hundred (4200). This means that an average of 200 measurements were taken at a typical load stage.

For each of the slabs S1 to S5, cracks were divided into two sets according to the direction of the grid lines at which the cracks were measured. The cracks in each set were classified in two different ways. The first way was to divide those cracks into four groups according to the region to which they belong. The second was to divide the cracks of one set into two groups: one for cracks over, and the other for cracks midway between steel bars as in slab S0.

Each crack width that was measured during a given load stage was divided by the relevant value of the average surface tensile strain in the principal moment direction. Then, by using a sorting routine, the values of crack widths divided by strain exceeded by 2, 5, 7.5, 10, 15, 20, 25, and 50% of the results were extracted; the average value was also calculated. This was done for each of the 12 groups of cracks mentioned above.

The average crack spacing in a particular type of region was calculated by dividing the sum of the components, in the principal moment direction, of the parts of grid lines that crossed the regions of that type by the number of cracks crossing those parts of the grid lines.

The detailed crack-width results will be presented in Chapter 6.

5. PRESENTATION OF TEST RESULTS: TENSION STIFFENING

5.1 Introduction

This chapter deals with the presentation and discussion of the results from the tests described in the previous chapter that have relevance to the tension stiffening phenomenon and ways of representing it. These data are: the properties of materials, loads, strains, and curvatures in addition to the geometrical dimensions of the cross section and the arrangement of the steel. The other data from the tests, i.e. crack width measurements, will be presented and discussed in Chapter 6.

5.2 Computer Programs

Two computer programs were written for the University Computer IBM 370. The first of these programs was an extension of the relevant program mentioned in Subsection 4.7.1. Its task was to carry out further analysis on the test data that have connection with tension stiffening as will be described in detail in the following sections. The program also carried out theoretical analysis based on the classical no-tension theory and on the theory presented in Chapter 3.

The second program made use of the University Computer Graphics Library to plot graphs of the different relationships that were found

using the first computer program. The graphs are presented and discussed in the remaining part of this chapter.

5.3 Moment-curvature relations

The dimensionless experimental and theoretical moment-curvature relations for each of the slabs S0 to S6 are shown in Figures 5.3-1a to 5.3-8a. The bending moment is taken as a ratio of the simplified theoretical cracking moment M_{crs} equal to $f_t bh^2/6$ and the curvature is taken as a ratio of the inverse of the slab thickness h. Note that S0 is the slab with the angle δ (between the reinforcement direction and the principal bending direction) equal to 0^o, S1 is the slab with $\delta = 10^o$ and so forth; slab S3N is a repeat of slab S30 and both have $\delta = 30^o$.

5.3.1 Experimental curves

The experimental load cell readings used in calculating the bending moments are those averaged from readings recorded before and after taking the deflection and strain gauge readings -- upon application of the load increment. However, during the processes of crack width measurements or when the slabs were left under load overnight, the load was left to drop down in order to maintain constant curvature. Hence, the stress-strain relation of concrete in compression has to be modified when used in the theoretical calculations so that it gives the long term response. This modification was achieved as described in Subsection 4.7.2 of the previous chapter.

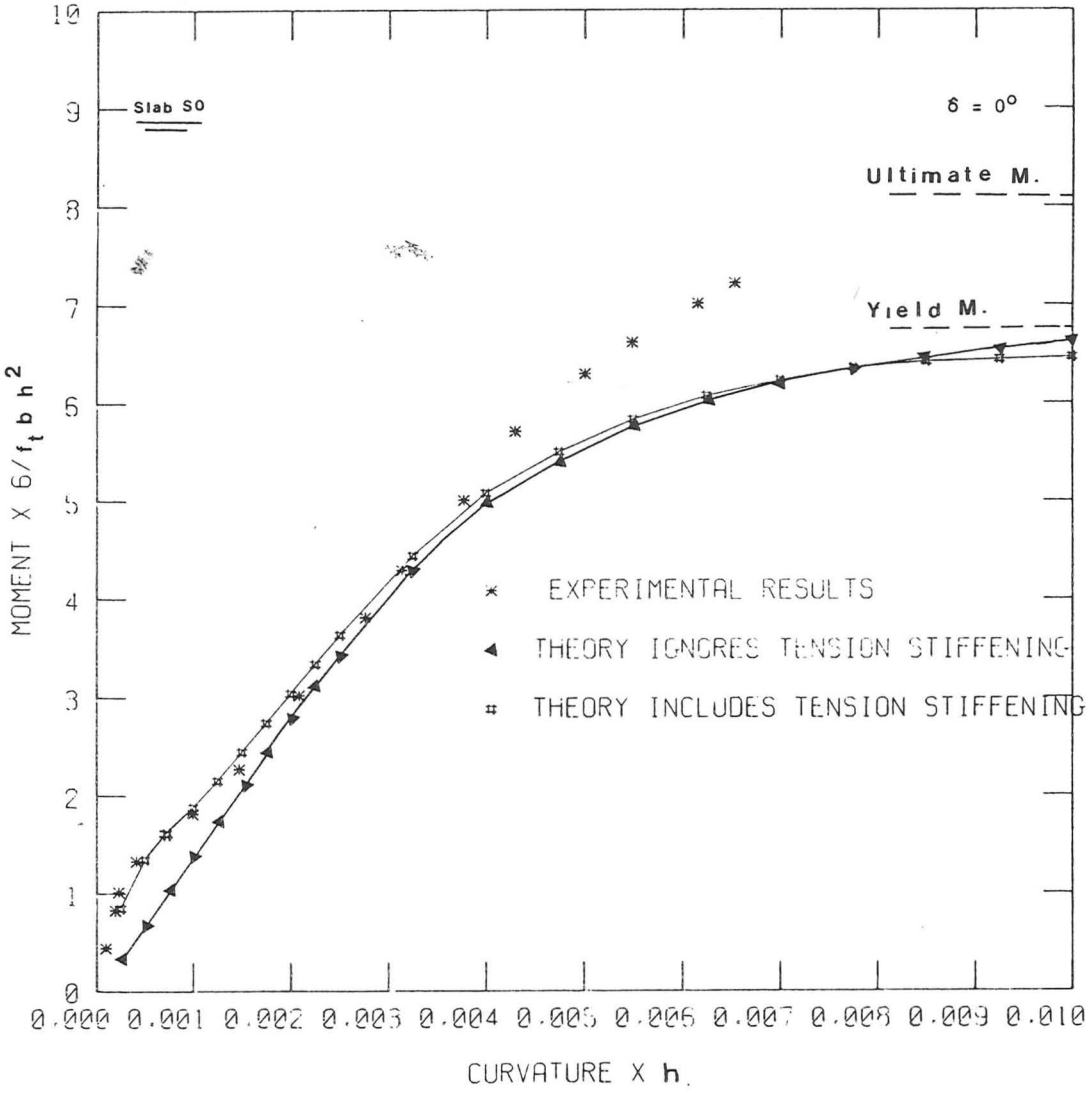

'a'

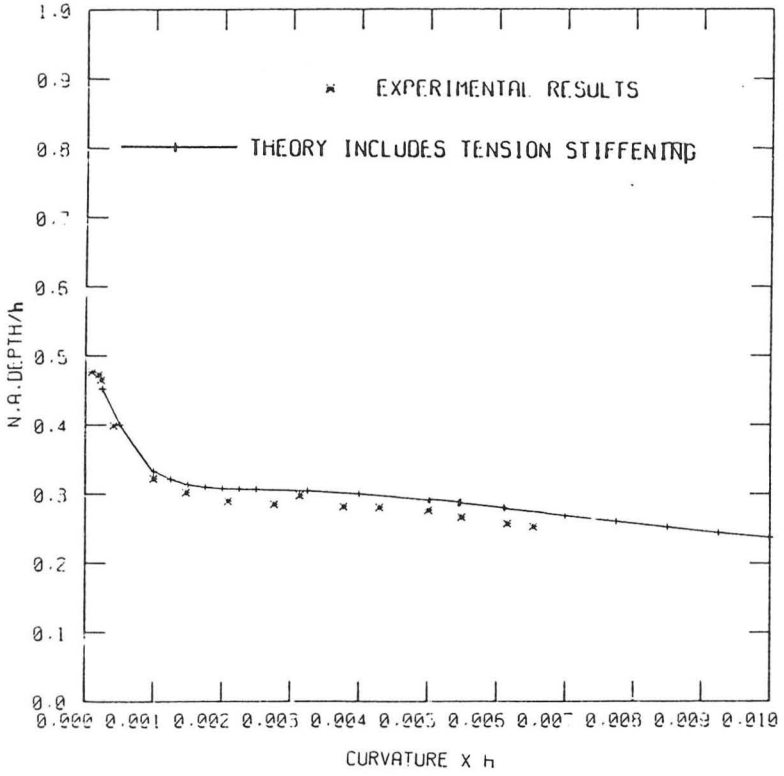

'b'

Figure 5.3-1 Experimental and theoretical moment-curvature and n. a. depth - curvature "χ" relationships or slabs S0 and S6.

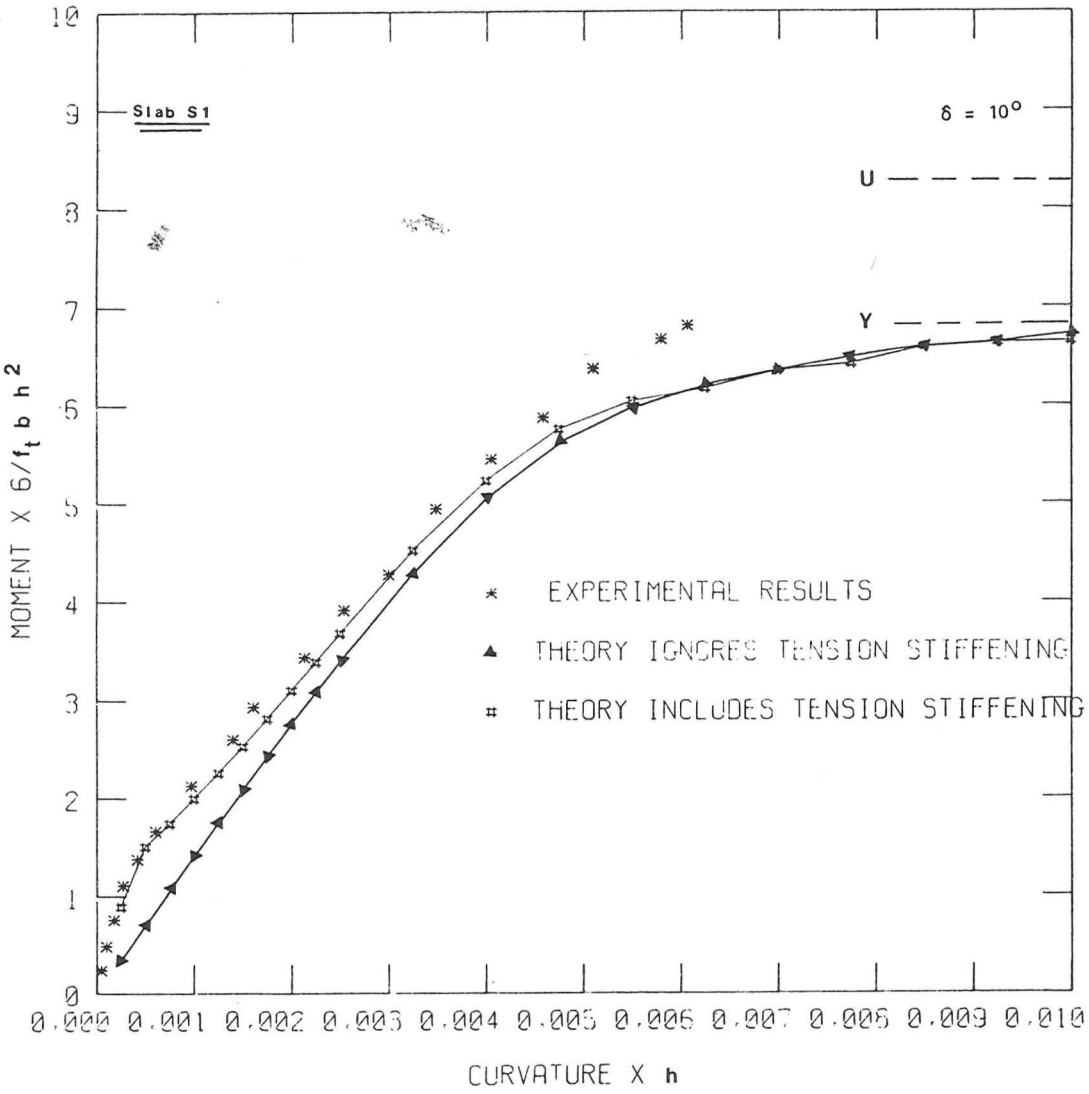

'a'

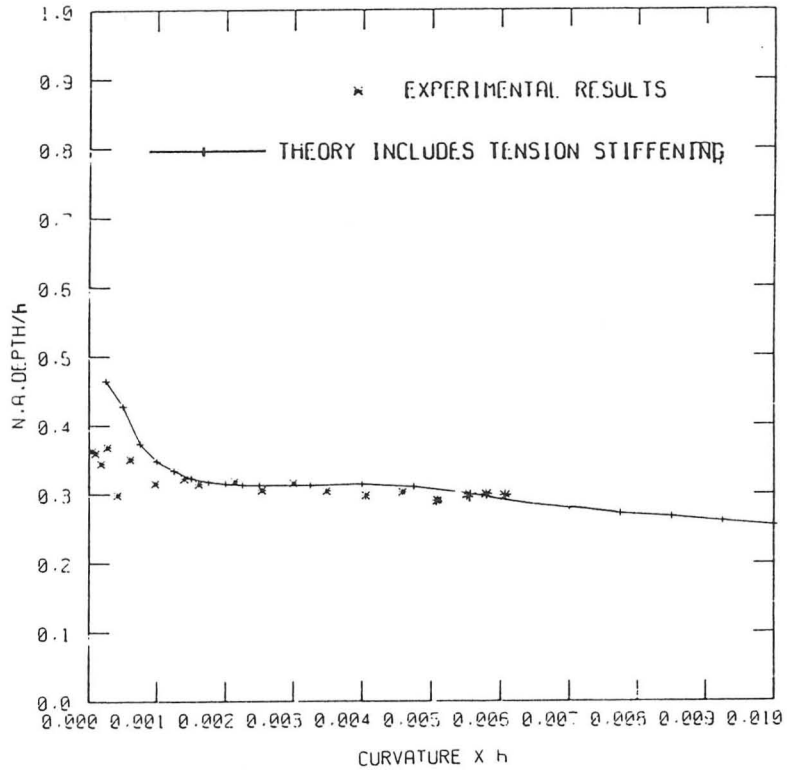

'b'

Figure 5.3-2 Experimental and theoretical moment-curvature & n a depth - relationships for slabs S1.

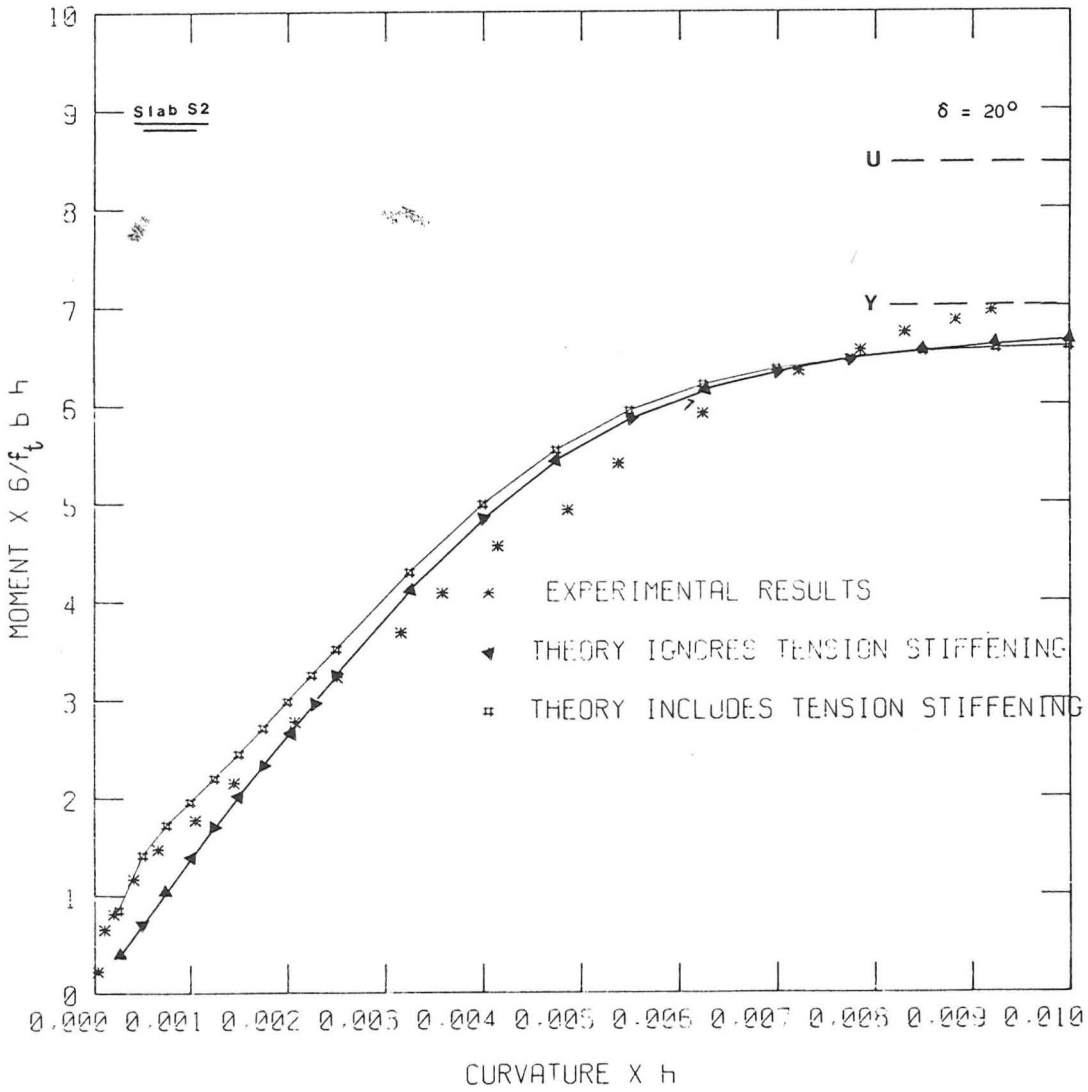

'a'

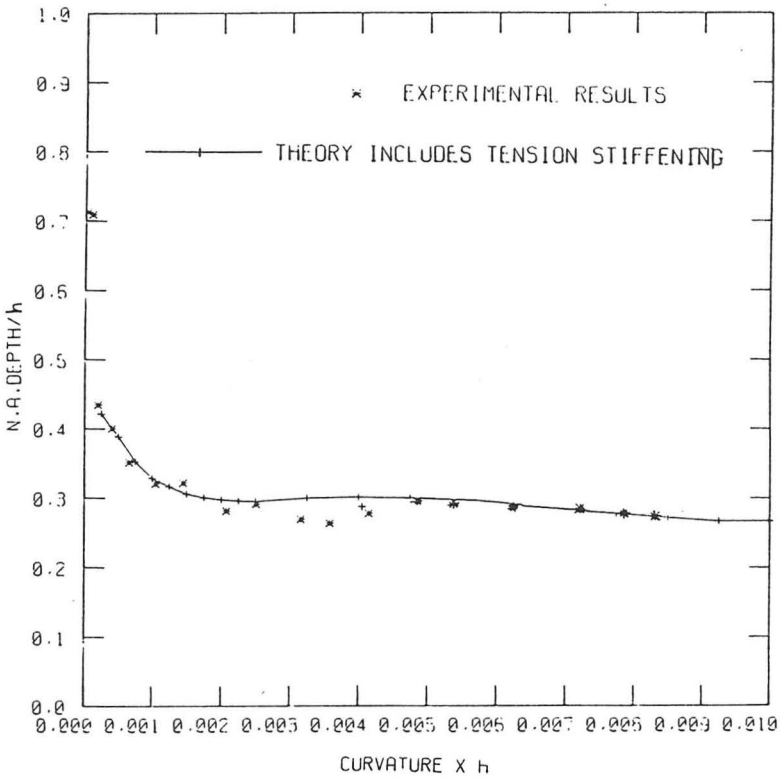

'b'

Figure 5.3-3 Experimental and theoretical moment-curvature & n. a. depth – $\mathcal{K}$ relationships for slab S2.

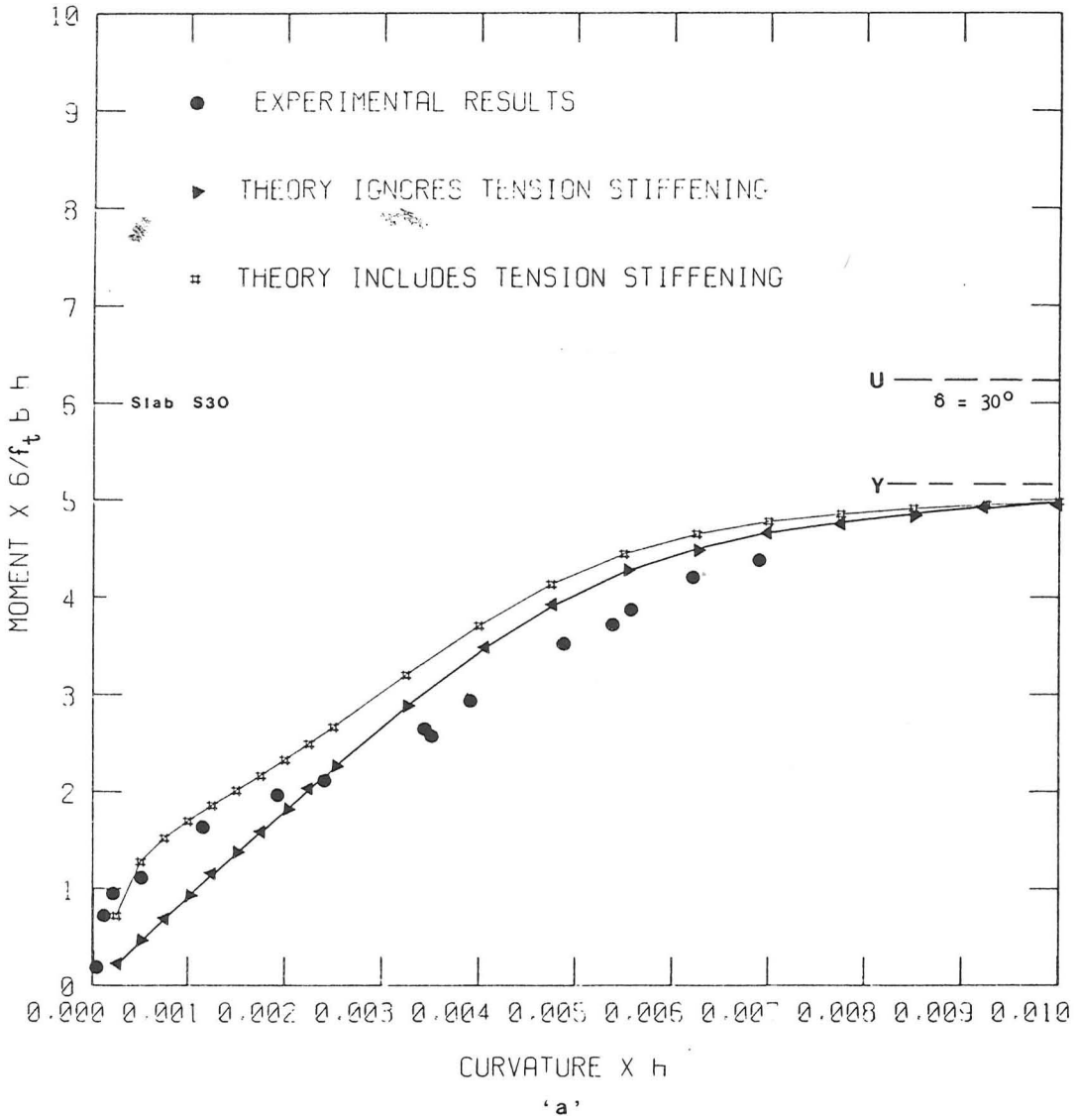

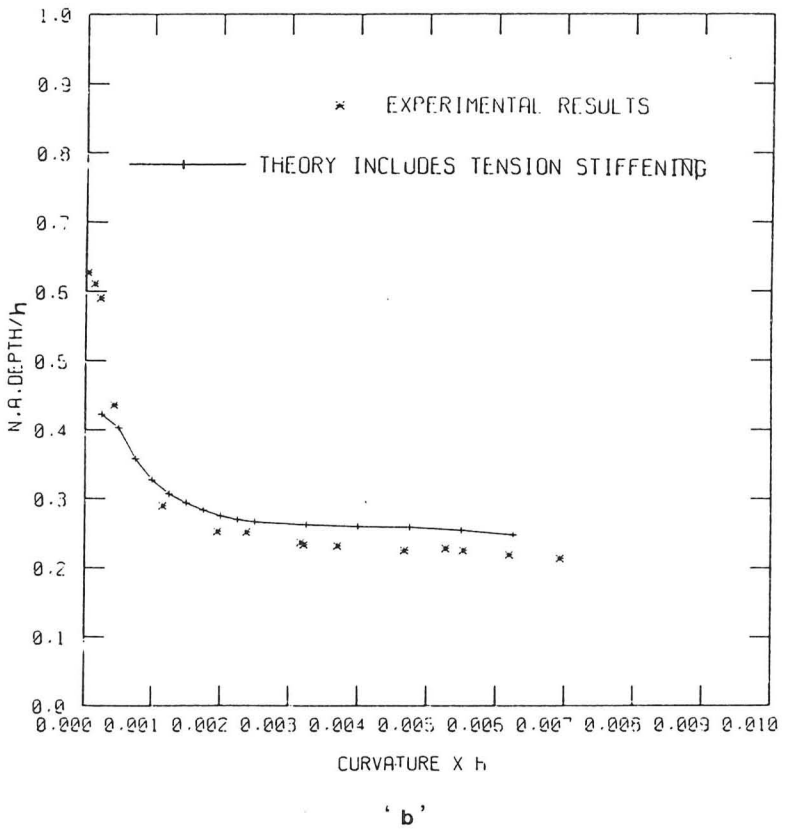

Figure 5.3-4 Experimental and theoretical moment-curvature & n. a. depth – curvature relationships for slab S30.

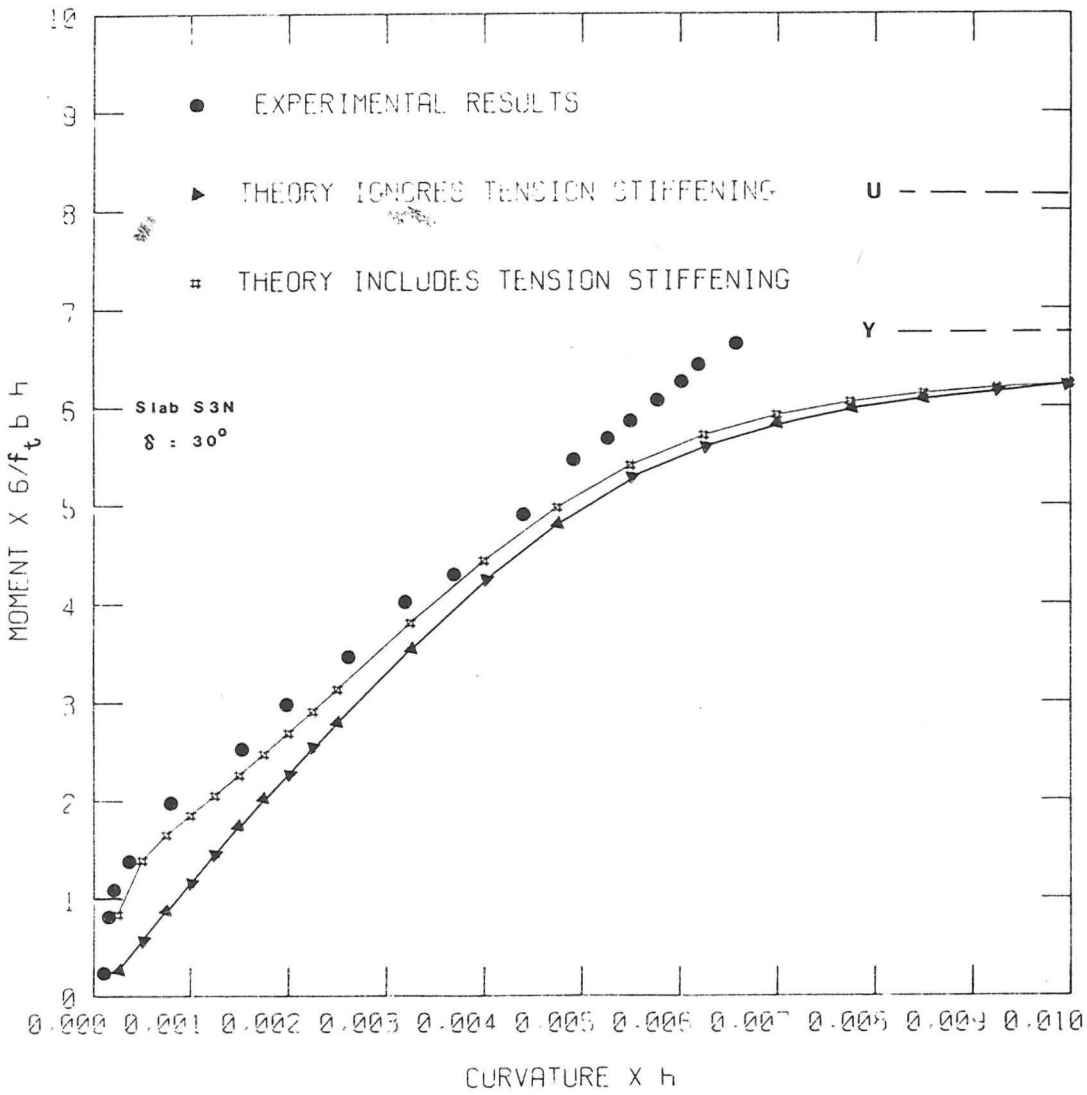

'a'

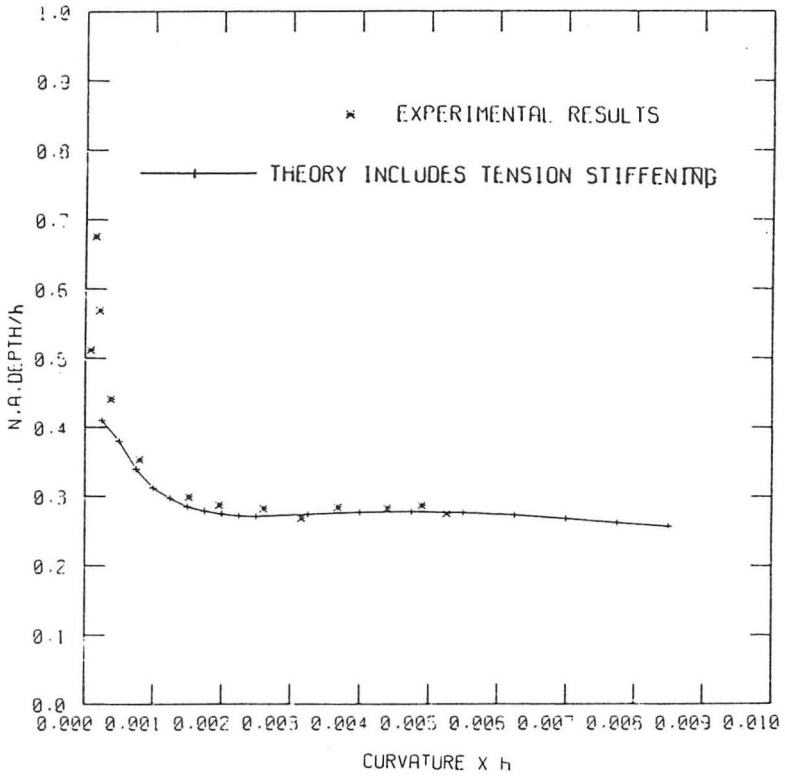

'b'

Figure 5.3-5 Experimental and theoretical moment-curvature & n. a. depth -curvature relationships or slab S3N.

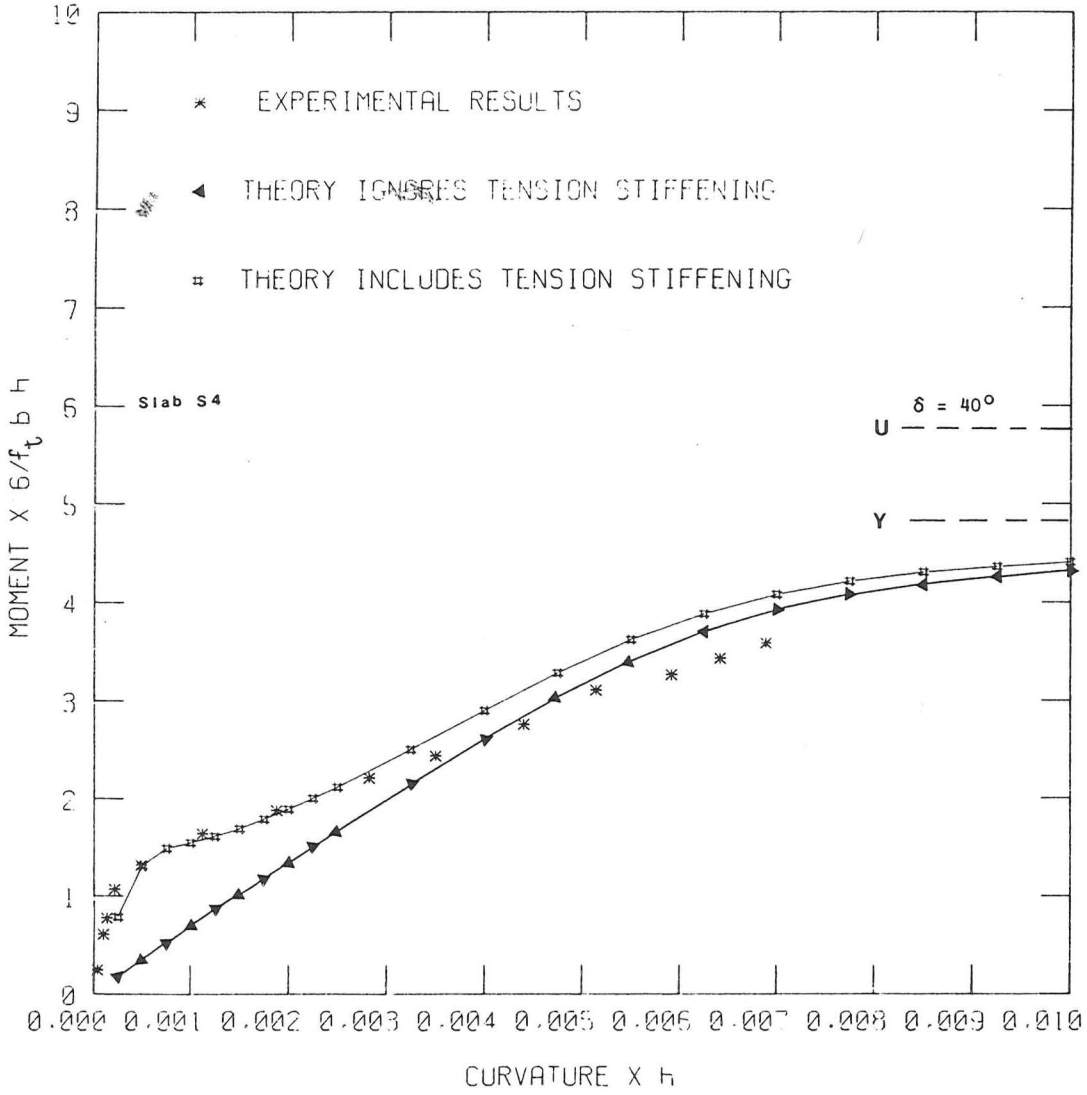

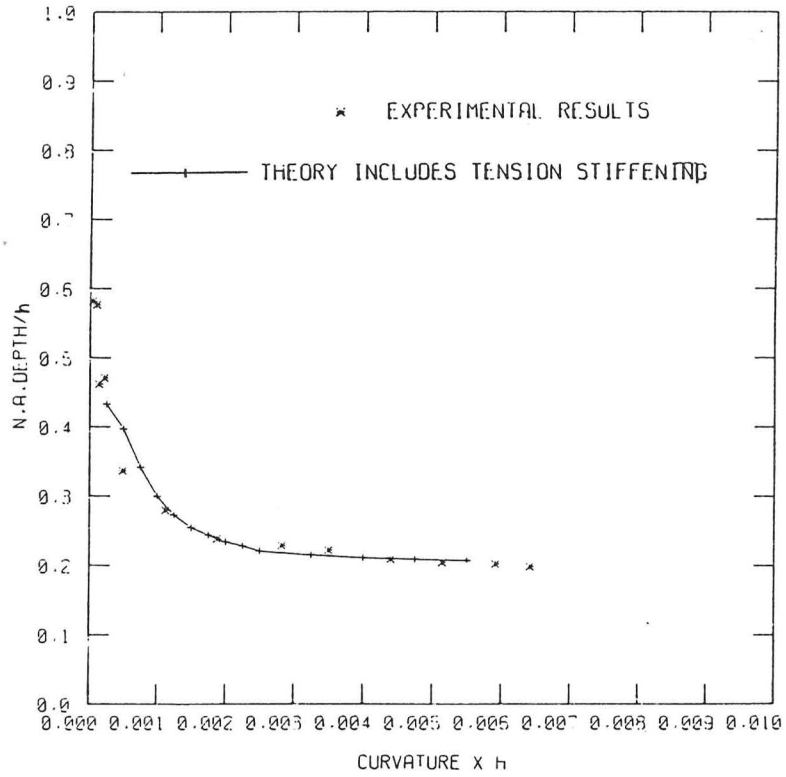

Figure 5.3-6 Experimental and theoretical moment-curvature & n.a. depth-curvature relationships for slab S4.

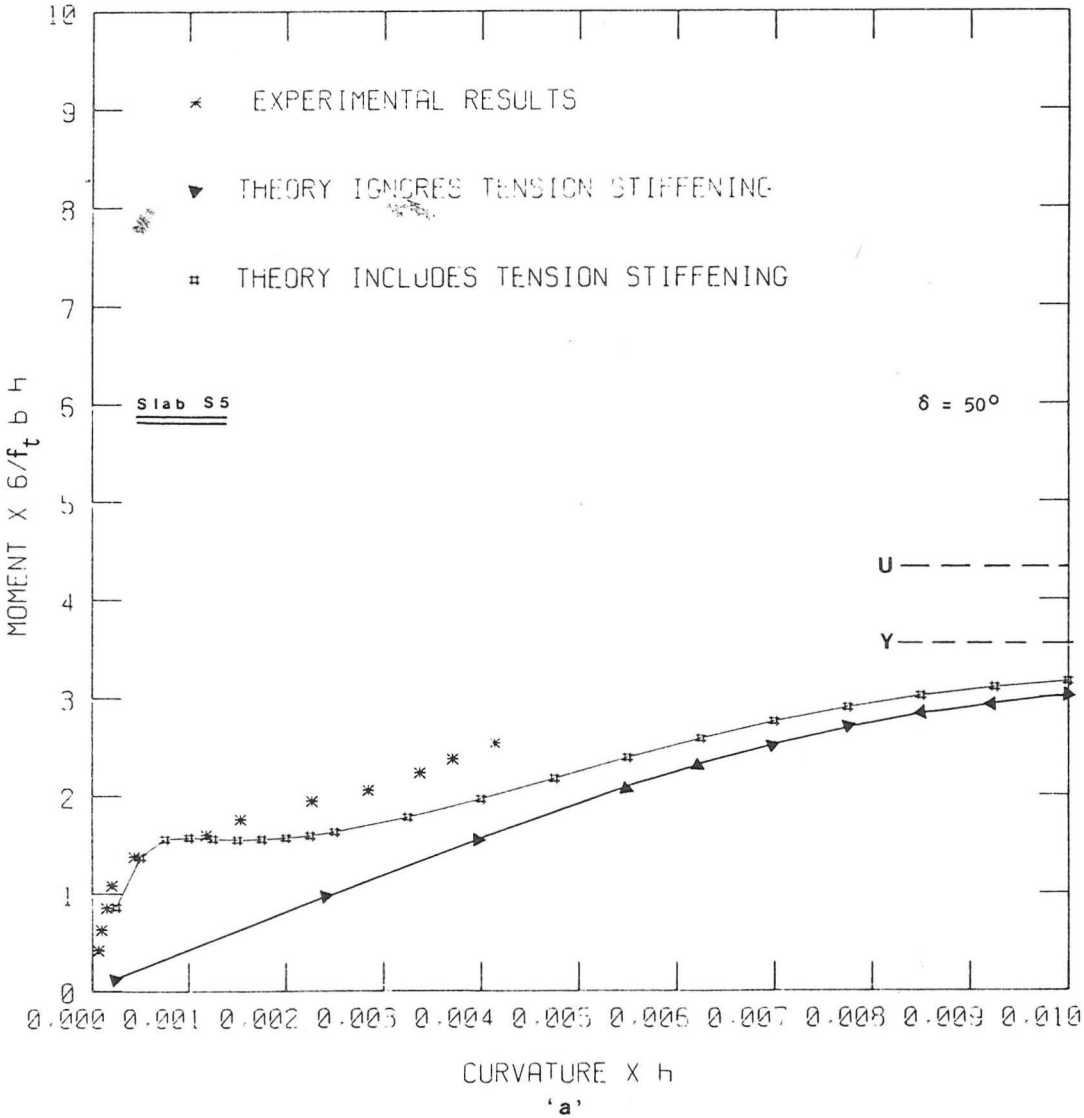

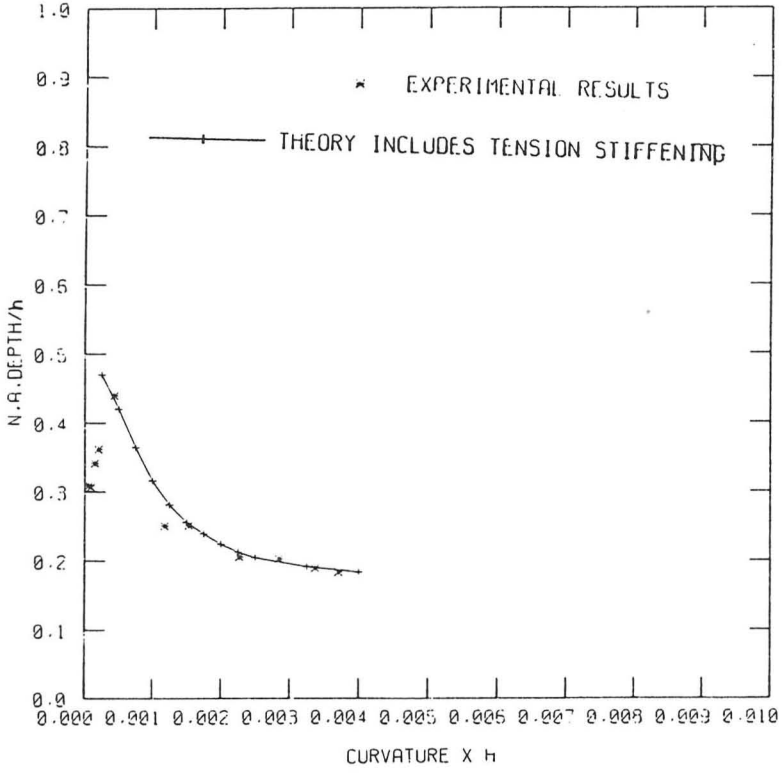

Figure 5.3-7 Experimental and theoretical moment-curvature and n. a. depth -curvature relationships for slab S5.

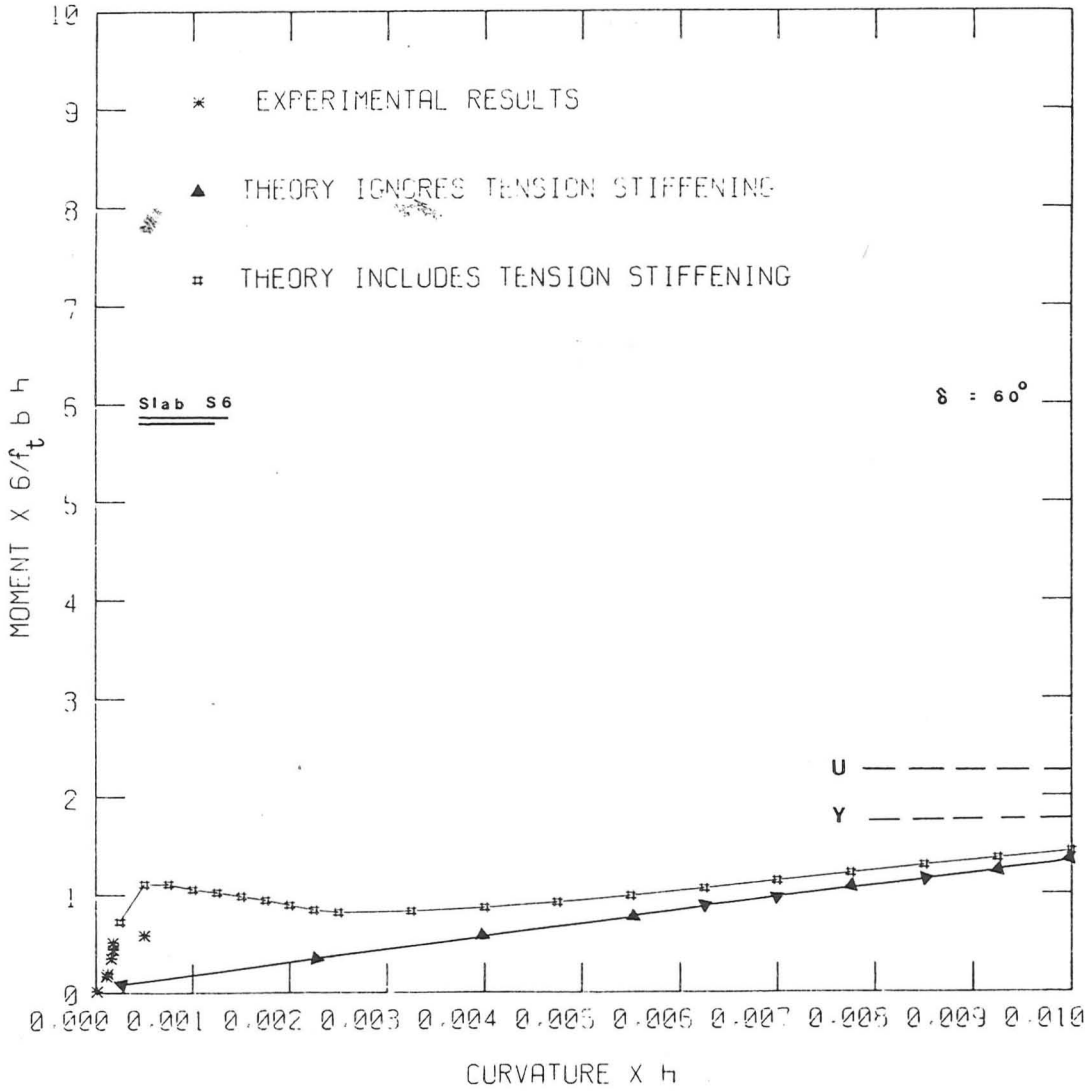

'a'

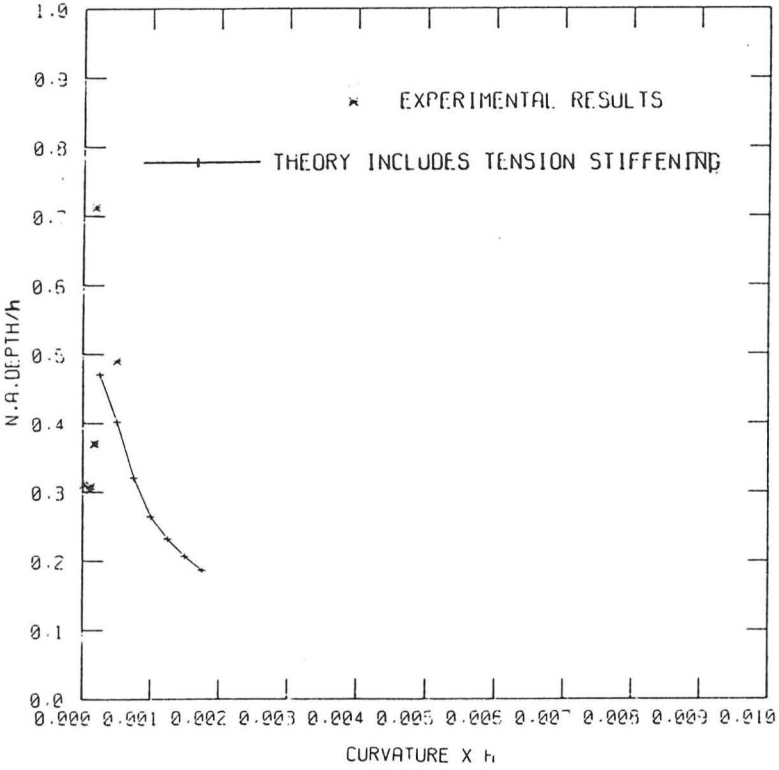

'b'

Figure 5.3-8 Experimental and theoretical moment-curvature and n.a. depth - χ relationships for slab S6.

The experimental curvatures are those obtained from the deflection measurements: the curvatures obtained from the strain gauge readings were used only as a check. The agreement was quite good for all the slabs and the difference between the two curvatures at any load stage fell within $\pm$ 5% of the average curvature.

5.3.2 Theoretical curves

Two theoretical moment-curvature relations are presented in each one of the graphs in Figures 5.3-1a to 5.3-8a. In the first of these theoretical curves, the tension stiffening of concrete in the tension zone was neglected -- this is the classical no-tension theory. In the other theoretical curve, the tension stiffening effect was allowed for using the concept of the 'enhanced stress'-strain relation for the tension steel developed in Chapter 3.

The theoretical moment-curvature curves were found by calculating the values of the bending moment that correspond to assumed values of the curvature according to the following procedure.

-I- Tension stiffening is neglected

The curvature is increased in suitable increments and the following steps are carried out for each curvature:

(1) An initial estimate of the neutral axis depth is calculated using the classical no-tension concept and allowing for non-linearity in the material properties. The secant moduli from the previous stage are used in this calculation.

(2) The strains in the principal moment direction are assumed to be linearly distributed across the thickness of the slab giving strain ε_s at the steel level; (note that there are two sets of bars and thus two strains ε_{s1} and ε_{s2} at each steel level).

(3) The equivalent steel stress σ_s (in our case σ_{s1} and σ_{s2}) in the principal bending direction are calculated using a modified stress-strain relationship that allows for the fact that the steel is at an angle δ to the principal bending direction. This uses the equations:

$$\varepsilon_{sb} = \varepsilon_s \cos^2 \delta \quad \ldots \qquad \ldots (5.3\text{-}1a)$$

$$\sigma_s = \sigma_{sb} \cos^2 \delta \quad \ldots \qquad \ldots (5.3\text{-}1b)$$

where ε_{sb} is the strain in the steel bar direction; and σ_{sb} is the corresponding stress in a uniaxial test on a bare steel bar.

The area of steel per unit width is that perpendicular to the steel direction and thus, the effective tensile force in the bending direction per unit width due to the steel bars is equal to the steel area times the equivalent steel stress σ_s.

(4) The compression zone is divided into 10 layers of equal thickness and the stress is calculated at the boundaries of each layer using the non-linear stress-strain curve for concrete. This curve is modified to give the long term response and to allow for the restraint on lateral displacement. The compressive force in concrete is then evaluated using the Simpson rule of integration.

The position or level at which this force acts is also calculated.

(5) To satisfy equilibrium, compression should equal tension and hence a check is carried out to see whether or not this condition is met. An iterative procedure (based on the Newton-Raphson method) is used to find the neutral axis depth that gives balanced forces. Practically, this is done by limiting the difference between the tensile and compressive forces to within certain limits; in our case the limits were taken to be $\pm$ 0.5% of the summation of the absolute values of the tensile and compressive forces.

(6) The secant modulus of elasticity for the steel in each set of bars is taken as the ratio σ_s/ε_s for that set. The modulus of elasticity for the concrete in compression is taken as the average of the secant moduli for the 10 layers. These values of secant moduli for the materials are used in calculating the initial neutral axis depth in the first step of the next stage.

(7) Finally, the bending moment is calculated by taking moments around the level at which the compressive force acts.

-II- Tension stiffening is taken into consideration

The same procedure as in 5.3.1 above is used except that in step 3, the 'modified' stress-strain relationship is the modified 'enhanced stress'-strain one developed in Chapter 3. It should be noted however that the procedure developed in Chapter 3 for calculating the 'enhanced stress'-strain relationship was derived from results from experiments on beams and slabs with reinforcement running in the principal bending direction. Therefore, in order that this procedure might be applicable to the case where the reinforcement lies at an angle to the principal bending direction, certain adjustments ought to be made when calculating the ratios ρ_e, s', and c' (Equations 3.4-4 to 3.4-6) and the ratios ρ_e", s", and c". (Equations 3.4-19, 3.4-20, and 3.4-32). These adjustments are as follows:

(i) The area of steel per unit width is transformed to an effective area per unit width in the principal bending direction. This was done by multiplying the area of steel per unit width by the ratio $\bar{\sigma}_s/(E_s\ \varepsilon_s)$. From Equation 5.3-1 the effective area of steel per unit width in the principal moment direction A_{se} is equal to $A_s \cos^4 \delta$.

(ii) The effective bar spacing in the cracks' direction s_e is used instead of the bar spacing s and is equal to $s/\cos\delta$. It should be also noted that in the slab tests the effective spacing of bars s_e varied from one position to another along the length of the slab due to the intersection of the two sets of bars. It ranged from half to once the average effective spacing s_{eav} (the average of the two bar spacings of the two sets). Thus the modified effective spacing s_{em} to be used in the theoretical calculations is 3/4 of the average effective bar spacing s_{eav};

i.e.

$$s_{em} = \frac{3}{4} \frac{s_1 + s_2}{2 \cos \delta} \quad \ldots \quad \ldots (5.3\text{-}2)$$

where s_1 and s_2 are the bar spacing for sets 1 and 2 respectively.

(iii) The cover c is multiplied by the ratio of the average steel strain in the bar direction to the average strain at steel level in the principal direction i.e. by $\cos^2 \delta$ to give the effective cover c_e. This assumption follows the hypothesis given in Section 6.4.3 as a result of the crack width analysis carried out in Chapter 6 since the cover c affects the tension stiffening by affecting crack spacing and widths. Thus,

$$c_e = c \cos^2 \delta \quad \ldots \quad \ldots (5.3\text{-}3)$$

5.3.3 Discussion

In Figures 5.3-1a to 5.3-8a, the classical no-tension theory can be seen to overestimate the curvatures at all load stages in the case of slabs S0, S1, S3N, and S5 (that is slabs with $\delta = 0^\circ$, 10°, 30°, and 50° respectively) and at early load stages in the case of slabs S2, S3O, and S4 (i.e. slabs with $\delta = 20^\circ$, 30°, and 40°). Attention must be drawn however to the fact that the strain gauge lengths on the tension faces of those latter slabs were both short (5 and/or 10mm long) and discontinuous and that the deflections were measured at mid-breadth and near one edge (i.e. one curvature value only inside the test zone) as explained in 4.5.2 and 4.5.3 in the previous chapter. In the case of S6, the slab with $\delta = 60^\circ$, the test was terminated soon after cracking because the deformations were concentrated at one narrow position that happened to be outside the area

of deflection measurements and next to one of the supports (i.e. outside the test zone).

The slabs in general showed a similar manner of behaviour to that reported by other researchers e.g. [51],[57]. A typical experimental moment-curvature relationship for a reinforced concrete member under pure bending moment would take the form shown in Figure 5.3-9 in relation to the classical no-tension theory. The theory can be seen to overestimate curvatures by amounts that depend on the stage of loading. Up to the cracking moment, the ratio of the theoretical to the experimental curvature (K_{th}/K_{ex}) is almost constant. This ratio decreases after cracking as the concrete in the tension zone looses its strength owing to crack propagation, until it reaches a value of about 1 at a high load stage just below the yield moment. As the bending moment approaches its yield value and thereafter, the ratio (K_{th}/K_{ex}) increases again for the following reasons.

Firstly, at or around yield the curvature tends to be concentrated at certain major cracks where a yield line or lines would later form. Thus, the experimental curvature which was measured over a great length of the constant moment zone would certainly be less than that calculated at a section containing a yield line. Secondly, the stress-strain relation for the steel reinforcement used in calculating the theoretical stresses in the steel bars was obtained from uniaxial tests on long steel bars (200mm gauge length). Therefore, the experimental moment-curvature relationship would probably be stiffer than the theoretical one since the exposed length of bars at a yield line would be much shorter than the gauge length of the steel control specimens. Finally, the stress-strain relation for the concrete in compression was basically that of a uniaxially loaded

cylindrical specimens, and although this relation was adjusted to allow for restraint on lateral displacement, still the actual behaviour of concrete in the compression zone of the slab could be different.

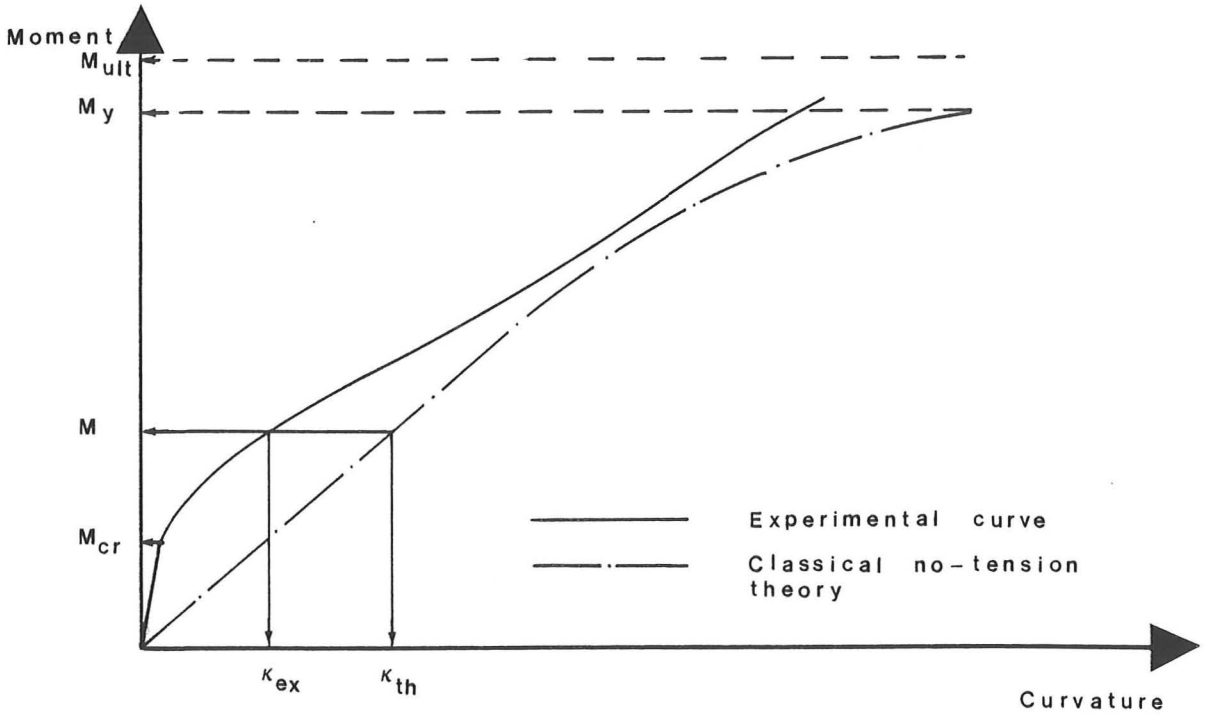

Figure 5.3-9 A typical experimental moment-curvature curve for a r.c. member in pure bending in relation to the classical no-tension theory.

The theoretical curves allowing for tension stiffening are in reasonable agreement with the test results. This demonstrates the ease with which the 'enhanced stress' - strain relation for steel derived in Chapter 3 is used to model tension stiffening in a computer program that uses the no-tension concept. No problems of numerical convergence were faced in running the program and only a slightly higher computing time was needed. Along with the moment - curvature relation one can directly obtain the average strain ε_m and the n. a. depth and hence the height h_{tm} of the tension zone at any load stage. Both ε_m and h_{tm} are needed for use in formulae for predicting crack widths. As can be seen from Figures 5.3-1b to 5.3-8b, there is quite a good agreement between the theoretical and experimental values of the average neutral axis depth.

5.3.4 Effect of reinforcement angle δ

It can be seen from Figures 5.3-1 to 5.3-8 that the classical no-tension theory overestimates experimental curvatures to a greater degree for greater values of the angle δ between the direction of the steel reinforcement and that of the principal bending. In other words, the tension stiffening due to concrete has a greater effect as δ increases. This is because the tensile stresses due to the steel reinforcement take smaller value for greater values of δ at comparable strains at the steel level in the principal bending direction as given by Equation 5.3-1. Hence, the ratio of the tension stiffening force to the tensile force due to steel (in the principal moment direction) will be greater as δ increases. This can be clearly seen from the graphs in the following sections.

The cracking moment can be seen to be almost the same for all the slabs (8 in all) and thus the range of loading between the cracking moment M_{cr} and the yielding moment M_y is less for greater values of δ since M_y is equal to $\cos^2 \delta$ times the yielding moment when $\delta = 0^\circ$. Also, the curvature at which the moment reaches its yielding is equal to the yielding curvature when $\delta = 0^\circ$ divided by $\cos^2 \delta$ and thus the slope of the straight part of the classical no-tension theory will be equal to $\cos^4 \delta$ times the slope of the straight part when $\delta = 0^\circ$. Again it is seen that the greater the value of δ is, the greater is the relative effect of tension stiffening.

The ultimate bending moment M_{ult} was calculated for each one of the slabs according to the simple plastic theory and allowing for δ by multiplying the ultimate steel stress σ by $\cos^2 \delta$. The values of M_{ult} are marked on the graphs in Figures 5.3-1 to 5.3-8. It can be seen that the applied bending moments are always well below the ultimate.

5.4 Tension stiffening force - mean strain relations

In Figures 5.4-1 to 5.4-4 are shown the experimental and theoretical relations between the tension stiffening force as a ratio of F_{tcr} (= $f_t bh/4$) and the strain at steel level as a ratio of ε_{syi} (= σ_{sy}/E_s). The experimental tension stiffening forces are those obtained from analysis based on the second approach explained in Subsection 3.2.3. The area of steel A_s used in Equations 3.2-5 and 3.2-6 is the area per unit width perpendicular to the bar direction but the stress-strain relation for the steel is modified to account for the effect of steel-bars' orientation and is given by Equation 5.3-1. The depth of the steel reinforcement was taken to be the average of the depths of both sets of bars. The strains at this depth were deduced from the strain measurements on the compression face and the deflection measurements.

The theoretical F_t-ε_{sm} relations are those obtained from the theory developed in Chapter 3. Note that in calculating the theoretical values of the strain ε_{sp} at steel level when F_t is maximum, Equation 5.3-2 should be used to obtain the average effective bar spacing. Also note that the area of steel A_s and the cover ratio c' used in calculating the factor β (Equation 3.4-14) should be multiplied by $\cos^4\delta$ and $\cos^2\delta$ respectively. The neutral axis depth needed for the calculation of the theoretical F_t in Equation 3.4-29 is interpolated from the experimental n.a. depth - ε_{sm} relation.

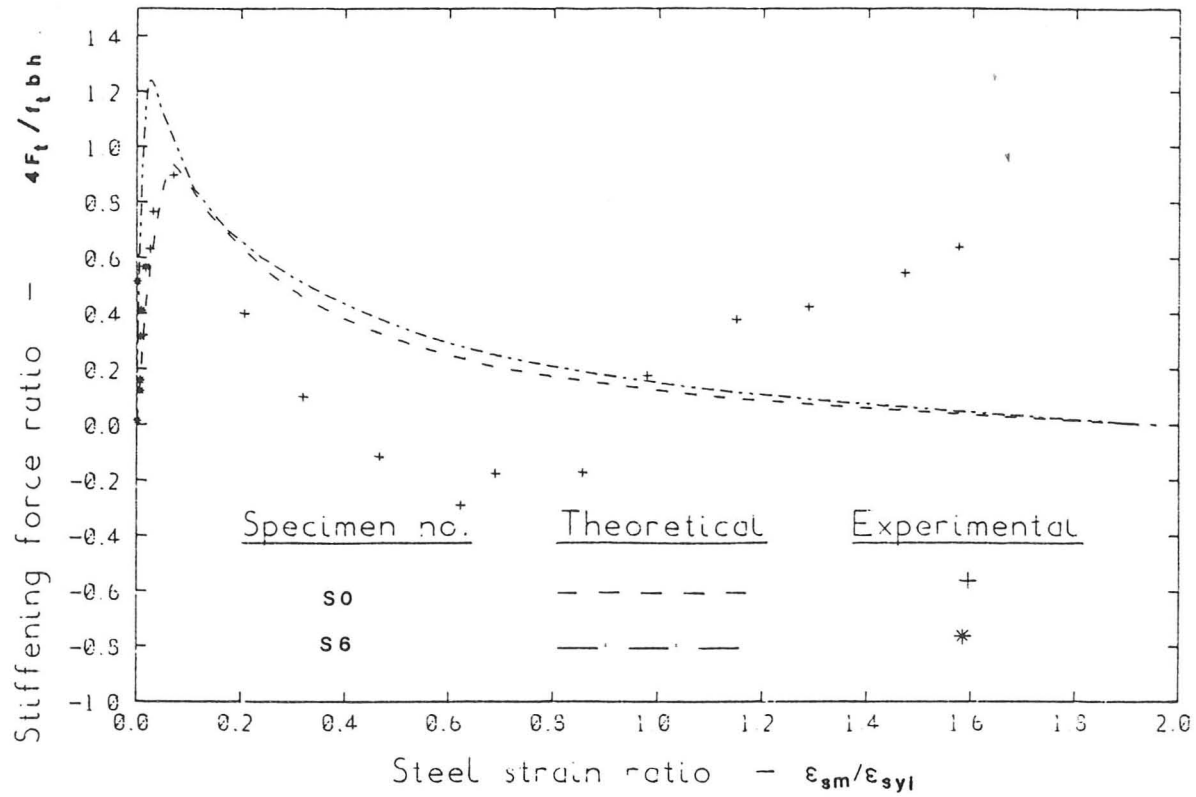

Figure 5.4-1 Experimental and theoretical relations between F_t/F_{tcr} and $\varepsilon_{sm}/\varepsilon_{syi}$ for slabs S0 and S6.

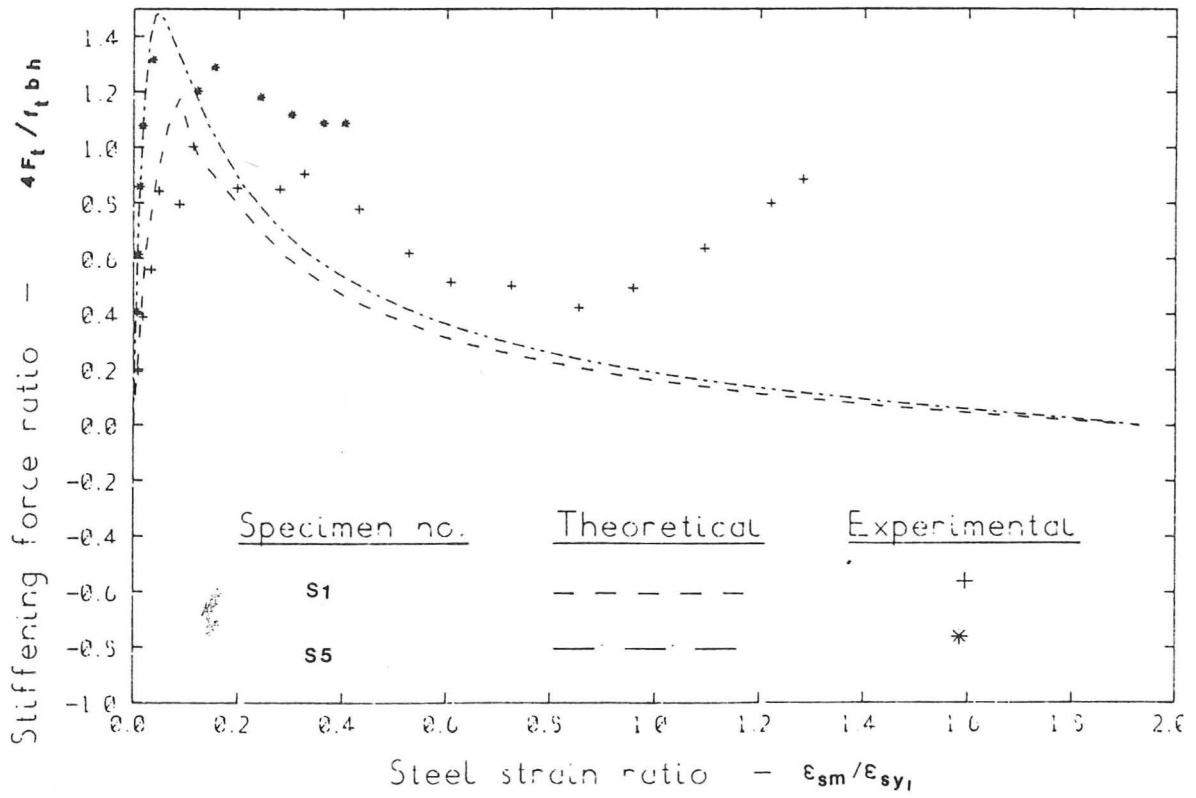

Figure 5.4-2 Experimental and theoretical relations between F_t/F_{tcr} and $\varepsilon_{sm}/\varepsilon_{syi}$ for slabs S1 and S5.

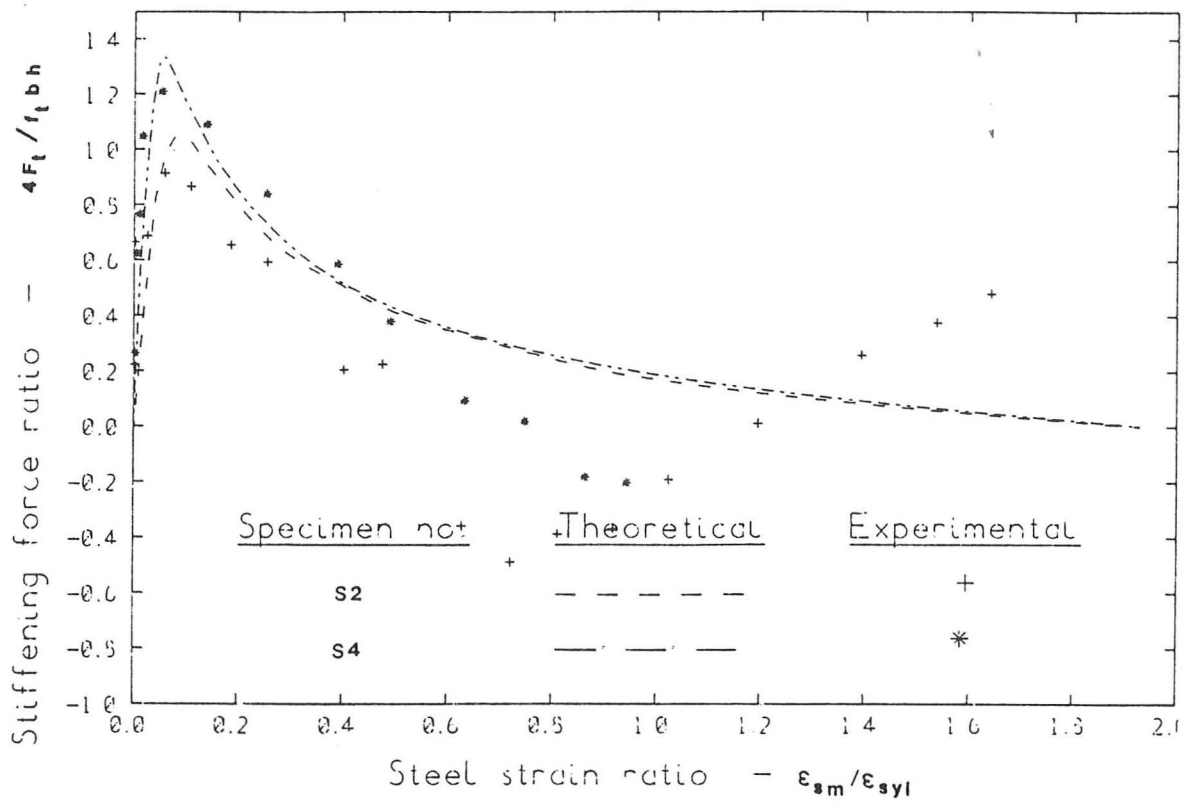

Figure 5.4-3 Experimental and theoretical relations between F_t/F_{tcr} and $\varepsilon_{sm}/\varepsilon_{syi}$ for slabs S2 and S4.

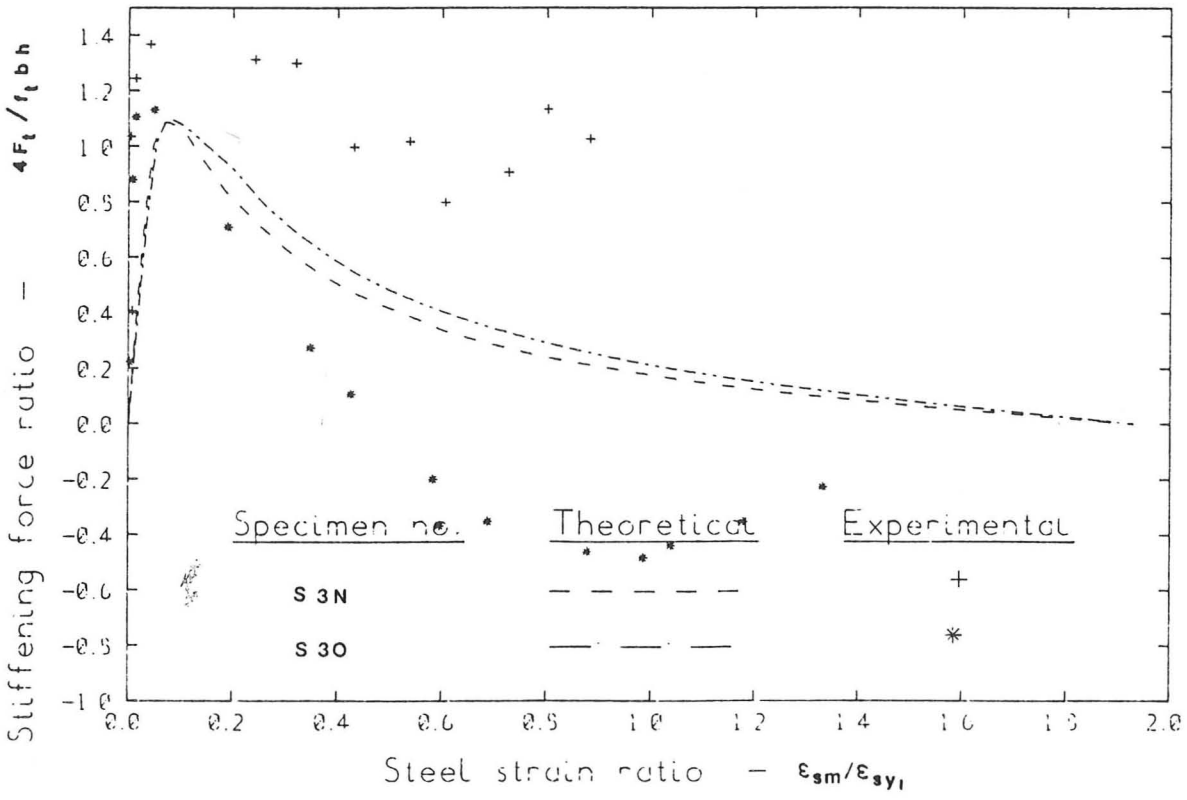

Figure 5.4-4 Experimental and theoretical relations between F_t/F_{tcr} and $\varepsilon_{sm}/\varepsilon_{syi}$ for slabs S3N and S30.

If we consider the experimental graphs in Figures 5.4-1 to 5.4-4, the following conclusions can be drawn:

(1) The peak value of F_t seems to increase with an increase in the angle δ (between the steel-bars' direction and that of the principal bending).

(2) The rate of the initial breakdown of tension stiffening decreases as the angle δ increases.

(3) At a steel strain of about 80% of the value of (σ_{sy}/E_s), the tension stiffening force F_t after reaching a minimum value, increases once again this time owing to the same reasons given in 5.3.3 above and not due to tension stiffening of concrete.

It can be seen from Figures 5.4-1 to 5.4-4 that reasonable agreement is obtained between the theoretical and experimental graphs especially in the early stages of loading. As expected, the value of F_{tp} predicted by the theory took greater values for slabs with greater angle δ; meanwhile, the amount of tension stiffening beyond the stage where major cracks are well established is almost the same for all the slabs. As mentioned before, this means that the ratio of the tension stiffening force F_t to the average force T_{sm} in the principal bending direction due to steel, in other words the ratio $(\sigma_{se} - \sigma_{sm})/\sigma_{sm}$, is greater for slabs with greater angle δ at comparable steel level strains as illustrated in the graph of the next section.

5.5 Enhanced steel properties

The experimental and theoretical enhanced stresses $\bar{\sigma}_{se}$, of the reinforcing steel, as a ratio of the yield stress σ_{sy}, are plotted against the mean strain at the steel level, as a ratio of the 'initial' yield strain ε_{syi} (= σ_{sy}/E_s), as shown in Figures 5.5-1 to 5.5-4. Also plotted on these graphs are the dimensionless properties of the bare steel bars. Both the experimental and theoretical enhanced stresses $\bar{\sigma}_{se}$ were calculated by adding the ratio F_t/A_s between the tension stiffening force and the area of tension steel to the stress σ_{sm} in the bare steel bar.

The agreement between the theoretical and experimental curves is reasonable; good agreement can be found at early load stages. At late load stages however, the experimental curve in some slabs is above and in others below the theoretical curve.

Comparing the theoretical curves in Figures 5.5-1 to 5.5-4 with the bare steel properties, one can see that enhanced steel stress increases as the reinforcement angle δ increases. Even at high steel strain, the enhanced stress is significantly higher than the bare steel curve for slabs with greater angle δ.

Thus, the theoretical 'enhanced steel' properties are ready for use in a structural analysis, such as a finite element program, to obtain the theoretical moment-curvature response of the slabs. This analysis was carried out as presented in Subsection 5.3.2 and is discussed in Subsection 5.3.3.

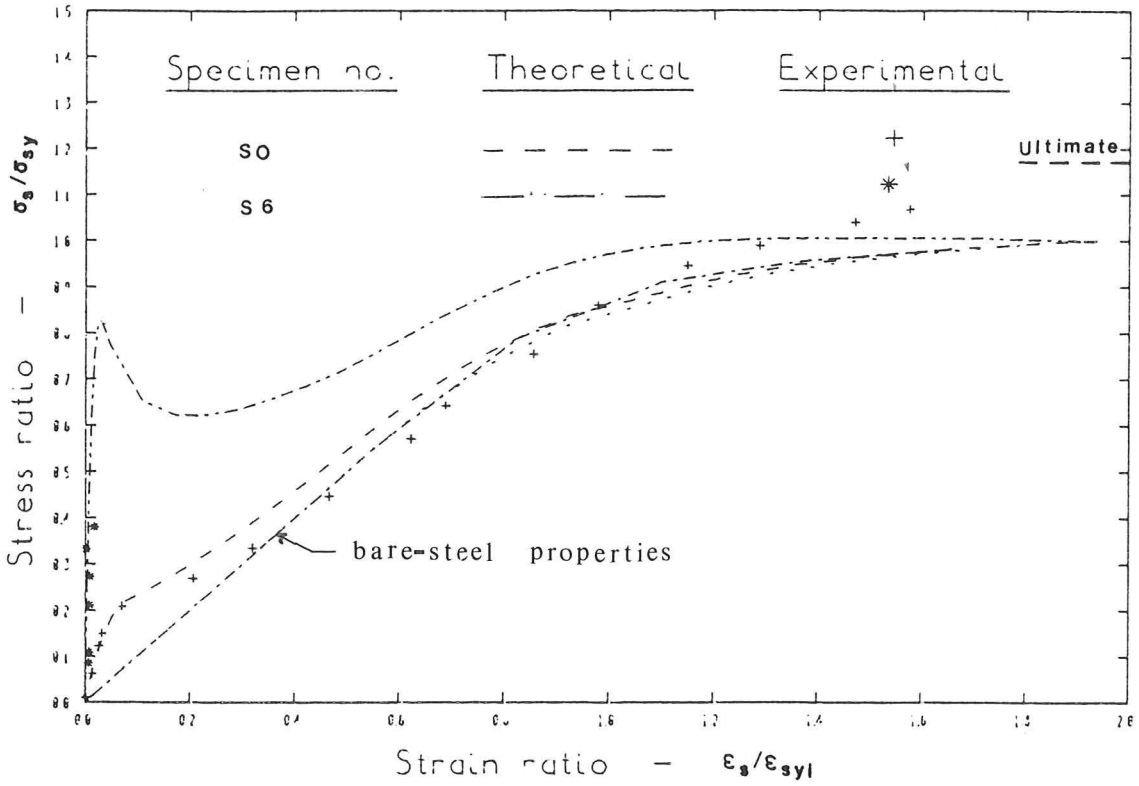

Figure 5.5-1 Experimental and theoretical relations between σ_{se}/σ_{sy} and $\varepsilon_{sm}/\varepsilon_{syi}$ for slabs S0 and S6.

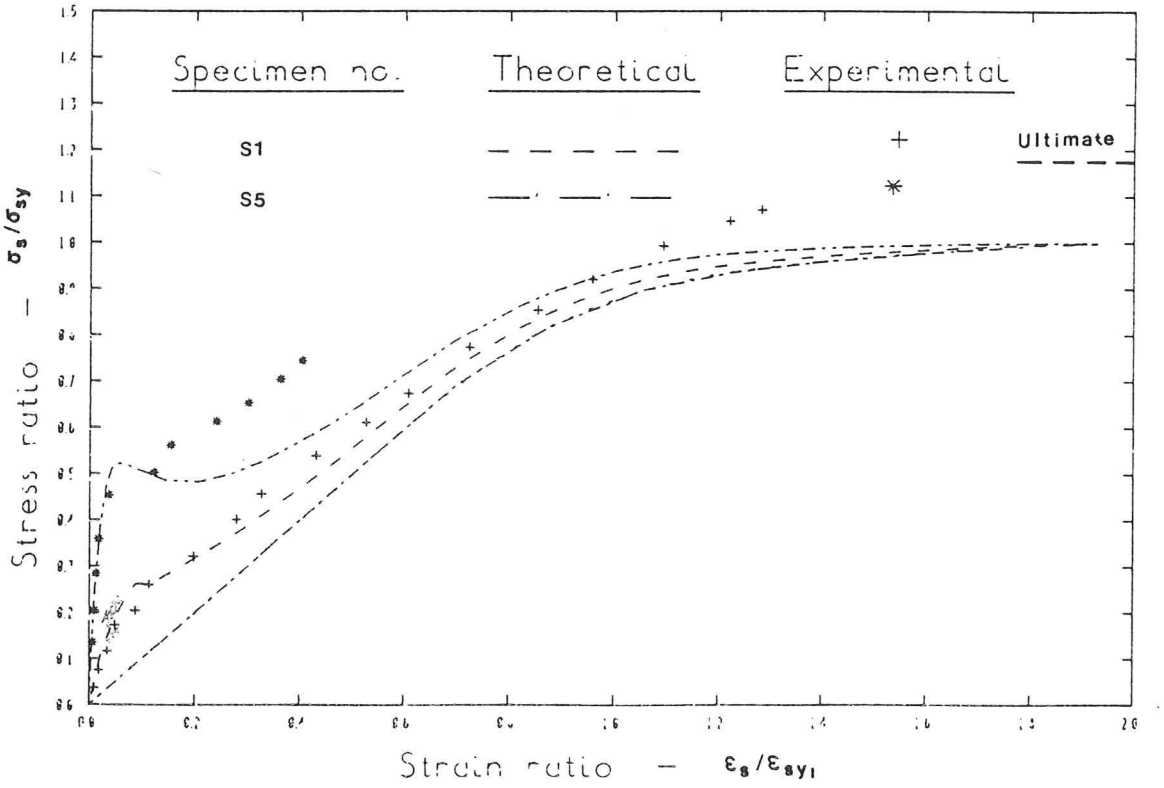

Figure 5.5-2 Experimental and theoretical relations between σ_{se}/σ_{sy} and $\varepsilon_{sm}/\varepsilon_{syi}$ for slabs S1 and S5.

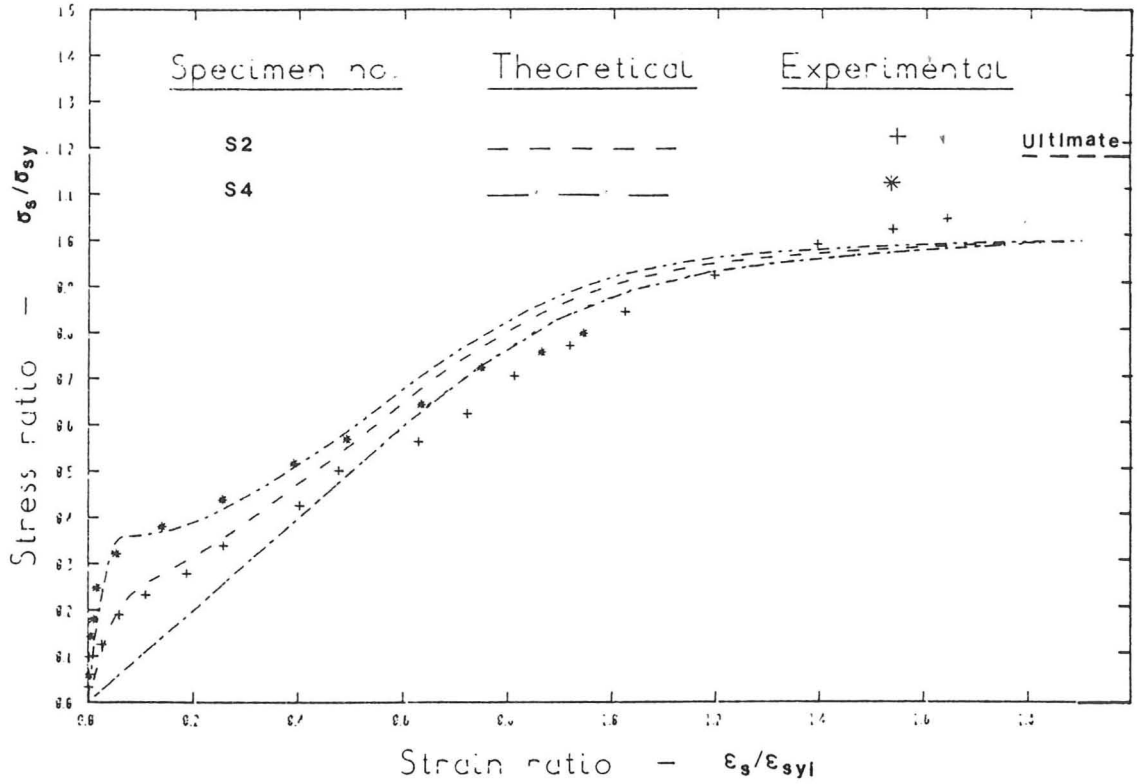

Figure 5.5-3 Experimental and theoretical relations between $\bar{\sigma}_{se}/\bar{\sigma}_{sy}$ and $\varepsilon_{sm}/\varepsilon_{syi}$ for slabs S2 and S4.

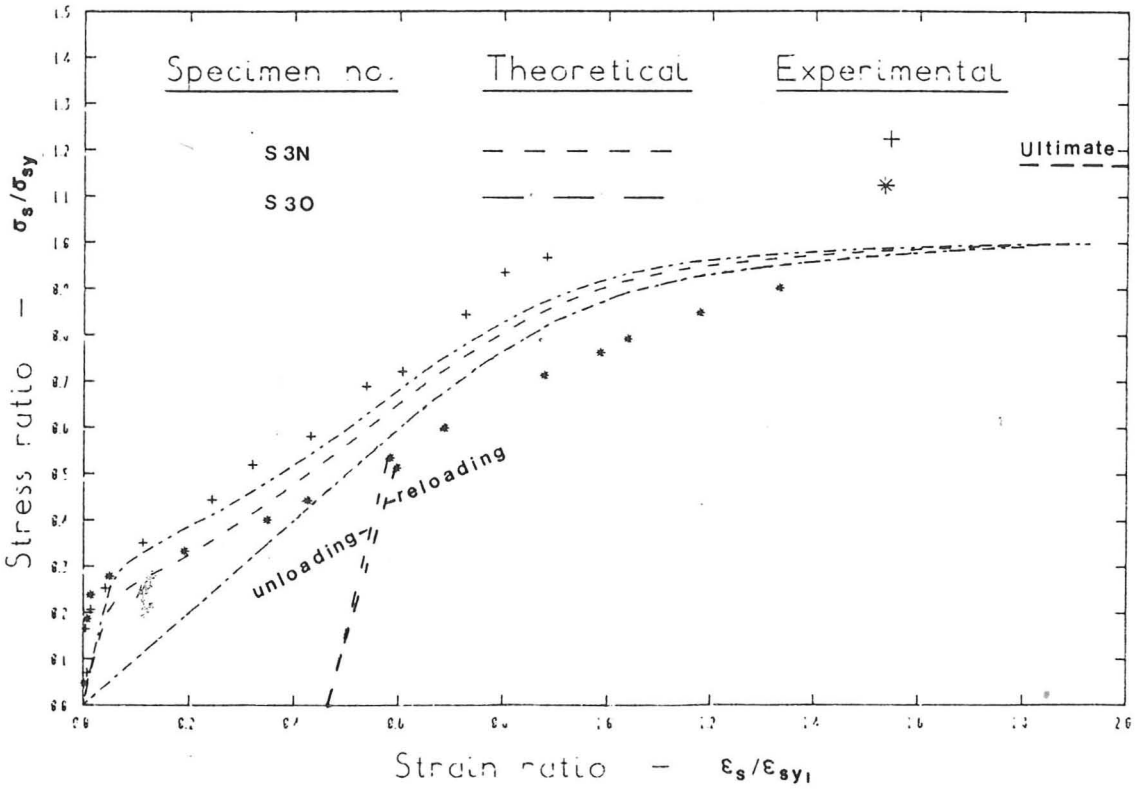

Figure 5.5-4 Experimental and theoretical relations between $\bar{\sigma}_{se}/\bar{\sigma}_{sy}$ and $\varepsilon_{sm}/\varepsilon_{syi}$ for slabs S3N and S3O.

6. PRESENTATION OF TEST RESULTS: CRACK SIZE

6.1 Introduction

In this chapter, the results from the tests described in Chapter 4 that have connection with the crack width analysis are presented and discussed. These results are: the properties of materials, crack width measurements, crack spacing data, and surface tensile strains as well as dimensions of the cross section and the arrangement of the steel reinforcement.

A computer program was written for the University computer IBM 370. Its task was to analyse these experimental results as will be described in detail in the following sections.

6.2 Crack Pattern

Figure 6.2-1 shows how the crack pattern on the slab S30 develops as the surface strain increases. Cracks first appeared at a surface strain of 24×10^{-5} (with general direction perpendicular to the principal bending direction) giving a fairly uniform crack spacing in that direction all over the tension face (Figure 6.2-1a and b). As the load increases, more cracks form right across the slab, though many of these are not continuous, and some short cracks start developing near the position of reinforcement.

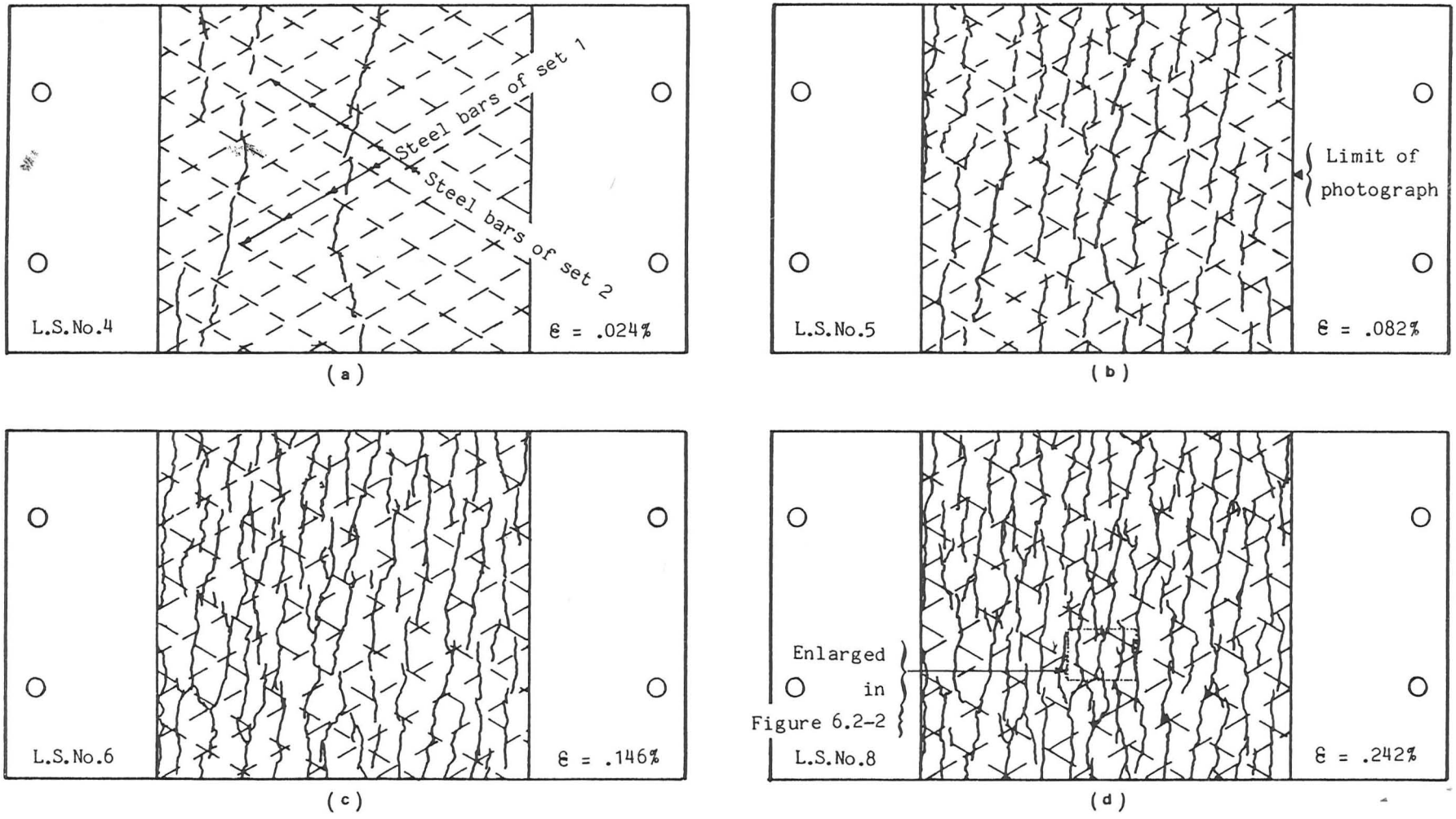

Figure 6.2-1 Development of the surface crack pattern for slab S30 traced from photographs.

Some of these short cracks join up with the other cracks giving what might be called forked cracks. The discontinuous cracks that have formed across the width of the specimen had an overlapping profile often in the region of the reinforcement as shown in Figure 6.2-1c. The formation of these overlapped and forked cracks meant that more cracks were produced over steel bars than midway between bars. Therefore, the average crack spacing s_{cr}, in the bar direction, becomes smaller along a grid line running over a steel bar, than along a grid line midway between two adjacent bars. Note that grid lines run in the relevant bar direction.

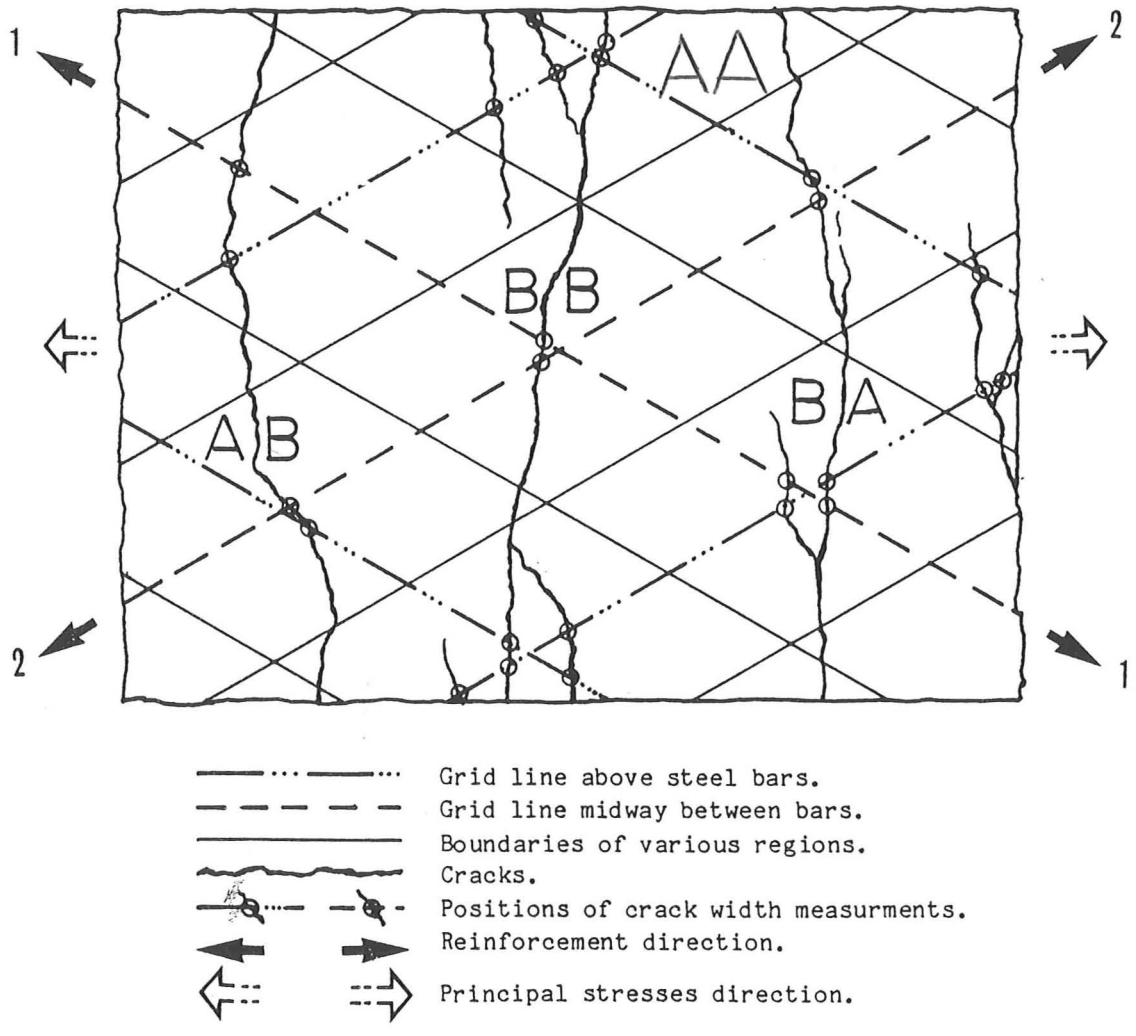

Figure 6.2-2 Definition of grid lines, regions, and number of cracks.

However, with the presence of two intersecting sets of bars, there will be an interaction between the two crack patterns each occuring in the presence of only one set of bars. Thus, the average crack spacing and the average crack width are expected to vary from one position to another on the same grid line. For this reason, it was decided to study cracking in each one of the four regions described in Subsection 4.5.3 (the regions are all equal in area for a given angle δ). The regions were designated jk where j and k are labels describing the positions of the two sets of grid lines running in the direction of steel sets 1 and 2 respectively. The labels j and k can either be the letter 'A' for a grid line above a steel bar or the letter 'B' for a grid line midway between bars. Thus, a region of type AB is a region above a steel bar of set 1 and midway between bars of set 2 and so forth as illustrated in Figure 6.2-2.

In Figure 6.2-3 are given the fully developed crack patterns of slabs S0 to S5 (see Figure 6.2-1d for the crack pattern of slab S30). Slab S0 (with one set of bars in the principal moment direction) gave a crack pattern similar to that described by Beeby [19], with more cracks forming over steel bars as the load increases than in between these bars. Slabs with skew reinforcement have also shown more cracking in the vicinity of reinforcement than away from it. However, as the reinforcement angle δ increases, the influence of the steel reinforcement on the crack pattern reduces and hence the different crack patterns become less distinct as can be seen from Figure 6.2-3.

Also clear from this figure is the increase in the average crack spacing in the principal bending direction as the angle δ (between this direction and the steel's) increases.

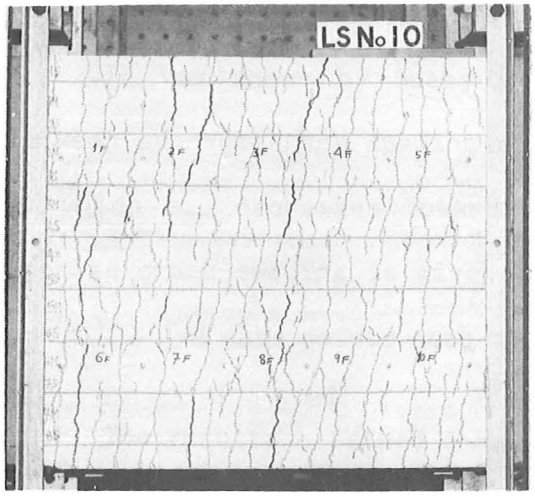

(a) S0: ε = 0.27 %

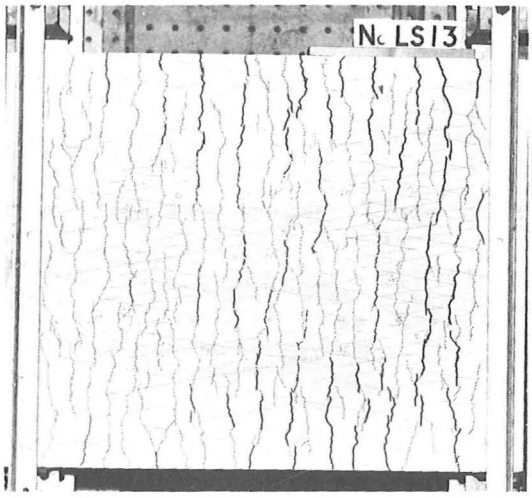

(b) S1: ε = 0.28 %

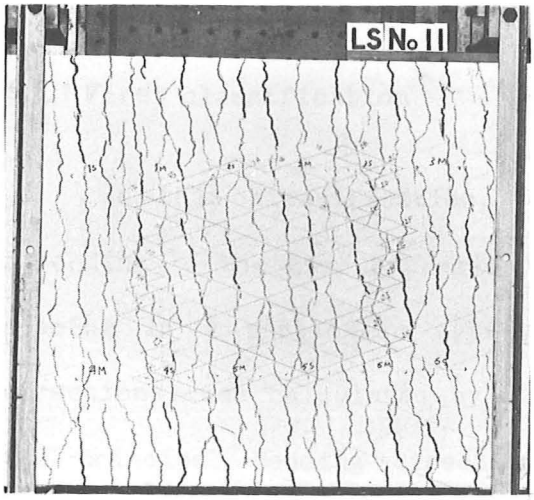

(c) S2: ε = 0.26 %

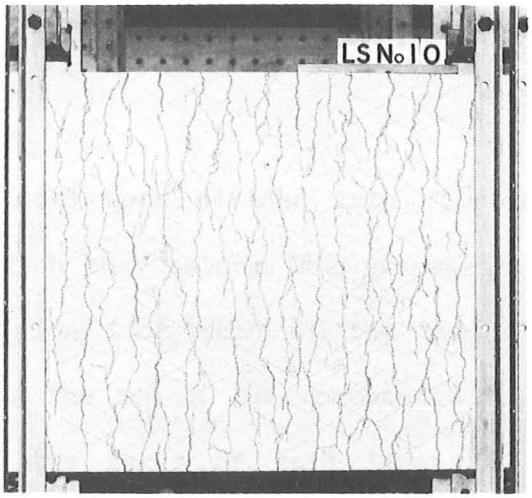

(d) S3N: ε = 0.26 %

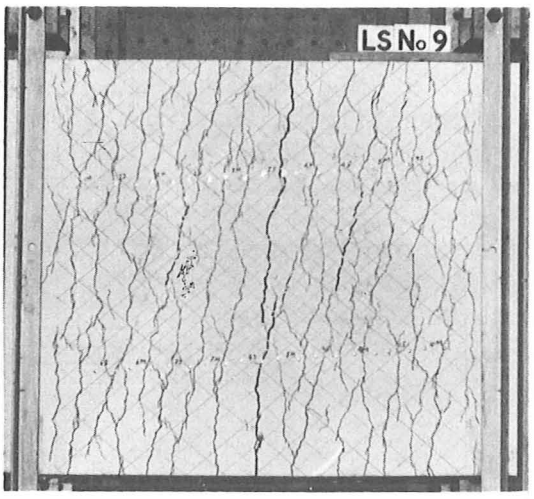

(e) S4: ε = 0.27 %

(f) S5: ε = 0.27 %

Figure 6.2-3 Fully developed crack pattern for slabs S0 to S5.

It was shown by Beeby [19] that there is a linear relationship between average crack spacing s_{cr} and $1/\varepsilon$ (were ε is the surface strain) in which s_{cr} decreases towards a minimum as ε increases. This minimum average crack spacing is given by the point where the best fit line for the s_{cr} - $1/\varepsilon$ data points cuts the axis of s_{cr}.

The results obtained from the slab tests (Chapter 4) will be treated in two different ways according to the way in which the cracks were classified as explained in Subsection 4.7.5.

6.3.1 First classification

In this classification, the cracks were divided into four sets according to the type of region to which they belong. The average crack spacing in a particular type of region (for each of the two steel directions) was calculated by dividing the sum of the components L_o, in the principal bending direction, of the parts of grid lines in the direction considered which passed through the regions of that type by the number of cracks crossing those parts of grid lines (see Figure 6.2-2). Grid lines in the two directions were treated separately because the bars of the two sets had different cover and spacing; thus, for a slab with skew reinforcement at an angle δ to the principal bending direction (see Figure 6.3-1), the following equation can be written.

$$L_{oi} = n_r \, l_i \cos \delta \quad \ldots \qquad \ldots (6.3\text{-}1)$$

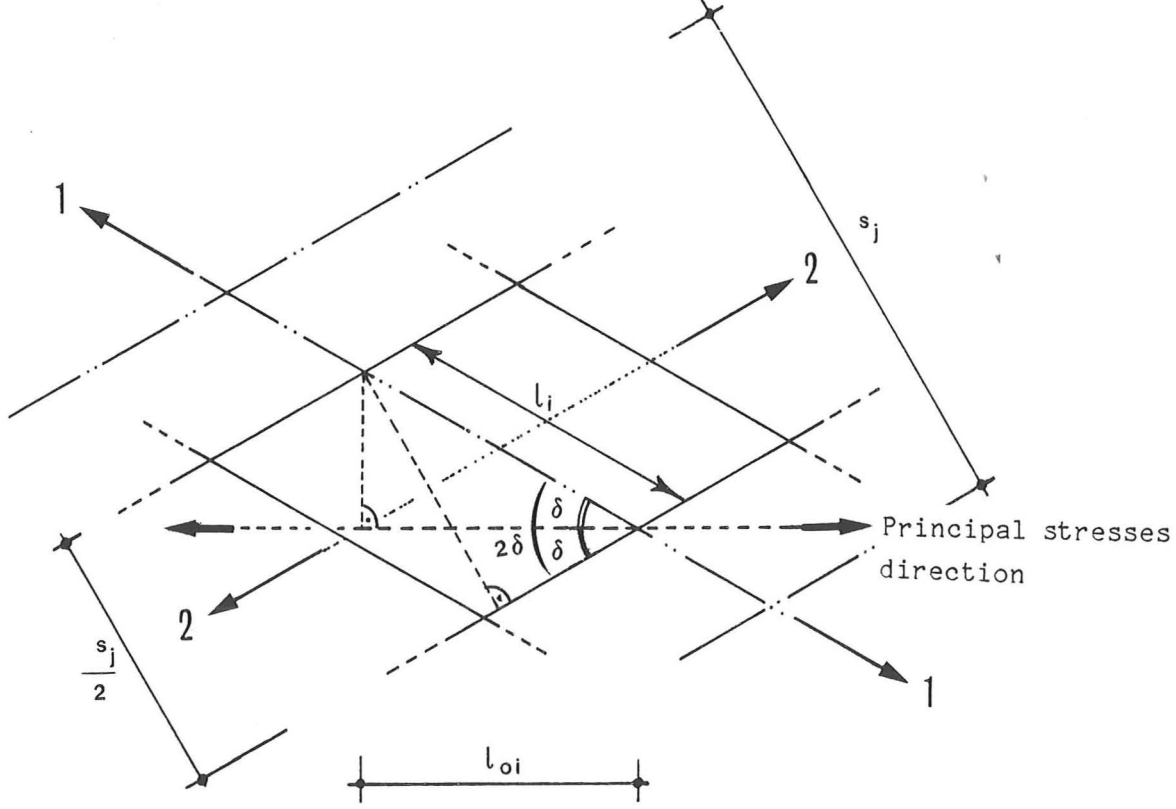

Figure 6.3-1 Calculating the horizontal projection of a length of a grid line.

where

L_{oi} is the value of L_o for reinforcement set i;

n_r is the number of regions of the type under consideration; and

l_i is the length of the part of the grid line, running in the direction of bars of set i, within one region.

If s_j is taken to be the spacing of bars of set j, then,

$$l_i = \frac{s_j/2}{\sin 2\delta} \qquad (6.3\text{-}2)$$

and hence

$$L_{oi} = \frac{n_r \, s_j \cos \delta}{2 \sin 2\delta} \qquad (6.3\text{-}3)$$

Dividing L_o by the number of cracks n_{cr} seen in the regions of the type considered and at grid lines in the direction considered for a given load stage, we obtain the average visible crack spacing s_{cr} for this particular group of cracks (8 groups in all) for this load stage.

Table 6.3-1 Number of regions n_r, number of cracks n_{cr}, and the average crack spacing s_{cr} (mm) for each of the eight region of classification 1 for slabs S1 to S5.

Steel sets	1			2		1			2		1			2		1			2	
type	n_r	n_{cr}	s_{cr}	n_{cr}	s_{cr}	n_r	n_{cr}	s_{cr}	n_{cr}	s_{cr}	n_r	n_{cr}	s_{cr}	n_{cr}	s_{cr}	n_r	n_{cr}	s_{cr}	n_{cr}	s_{cr}
Slab S1																				
ε (%)	0.110					0.176					0.242					0.362				
AA	8	23	50.1	32	45.0	8	32	36.0	37	38.9	8	36	32.0	41	35.1	7	36	28.0	44	28.6
BB	7	19	53.1	24	52.5	8	24	48.0	31	46.5	8	26	44.3	39	45.0	8	31	37.2	35	41.1
AB	8	23	50.1	27	53.3	8	34	33.9	37	38.9	8	38	30.3	45	32.0	8	43	26.8	49	29.4
BA	8	20	57.6	25	57.6	7	25	40.3	30	42.0	8	32	36.0	44	32.7	8	36	32.0	47	30.6
Slab S2																				
ε (%)	0.178					0.300					0.445									
AA	16	25	46.7	29	50.3	16	41	28.5	37	39.5	16	48	24.3	39	37.4					
BB	13	15	63.3	21	56.5	13	19	49.9	29	40.9	13	20	47.5	31	38.3					
AB	16	19	61.5	26	56.2	16	24	48.7	33	44.2	16	27	43.3	37	39.5					
BA	14	16	63.9	24	53.2	14	23	44.4	30	42.6	14	27	37.9	36	35.5					
Slab S3N																				
ε (%)	0.140					0.231					0.315									
AA	24	30	42.0	35	42.9	24	41	30.7	45	33.3	24	44	28.6	52	28.8					
BB	13	8	85.3	9	90.3	13	13	52.5	13	62.5	13	15	45.5	13	62.5					
AB	18	26	36.3	28	40.2	18	35	27.0	34	33.1	18	40	23.6	34	33.1					
BA	17	21	42.5	24	44.3	17	24	37.2	29	36.6	17	25	35.7	30	35.4					
Slab S4																				
ε (%)	0.218					0.272					0.348					0.410				
AA	24	23	42.7	23	50.9	24	27	36.4	24	48.8	24	32	30.7	32	36.6	24	36	27.3	33	35.5
BB	13	13	41.0	9	70.4	13	15	35.5	9	70.4	13	16	33.3	9	70.4	13	16	33.3	9	70.4
AB	17	20	34.8	17	48.8	17	20	34.8	18	46.0	17	23	30.3	21	39.5	17	24	29.0	23	36.0
BA	18	15	49.1	17	51.6	18	15	73.7	18	48.8	18	16	46.1	18	48.8	18	17	43.4	19	46.2
Slab S5																				
ε (%)	0.115					0.180					0.273									
AA	18	9	68.5	10	73.4	28	17	56.4	20	57.1	28	20	47.9	27	42.3					
BB	12	3	137.	7	69.9	17	4	146.	11	63.0	17	5	116.	11	63.0					
AB	14	6	79.9	6	95.1	22	12	69.8	14	64.0	22	15	50.2	17	52.7					
BA	16	8	68.5	9	72.4	22	16	47.1	20	44.8	22	19	39.6	24	37.4					

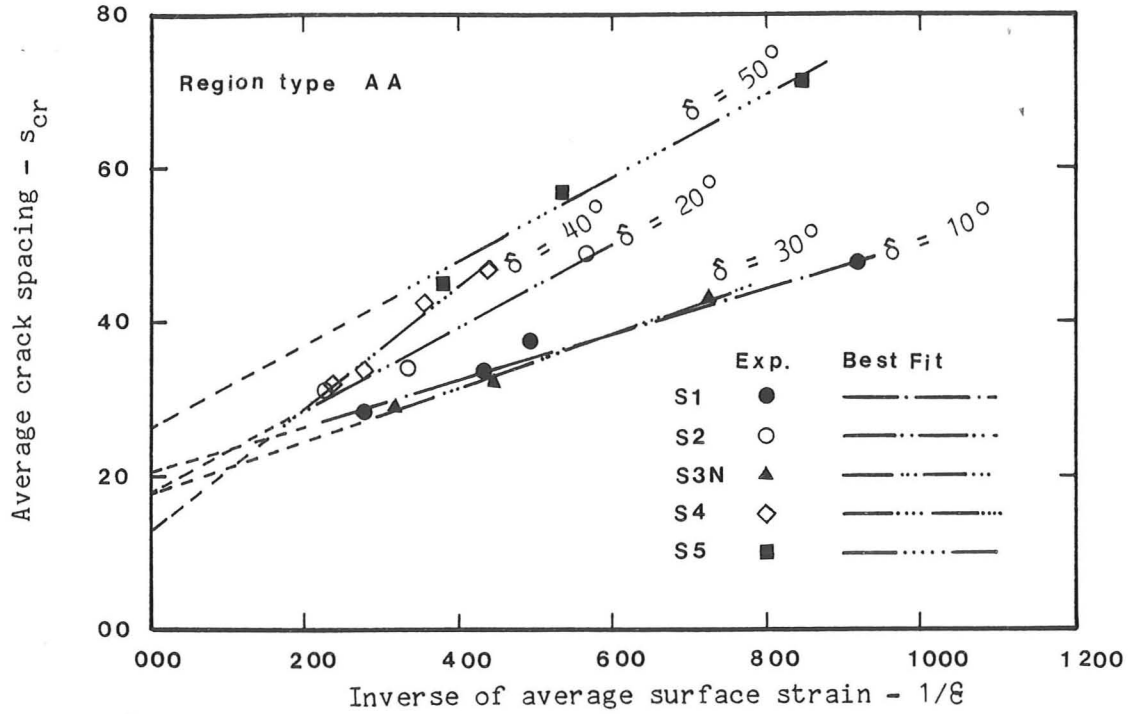

Figure 6.3-2 Experimental relations between average crack spacing, in regions above two intersecting bars, and the inverse of average surface strain for slabs S1 → S5.

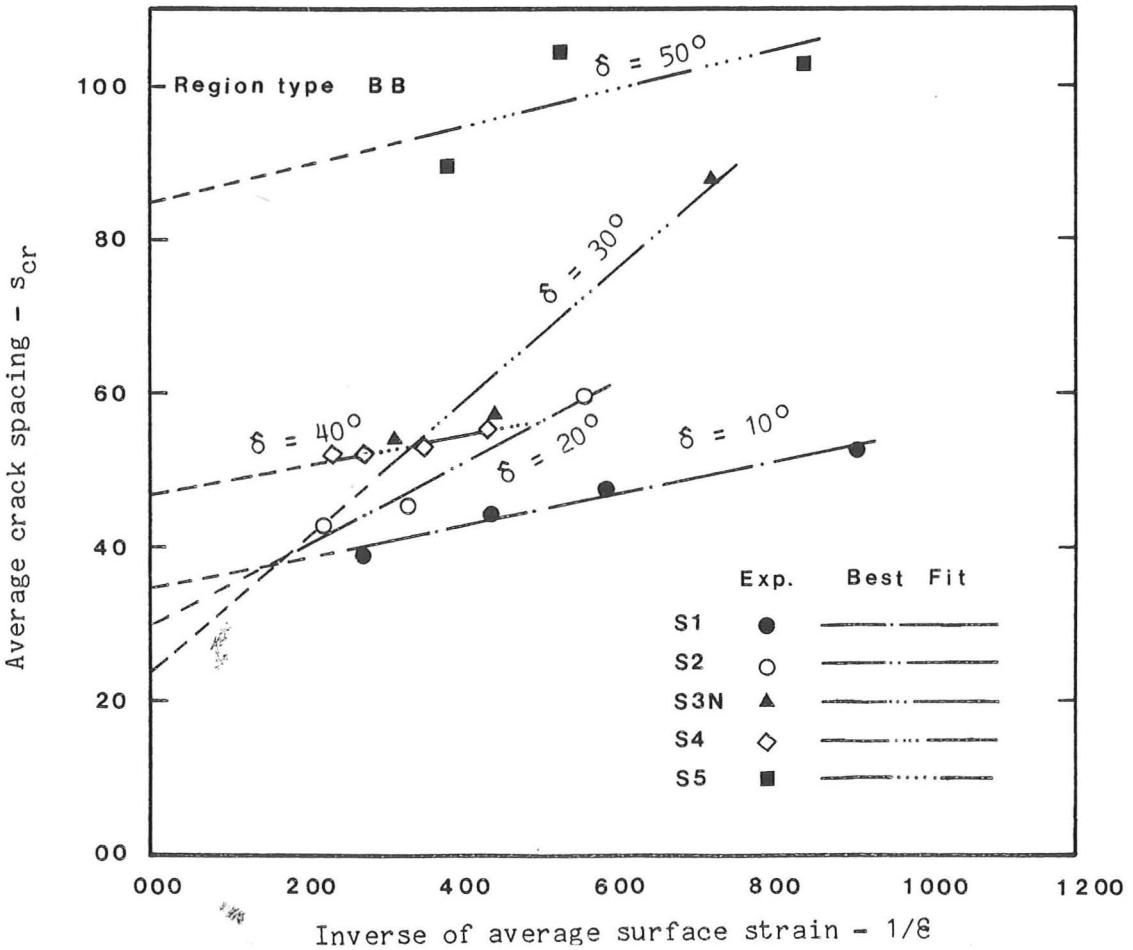

Figure 6.3-3 Experimental relations between average crack spacing, in regions midway between bars of both sets, and the inverse of average surface strain for slabs S1 → S5.

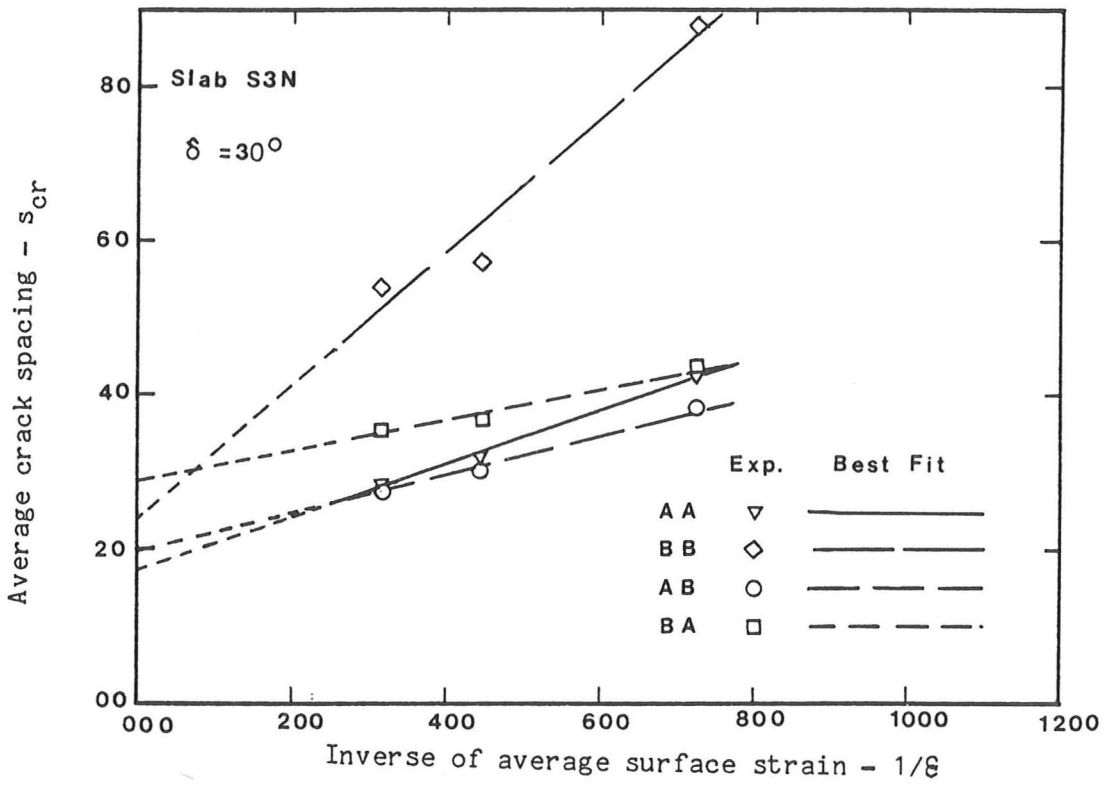

Figure 6.3-4 Experimental relations between average crack spacing and the inverse of average surface strain for different types of regions in slab S3N.

Table 6.3-1 gives the number of cracks n_{cr}, the number of regions n_r and the average crack spacing s_{cr} for each of the eight groups of cracks (4 types of region x two steel directions) for slabs S1 to S5. It can be seen that the number of cracks is usually fairly large, so that the effect of errors due to cracks passing just outside the region in question is low. In Figure 6.3-2, the average crack spacing s_{cr} for region type AA (average of two directions) is plotted against the inverse of the surface strain ε for each of the slabs S1 to S5. It can be seen from this figure that, as the angle δ increases, the average crack spacing at early post-cracking stages becomes greater though it approaches a value of the same order as the other slabs at higher load stages. Figure 6.3-3 shows a graph of s_{cr} against $1/\varepsilon$ for region type BB for slabs S1 to S5. In this figure, it can be seen that there is a less distinct relation between the angle δ and the average spacing; this perhaps is due to the fewer cracks and regions involved in the calculation of s_{cr} as compared with region type AA (see Table 6.3-1). However, the lowest and the highest s_{cr}-$1/\varepsilon$ relation is given by slabs S1 and S5 (with $\delta=10^{o}$ and 50^{o}) respectively. Typical graphs of s_{cr} plotted against $1/\varepsilon$ for each of the four types of region (slab S3N) are given in Figure 6.3-4.

6.3.2 Second classification

Here in this classification, cracks which were measured at each set of grid lines, each running in the direction of one set of bars, were divided into two groups: one for grid lines over, and the other for grid lines midway between, steel bars. Table 6.3-2 gives the value of n_r, n_{cr} and s_{cr} for each of the four groups - the number of grid lines is given instead of number of regions for slab S0. Figure 6.3-5 shows the straight line best fit for the s_{cr}-$1/\varepsilon$ graphs of slabs S0 to S5 for each of the four groups.

Table 6.3-2 Values of n_r through which the grid line passes, n_{cr}, and s_{cr} (mm) for each of the four groups of classification 2 for slabs S0 to S5.

G. l.	n_r	n_{cr}	s_{cr}	n_r	n_{cr}	s_{cr}	n_r	n_{cr}	s_{cr}	n_r	n_{cr}	s_{cr}
Slab S0												
ε (%)	0.067			0.103			0.148			0.220		
A1	6	60	100	6	93	64.5	6	114	52.6	6	161	37.3
B1	6	63	95.2	6	90	66.7	6	95	63.2	6	115	52.2
Slab S1												
ε (%)	0.110			0.176			0.242			0.362		
A1	16	46	50.1	16	66	34.9	16	74	31.1	15	79	27.3
B1	15	39	55.4	15	49	44.1	16	58	39.7	16	67	34.4
A2	16	57	50.5	15	67	40.3	16	85	33.9	15	91	29.7
B2	15	51	52.9	16	61	47.2	16	77	37.4	16	84	34.3
Slab S2												
ε (%)	0.178			0.300			0.445					
A1	32	44	53.1	32	65	35.9	32	75	31.1			
B1	27	31	63.6	27	42	46.9	27	47	41.9			
A2	30	53	51.7	30	67	40.9	30	75	36.5			
B2	29	47	56.3	29	62	42.7	29	68	38.9			
Slab S3N												
ε (%)	0.14.			0.231			0.315					
A1	42	56	39.4	42	76	29.0	42	84	26.3			
B1	30	29	54.3	30	37	42.6	30	40	39.4			
A2	41	59	43.4	41	74	34.6	41	82	31.3			
B2	31	37	52.4	31	47	41.2	31	47	41.2			
Slab S4												
ε (%)	0.218			0.272			0.348			0.410		
A1	41	43	39.0	41	47	35.7	41	55	30.5	41	60	28.0
B1	31	28	45.3	31	30	42.3	31	32	39.7	31	33	38.5
A2	42	40	51.2	49	42	48.8	42	50	41.0	42	59	39.4
B2	30	26	56.3	30	27	54.2	30	30	48.8	30	32	45.7
Slab S5												
ε (%)	0.115			0.180			0.273					
A1	32	15	73.0	50	29	59.0	50	35	48.9			
B1	28	12	79.9	39	20	66.7	39	24	55.6			
A2	34	19	72.9	50	40	50.9	50	51	40.0			
B2	26	13	81.5	39	24	66.2	39	28	56.8			

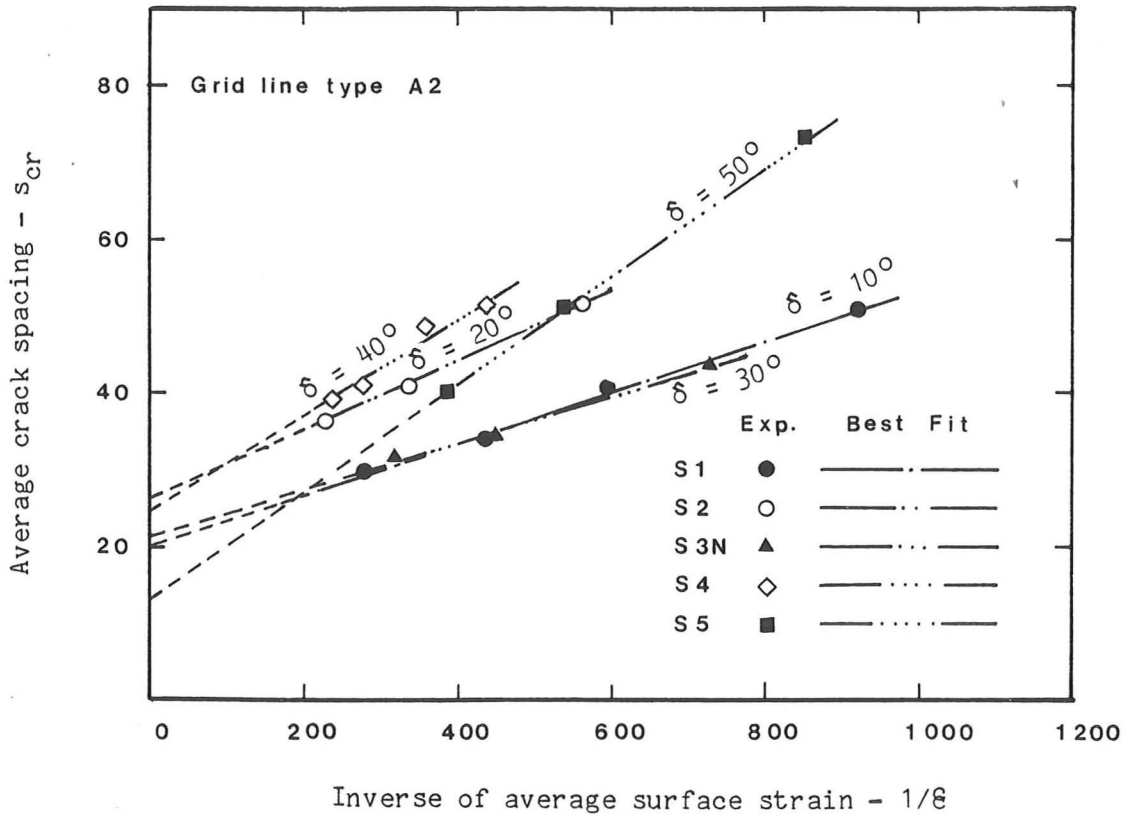

Figure 6.3-5 Experimental relations between average crack spacing, for a grid line above a bar of set 1, and the inverse of average surface strain for slabs S0 → S5.

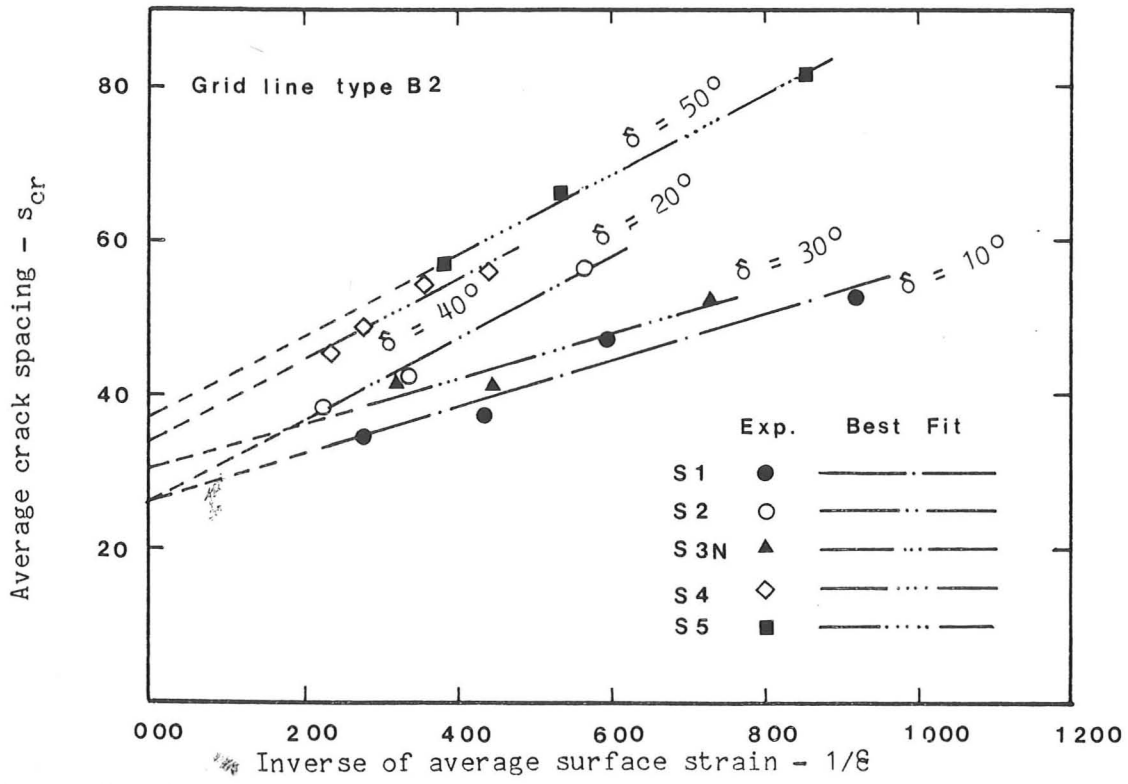

Figure 6.3-6 Experimental relations between average crack spacing, for a grid line midway between a bar of set 1, and the inverse of average surface strain for slabs S0 → S5.

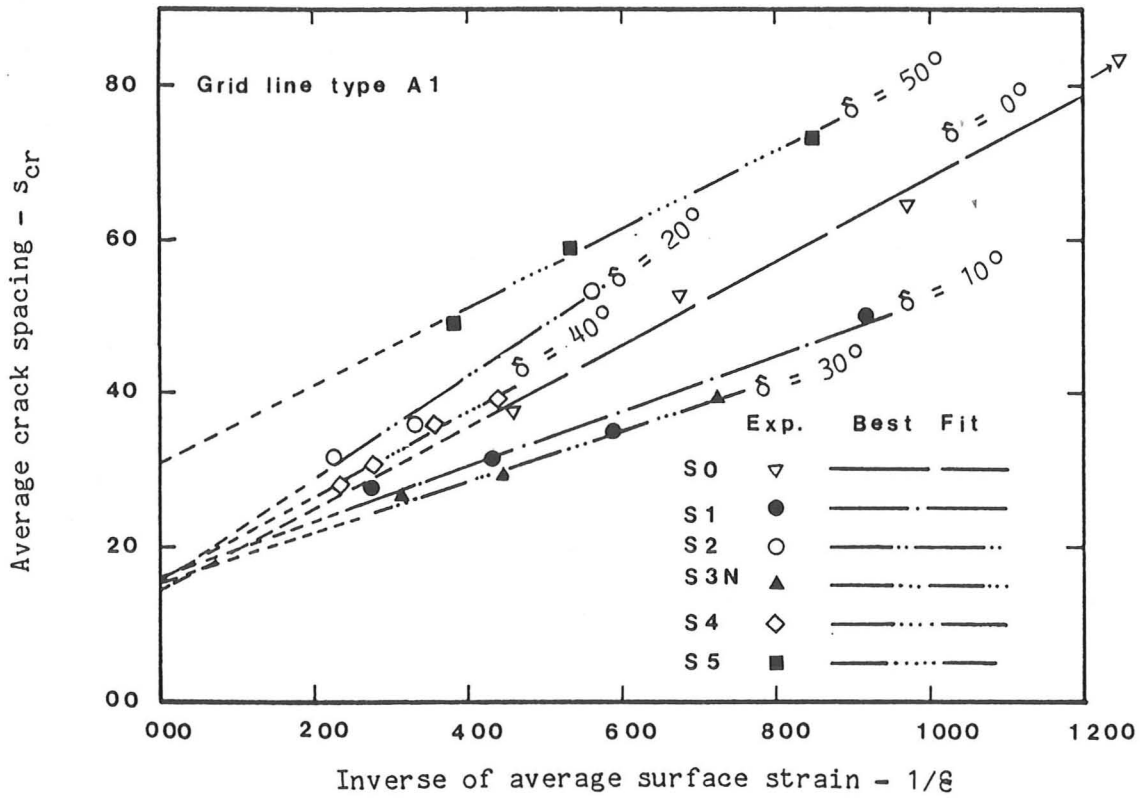

Figure 6.3-7 Experimental relations between average crack spacing, for a grid line above a bar of set 2, and the inverse of average surface strain for slabs S0 → S5.

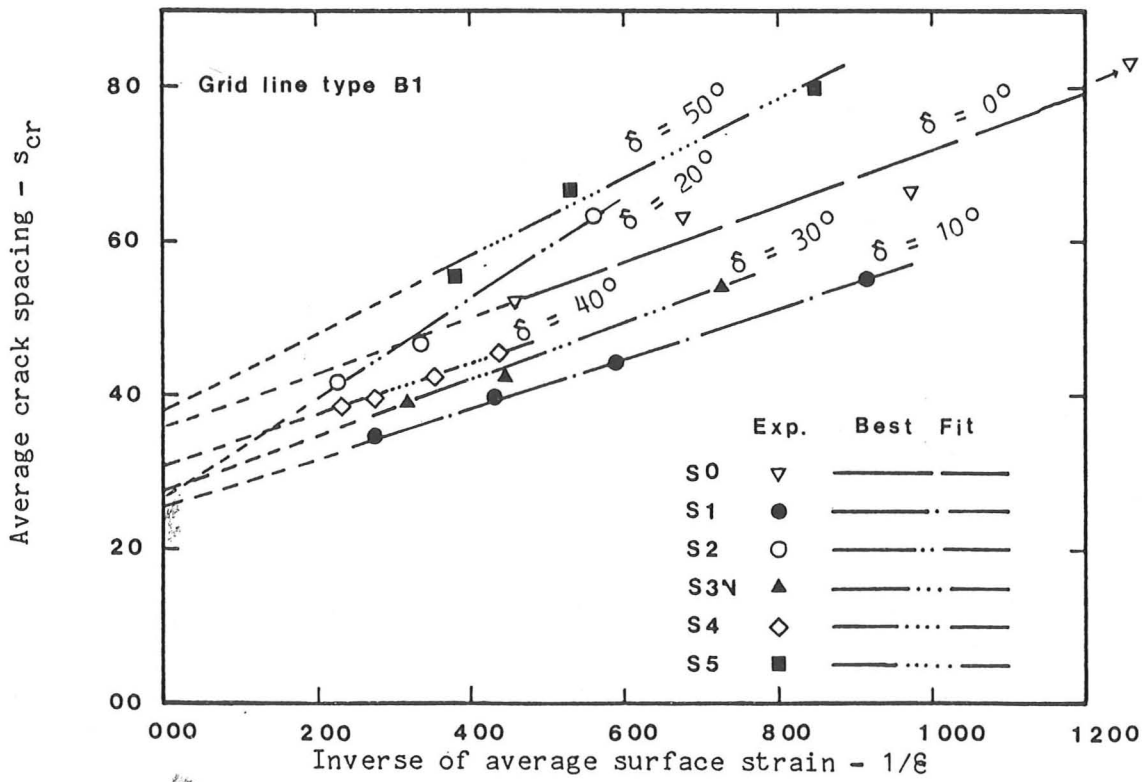

Figure 6.3-8 Experimental relations between average crack spacing, for a grid line midway between a bar of set 2, and the inverse of average surface strain for slabs S0 → S5.

6.4.1 Crack width - surface strain relations

In the extensive research on flexural cracks in beams by Base et al [9],[10], it was found that the crack width is proportional to the measured surface strain at the level where the cracks were measured. This conclusion was found to be true in the case of slabs with reinforcement in the principal moment direction as demonstrated by Beeby [19].

For each of slabs S0 to S5, the average crack width W_{av} at each load stage in which cracks were measured was plotted against the relevant average surface strain ε as shown in Figure 6.4-1. Also plotted on the graphs of this figure is the maximum crack width W_{max}. The values of W_{av}, W_{max} and ε at load stages of crack width measurements for slabs S0 to S5 are given in Table 6.4-1

Table 6.4-1 Values of W_{av}, W_{max}, and ε.

Slab No.	strain ε %	No. of cracks	W_{av} mm	W_{max} mm		Slab No.	Strain ε %	No. of cracks	W_{av} mm	W_{max} mm
S0	0.068	158	0.022	0.054		-	-	-	-	-
	0.103	228	0.027	0.063		S3N	0.140	181	0.051	0.123
	0.148	242	0.044	0.121			0.231	234	0.072	0.197
	0.197	339	0.071	0.172			0.315	253	0.100	0.263
S1	0.110	181	0.036	0.084		S4	0.218	134	0.085	0.226
	0.176	237	0.051	0.156			0.272	142	0.104	0.290
	0.242	263	0.068	0.178			0.348	162	0.118	0.343
	0.362	303	0.092	0.267			0.410	172	0.141	0.395
S2	0.178	175	0.05	0.116		S5	0.115	58	0.082	0.189
	0.300	236	0.078	0.192			0.180	114	0.095	0.258
	0.445	265	0.122	0.308			0.273	139	0.124	0.328

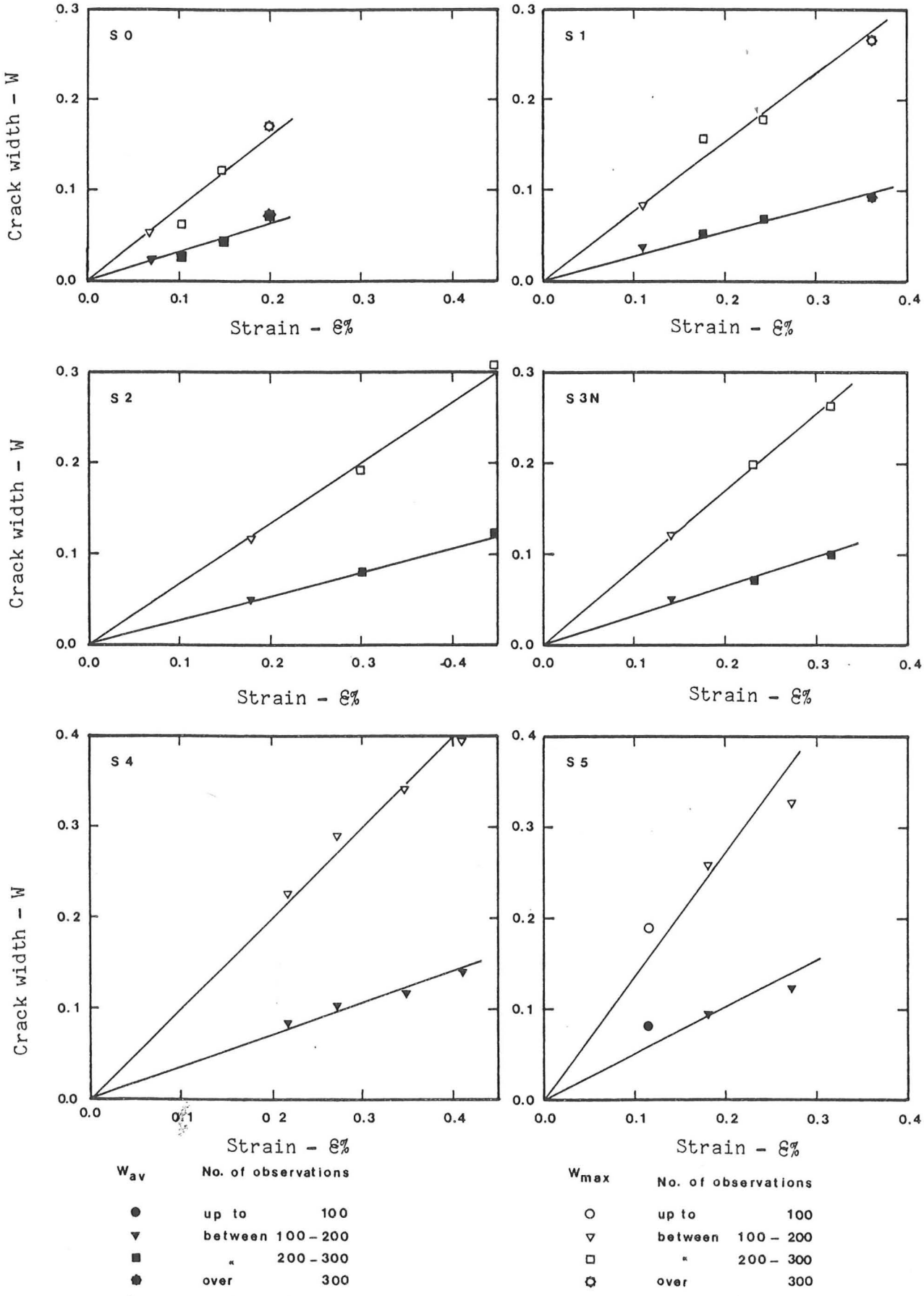

Figure 6.4-1 Experimental relationships between each of average and maximum crack widths and corresponding average surface strains for slabs S0 → S5 with best fit straight lines forced through the origin.

It can be seen from Figure 6.4-1 that, with the exception of slab S5, a straight line best fit forced through the origin agrees well with the data points. Therefore, the parameter $W/\hat{\epsilon}$ (i.e. the slope of the $W-\hat{\epsilon}$ graph) will be used in the analysis carried out here. Thus, we will be able to deal with all the cracks measured in one slab test as one sample by dividing each crack width by the relevant surface strain.

6.4.2 Effect of angle δ - some theoretical considerations

Tests by Beeby [19] on slabs spanning one way and reinforced in the main bending direction have led to a new hypothesis describing the cracking process in concrete members as reviewed in Chapter 2. This may be outlined as follows.

The actual crack pattern occuring at any point on a member is the result of an interaction between two basic crack patterns:

(1) A crack pattern controlled by the initial crack height h_o.

(2) A crack pattern controlled by the proximity of the reinforcement.

Directly over the reinforcement, pattern 2 dominates but, with increasing distance from the bars, the crack pattern approaches 1 asymptotically.

Formulae for the prediction of crack width and crack spacings were derived from these tests by Beeby [19]. These formulae are only directly applicable to situations in which cracks are perpendicular to the steel; thus, problems of interpreting these formulae arise in situations in which the crack direction is at an angle to the principal bending direction.

Clark [38] suggested a certain procedure to allow for the effect of the angle δ when using Beeby's formulae (see Subsection 2.2.3). Note that Clark had based his procedure on Beeby's formulae given in reference [19] but, in a later report on cracking in r.c. members subject to pure tension [33], Beeby gave a revised version of these formulae.

The procedure used by Clark can be outlined as follows:

(1) The steel is resolved into the principal bending direction. For a slab cracked in one direction only, the equivalent area of steel per unit width in this direction is A_{se} where

$$A_{se} = A_s \cos^4 \delta \quad \ldots \quad \ldots (6.4\text{-}1)$$

where A_s is the area per unit width normal to the steel bars. If there are more than one set of bars, then the effect of these will be added up in the usual way.

(2) The initial crack height h_o is calculated using the classical no-tension theory and the appropriate A_{se} value from Equation 6.4-1.

(3) The ratio W_{lim}/ε is calcuated - W_{lim} is the crack width which is approached as $a_{cr} \rightarrow \infty$, where a_{cr} is the distance from point of measurement of crack to surface of nearest reinforcing bar. W_{lim} depends mainly on h_o.

(4) The area of concrete surrounding a bar A_c is calculated for each set of bars independently, according to the definition given by Beeby (see Figure 2.2-6a page 26).

(5) The ratio W_o/ε, where W_o is the crack width directly over a bar, is calculated for each set of bars independently using

Equation 2.2-13.

(6) The crack width at any given required point is calculated using Equation 2.2-11 with a_{cr} measured perpendicular to the bars.

It is felt that the above procedure may not give enough allowance for the effect of the angle δ on crack widths directly over bars. The only adjustments made to Beeby's crack width formulae was resolving the steel into a direction perpendicular to the cracks'. This will only influence the initial crack height h_o which in its turn has a minor effect on the value of W_o as can be seen from Equation 2.2-13. To illustrate this, three hypothetical slabs are considered with identical dimensions, material properties, and steel arrangements except for the steel skewness angle δ which takes the values 10^o, 45^o, and 80^o (see Table 6.4-2). The values of W_o/ε for each of the three slabs were calculated using Clark's procedure plus the following equation (as revised by Beeby [33]) instead of Equation 2.2-13:

$$\frac{W_o}{\varepsilon} = K_1\, c + K_2 \sqrt{\frac{C1}{C2}} \left(\frac{c\ C2}{2\ D}\right) \exp(-4\ c/h_o) \quad \ldots\ldots\ (2.2\text{-}15)$$

In Figure 6.4-2, the theoretical values of W_o/ε are plotted against $\cos^4 \delta$ which is a convenient measure of the influence of δ on the stiffness provided by a set of bars (Equation 6.4-1). The experimental curve drawn on the graph is an approximation of results from tests on similar slabs (Chapter 4). It can be seen that the crack width over bars for a slab with $\delta=80^o$ is in theory only about 15% higher than that for an identical slab but with $\delta=10^o$. This may be unreasonable, since for a slab with $\delta \rightarrow 90^o$ we face a slab equivalent to a plain concrete slab.

Table 6.4-2 Dimension of hypothetical slabs.

Slab No.	Angle δ^o	Breadth mm	Height mm	Diameter D	Cover c_1	Cover c_2	Spacing s_1	Spacing s_2
1	10	1000.0	80.0	8.0	10.0	18.0	125.0	105.0
2	45	1000.0	80.0	8.0	10.0	18.0	125.0	105.0
3	80	1000.0	80.0	8.0	10.0	18.0	125.0	105.0

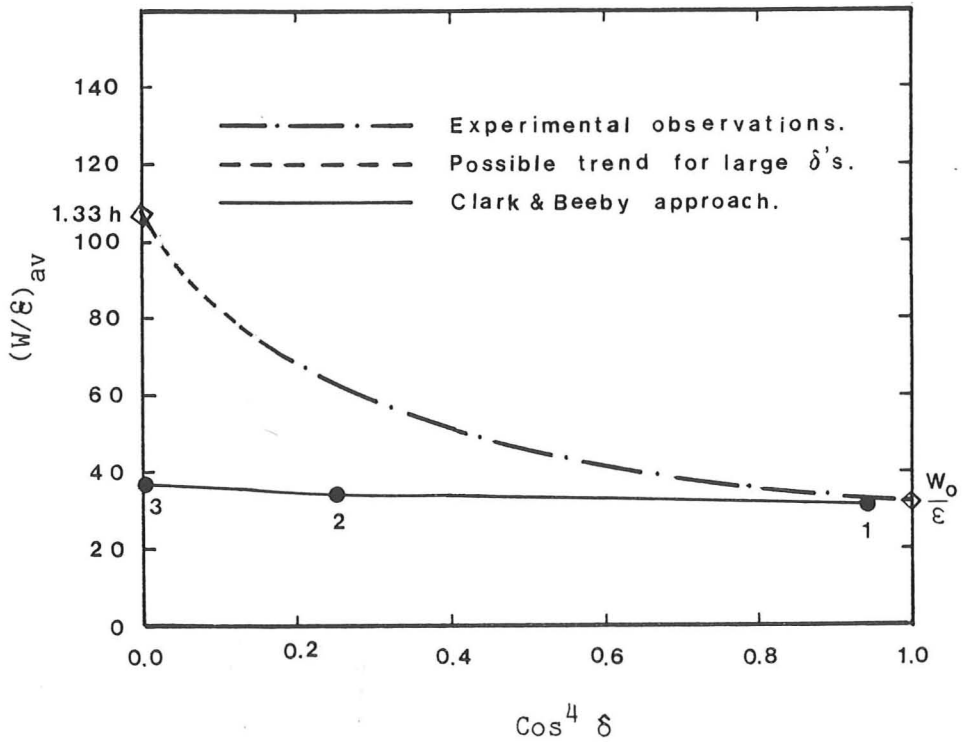

Figure 6.4-2 Theoretical relations between ratio of average crack width to average surface strain and the 4th power of cosine the angle δ.

Table 6.4-2 Dimension of hypothetical slabs.

Slab No.	Angle δ^o	Breadth mm	Height mm	Diameter D	Cover c_1	Cover c_2	Spacing s_1	Spacing s_2
1	10	1000.0	80.0	8.0	10.0	18.0	125.0	105.0
2	45	1000.0	80.0	8.0	10.0	18.0	125.0	105.0
3	80	1000.0	80.0	8.0	10.0	18.0	125.0	105.0

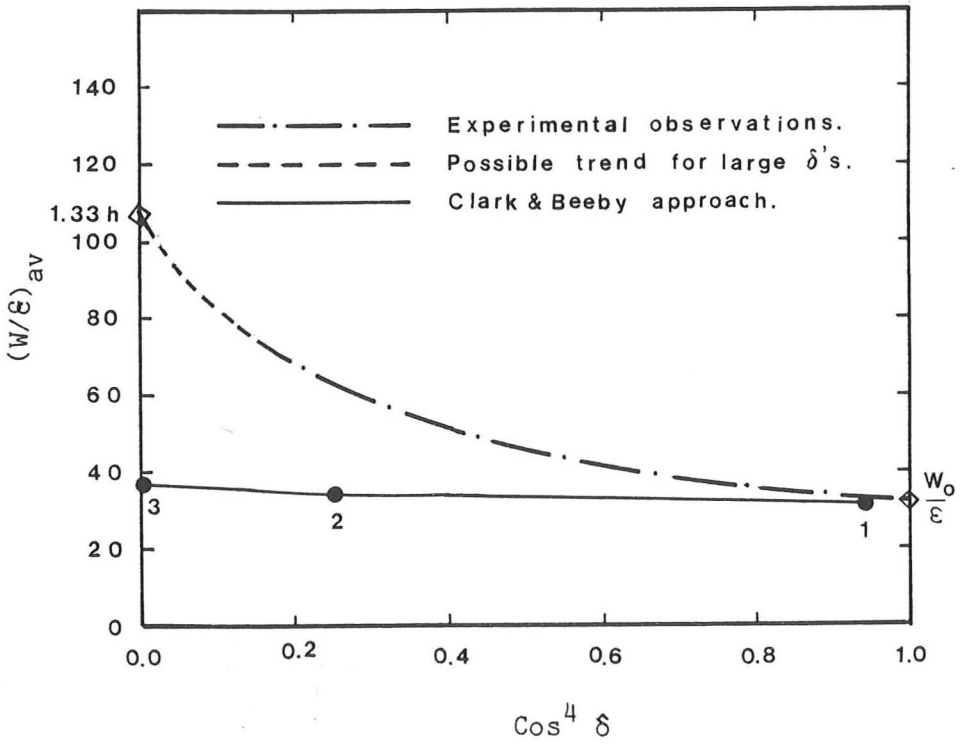

Figure 6.4-2 Theoretical relations between ratio of average crack width to average surface strain and the 4th power of cosine the angle δ.

In a plain concrete member subject to uniaxial bending, only one major crack can form. The ratio W/ε, which is closely related to the crack spacing, would then be expected to be very large: though not well defined for a single crack, W/ε would be of the order of the span of the beam. However, if we assume that there will always be some small amount of steel crossing the cracks, so that more than a single crack forms, then W_o/ε will take a finite value even over bars which have a value of $\delta \to 90^o$. This limited value of W_o/ε for cracks over the set of bars with $\delta \to 90^o$ will presumably be equal to W_{lim}/ε calculated using a value of h_o equal to the thickness of the slab h (the maximum possible value of h_o, for a very low equivalent steel percentage) as shown in Figure 6.4-3. Here we assume that as $\delta \to 90^o$ the influence of bond and cover diminishes, and the distinction between cracks over and cracks between bars tends to vanish. Thus, the ratio $(W_o/\varepsilon)_\delta$ is expected to vary from $(W_o/\varepsilon)_o$ to $(W_{lim}/\varepsilon)_{90^o}$ as the angle δ changes from 0^o to 90^o. This point will be discussed further in the next subsection on experimental results.

6.4.3 Effect of angle δ: Experimental results

Figure 6.4-4 shows the experimentally obtained frequency distribution of the crack width - surface strain ratios for region type AA of slab S4. Superimposed on this graph is the distribution of the W/ε values for region type BB of the same slab. The value of ε used are the surface strains averaged over the constant moment zone and are the same for all types of region. It can be seen from this figure that in regions above steel reinforcement (type AA), a higher percentage is obtained of values of W/ε below average than in regions away from reinforcement (type BB). This is compatible with the theory of cracking in slabs given by

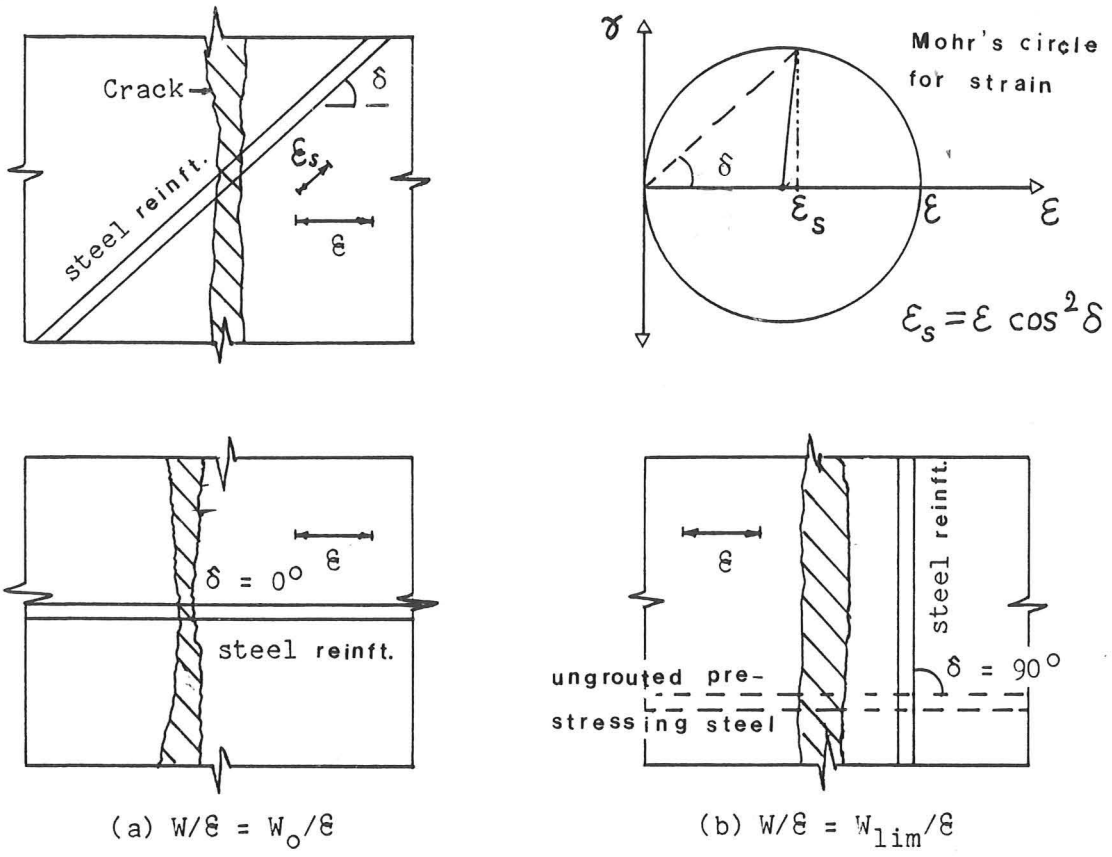

Figure 6.4-3 Limiting cases for a situation in which a reinforcing bar crosses a crack at an angle.

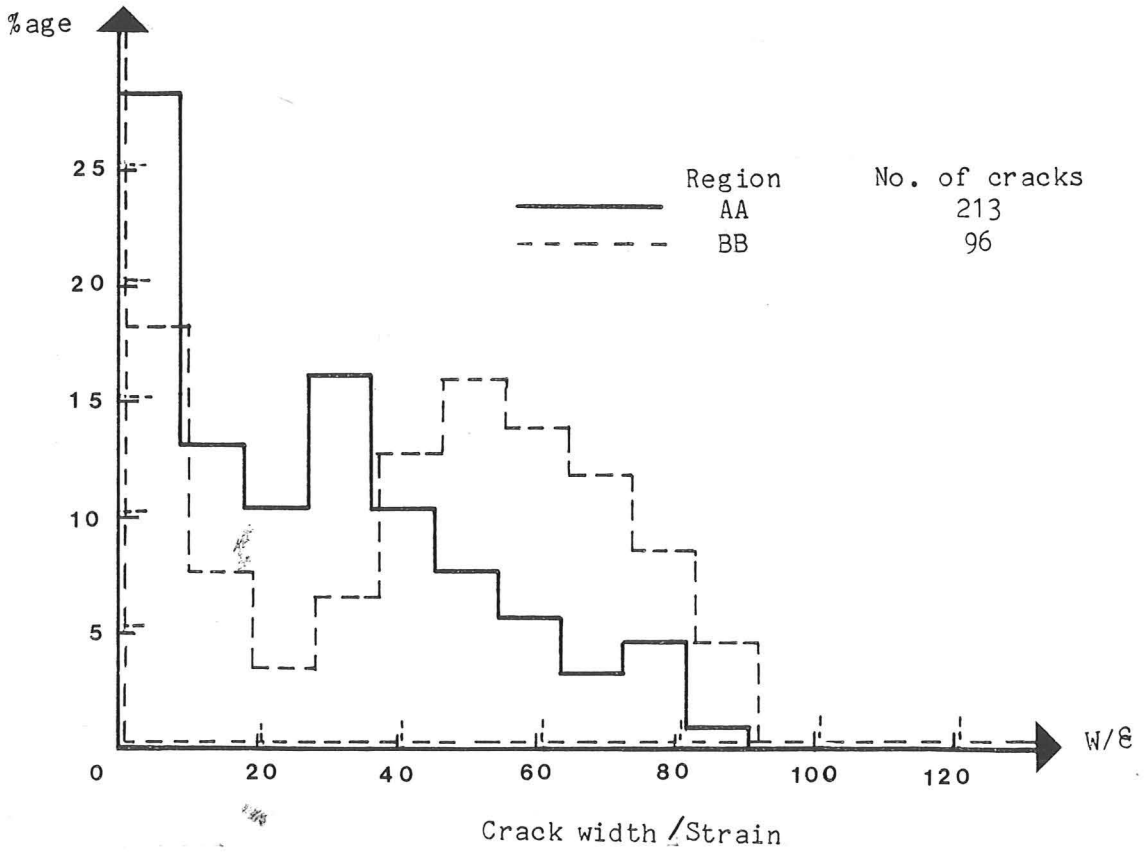

Figure 6.4-4 Experimentally obtained frequency distributions of W/ε for regions type AA and BB of slab S4.

Beeby [54],[65] which predicts smaller crack spacing and hence smaller crack widths in the proximity of reinforcement.

The experimentally obtained frequency distributions of the W/ℓ values for each of the slabs S0 $\rightarrow$ S5 are drawn against $\cos^4\delta$ in Figure 6.4-5. The W/ℓ values from all load stages and at all the different positions are treated as one sample. The number of crack measurements each histogram represents is given in between curled brackets. The median of each of these histograms (value of W/ℓ exceeded by 50% of the results) and that exceeded by 2% of the results are marked along the base of each histogram. It can be seen from Figure 6.4-5 that as δ increases, the values of $(W/\ell)_{50\%}$ and $(W/\ell)_{2\%}$ increase. This increase becomes sharper beyond a value of δ equal to 45° ($\cos^4 45^\circ = 0.25$). This indicates a need perhaps for more experimental data from tests on slabs with steel skewness angle of $\delta > 45^\circ$. However, experiments become difficult in such situations, since the yielding moment decreases towards the cracking moment as δ increases and becomes lower than this moment for high values of δ. In cases like this, as in slab S6, the zone where cracks first appear becomes the failure zone before the cracks have the chance to spread all over the tension zone.

The general shape of the histograms of Figure 6.4-5 does not seem to change significantly as the angle δ changes. The histograms for slabs with higher δ values have more intermediate shapes than those for slab S0 ($\delta = 0^\circ$) due to the increase in the number of blocks into which the data are divided. Thus, when the histogram of slab S5 ($\delta = 50^\circ$) was redrawn with a reduced base length equal to that of the histogram of slab S0, it was made clear that there is no significant difference between the shapes of the two histograms as demonstrated in Figure 6.4-6.

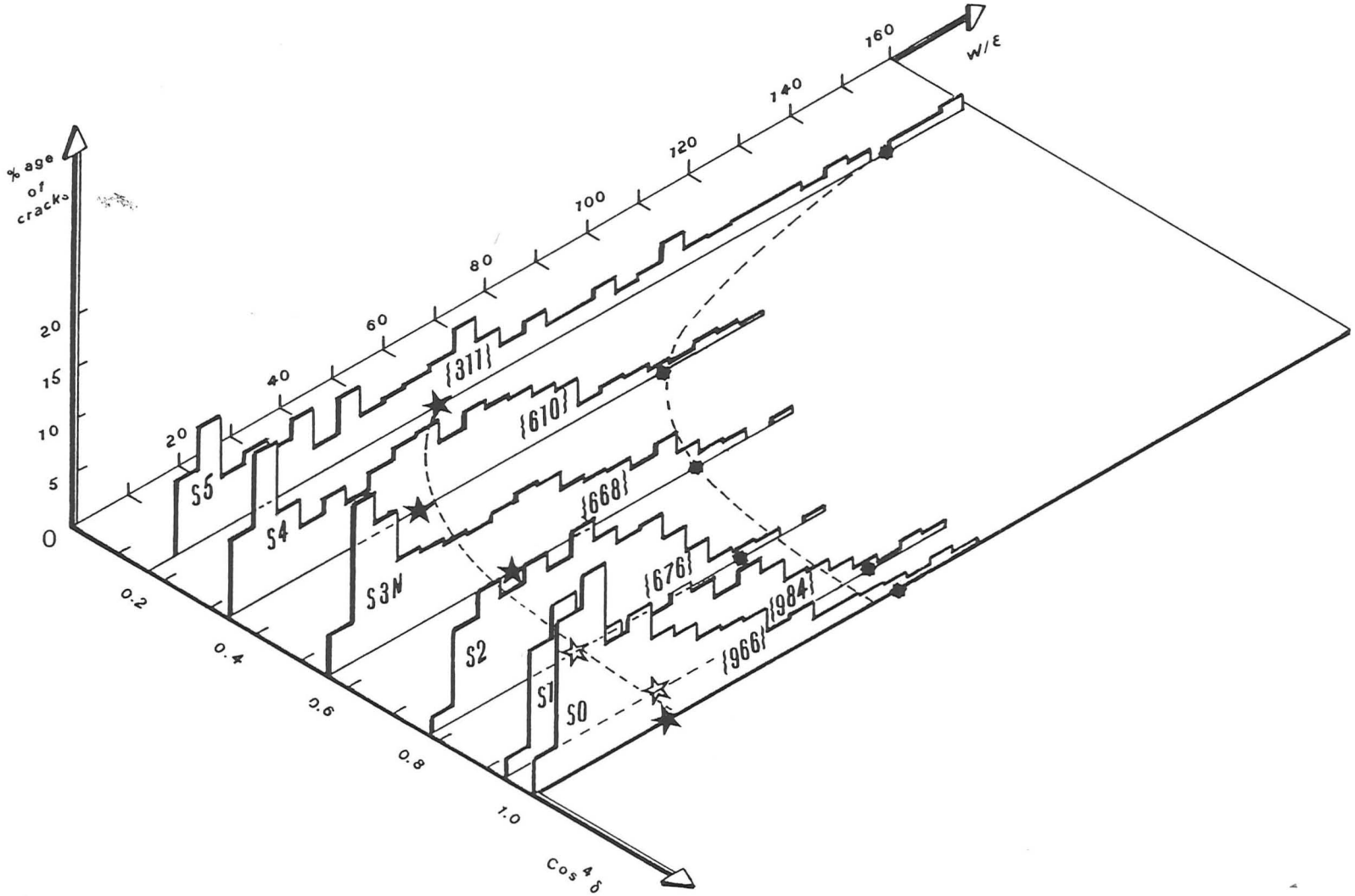

Figure 6.4-5 A three dimentional view showing the experimentally obtained histograms of W/ε for slabs S0 → S5 drawn against $\cos^4 \delta$.

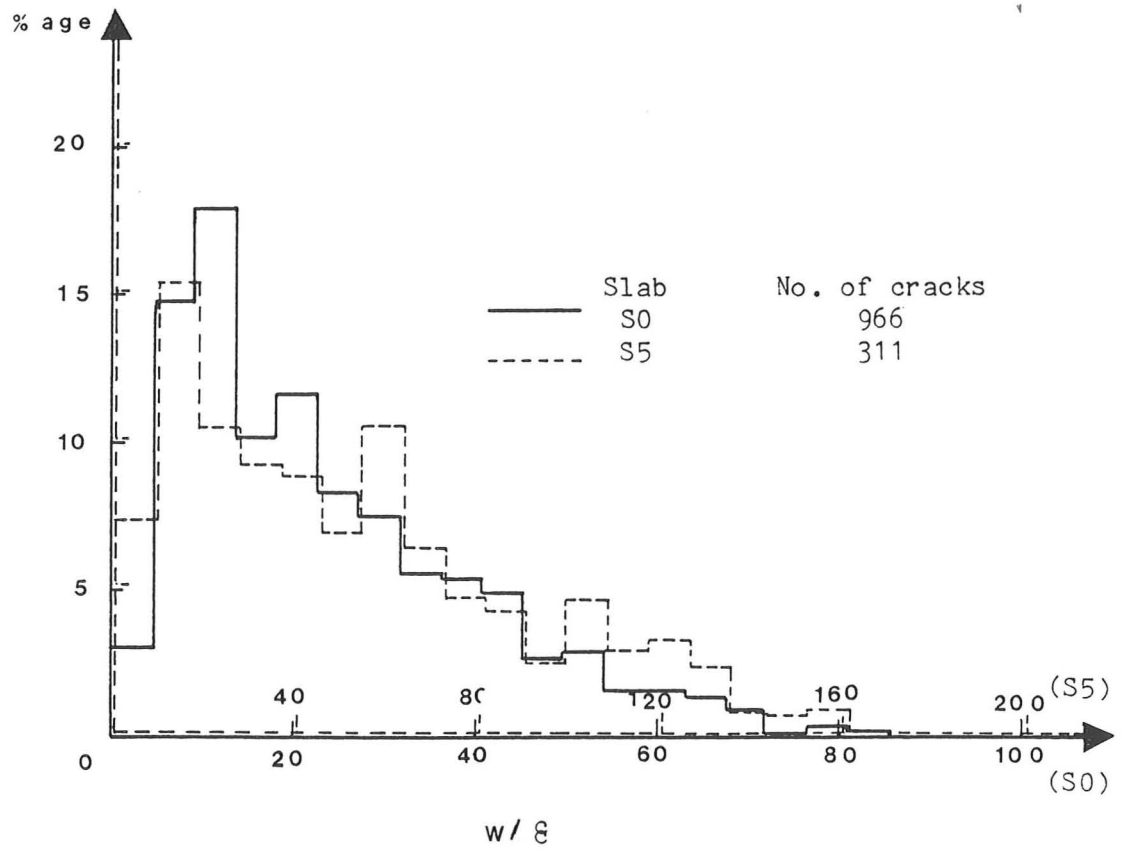

Figure 6.4-6 Comparison between the experimentally obtained histograms of W/ℓ for slabs S0 and S5.

Table 6.4-5 gives the experimental values of $(W/\ell)_{av}$, $(W/\ell)_{2\%}$ and $(W/\ell)_{max}$ for both directions in each of the four regions for slabs S1 → S5. In Table 6.4-4, the experimental values of the same parameters for each of the four types of grid lines are given for slabs S0 → S5.

Experimental results from Table 6.3-5 show that differences between regions of different types reduces as the angle δ increases. This means that the influence of steel reinforcement on the crack pattern reduces as δ increases. This conclusion has already been drawn from observations of the fully developed crack patterns of slabs S0 → S5 shown in

Figure 6.2-3. Based on these experimental observations and on the theoretical considerations given in Section 6.4-2, a hypothesis is put forward for cracking over reinforcing bars that cross the cracks at an angle. This hypothesis may be outlined as follows:

(1) The crack pattern at a position away from reinforcement is governed by the initial crack height ho (pattern 1 in Beeby's hypothesis) assuming a minimum amount of steel in the principal bending direction.

(2) The addition of steel bars in the crack direction will not in theory affect the crack pattern (see Figure 6.4-3b). Some experiments [25] showed that the effect of transverse bars is insignificant.

(3) As the angle δ between the reinforcement direction and that normal to the cracks decreases, the initial crack pattern is gradually modified until, at $\delta = 0^{o}$, the crack pattern governed by the proximity of the steel (pattern 2 in Beeby's case) is obtained (Figure 6.4-3a).

(4) The amount of modification made to the initial crack pattern by the skew steel bars is likely to depend on the ratio of the strain in the steel direction to the strain in the principal stresses direction. This ratio is equal to $\cos^{2}\delta$ and thus varies from 0 to 1 as δ decreases from 90^{o} to 0^{o}.

In order to examine the above hypothesis, the values of $(\varepsilon/W)_{av}$ for grid line of type A1 and B1 (above and midway between bars of steel set 1) are plotted against $\cos^{2}\delta$ as shown in Figure 6.4-7. A straight line is fitted to each of the two groups of data points. The values of $(W/\varepsilon)_{av}$ for

$\delta = 90^{\circ}$ may be obtained from the (ℓ/W)-axis intercepts of the best fit lines of Figure 6.4-7. The two values of $(W/\ell)_{av}$ thus obtained were found to be about 109 mm - a value which is very close to 1.33 times the thickness of the slab h nominally equal to 80mm. This value (1.33h) forms a lower bound to W_{lim}/ℓ and can be obtained when $h_o \rightarrow h$ as it does the case in slabs with steel skewness angle $\delta = 90^{\circ}$. Thus, the hypothesis given above adequately describes the effect of the skewness angle δ on cracking above skew reinforcing bars in slabs.

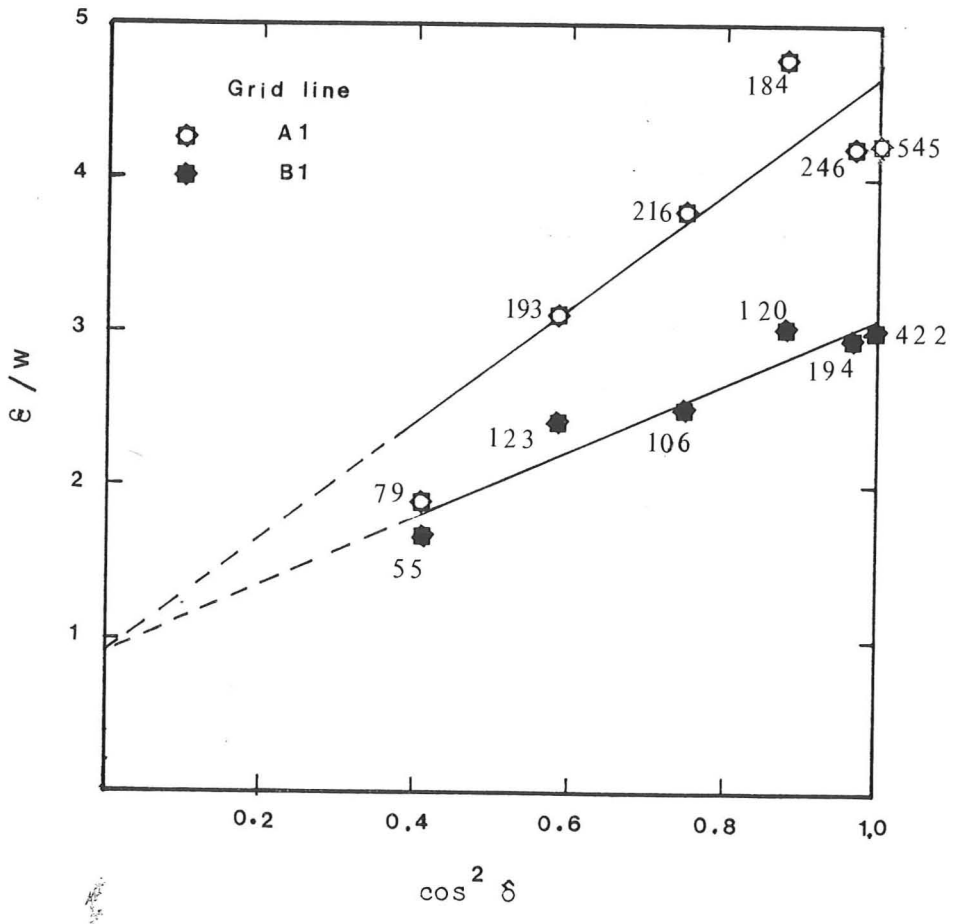

Figure 6.4-7 A graph of $(\ell/W)_{av}$ plotted against $\cos^2 \delta$ for grid lines above and midway between bars of set 1.

The value of $(W_o/\varepsilon)_\delta$, i.e. the ratio W/ε over steel bars with an angle δ to the principal bending direction, may be calculated from the equation given below which was derived using the linear relationship between ε/W_o and $\cos^2\delta$ demonstrated in Figure 6.4-7.

$$\frac{W_o}{\varepsilon}_\delta = \frac{(W_o/\varepsilon)(W_{lim}/\varepsilon)}{(W_{lim}/\varepsilon)\cos^2\delta + (W_o/\varepsilon)(1 - \cos^2\delta)}$$

or

$$(W_o)_\delta = \frac{W_o\, W_{lim}}{W_{lim}\cos^2\delta + W_o \sin^2\delta} \quad \ldots \quad \ldots (6.4\text{-}2)$$

where

W_{lim}/ε is given by Equation 2.2-12, and

W_o/ε is given by Equation 2.2-15.

To estimate the crack width exceeded by a certain percentage of the results or the average value of W at any position on the slab, Equation 2.2-11 might be used with due regard to the value of a_{cr} in cases where $\delta > 0$. The evaluation of the distance a_{cr} in such cases is not a straight forward task and is discussed in the following section.

6.4.4 Calculating a_{cr} when $\delta > 0^o$

The first question that one faces when calculating the distance a_{cr}, from the point considered to the nearest reinforcing bar, in situations where $\delta > 0^o$ is whether to calculate this distance in a direction along the crack or else in a direction normal to the bar. Clark [38] suggested

the latter distance since it is the shorter of the two, however, it becomes clear that this is not the right solution when the nearest bar runs in the crack direction, i.e. $\delta = 90^{o}$. Furthermore, proximity of the steel controls cracking by passing across cracks and thus the distance to the position where the nearest bar crosses the crack is what should be calculated and not the shortest distance to the nearest bar.

Another question arises when calculating a_{cr} for δ values $> 0^{o}$, and that is how to account for the interaction between the two sets of bars. The presence of two sets of intersecting bars means that calculating a_{cr} is not simple or straight-forward. Considering Figure 6.4-8 which shows two set of intersecting grid lines above and midway between steel bars we can see that the distance a_{cr} varies as we go along a grid line. For example, the distance a_{cr} from a grid line midway between bars of set 1 (type B1) to the nearest steel bar changes from a minimum equal to c_2 (the cover to the steel of the other direction) to a maximum equal to a_x. The distance a_x is taken to be the least of the two space distances each measured from the point of intersection of two grid lines of type B (e.g. point x in Figure 6.4-8) to the nearest bar of one of the two sets of bars in a direction parallel to that of cracks. Thus, the following expressions can be written for a_{cr} for each of the four types of grid lines.

(1) For grid lines of type A1 (above reinforcing bars in direction 1 closest to the tension face),

$$a_{cr} = c_1 \quad \ldots \qquad \ldots (6.4\text{-}3)$$

(2) For grid lines of type A2 (above reinforcing bars in direction 2),

$$a_{cr} = c_2 \quad \ldots \qquad \ldots (6.4\text{-}4)$$

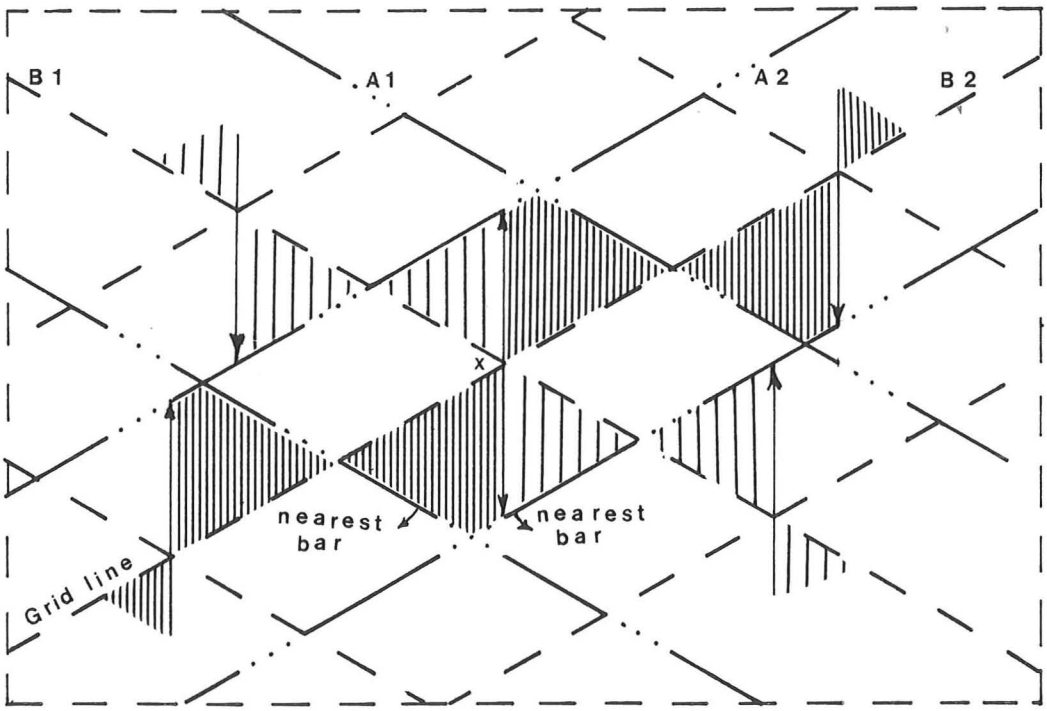

Figure 6.4-8 Variation of distance to the nearest reinforcing bar along grid lines midway between bars measured in the direction of cracks.

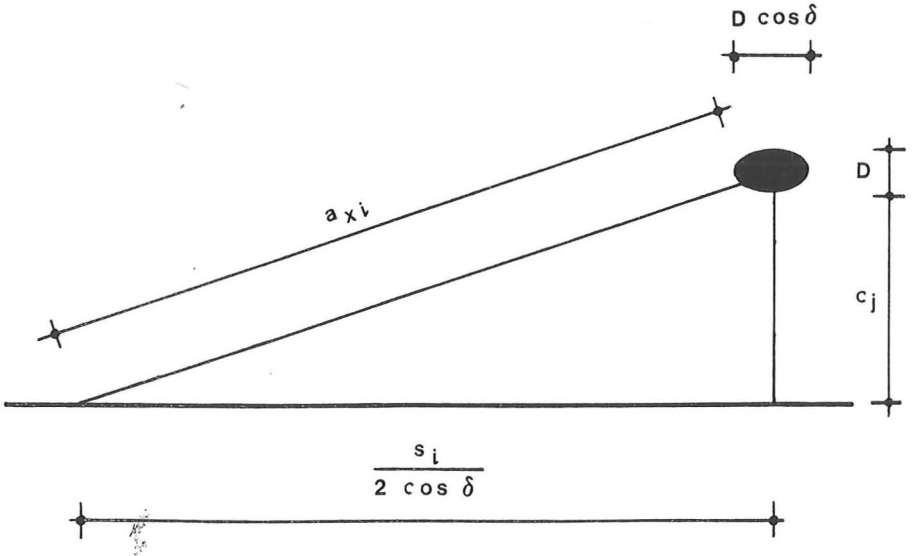

Figure 6.4-9 Illustration of calculating the distance a_{xi} from the point of intersection of grid lines B1 and B2 to the surface of nearest bar of set 2 (with smaller bar spacing).

In equation 6.4-4, the proximity of bars in direction 1 at and around points of intersection of bars has been neglected since it has small effect (less than 10%).

(3) For grid lines of type B2 (midway between bars in direction 2),

$$a_{cr} = \left\{\frac{s_2}{s_1}\right\}\left\{\frac{c_1 + a_{x1}}{2}\right\} + \left\{1 - \frac{s_2}{s_1}\right\}(a_{x2}) \quad \ldots \quad \ldots (6.4\text{-}5)$$

where s_2 and s_1 are the bar spacing in directions 2 and 1 respectively, with $s_2 < s_1$; and a_{x1} and a_{x2} are the space distances from grid lines type B1 and B2 to nearest bar in directions 1 and 2 respectively, both measured in the direction of cracks.

Thus, if i and j represent the two reinforcement directions (see Figure 6.4-9), then

$$a_{xi} = \sqrt{\left(\frac{s_i}{2\cos\theta}\right)^2 + \left(c_j + \frac{D}{2}\right)^2} - \frac{D}{2\cos\theta} \quad \ldots\ldots (6.4\text{-}6)$$

The last term at the right hand side of Equation 6.4-7 is an approximation of the actual distance from the center to the surface of the bar.

(4) For grid lines of type B1,

$$a_{cr} = \frac{c_2 + a_{ax2}}{2} \quad \ldots \quad \ldots (6.4\text{-}7)$$

where a_{x2} is given by Equation 6.4-6.

Table 6.4-3 gives the values of a_{cr} for each of the four types of grid line calculated for each slab using Equations 6.4-3 to 6.4-7. In Figure 6.4-10, values of $(\varepsilon/W)_{av}$ from Table 6.4-3 are plotted against $1/a_{cr}$ for each of the slabs S0 to S5 and a straight line is fitted to each set of data points. It can be seen that this linear relation seems reasonable and thus Equation 2.2-11 (page 23) for calculating W at any point on a slab's surface is still applicable in our case.

Table 6.4-4 gives the values of $(W/\varepsilon)_{av}$, $(W/\varepsilon)_{2\%}$, and $(W/\varepsilon)_{max}$ for each of the four types of grid line. The values of $(W/\varepsilon)_{av}$ are plotted aginst $\cos^2 \delta$ as shown in Figures 6.4-11a and b. The confidence interval is also shown on these graphs. In calculating the 95% confidence intervals, the frequency distributions of W/ε were assumed to be normal whereas in some cases (above steel bars) the distributions are skewed towards higher values. Thus, if ss is the sample standard deviation, the 95% confidence interval will be equal to $\pm\ t_{.025}\ ss/\sqrt{n}$, where $t_{.025}$ is the Student's t value. The theoretical curves shown in Figure 6.4-11 are those obtained using the procedure outlined in the next chapter. The agreement is good for grid lines over steel bars of set 1 and an over estimate is obtained for grid lines between steel bars. This overestimate might be due to the discontinuity in the theoretical relationship between the crack width and the distance from steel bars which results from ignoring interaction between the influence of parallel adjacent bars on cracking as illustrated in Figure 6.4-13.

Table 6.4-5 gives the experimental average, 2% chance of being exceeded, and the maximum values of W/ε for different types of region. In Figure 6.4-13, the values of $(W/\varepsilon)_{av}$ from table 6.4-5 are plotted against $\cos^2 \delta$. It can be noticed that the regions of type AA and AB have similar

Table 6.4-3 Values of a_{cr} calculated for each type of grid line (Equations 6.4-3 to 6.4-8).

Slab	Above steel bars		Midway between steel bars	
	set 1	set 2	set 1	set 2
S0	13.8	--	59.6	--
S1	11.1	19.1	34.0	39.6
S2	11.3	20.4	35.8	41.4
S3N	11.4	20.1	39.0	44.1
S4	13.0	21.8	43.6	49.7
S5	10.9	19.4	48.1	56.3

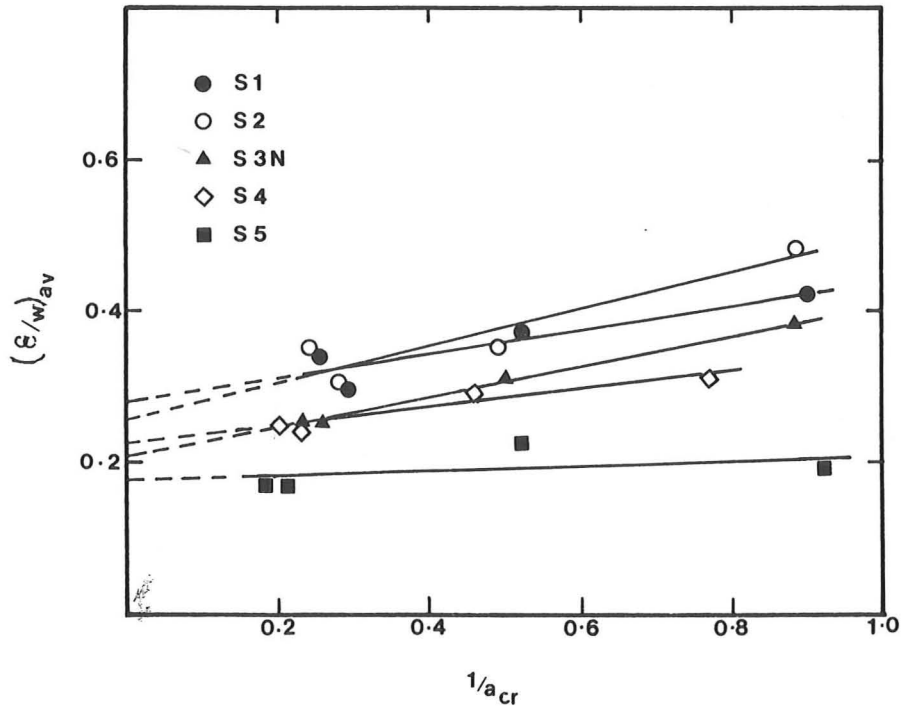

Figure 6.4-10 Experimental values of $(\epsilon/W)_{av}$ plotted against calculated values of $(1/a_{cr})$.

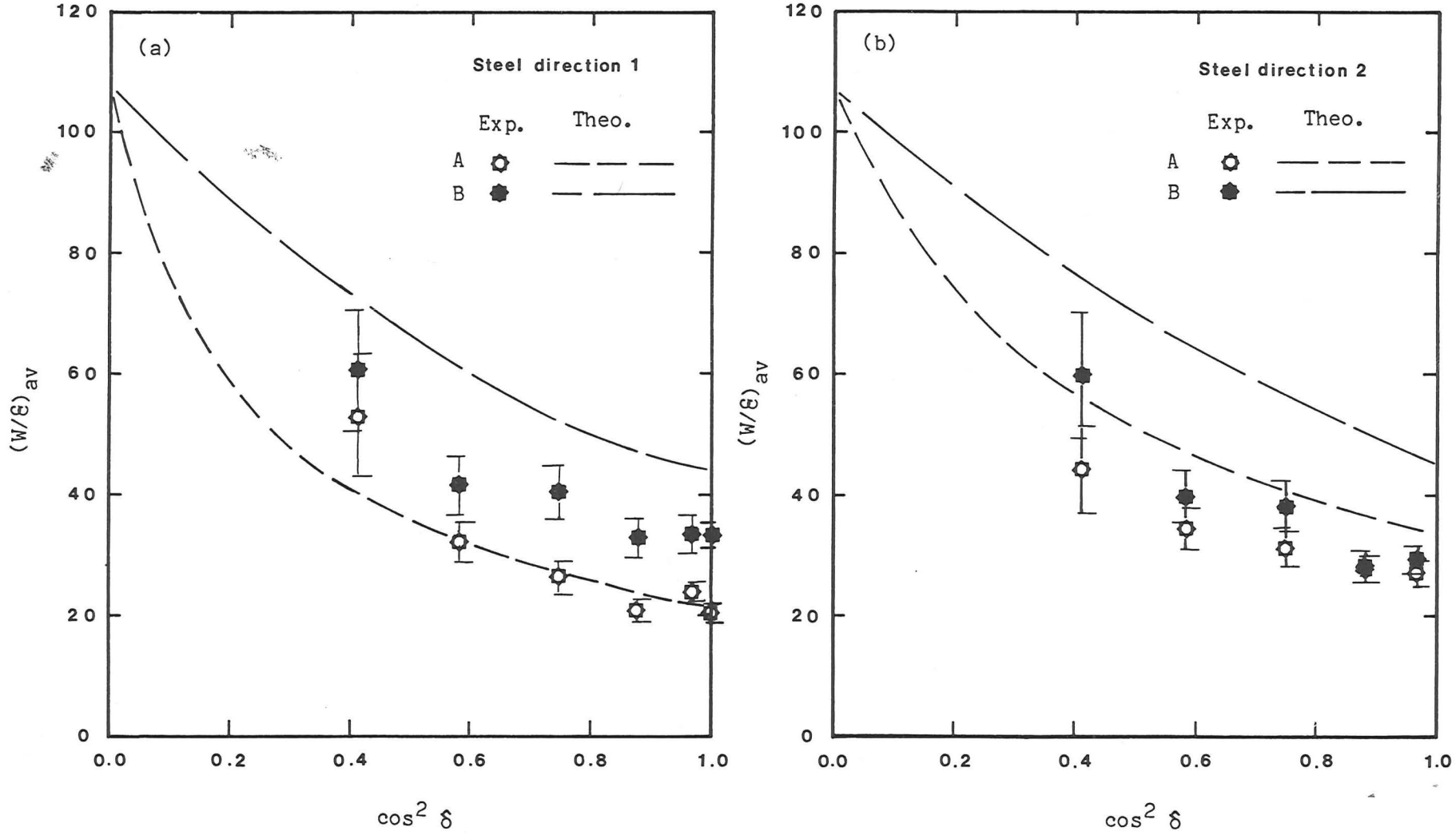

Figure 6.4-11 Experimental and theoretical relations between $(W/\varepsilon)_{av}$ and $\cos^2 \delta$ for different types of grid line.

Table 6.4-4 Experimental results according to the second classification.

Slab No.	Grid line type	Steel set 1				set 2			
		No. of observations	Value of W/ε mm			No. of observations	W/ε mm		
			av	2%	max		av	2%	max
S0	A	545	23.4	56.9	80.5	–	–	–	–
	B	422	36.3	77.9	90.8	–	–	–	–
S1	A	246	23.8	49.8	56.6	275	27.2	57.6	61.3
	B	194	33.8	76.0	80.0	269	29.7	65.6	79.3
S2	A	184	20.9	44.8	52.4	195	28.3	58.4	60.4
	B	120	33.0	64.4	74.5	177	28.9	58.1	64.1
S3N	A	216	26.5	73.1	78.5	215	31.8	75.2	86.0
	B	106	40.3	80.5	85.5	131	38.6	82.6	96.9
S4	A	193	32.1	83.5	113.8	179	34.6	89.4	102.0
	B	123	41.7	102.4	105.8	115	40.0	88.9	92.0
S5	A	79	52.9	158.3	165.1	111	44.5	135.0	165.1
	B	55	60.4	132.1	142.9	66	59.8	133.3	150.7

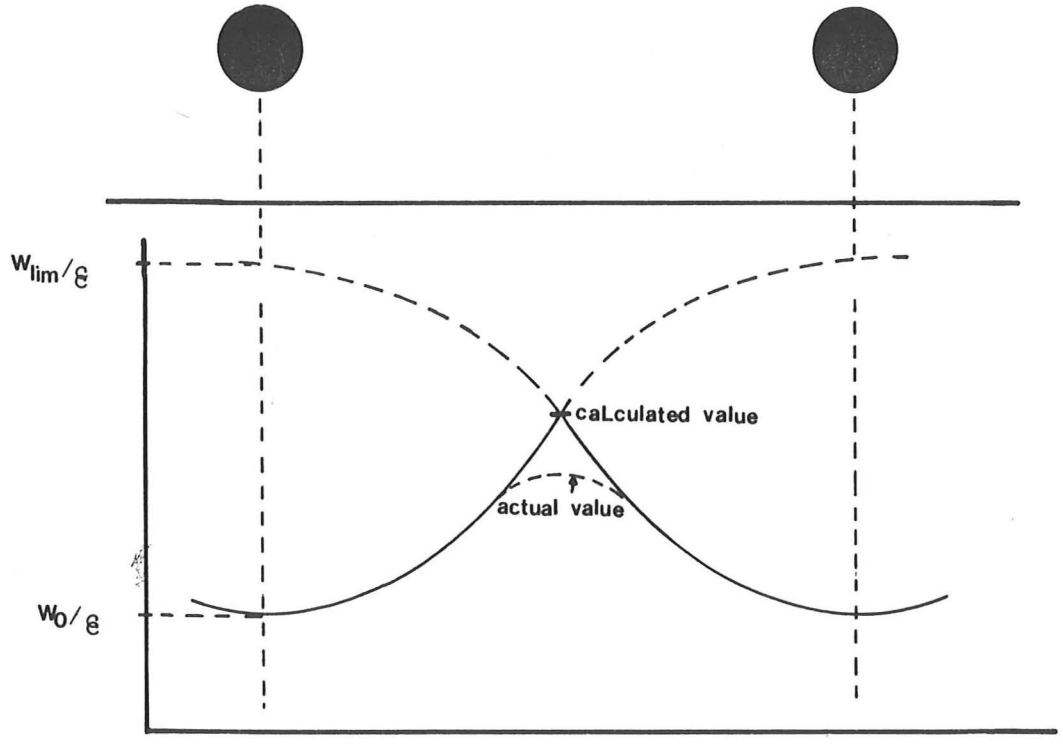

Figue &.4-12 Illustration of cause of overestimate in theoretical calculation of W/ε midway between two steel bars.

values of $(W/\varepsilon)_{av}$. This is because in both regions, the crack spacing which is governed by the minimum cover would be the same. Thus, the number of region types can be reduced from 4 to 3 different types of region as far as crack width calculations are concerned.

The value of a_{cr} for each type of region is calculated in a similar way to that explained above for different types of grid line. The following values of a_{cr} can thus be adopted for the different types of region:

(1) For regions of types AA and AB,

$$a_{cr} = c_1 \quad \ldots \qquad \ldots \text{ (Equation 6.4-3)}$$

(2) For regions of type BA,

$$a_{cr} = c_2 \quad \ldots \qquad \ldots \text{ (Equation 6.4-4)}$$

(3) For regions of type BB,

$$a_{cr} = (3\, c_2 + a_{x2})/4 \quad \ldots \qquad \ldots (6.4\text{-}8)$$

where a_{x2} is given by Equation 6.4-6.

The variability of a_{cr} within the boundaries of one region is much less than that along a grid line. Therefore, the division of the slab surface into regions seems to be a better alternative to the traditional 'grid lines' approach. In design, one needs to check crack widths at certain positions on the surface of r. c. members, e.g. over the reinforcement, and thus the 'regions' approach can be as useful in this respect as the 'grid lines' one.

6.5 Crack Width Prediction Procedure

The following is an outline of a procedure for calculating crack widths at any point of r. c. bending slabs with cracks running at an angle to the direction of main reinforcement.

(1) The crack width W_{lim} at a point well away from steel is calculated using Equation 2.2-12 (page 23).

(2) The crack width W_o over a reinforcing bar that runs in the principal bending direction is calculated using Equation 2.2-15 (page 25).

(3) Using the values of W_{lim} and W_o obtained in 1 and 2 above, the crack width $W_{o\delta}$ over a reinforcing bar that runs at an angle δ to the principal bending direction is calculated using Equation 6.4-2.

(4) The values of a_{cr} for different types of region (or of grid line if so wished) are calculated using Equations 6.4-3 to 6.4-8.

(5) Finally, Equation 2.2-11 (page 23) is used to calculate the crack width W in any type of region or grid line.

In Equations 2.2-11, 12, and 15, the constants used are chosen so that a crack width with some chance of being exceeded is obtained. This is the crack width needed in design.

Table 6.4-5 Experimental results according to the first classification.

Slab No.	Region type	Steel set 1				set 2			
		No. of observations	Value of w/ε - mm				w/ε - mm		
			av	2 %	max		av	2 %	max
S1	AA	116	23.9	48.5	56.6	145	26.8	57.7	59.7
	BB	95	37.1	77.1	80.2	111	34.8	72.5	79.3
	AB	130	23.7	49.8	52.9	158	26.2	61.5	69.7
	BA	99	30.6	62.2	64.7	130	27.6	56.5	61.3
S2	AA	114	21.2	43.8	52.4	105	29.9	55.8	60.4
	BB	54	38.6	65.2	74.5	81	31.7	63.2	64.1
	AB	70	20.5	41.2	46.8	96	26.6	55.6	56.1
	BA	66	28.3	54.5	60.4	90	26.5	55.4	60.4
S3N	AA	115	25.1	73.5	78.5	132	25.2	67.2	72.6
	BB	36	33.2	77.9	79.9	35	45.5	93.0	96.2
	AB	101	28.1	70.1	76.5	96	36.1	76.0	79.6
	BA	70	43.9	80.6	85.5	83	42.4	81.9	86.0
S4	AA	106	31.6	84.9	113.8	107	31.0	84.5	89.4
	BB	60	38.2	80.1	95.1	36	61.5	91.9	92.0
	AB	87	32.6	70.0	74.3	79	30.2	66.2	67.6
	BA	63	45.0	104.4	105.8	72	40.0	95.9	102.0
S5	AA	46	53.56	164.3	165.1	58	39.7	124.0	165.1
	BB	12	47.2	82.5	86.7	29	60.3	142.3	150.7
	AB	33	52.1	153.9	160.3	37	59.5	134.4	138.8
	BA	43	64.1	142.0	142.9	53	49.7	116.4	144.4

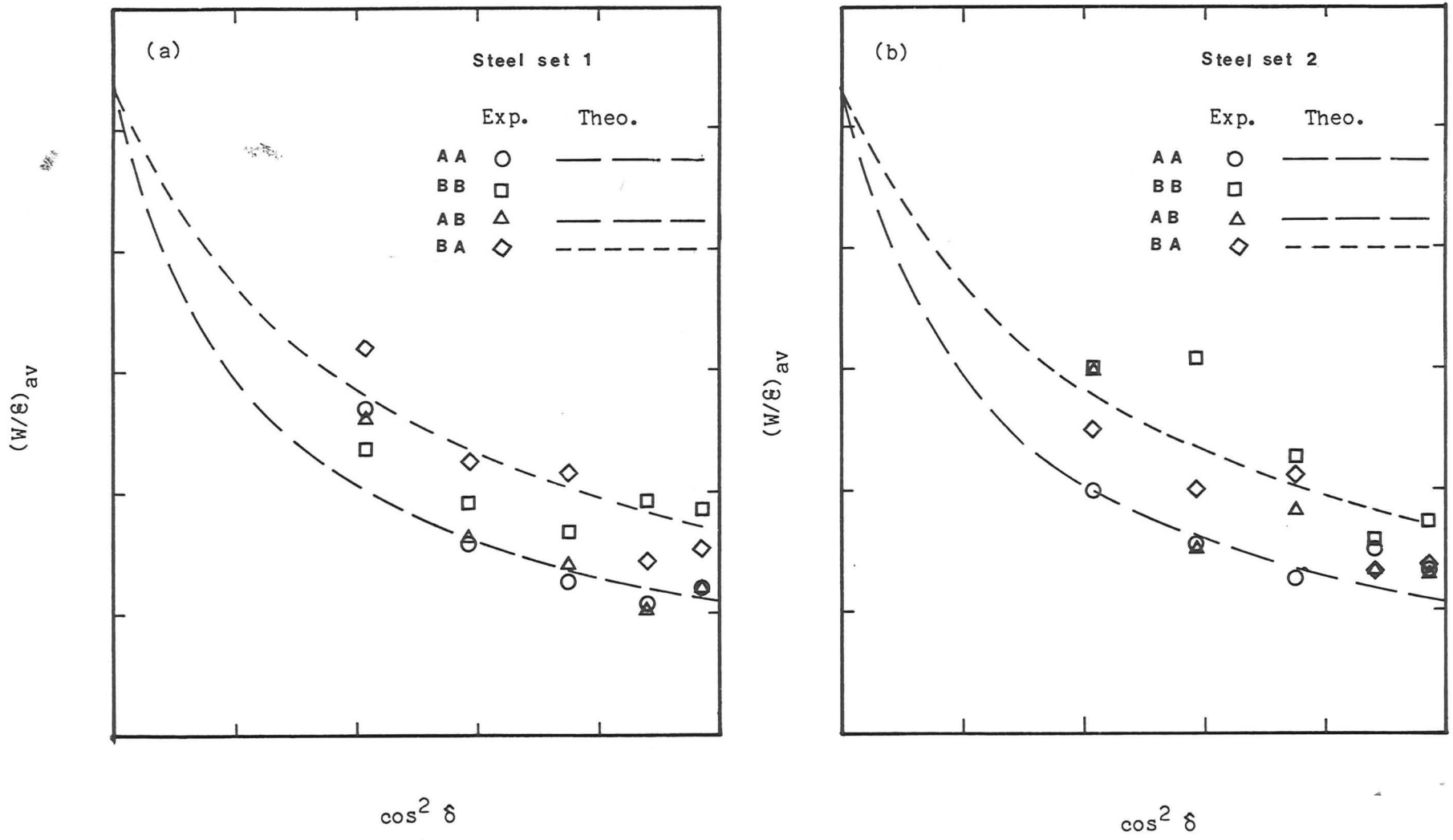

Figure 6.4-13 Experimental and theoretical relations between $(W/\mathcal{E})_{av}$ and $\cos^2 \delta$ for different types of region.

7. CONCLUSIONS

This chapter summarizes and brings together the main conclusions drawn in various places in the dissertation. Suggestions are also given for further research.

7.1 Summary

In this dissertation, a new method of representing the tension stiffening of cracked tensile concrete, by modifying the properties of the tension steel, is developed as described in detail in Chapter 3. This new method is extended to cover situations in which the tension steel crosses the crack at an angle as it has been done in Chapter 5. The various theoretical curves thus obtained were compared with experimental results from tests on slabs with skew reinforcement carried out by the author and described in detail in Chapter 4; good agreement was obtained. The modified steel properties were successfully used in a computer program that analyses r. c. bending members by the no-tension concept to obtain the moment-curvature relations for the slabs of Chapter 4.

A new hypothesis is given in Chapter 6 for cracking over steel bars when they cross the cracks at an angle. This came as a result of experimental observations of analysis on more than 4200 crack width measurements taken during the slab test (Chapter 4) plus some theoretical considerations. A procedure is also given for calculating the crack width at any point on the surface of a r.c. member taking into account the

interaction between the two intersecting sets of steel reinforcement.

7.2 Modified Steel Properties

The modified stress - strain curve for steel developed in Chapter 3 was based on experimental results from tests on beams and slabs by Clark et al [51], [57]. The following were conclusions drawn from the analysis of these results.

(1) The modified steel properties are stiffer than those of a bare steel bar with an enhanced steel stress σ_{se} (corresponding to a mean steel strain over a long gauge length) equal to the mean steel stress plus the tension force F_t contributed by concrete divided by the steel area (Equation 3.2-7). The enhanced steel stress σ_{se} is also equal to the steel stress at a major crack.

(2) The tension stiffening force F_t (Equation 3.4-1) is basically a direct function of the tensile strength of concrete, the average area of concrete in the tension zone, and a function of the factors β and α (see 3 and 4 below).

(3) The factor β (Equation 3.4-14), defining the effective area of concrete contributing to the tension stiffening, was found to be a function of the effective steel ratio ρ_e and the cover ratio c' after neglecting the effect of bar spacing (definitions are given by Equations 3.4-4 to 3.4-6).

(4) The factor α (Equations 3.4-18 and 3.4-28) describes the manner in which the tension stiffening force F_t attains its peak value

and then decays to zero as the average strain at the steel level reaches its yield value. By definition, α is equal to the average concrete tensile stress as a proportion of the average tensile stress in concrete when F_t equals its peak value. It was found that α is a function of, mainly, the strain ratio ε_{sr} (equal to $\varepsilon_{sm}/\varepsilon_{sp}$ or $\varepsilon_{sp}/\varepsilon_{sm}$ and always less than unity), and of β and the ratio $\varepsilon_{sp}/\varepsilon_{scr}$; where ε_{sm}, ε_{sp} and ε_{scr} are the mean strain at the load stage considered, at peak F_t and at cracking respectively.

(5) The ratio $\varepsilon_{sp}/\varepsilon_{scr}$ (Equation 3.4-26) was found to be a function of the effective steel ratio ρ_e", bar spacing s", and the depth ratio y_s" of the steel below the neutral axis (Equations 3.4-19 to 3.4-21).

(6) The line of action of the total tensile force starts at a depth d_t (below the n. a.) equal to 2/3rd of the tension zone height and then, as the strain increases, moves towards the steel level. Once cracks are well established (i.e. after the peak tension stiffening is attained and major cracks have ceased to form), the only way the tensile forces can be transmitted across major cracks is through the tension steel. Hence, beyond some limiting steel-level strain ε_{slim}, the total tensile force will act at that level.

(7) The limiting strain ε_{slim} (Equation 3.4-34) was found to be a function of the steel strain at cracking ε_{scr} (Equation 3.4-17), the effective steel percentage ρ_e", and the cover ratio c" (Equation 3.4-32).

7.3 Effect of Angle of Steel Skewness δ on Tension Stiffening

Consideration of Tension Stiffening force - steel strain relations led to the following main conclusions:

(1) The peak value of F_t increases with an increase in the angle δ enclosed by the steel bars and the principal bending directions.

(2) The rate of the initial breakdown of tension stiffening decreases as the angle δ increases.

The effect of the angle δ was allowed for by modifying the ratios ρ_e, s', and c' (Equations 3.4-4 to 3.4-6) and the ratios ρ_e", s", and c" (Equations 3.4-19, 3.4-20, and 3.4-32). This can be summarized as follows:

(i) The effective steel area A_{se} is equal to the cross-sectional steel area A_s times the 4th power of cosine the angle δ according to Equation 5.3-1.

(ii) The effective mean bar spacing s_{em} is equal to 3/4 of the average spacing of the two sets of bars divided by cosine the angle δ (Equation 5.3-2).

(iii) The effective cover c_e is equal to the cover c times $\cos^2 \delta$ (Equation 5.3-3).

Theoretical curves of F_t versus ε_{sm} and of σ_{se} versus ε_{sm}, obtained using the above modifications, showed good agreement with the test results, especially in the early stages of loading.

7.4 Modelling of Tension Stiffening

The 'enhanced stress' - strain curve for the tension steel was used successfully in modelling the tension stiffening of concrete in a computer program that predicts the moment - curvature response of r.c. bending members by means of no-tension concept. The theoretical moment - curvature curves were found by calculating the values of the bending moment that correspond to assumed values of the curvature. The procedure used (Subsection 5.3.2) is similar to subroutines usually used in a finite element program to solve a global structural problem.

The computer program used in the analysis of results presented in Chapter 5 employed a layered approach with 10 layers in the compression zone with concrete material and one layer in the tension zone with steel material that has modified properties. Nonlinearity of both materials has been taken into account and thus the material properties matrix is updated at each step of calculation according to the nonlinear stress - strain curves of concrete and steel.

Since the enhanced steel stress σ_{se} is mainly a function of the tension zone properties, it can directly be used in conjunction with the layered finite element technique to analyse r.c. member under combined bending moments and normal forces.

7.5 Crack Widths in a General Situation

Analysis of more than 4200 crack width measurements from tests on slabs with skew reinforcement carried out by the author (Chapter 4) provided information on the effect of the angle δ on crack widths.

Based on experimental observations and some theoretical considerations (Subsections 6.4.2 and 6.4.3) a hypothesis is given for cracking over reinforcing bars that cross the cracks at an angle. This hypothesis may be outlined briefly as follows:

(1) The crack pattern at a position away from reinforcement is governed by the initial crack height h_o assuming a minimum amount of steel in the principal bending direction. The crack width W_{lim} for this pattern was first given by Beeby [19] (Equation 2.2-12).

(2) The addition of a steel bar in the crack direction should not in theory affect the crack pattern.

(3) As the angle δ between the reinforcement direction and that normal to the cracks decreases, the initial crack pattern is gradually modified until, at $\delta = 0^o$, the crack pattern associated with steel bars that crosses the cracks at right angles is obtained. The crack width W_o for this pattern (in slabs) was first given by Beeby [19],[33] (Equation 2.2-15).

(4) The amount of modification made to the initial crack pattern by the skew steel bar was found to depend on $\cos^2 \delta$.

Thus the crack width over a bar varies with δ from W_o when δ is 0^o to W_{lim} when δ is 90^o according to the new formula given in Section 6.4.3 (Equation 6.4-2).

A procedure is given in Section 6.5 for predicting crack widths at any point on the surface of r. c. bending members. The procedure takes into account the effects of the angle δ of steel skewness and of the interaction between two sets of reinforcing bars on crack widths.

The interaction between the two intersecting sets of bars is concidered by its effect on the value of the distance a_{cr} from the point of interest to the nearest steel bar. With only one set of bars, a_{cr} can have a fixed value along lines parallel to the bars, whereas, in the presence of two intersecting sets of bars, a_{cr} varies from one point to another on a line parallel to the bars. It might therefore be useful to divide the slab surface into regions according their position in relation to both sets of bars. In this case, the value of a_{cr} will vary less within one region than along a grid line.

Finally, the distance a_{cr} should be measured in the cracks' direction rather than in a direction normal to the reinforcing bar. The crack widths can then be predicted for any of these regions.

7.6 Further Research

It is suggested that further experiments be conducted on slabs with skew steel reinforcement, this time allowing shear displacement to take place across the cracks in order to study the effect of shear on crack widths.

Another research area would be the testing of the enhanced steel properties as a tension stiffening model in a finite element programme against more experimental data especially those from members tested under combined bending and membrane forces.

REFERENCES

In the following list, only references directly relevant to the dissertation are given. The list is arranged chronologically.

[1] (0080's) John Ben Zebedee: "The Gospel (i.e. Good News) of Jesus Christ". New Testament, Holy Bible. New International Version. Hodder and Stoughton. Chapter 1, Verse 12.

[2] (1965, January) B.B. BROMS: "Techniques for investigation of internal cracks in reinforced concrete members." Journal of the ACI. pp.35 - 44.

[3] (1965, September) B.B. BROMS: "Stress distribution in reinforced concrete members with tension cracks." Journal of the ACI. pp.1095 - 1108.

[4] (1965, September) A. ATLAS, M. RAPHAEL, and R. SHALON, L.A. LUTZ: "Discussion of 'Techniques for investigation of internal cracks in reinforced concrete members,' by B.B. Broms." Journal of the ACI, Detroit. pp.1139 - 1143.

[5] (1965, October) B.B. BROMS: "Crack width and crack spacing in reinforced concrete members." Journal of the ACI, pp.1237 - 1255.

[6] (1965, November) B.B. BROMS, and A. LUTZ: "Effects of arrangement of reinforcement on crack width and spacing of reinforced concrete members." Journal of the ACI. pp.1395 - 1409.

[7] (1966, June) G.D. BASE, A.W. BEEBY, J.B. READ, and H.P.J. TAYLOR; A. HELFGOT; N. SWAMY, and D. ADEPEGBA: "Discussion of 'Crack width and crack spacing in reinforced concrete members,' by B.B. Broms." Journal of the ACI. Part 2. pp.1749 - 1755.

[8] (1966, June) S. MORITA, B.B. BROMS, and A. LUTZ: "Discussion of 'Effects of arrangement of reinforcement on crack width and spacing of reinforced concrete members,' by B.B. Broms and A. Lutz." Journal of the ACI. Part 2. pp.1807 - 1812.

[9] (19 66, December) G.D. BASE, J.B. READ, A.W. BEEBY, and H.P.J. TAYLOR: "An investigation of the crack characteristics of various types of bar in reinforced concrete beams." Cement and Concrete Association (C&CA), London. Research Report No.18 - Part 1. pp.44.

[10] (1966, December) G.D. BASE, J.B. READ, A.W. BEEBY, and H.P.J. TAYLOR: "An investigation of the crack characteristics of various types of bar in reinforced concrete beams." Cemennt and Concrete Association. Research Report No.18 - Part 2. pp.31.

[11] (1966) J. PETER: "Zur bewehrung von scheiben und schalen fur hauptspannungen scheifwinklig zur bewehrungscrichtung." Die Bautechnik 43.H.5, S.149 - 154; H.7, S.240 - 248.

[12] (1967, March) D. NGO, and A.C. SCORDELIS: "Finite element analysis of reinforced concrete beams." Journal of the ACI, Detroit. pp.152 - 163.

[13] (1967, May) R. LENSCHOW, and M.A. SOZEN: "A yield criterion for reinforced concrete slabs. Journal of the ACI. pp.266 - 273.

[14] (1968, January-February) R.H. EVANS, and M.S. MARATHE: "Microcracking and stress-strain curves for concrete in tension." Materiaux et constructions No.1. pp.61 - 64.

[15] (1968, May) A.E. CARDENAS, and M.A. SOZEN: "Strength and behaviour of isotropically reinforced concrete slabs to combinations of flexural and torsional moments." Civil Engineering Studies. Structural Research Report No.336, University of Illinois. Urbana, Illinois. pp. 250.

[16] (1968, June) S.I. HUSAIN, and P.M. FERGUSON: "Flexural crack widths at the bar in reinforced concrete beams." Center for Highway Research, University of Texas at Austin. Research Report no.102-IF. 44p.

[17] (1968) E.G. NAWY: "Crack width control in welded fabric reinforced centrally loaded two-way concrete slabs." Causes, Mechanism, and Control of Cracking in Concrete." American Concrete Institute Publication SP-20, Detroit. pp.211 235.

[18] (1970, March) E.G. NAWY and G.S. ORENSTEIN: "Crack width control in reinforced concrete two-way slabs." Proceedings of the American Society of Civil Engineers (Proc. of the ASCE). Vol.93,No.ST3. pp.701 - 721.

[19] (1970, April) A.W. BEEBY: "An investigation of cracking in slabs spanning one way." C&CA, London. Technical Report No.TRA 433. pp.31.

[20] (1970, June) COMITE EUROPEEN DU BETON/FEDERATION INTERNATIONALE DE LA PRECONTRAINTE. International recommendations for the design and construction of concrete structures. London. pp.80.

[21] (1970, November) L.A. CLARK: "The provision of reinforcement in simply supported skew bridge slabs in accordance with elastic moment fields." C&CA, London. Technical Report No.42.450. pp.18.

[22] (1971, March) L.A. CLARK: "Crack similitude in 1/3.7 scale models of slabs spanning one way." C&CA, London. Technical Report No.42.455. pp.24.

[23] (1971, March) J.C. JOFRIET and G.M. McNEICE: "Finite element analysis of reinforced concrete slabs." Journal of the Structural Division (Journal of the Struct. Div.). Proceedings of the American Society of Civil Engineers (Proc. of the ASCE). No.ST3. pp.785 - 806.

[24] (1971, April) Y. GOTO: "Cracks formed in concrete around deformed tension bars." Journal of the ACI. pp.244 - 251.

[25] (1971) A.W. BEEBY: "The prediction of cracking in reinforced concrete members." Thesis submitted to the University of London for the degree of PhD. pp. 252.

[26] (1971) A. SCANLON: "Time dependent deflections of reinforced concrete slabs." Thesis presdented to the University of Alberta, at Edmonton, Alberta, Canada, in partial fulfilment of the requirements for the degree of Doctor of Philosophy.

[27] (1971, December) A.W. BEEBY: "An investigation of cracking on the side faces of beams." C&CA, London. Technical Report No.42.466. pp.11.

[28] (1971) AMERICAN CONCRETE INSTITUTE. Building code requirements for reinforced concrete. (ACI318-71). Detroit.

[29] (1971) E.G. NAWY and K.W. BLAIR: "Further studies on flexural crack control in structural slab systems." Cracking, Deflection, and Ultimate Load of Concrete Slab Systems. American Concrete Institute Publication SP-30, Detroit. pp.1-42.

[30] (1971) J. DIAZPADILLA and F. ROBLES: "Human response to cracking in concrete slabs." Cracking, Deflection, and Ultimate Load of Concrete Slab Systems. American Concrete Institute Publications, SP-30, Detroit. pp.43 - 54.

[31] (1971) J.C. BELL and D.G. ELMS: "A finite element approach to post elastic slab behaviour." Cracking, Deflection, and Ultimate Load of Concrete Slab Systems. American Concrete Institute Publication, SP-30, Detroit. pp.325 - 344.

[32] (1972, May) L.A. CLARK: "The service load response of short-span skew slab bridges designed by yield-line theory." C&CA, London. Technical Report No.42.464. pp.40.

[33] (1972, June) A.W. BEEBY: "A study of cracking in reinforced concrete members subjected to pure tension." C&CA, London. Technical Report No.42.468. pp.25.

[34] (1972, September) L.A. CLARK: "Tests on slab elements and skew slab bridges designed in accordance with the factored elastic moment field." C&CA, London. Technical Report No.42.474. pp.46.

[35] (1972, November) A.E. CARDENAS, R.J. LENSCHOW and M.A. SOZEN: "Stiffness of reinforced concrete plates.". Journal of the Struct. Div. Proc. of the ASCE. No.ST11. pp.2587 - 2603.

[36] (1972, December) J.M. ILLSTON and R.F. STEVENS: "Long-term cracking in reinforced concrete beams." Proceedings of the Institute of Civil Engineers (Proc. of ICE). Part II, Research and Theory. Vol.53, pp. 445 - 459.

[37] (1972) BRITISH STANDARDS INSTITUTION, CP110. The structural use of concrete. Part 1: Design, materials and workmanship. London. pp.154.

[38] (1973, May) L.A. CLARK: "Flexural cracking in slab bridges." C&CA, London. Technical Report No.42.479. pp.12.

[39] (1973, May) P.S. RAO and B.V. SUBRAHMANYAN: "Trisegmental moment-curvature relations for reinforced concrete members. Journal of the ACI, Detroit. pp.346 - 351.

[40] (1973, July) F.R. HAND, D.A. PECKNOLD and W.C. SCHNOBRICH: "Nonlinear layered analysis of reinforced concrete plates and shells." Journal of the Structural Division. Proc. of ICE. No.ST7. pp.1491 - 1505.

[41] (1973) J.-C. DOTREPPE, W.C. SCHNOBRICH and D.A. PEACKNOLD: "Layered finite element procedure for inelastic analysis of reinforced concrete slabs." International Association for Bridge and Structural Engineering. Vol.33-II. pp.53 - 68.

[42] (1973)P.E. REGAN and C.W. YU: "Limit state design of structural concrete." London. Chatto and Windus.

[43] (1974, October) L.A. CLARK: "Flexural crack similitude in slabs spanning one way." C&CA, London. Technical Report No.42.496. pp.25.

[44] (1975, January) M.K. WANCHOO and G.W. MAY: "Cracking analysis of reinforced concrete plates." Journal of the Struct. Div. Proc. of the ASCE. No.ST1. pp.201 - 215.

[45] (1975, March) C.-S. LIN and A.C. SCORDELIS: "Nonlinear analysis of reinforced concrete shells of general form." Journal of the Struct. Div. Proc. of the ASCE. No.ST3. pp.523 - 538.

[46] (1975) D.C. Teychenne, R.E. Franklin, and H.C. Erntroy: "Design of normal concrete mixes." Department of the Environment, London. pp 31.

[47] (1976, November) COMITE EUROPEEN DU BETON/FEDERATION INTERNATIONALE DE LA PRECONTRAINTE. Model Code for Concrete Structures. London. (3rd Edition, 1978. pp.348).

[48] (1976) BRITISH STANDARDS INSTITUTION, BS5337. Code of practice for the structural use of concrete for retaining aqueous liquids. London.

[49] (1977) W.C. SCHNOBRICH: "Behaviour of reinforced concrete structures predicted by the finite element method." Computers and Structures. Vol.7. pp.365 - 376. Pergamon Press.

[50] (1978, April) R.P. JOHNSON and C. ARNAOUTI: "Cracking in composite bridge decks in uniaxial and biaxial tension." University of Warwick Engineering Department. Final Report No.9. pp.40.

[51] (1978, July) L.A. CLARK and D.M. SPEIRS: "Tension stiffening in reinforced concrete beams and slabs under short-term loading." C&CA, London. Technical Report No.42.521. pp.19.

[52] (1978, July) A.W. BEEBY: "Cracking - What are crack width limits for?" Concrete. Vol.12, No.7. pp.31 - 33.

[53] (1978, December) R.I. GILBERT and R.F. WARNER: "Tension stiffening in reinforced concrete slabs." Journal of the Struct. Div. Proc. of the ASCE. STI12. pp.1885 - 1900.

[54] (1979, January) A.W. BEEBY. "The prediction of crack widths in hardened concrete." The Structural Engineer. Vol.57A, No.1. pp.9 - 17.

[55] (1979, August) O.K. HILLINGSTAD, T.O. OLSEN and O.J. STOVE: "Practical design of reinforcement in plates and shells including the effects of reinforcement directions, crack widths, and imposed deformation." Boss '79. Second International Conference on Behaviour of Offshore Structures. Held at Imperial College, London. pp.267 - 280.

[56] (1979, December) P. DESAYI and A. PRABHAKARA: "Determination of maximum crack width in reinforced concrete skew and rectangular slabs." Proc. of ICE. Vol.67, Part2. pp.1077 - 1090.

[57] (1979) L.A. CLARK and W.B. CRANSTON: "The influence of bar spacing on tension in reinforced concrete slabs." Proceedings of the International Conference on Concrete Slabs, Dundee. pp.25 - 38.

[58] (1979) A.W. BEEBY: "Cracking and corrosion." Concrete in the Oceans. Technical Report No.1. Cement and Concrete Association, Department of Energy. Ref.15.286. pp.77.

[59] (1979) P.G. BERGAN and I. HOLLAND: "Nonlinear finite element analysis of concrete structures." Computer Methods in Applied Mechanics and Engineering. Vol.17/18. pp.443 - 467. Published by North-Holland.

[60] (1980, September) R.J. COPE, P.V. RAO and K.R. EDWARDS: "Nonlinear finite element analysis techniques for concrete slabs." Numerical Methods of Nonlinear Problems. Vol.1. Proceedings of the International Conference, University College, Swansea. pp.445 - 456.

[61] (1980, September) R.J. COPE, P.V. RAO, L.A. CLARK and P. NORRIS: "Modelling of reinforced concrete behaviour for finite element analysis of bridge slabs." Numerical Methods for Nonlinear Problems. Vol.1. Pro. of the Int. Conf. University College, Swansea. pp.457 - 470.

[62] (1980, September) H.H. ABDEL RAHMAN, E. HINTON and M.M. HUQ: "Nonlinear finite element analysis of reinforced concrete slab and slab-beam structures." Numerical Methods for Nonlinear Problems. Vol.1. Proc. of the Int. Conf. University College, Swansea. pp.493 - 502.

[63] (1980, September-October) G.C. FRANTZ and J.E. BREEN: "Cracking on the side faces of large reinforced concrete beams." Journal of the ACI. pp.307 - 313.

[64] (1980, October) AMERICAN CONCRETE INSTITUTE. Control of cracking in concrete structures. ACI Committee 224. Concrete International. pp.35 - 76.

[65] (1980, October) A.W. BEEBY, et.al.: "Discussion of 'The prediction of crack widths in hardened concrete,' by A.W. Beeby." The Structural Engineer. Vol.58A, No.10. pp.326 - 332.

[66] (1980, December) V.A. PULMANO and R.F. WARNER: "Serviceability tests of prestressed concrete beams." UNICIV Report No.R-198. The Univeristy of New South Wales, Kensington, NSW, Australia. pp.42.

[67] (1981) F. VECCHIO and M.P. COLLINS: "Stress-strain characteristics of reinforced concrete in pure shear." Advanced Mechanics of Reinforced Concrete. International Association for Bridge and Structural Engineering. Colloquium. Delft.

[68] (1981) R.J. COPE and P.V. RAO: "Nonlinear finite element strategies for bridge slabs." Advanced Mechanics of Reinforced Concrete. IABSE. Colloquium, Delft. pp.275 - 290.

[69] (1981) H.A. MANG H. FLOEGL: "Tension stiffening concept for reinforced concrete surface structures." Advanced Mechanics of Reinforced Concrete. IABSE. Colloquium, Delft. pp.331 - 349.

[70] (1981) W. MOOSECKER and E. GRASSER: "Evaluation of tension stiffening effects in reinforced concrete linear members." Advanced Mechanics of Reinforced Concrete. IABSE. Colloquium, Delft. pp.541 - 550.

[71] (1981) P.E. REGAN and Y.D. HAMADI: "Behaviour of concrete caisson and lower members." Concrete in the Oceans. Technical Report No.4 (Ref.15.611), Part 2: Axial tensile tests of reinforced concrete. C&CA, Department of Energy, London. pp.36 - 82.

[72] (1981) J.C. WALRAVEN and H.W. REINHARDT: "Theory and experiments on the mechanical behaviour of cracks in plain and reinforced concrete subject to shear loading." Concrete Mechanics. Vol.26, No.1A. Heron. pp.68.

[73] (1982, March) M.A. CRISFIELD: "Local instabilities in the nonlinear analysis of reinforced concrete beams and slabs." Proc. of ICE. Vol.73, Part 2. pp.135 - 145.

[74] (1982, December) H. FLOEGL and H.A. MANG: "Tension stiffening concept based on bond slip." Journal of the Struct. Div. Proc. of the ASCE. No. ST12. pp.2681 - 2701.

[75] (1983, February) A.W. BEEBY: "Cracking, cover, and corrosion of reinforcement." Concrete International. pp.35 - 40.

[76] (1983, June) A. NEVILLE: "Corrosion of reinforcement." Concrete. pp. 48 - 50.

[77] (1983) J.A. STILLWELL: "Exposure tests on concrete for offshore structures." Concrete in the Oceans. Technical Report No.8 (Ref. 15.638). C&CA, London.